

Petrogenesis of basanite-phonolite series of an oceanic intraplate volcano: combining experimental data and field observations

Experimental constraints on the magma storage conditions and melt evolution of the Cumbre Vieja volcano (La Palma, Canary Islands)

Von der Naturwissenschaftlichen Fakultät der
Gottfried Wilhelm Leibniz Universität Hannover

zur Erlangung des Grades
Doktorin der Naturwissenschaften (Dr. rer. nat.)

genehmigte Dissertation
von
M.Sc. Parveen Fuchs
geboren am 17.05.1983 in Bielefeld

2014

Referent: Prof. Dr. rer. nat. François Holtz

Korreferenten: Prof. Dr. rer. nat. Andreas Klügel

Tag der Promotion: 04.08.2014

Erklärung zur Dissertation

Hierdurch versichere ich, dass ich die Dissertation selbstständig verfasst und alle benutzten Hilfsmittel und Quellen sowie evtl. zur Hilfestellung herangezogene Institutionen vollständig angegeben habe. Die Dissertation wurde nicht schon als Diplomarbeit oder ähnliche Prüfungsarbeit verwendet.

Hannover, den 23.04.2014

Parveen Fuchs

Acknowledgements

This study was conducted at the institute of mineralogy at the Leibniz Universität Hannover under the supervision of Dr. Renat Almeev, Prof. Dr. François Holtz and PD Dr. Andreas Klügel from Universität Bremen. I would like to express my very great appreciation to Dr. Renat Almeev and PD Dr. Andreas Klügel for initiating the DFG project (Project AL 1189/2-1) and for giving me the opportunity to work on this project. Their intense supervision, support and patient guidance over the past three years was very helpful to me. I am very thankful for their confidence and encouragement and for giving me the chance to work independently on this research project. Special thanks to PD Dr. Andreas Klügel for providing the samples, the very nice and informative field trip to La Palma and for sharing his compelling knowledge and expertise of the Cumbre Vieja system.

Furthermore, I would like to thank Prof. Dr. Harald Behrens, Dr. Roman Botcharnikov and Dr. Francesco Vetere for many lively discussions and their constructive comments on various parts of this project.

I also would like to extend my grateful acknowledgements to all the technicians in the workshop, Ulrich Kroll, Björn Ecks, Fabian und Manuel Christ, Otto Dietrich and Julian Feige, especially for their fast and reliable support in the sample preparations and for solving the countless technical issues encountered during the project.

Many thanks to all my colleagues, especially Adrian Fiege, Andre Stechern, Alexander Bartels, Malte Junge, Eric Wolf, Anika Husen and Insa Derrey.

Finally, I want to thank Clemens Kirchner und my sister Nilam Fuchs for their encouragement throughout the last years.

Contents

Abstract	11
Zusammenfassung.....	13
1. Introduction	17
1.1 Previous studies on phonolitic rocks	18
1.2 Experimental strategy of our study	20
2. Geological setting	21
2.1 Model of magma plumbing system beneath Cumbre Vieja volcano.....	28
2.2 Prediction of the natural LLD by thermodynamic calculations	30
3. Experimental Methods	32
3.1 Starting Material.....	32
3.2 Experimental setup.....	35
3.3 Fe pre-saturation of the capsule material.....	35
3.4 Analytical techniques.....	36
3.4.1 Electron-probe microanalysis	36
3.4.2 Karl-Fischer titration	37
3.4.3 Fourier transform infrared spectroscopy	37
3.4.4 Determination of Fe^{2+} and Fe^{3+}	38
3.5.1 Calculation of $a\text{H}_2\text{O}$ and $f\text{O}_2$	41
3.5.2 Calculation of $\text{Fe}^{2+}/\Sigma\text{Fe}$ ratio in glasses	45
4. Results.....	48
4.1 Phase relations	48
4.2 Phase proportions.....	57
4.2.1 Solid phase proportions	57

4.2.1 Melt proportions.....	64
4.3 Phase compositions	69
4.3.1 Olivine.....	69
4.3.2 Pyroxene.....	77
4.3.3 Amphibole	89
4.3.4 Plagioclase	90
4.3.5 Spinel.....	93
4.3.6 Glass	105
4.3.7 Effect of $f\text{O}_2$ conditions on glass compositions.....	105
4.3.8 Effect of $a\text{H}_2\text{O}$ and temperature on glass compositions	107
4.3.9 Effect of mineral assemblages on glass compositions	110
4.4 Experiments with tephriphonolite.....	117
4.4.1 Mineral compositions.....	120
4.4.1.1 Pyroxene.....	120
4.4.1.2 Amphibole	123
4.4.1.3 Magnetite	124
4.4.1.3 Glass	125
5. Discussion.....	129
5.1 Melt compositions	129
5.1.1. Database used in discussion	129
5.1.2 Effect of redox conditions on the liquid line of descent	129
5.1.3 Effect of $a\text{H}_2\text{O}$ on the liquid line of descent	130
5.1.5 Effect of pressure on the liquid line of descent.....	134
5.2 Mineral compositions	135
5.2.1 Comparison of olivine compositions.....	135

5.2.2 Comparison of Cpx compositions	136
5.2.2.1 Clinopyroxene-melt barometry	138
5.2.3 Comparison of amphibole compositions	142
5.2.4 Comparison of spinel compositions.....	144
5.3 Pre-eruptive storage conditions.....	147
5.3.1 Primitive basanite (168-1).....	147
5.3.2 Evolved basanite (KLA-1-6-22).....	147
5.3.3 Tephriphonolite (PF22; Wengorsch, 2013)	148
5.4 Open versus closed system fractionation	150
6. Conclusions	152
7. References	155
Appendix.....	161

Abstract

Eruptive products of the recent Cumbre Vieja volcano (CV) cover a large spectrum of alkali-rich rocks ranging from basanites to phonolites. The current model of magma plumbing beneath the Cumbre Vieja volcano is largely based on barometric studies of phenocrysts and xenoliths and includes three major intervals of magma stagnation and fractionation at mantle and crustal depths (Klügel et al., 2005). However, the relative influence of different thermodynamic parameters on phase equilibria is still unknown. We present results of an experimental study aimed for evaluating p - T - $a\text{H}_2\text{O}$ - $f\text{O}_2$ conditions in the genesis of a basanite-tephrite-phonolite system. High pressure and temperature experiments in the presence of H_2O - CO_2 fluid ($X_{\text{H}_2\text{O}}$ varied between 0-1, keeping $f\text{O}_2$ between $\sim\text{FMQ}$ and $\text{FMQ}+3.8$) were conducted in an internally heated pressure vessel using two natural basanites (700, 550, 400 MPa; 1010-1175°C) with 14 wt.% and 9 wt.% of MgO and a tephriphonolite (400 and 200 MPa; 950-1100°C; Wengorsch, 2013) with 2.8 wt.% of MgO, respectively, representing three differentiation stages in the evolution of CV magmas. Compositions and proportions of experimental phases were determined by electron microprobe and compared to their natural counterparts.

The natural phase assemblage (Ol+Cpx+Spl) in the range of natural mineral compositions was reproduced at 400 and 700 MPa, 1100-1125°C, 1.3-2.2 wt.% H_2O in the melt (H_2O^m) and $f\text{O}_2$ conditions of FMQ+1.3 to FMQ+2.3 for the primitive basanite and at 400 and 550 MPa, 1125-1175°C, 1.5-2.2 wt.% H_2O^m and $f\text{O}_2$ conditions of FMQ+1.1 to FMQ+2.3 for the evolved basanite. Tephritic residual melts were generated by $\pm\text{Ol}+\text{Cpx}\pm\text{Amph}+\text{Spl}$ crystallization at 400, 550 and 700 MPa, 1010-1175°C, H_2O^m between 1.0-6.3 wt.% and $f\text{O}_2$ conditions of FMQ+1.1 to FMQ+3.3. However, tephritic residual melts resemble the natural LLD only if the proportion of Cpx is below 32%, because higher proportions of Cpx result in strong CaO depletion in the residual melt and deviations from the natural trend. Those conditions were achieved at 700 and 400 MPa for the primitive basanite and 550 and 400 MPa for the evolved basanite. Phonotephritic melts were generated by $\text{Cpx}\pm\text{Ol}\pm\text{Krs}+\text{Mt}\pm\text{Ap}$ crystallization at 400 and 700 MPa, 1050-1100°C and 0.5-2.5 wt.% H_2O^m and $f\text{O}_2$ conditions of FMQ+1.0 to FMQ+2.5. Tephriphonolitic melts were generated by $\pm\text{Ol}+\text{Cpx}+\text{Pl}\pm\text{Krs}-\text{Mt}+\text{Ap}$ crystallization at 400 MPa,

1050-1025°C, 0.7-1.1 wt.% H₂O^m and *fO₂* conditions of FMQ+0.5 to FMQ+1.6. The natural mineral assemblage of the tephriphonolite (Cpx+Krs+Pl+Mt+Ap) in the compositional range of natural minerals, was reproduced in equilibrium with a phonolitic melt at 200 MPa, 950-1000°C, 0.5-2.0 wt.% H₂O in the melt and *fO₂* conditions of FMQ to FMQ+1.8 and at 400 MPa, 900-1000°C and 0.5-3.1 wt.% H₂O in the melt and *fO₂* conditions of FMQ to FMQ+2.2 (Wengorsch et al, 2013).

Slightly reducing conditions of FMQ+1 to FMQ+2 are crucial for the evolution of alkali-rich, silica undersaturated melts, because higher *fO₂* results in extensive Mt crystallization leading to Qz-normative residual liquids instead of Ne-normative. Natural variations in CaO, Al₂O₃ in evolved rocks can be explained by different proportions of Amph and Cpx depending on *aH₂O* and temperature. At low *aH₂O* and high temperature Cpx predominates over Amph in the Cpx+Amph assemblage resulting in CaO depletion and relative enrichment in Al₂O₃ in the residual melt. At high *aH₂O* and low temperature Amph predominates over Cpx resulting in less pronounced enrichment of Al₂O₃ and higher CaO contents in the residual melt. However, Krs is an amphibole that can be stable even in melts with <1 wt.% H₂O^m (>0.1 X_{H₂O}), suggesting that CV melts can be H₂O-poor even in evolved magmas.

Our results indicate that single-step differentiation (by equilibrium crystallization) from basanites to phonotephrites is possible in a pressure range of at least 400 to 700 MPa. At 700 MPa Pl crystallization in basanites is suppressed, indicating that tephriphonolitic or phonolitic melts can only be generated at lower pressures or from parent more evolved than basanite in a closed system. From our experimental data we can assume that genesis of tephriphonolitic and phonolitic magmas can occur up to pressures of at least 400 MPa, which is in contrast to the relatively low pre-eruptive storage pressures of phonolites from comparable systems (e.g. 200-250 MPa for Kerguelen (Freise et al., 2003) and 130 MPa for El Abrigo, Tenerife (Andujar et al., 2008)).

Keywords: La Palma, liquid line of descent, phonolite-basanite

Zusammenfassung

Der aktive Cumbre Vieja Vulkan (La Palma, Kanarische Inseln) zeigt ein breites Spektrum an alkalireichen Gesteinen, das von primitiven Basaniten zu entwickelten Phonoliten reicht. Das derzeitig akzeptierte Modell der Magmaförderung unterhalb des Cumbre Vieja Vulkans (CV) basiert überwiegend auf barometrischen Untersuchungen von Phänokristallen und Xenolithen. Dieses Modell umfasst drei Hauptintervalle von Magmenstagnation und Magmenfraktionierung innerhalb des Mantels und der Kruste (Klügel et al., 2005). Der relative Einfluss von thermodynamischen Parametern auf die Phasenbeziehungen ist bis heute allerdings ungeklärt. Ziel dieser Arbeit ist es, die herrschenden p - T - αH_2O - fO_2 Bedingungen zu ermitteln, die bei der Genese eines Basanit-Tephrit-Phonolit Systems von Bedeutung sind. Dafür wurden Hochdruck- und Hochtemperatur-Experimente in Anwesenheit eines H_2O - CO_2 Fluides (XH_2O : 0-1, fO_2 : FMQ - FMQ+3.8) in intern beheizten Hochdruck-Autoklaven durchgeführt. Als Startmaterialien für die Experimente wurden zwei natürliche Basanite (Experimentelle Bedingungen: 700, 550, 400 MPa; 1010-1175°C) mit 14 Gew.% (primitiver Basanit) und 9 Gew.% MgO (entwickelter Basanit) und ein Tephriphonolith (Experimentelle Bedingungen: 400 und 200 MPa; 950-1100°C; Wengorsch, 2013) mit 2.8 Gew.% MgO genutzt, da sie repräsentative Stadien der Differentiation in der Entstehung der CV Magmen nachbilden. Die chemische Zusammensetzung der experimentell synthetisierten Phasen wurde mittels Elektronenstrahlmikrosonde und Phasenanteile anhand von Massenbilanzen bestimmt und darauffolgend mit ihrem natürlichen Äquivalent verglichen.

Die natürliche Paragenese (Ol+Cpx+Spl) konnte in den Experimenten mit vergleichbaren chemischen Mineralzusammensetzungen reproduziert werden; für den primitiven Basanit bei 400 und 700 MPa, 1100-1125°C, 1.3-2.2 Gew.% H_2O in der Schmelze (H_2O^m) und fO_2 Bedingungen von FMQ+1.3 bis FMQ+2.3 und für den entwickelten bei 400 und 550 MPa, 1125-1175°C, 1.5-2.2 wt.% H_2O^m und fO_2 Bedingungen von FMQ+1.1 bis FMQ+2.3. Durch die Kristallisation von $\pm Ol + Cpx \pm Amph + Spl$ in Experimenten bei 400, 550 and 700 MPa, 1010-1175°C, H_2O^m von 1.0-6.3 Gew.% und fO_2 Bedingungen von FMQ+1.1 bis FMQ+3.3 konnten erfolgreich tephritische Restschmelzen generiert werden. Es muss jedoch festgehalten werden, dass die chemischen Zusammensetzungen der tephritischen Restschmelzen nur dann dem

natürlichen Trend (LLD) entsprechen, wenn der Anteil an Klinopyroxen unterhalb von 32 Gew.% bleibt, da höhere Anteile an Cpx eine starke Abreicherung an CaO in der Restschmelze zur Folge haben und als Konsequenz eine Abweichung vom natürlichen Trend zu beobachten ist. Durch die Kristallisation von $\text{Cpx} \pm \text{Ol} \pm \text{Krs} + \text{Mt} \pm \text{Ap}$ in Experimenten bei 400 und 700 MPa, 1050-1100°C, 0.5-2.5 wt.% H_2O^m und $f\text{O}_2$ Bedingungen von FMQ+1.0 bis FMQ+2.5 konnten erfolgreich phonotephritische Schmelzen generiert werden. Durch die Kristallisation von $\pm \text{Ol} + \text{Cpx} + \text{Pl} \pm \text{Krs} - \text{Mt} + \text{Ap}$ in Experimenten bei 400 MPa, 1050-1025°C, 0.7-1.1 Gew.% H_2O^m und $f\text{O}_2$ Bedingungen von FMQ+0.5 bis FMQ+1.6 konnten erfolgreich tephriphonolithische Schmelzen generiert werden. Die natürliche Paragenese des Tephriphonoliths ($\text{Cpx} + \text{Krs} + \text{Pl} + \text{Mt} + \text{Ap}$) konnte im Zusammensetzungsbereich der natürlichen Minerale im Gleichgewicht mit einer phonolithischen Restschmelze reproduziert werden (in Experimenten bei 200 MPa, 950-1000°C, 0.5-2.0 Gew.% H_2O in der Schmelze und $f\text{O}_2$ Bedingungen von FMQ bis FMQ+1.8 sowie bei 400 MPa, 900-1000°C, 0.5-3.1 Gew.% H_2O in der Schmelze und $f\text{O}_2$ Bedingungen von FMQ bis FMQ+2.2 (Wengorsch et al, 2013)).

Leicht reduzierende Bedingungen (FMQ+1 bis FMQ+2) sind zur Bildung von alkalireichen, Si-untersättigten Schmelzen zwingend erforderlich, da höhere $f\text{O}_2$ Bedingungen zur ausgeprägten Kristallisation von Magnetit und zur Generierung von Qz-normativen anstelle von Ne-normativen Restschmelzen führen. Natürlich auftretende Variationen von CaO und Al_2O_3 Gehalten in entwickelten Gesteinen können durch variierende Phasenanteile von Amph und Cpx in Abhängigkeit von $a\text{H}_2\text{O}$ und Temperatur erklärt werden. Bei niedrigen $a\text{H}_2\text{O}$ und Temperaturen über 1075°C sind deutlich höhere Anteile an Cpx als Amph zu beobachten, dies hat eine starke Abreicherung von CaO und ausgeprägte Anreicherung an Al_2O_3 in der Restschmelze zur Folge. Bei hohen $a\text{H}_2\text{O}$ und niedrigeren Temperaturen sind deutlich höhere Anteile an Amph als Cpx zu beobachten, dies hat eine weniger starke Anreicherung an Al_2O_3 und höhere CaO Gehalte in der Restschmelze zur Folge. In unseren Experimenten konnten wir feststellen, dass Krs ein Amphibol ist, der noch bei H_2O^m unterhalb eines Gewichtsprozentes stabil ist, was uns zu der Annahme bringt, dass entwickelte CV Schmelzen H_2O arm sein können.

Die Ergebnisse dieser Studie zeigen, dass eine "single-step" Differentiation (durch Gleichgewichtskristallisation) von Basaniten zu Phonotephriten in einem Druckbereich von 400

bis 700 MPa möglich ist. Tephriphonolitische Schmelzen können nur bei Druckbedingungen unterhalb von 700 MPa oder von einem entwickelteren Stammagma als Basanite generiert werden, da die Kristallisation von Plagioklas bei hohen Druckbedingungen in einem geschlossenen System unterdrückt wird. Auf der Grundlage unserer experimentellen Daten können wir davon ausgehen, dass die Genese von tephriphonolitischen Schmelzen bei Drücken von mindestens 400 MPa möglich ist, was im Widerspruch zu den bisher veröffentlichten relativ niedrigen prä-eruptiven Bedingungen von vergleichbaren Systemen ist (z.B. 200-250 MPa für Kerguelen (Freise et al., 2003) und 130 MPa for El Abrigo, Tenerife (Andujar et al., 2008)).

Schlagwörter: La Palma, Differentiationstrend, Phonolith-Basanit

1. Introduction

Eruptive products of the recent Cumbre Vieja volcano (CV) cover a large spectrum of alkali-rich rocks ranging from basanites to phonolites. Phonolites can be regarded as the differentiated residual end-members of alkalic, SiO_2 -undersaturated melts and can occur as products of intraplate magmatism. Compositional variations of phonolites cover sodic, potassic, peraluminous, and peralkaline varieties. Phonolites are common volcanic products on Earth but are volumetrically subordinate to corresponding alkalic basalts in most places, the Miocene flood phonolites of the Kenya Rift being a remarkable exception (Hay and Wendlandt, 1995). In the East Eifel and Hegau volcanic fields (Germany) and on many volcanic islands such as La Gomera, La Palma, and Tenerife (Canary Islands), São Tomé, Fernando de Noronha, Tristan da Cunha, and Kerguelen Archipelago (e.g. Mitchell-Thomé, 1970; Schmincke, 1976; Weis et al., 1993) phonolite domes and cryptodomes form preeminent landmarks. Strongly explosive eruptions of pyroclastic phonolite deposits are major characteristics e.g. in the East Eifel and on the islands of Tenerife and Brava (Schmincke, 1977; Ablay et al., 1995; Wolff and Turbeville, 1985). Also, the well-known catastrophic Plinian 79 AD Vesuvius eruption produced phonolite (Carey and Sigurdsson, 1987). Phonolitic magma currently also erupts at Mt. Erebus (Antarctica) as a continuous lava lake and Strombolian eruptions (e.g. Kelly et al., 2008). Notably, phonolitic products are abundant at some volcanic areas but are absent at nearby similar areas, as is exemplified by the neighboring East Eifel (phonolite abundant) and West Eifel (phonolite rare) volcanic systems (reviewed in Schmincke, 2008). Many phonolite domes and lava flows are present at the recently active Cumbre Vieja volcano on La Palma (Canary Islands), whereas the island's older volcanic series lacks in phonolitic rocks almost entirely. Additionally, the adjacent island of El Hierro (Canary Islands), comparable to La Palma in age, activity and lava compositions, hosts no phonolites but a few trachytes (summarized in Carracedo et al. 2001). This phenomenon can also be observed at the "sister islands" of Fogo and Brava (Cape Verde). Both islands are located on a common submarine platform and are both characterized by highly SiO_2 -undersaturated alkalic magmas. On the active Fogo volcano phonolite is virtually absent (only one occurrence known; S. Day, pers. commun.), Brava is mainly built up by phonolite lavas

and pyroclastics and only minor mafic rocks (Wolff and Turbeville, 1985; field observations A.Klügel).

1.1 Previous studies on phonolitic rocks

Knowledge on the petrogenesis of phonolitic melts is limited. There is an overall consensus of phonolitic rocks being derived from alkalic basaltic melts through extensive, often polybaric fractional crystallization. However, the relative influence of different thermodynamic parameters on phase equilibria on the petrogenesis of phonolitic melts are still matter of extensive research. Several basanite-phonolite series were studied by different authors showing a general consistency in observed phenocryst phases and corresponding liquid lines of descent (e.g., Price and Chappell, 1975; Wörner and Schmincke, 1984; Price et al., 1985; LeRoex et al., 1990; Ablay et al., 1995; Johansen et al., 2005; Melluso et al., 2007). Pargasitic to kaersutitic amphibole is a major phase controlling melt evolution in many cases (Ablay et al., 1998; Irving and Green, 2008). Timescales for differentiation from basanite to phonolite, obtained by U-series isotope studies, ranging from approximately 100 years to 1600 years for small systems (Johansen et al. 2005; Reagan et al., 2008) and to 100-230 ka for larger systems (Bourdon et al., 1994; Hawkesworth et al., 2000).

Pre-eruptive storage conditions of phonolite were published by e.g. Ablay et al. (1998); Marziano et al. (2007); Schmidt and Behrens (2008) using volatile concentrations of trapped melts indicating a storage level at relatively shallow depths (<300 MPa), a result which is supported by the occurrence of crustal type xenoliths (Wörner and Schmincke, 1984) and feldspar fractionation (Price and Chappell, 1975; Price et al., 1985; Kelly et al., 2008). However, phonolites may also form at mantle pressures without significant feldspar fractionation as it is suggested by lacking Eu anomalies and by some phonolites carrying Iherzolite xenoliths (Irving and Price, 1981; Klügel and Hansteen, 1998; Kunzmann, 1996; Irving and Green, 2008).

Experimental phase equilibria studies using phonolites as starting composition have been carried out in order to constrain pre-eruptive storage conditions. Authors could successfully reproduce mineral assemblages and reported the following pressure ranges for storage of phonolitic magmas:

- 115-145 MPa for Laacher See, Eifel (Harms et al., 2004; Berndt et al., 2001),

- 200-250 MPa for Kerguelen (Freise et al. 2003),
- 130 MPa for El Abrigo, Tenerife (Andujar et al., 2008),
- 150 ± 50 MPa for last eruption of Teide, Tenerife (Andujar et al., 2010),
- 140-200 MPa for Campania, Campi Flegrei (Fabbrizio and Carroll, 2008)
- 50-350 MPa for Vesuvius (Scaillet et al., 2008).

However, this data does not provide detailed information on the evolution from primitive basanitic melts to phonolitic liquids. In order to investigate the different stages in the petrogenesis from primitive to evolved melts, only few experimental studies were conducted on basanites, phonotephrites and alkali basalts (Sack et al., 1987; Freise et al., 2003; Kaszuba and Wendlandt, 2000; Irving and Green, 2008) (See Supplementary Material Figure A1). Their experimental results basically support the hypothesis of alkali basalt/basanite-phonolite series being formed by polybaric fractional crystallization leading to a genetic sequence from primitive to evolved rocks. However, differences in composition of starting materials (especially SiO_2 , TiO_2), different P-T-conditions, or different fluid compositions (H_2O , Cl, S), may strongly affect the presence or absence of phases and their compositions. Therefore, extrapolating phase equilibria results obtained on a specific phonolite to constrain the pre-eruptive conditions of other phonolites is not straightforward. Hence, these studies are not directly applicable to every basanite-phonolite series in general. Additionally, the lack of experimental data on melts coexisting with kaersutite/pargasite emphasizes the importance of further studies. The current model of the magma plumbing system of the Cumbre Vieja volcano is largely based on barometric studies of phenocrysts and xenoliths and includes three major intervals of magma stagnation and fractionation at mantle and crustal depths (Klügel et al., 2005). However, many aspects such as fractionation depths of basanites, tephrites and evolved phonolites, corresponding phase relations, and their dependency on water content and oxygen fugacity are unknown, which is due to lacking experimental data for such compositions. We present results of an experimental study aimed for evaluating p-T- $a\text{H}_2\text{O}$ - $f\text{O}_2$ conditions in the genesis of a basanite-tephrite-phonolite system. This experimental study on phase equilibria aims towards a better knowledge of the petrogenesis of evolved and intermediate Cumbre Vieja melts. The results of this are relevant not only for La Palma, because such a study deals with fundamental

petrogenetic processes, but also applicable to other alkalic provinces and other geotectonic settings. Additionally, our experimental study increases the range of investigated pressures, which distinguishes our work from the previously published data of phonolites.

1.2 Experimental strategy of our study

The main aim of this study is to constrain the evolution of a typical basanite-tephrite-phonolite series by experimental simulation, in particular the formation conditions of magmas representing basanite-phonolitic series of the Cumbre Vieja volcano (La Palma, Canary Islands). Particular emphasis is given to the role of melt evolution at different pressures (700, 550 and 400 MPa for basanites and 400 and 200 MPa for tephriphonolite), and to the role of volatiles (mainly H₂O) and redox conditions in the genesis of evolved magmas. To provide constraints on petrochemical trends of Cumbre Vieja magmas mineral assemblages, phase compositions and proportions are compared to their natural counterparts.

For crystallization experiments three different samples (primitive basanite, evolved basanite and tephriphonolite [study of Wengorsch, 2013]) from Cumbre Vieja were used as starting materials. Fluid saturated crystallization experiments were conducted in internally heated pressure vessels at different pressures and temperatures. The well-known problem of iron loss into noble metal capsules at reducing conditions was specifically addressed in an additional series of superliquidus experiments. For comparison we used iron pre-saturated Au₈₀Pd₂₀ capsules and Au₈₀Pd₂₀ capsules without pre-treatment at reducing conditions in our experiments.

One important thermodynamic parameter in the evolution of evolved melts is aH₂O as it controls phase stabilities and proportions at constant temperature. For calculation of aH₂O different models were published, e.g. the model of Burnham (1979) and the empiric model of Moore et al. (1998). It is well-known that the model of Burnham (1979) significantly underestimates H₂O solubility at high pressure and corresponding calculations of aH₂O are too high, therefore calculations of aH₂O of experimental melts generated at high pressure have to be improved. We conducted experiments at superliquidus conditions at 50, 400 (study of Fritzsche 2013) and 700 MPa, H₂O concentrations in the melt were measured by Infrared

spectroscopy (IR), Karl-Fisher titration (KFT) to test the applicability of the H₂O solubility models of Burnham (1979) and Moore et al. (1998) for alkali-rich compositions and pressures between 50 to 700 MPa.

Another important thermodynamic parameter for phase compositions is oxygen fugacity. It is well-known that the redox state of iron in a silicate melt is influenced by aH₂O and redox conditions of the system (e.g. Schuessler, 2008). So far no experimental data on nominally dry to hydrous conditions of basanitic compositions exists. For estimation of Fe²⁺/ΣFe ratios in experimental glasses and calculation of partition coefficients for Fe²⁺ between melt and minerals, we performed experiments at superliquidus and at nominally dry to H₂O-saturated conditions using the basanitic starting material KLA-1-6-22 at 50, 400 and 700 MPa.

H₂O concentrations in the melt were measured by IR, KFT and Fe²⁺/ΣFe ratios by colorimetric Fe²⁺/Fe³⁺ determination to test the applicability of the Kress and Carmichael (1991) and Moretti (2005) for estimation of Fe²⁺/ΣFe ratios.

The applicability of the commonly used clinopyroxene-melt thermobarometer of Putirka et al. (2003) to alkalic magmas is not clear. Our crystallization experiments yielded Cpx-melt pairs equilibrated at 400, 550 or 700 MPa, which can be used to test the applicability of the barometer of Putirka et al. (2003) for hydrous tephritic melts.

2. Geological setting

La Palma belongs to the Canary Archipelago and is located approximately 500 km off the northwestern African coast (see Figure 1). All seven volcanic islands are underlaid by Jurassic oceanic lithosphere as it is indicated by the occurrence of tholeiitic mid-ocean ridge basalts (MORB) gabbro xenoliths on Gran Canaria, Lanzarote and La Palma (Hoernle, 1998; Schmincke et al., 1998). The subaerial volcanic activity started more than 20 million years ago with the formation of the eastern islands Lanzarote and Fuerteventura. The islands were generated by hotspot related magmatism which is fixed beneath the slowly eastward progressing oceanic lithosphere. The relative topographic heights and the submarine to subaerial ratios of the islands reflect the stage of development. Compared to La Gomera, eastern Gran Canaria and

Lanzarote, which are already deeply eroded, Tenerife is on the peak of volcanic island growth, while La Palma and El Hierro are still in the juvenile stage of development and still active.

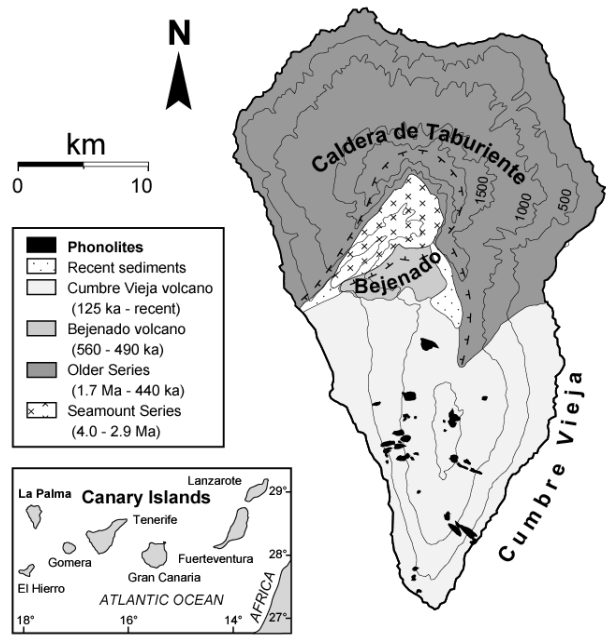


Figure 1: Simplified geological map of La Palma, modified after Carracedo et al. (2001) and Galipp et al. (2006). Phonolite occurrences at Cumbre Vieja are marked in black.

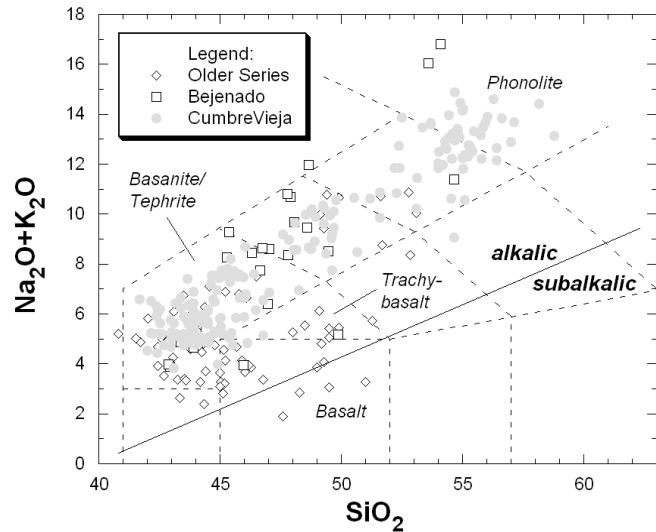


Figure 2: Total alkalis vs. silica diagram of La Palma rocks with field boundaries after LeMaitre et al. (1989). Data sources: Hernandez-Pacheco and Valls (1982), Hernandez-Pacheco and de la Nuez (1983); Carracedo et al. (2001), Klügel et al. (2000), Galipp (2005). Highly evolved compositions are restricted to Cumbre Vieja volcano and to some Bejenado lavas.

Carracedo et al. (1999, 2001) published a detailed description of the geological evolution of La Palma; therefore it is just briefly summarized here. La Palma consists of three major volcanic units: (1) the basal complex (4.0-2.9 Ma), (2) the older volcanic series (1.7-0.4 Ma) including Bejenado volcano in the north (0.56-0.49 Ma), and (3) the highly active Cumbre Vieja volcano forming the southern half of the island (125 ka to present). Most lavas are alkalic in composition, ranging from alkali basalts and basanites to evolved rocks (see Figure 2). Phonolites are virtually absent in the older series, rare at Bejenado volcano, but commonly occur as domes and lava flows at Cumbre Vieja (Hernández-Pacheco and De la Nuez, 1983). It is suggested that submarine volcanism that formed La Palma started around 3 Ma ago. The submarine volcanic seamount (which crops out in the Caldera de Taburiente) consists of pillows, lavas breccias and hyaloclastites. Due to intensive intrusions by dike swarms and plugs

of gabbros the whole volcanic edifice was lifted up about 1500 m and tilted by 45-50° towards SW direction. This was followed by a break in volcanic activity which results in a discordance through erosion. Next subaerial volcanism (1.77 Ma ago) was dominated by explosive volcanism producing volcanoclastic and phreatomagmatic deposits. The Garafia volcano was formed by extensive volcanism which results in steep flanks and an estimated height of up to 3000 m. The unstable volcano collapsed in a landslide 1.2 Ma ago due to its rapid growth. Around 0.78 Ma ago volcanism formed three defined rifts (NW, NE and N-S) with the shield volcano in the center.

Afterwards the Cumbre Nueva rift was formed by the development of the N-S rift most likely associated with the southwards moving volcanism. About 560 ka ago a second landslide occurred, which also affected the morphology of the Taburiente volcano forming the Aridane Valley. The Bejenado volcano was created by continuous volcanism, the active magmatic phase ended about 0.4 Ma ago. The formation of the Cumbre Vieja rift can be regarded as the last stage of volcanism on La Palma. The oldest dated rocks of the Cumbre Vieja volcano are 123 ka. Most abundant rocks are basanitic in composition, tephrites and tephriphonolites are common, phonolite tends to occur as domes and subordinate as lava flows. Most historic eruptions on Cumbre Vieja involved effusive, Strombolian, and/or phreatomagmatic activity (Carracedo et al., 2001) producing olivine-clinopyroxene-phyric basanites (Figure 3a) and clinopyroxene-amphibole-phyric tephrites. Evolved Cumbre Vieja rocks contain Ti-rich clinopyroxene + kaersutite/pargasite + plagioclase ± haüyne ± titanite ± apatite phenocrysts; alkali feldspar occurs in the groundmass (Figure 3b and 3c).

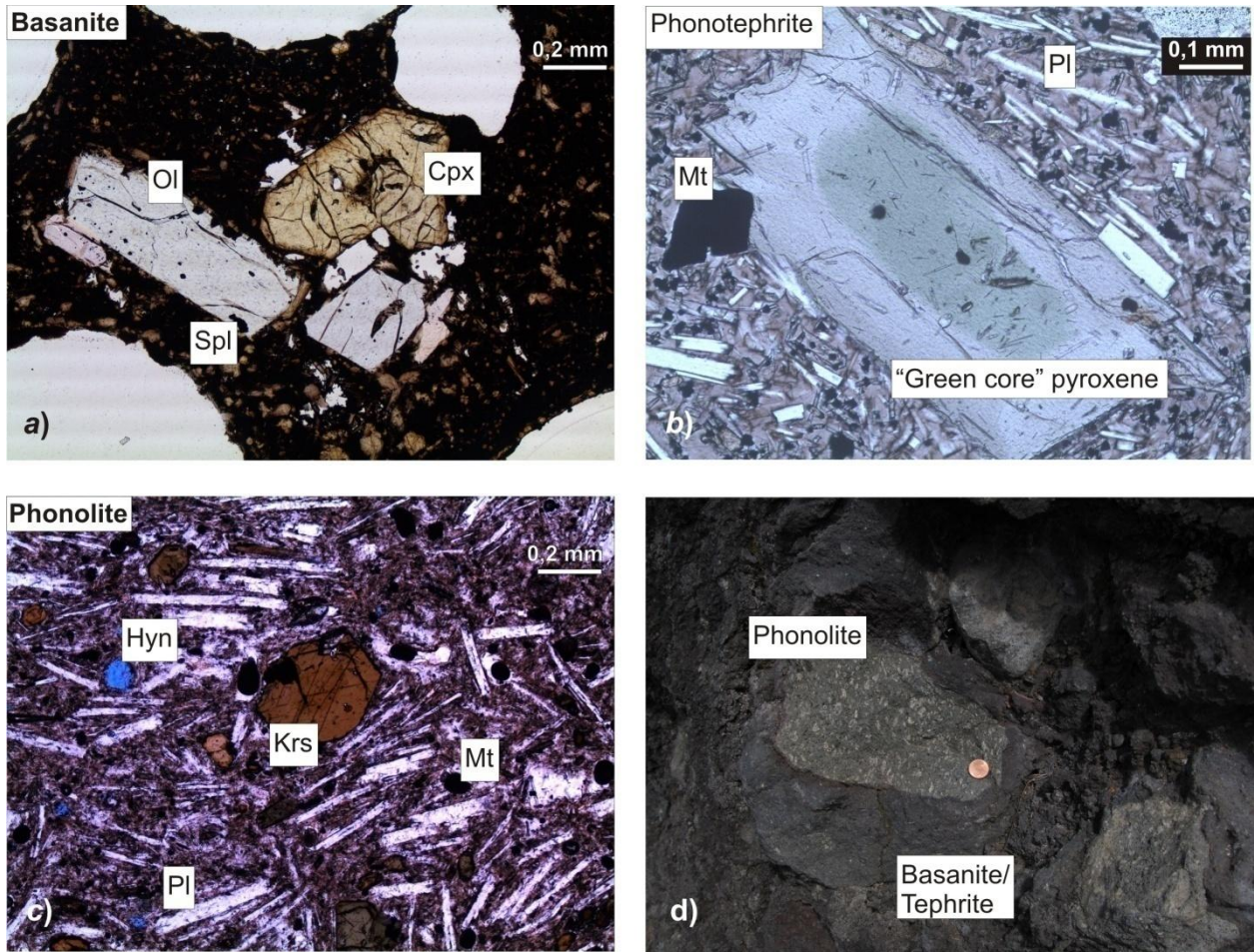


Figure 3: Microscopic pictures of a) basanite (168-1), b) an evolved phonolitic lava and c) "Green core" pyroxene in phonotephritic lava. d) Phonolitic xenolith with reaction rim within basanitic/tephritic host rock.

Major elements of Cumbre Vieja bulk rock data from Klügel (1997), Kaiser (1988), Praegel and Holm (2006), Hernandez-Pacheco and Valls (1982), Hernandez-Pacheco and de la Nuez (1983) and Carracedo et al. (2001) are plotted in Harker-diagrams in Figure 4 and in Figure 5 as a function of MgO content. In those diagrams it becomes evident that Cumbre Vieja lavas show well defined trends for all major elements. Basanitic bulk rock compositions (black dots in Figure 4 and Figure 5) are characterized by strong MgO depletion (12.8-5.2 wt.%) at almost constant SiO₂ contents (42.0-47.3 wt.%), and slight variations in TiO₂ (4.8-2.5 wt.%), FeO (12.7-9.3 wt.%) and CaO contents (13.4-9.4 wt.%). With decreasing MgO from 12.8 to 5.2 wt.% content slightly increasing Al₂O₃ contents between 11.1 and 16.5 wt.% and Na₂O+K₂O between 3.8 and 7.5 wt.% can be observed. The natural bulk rock compositions proceed until an

inflection point at approximately 5 wt.% MgO (tephritic rocks, dark gray dots in Figure 4 and 5)) at which CaO (10.6-7.4 wt.%), FeO (11.3-7.7 wt.%) and TiO₂ (3.9-2.5 wt.%) start to decrease and SiO₂ increases from 44.7 up to 50.1 wt.% until the magma reaches phonotephritic compositions (light gray dots in Figure 4 and Figure 5). Phonolitic rocks (white dots in Figure 4 and Figure 5) are characterized by further increasing SiO₂ content (up to 58.2 wt.%), Al₂O₃ (up to 22.9 wt.%) and Na₂O+K₂O (up to 16.3 wt.%) with decreasing MgO content from 4.0 to 0.1 wt.%. However, in the Harker-diagrams it becomes evident that with increasing SiO₂ content TiO₂, FeO and CaO decrease in a narrow range at constant SiO₂ content. Contrary to MgO, Al₂O₃ and Na₂O+K₂O contents which show variations of approximately 2 wt.% at constant SiO₂ content.

Figure 6 presents compositional variations of natural bulk rock compositions projected from the Pl apex on the pseudoternary plane Ol-Di-Ne, using the projection scheme after Sack et al. (1987). Normative components used in this and subsequent figures are calculated after Sack et al. (1987). This projection is very useful for investigations of the melt evolution of alkali-rich, silica undersaturated magmas, as it is very sensitive for slight changes in SiO₂, Al₂O₃, MgO, CaO and alkalis. In this diagram basanites (black dots) shift from the Ol apex in the direction of the Ol+Di cotectic line. Natural basanitic and tephritic bulk rock compositions proceed further along Ol+Di cotectic line. Kaersutite-bearing evolved compositions (phonotephrite: light gray dots and phonolite: white dots in Figure 6) are lower in Di component and move in the direction of the Ne apex.

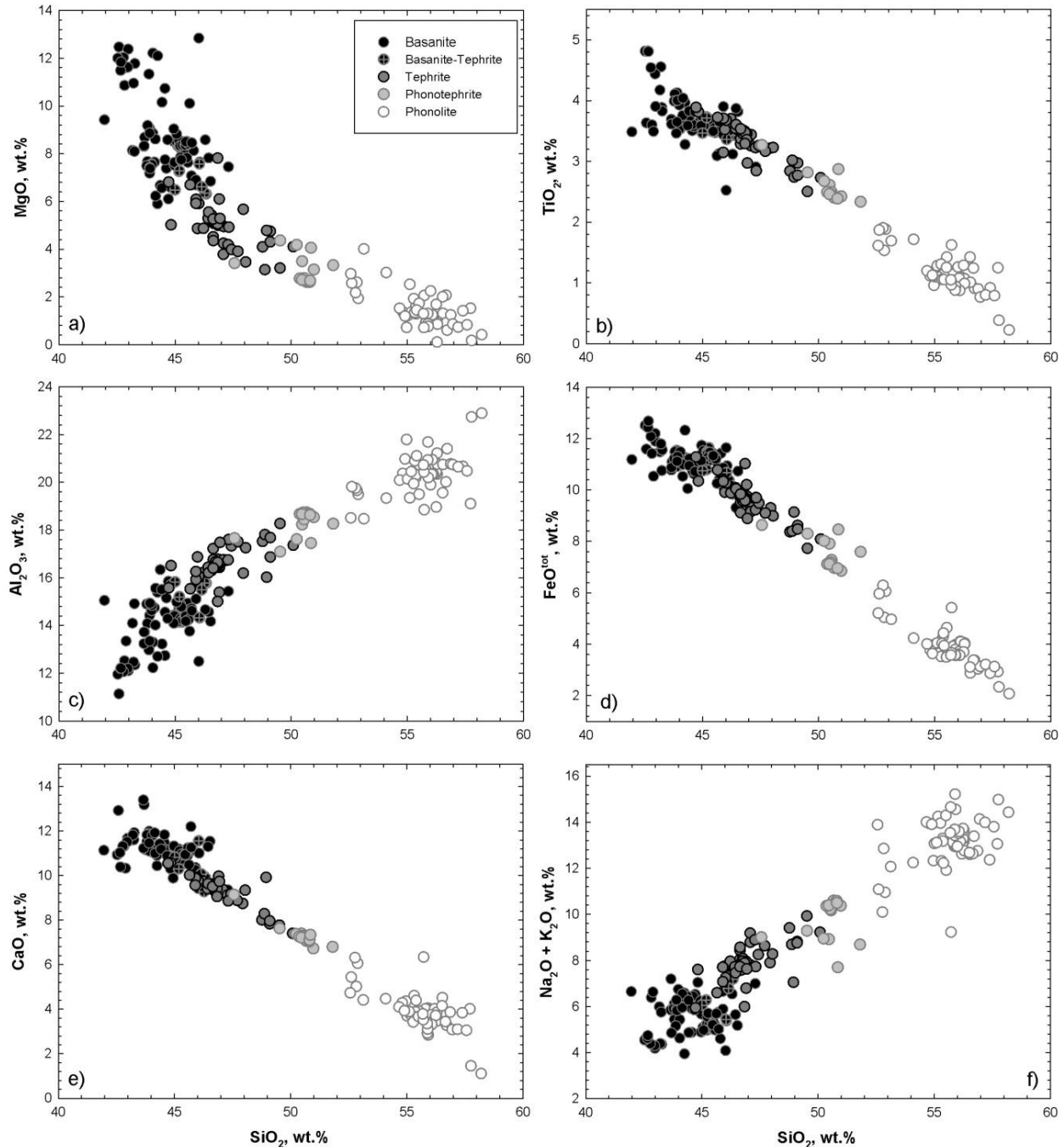


Figure 4: Harker diagrams showing Cumbre Vieja bulk rock compositions. Data source: Klügel (1997), Kaiser (1988), Praegel and Holm (2006), Hernandez-Pacheco and Valls (1982), Hernandez-Pacheco and de la Nuez (1983) and Carracedo et al. (2001).

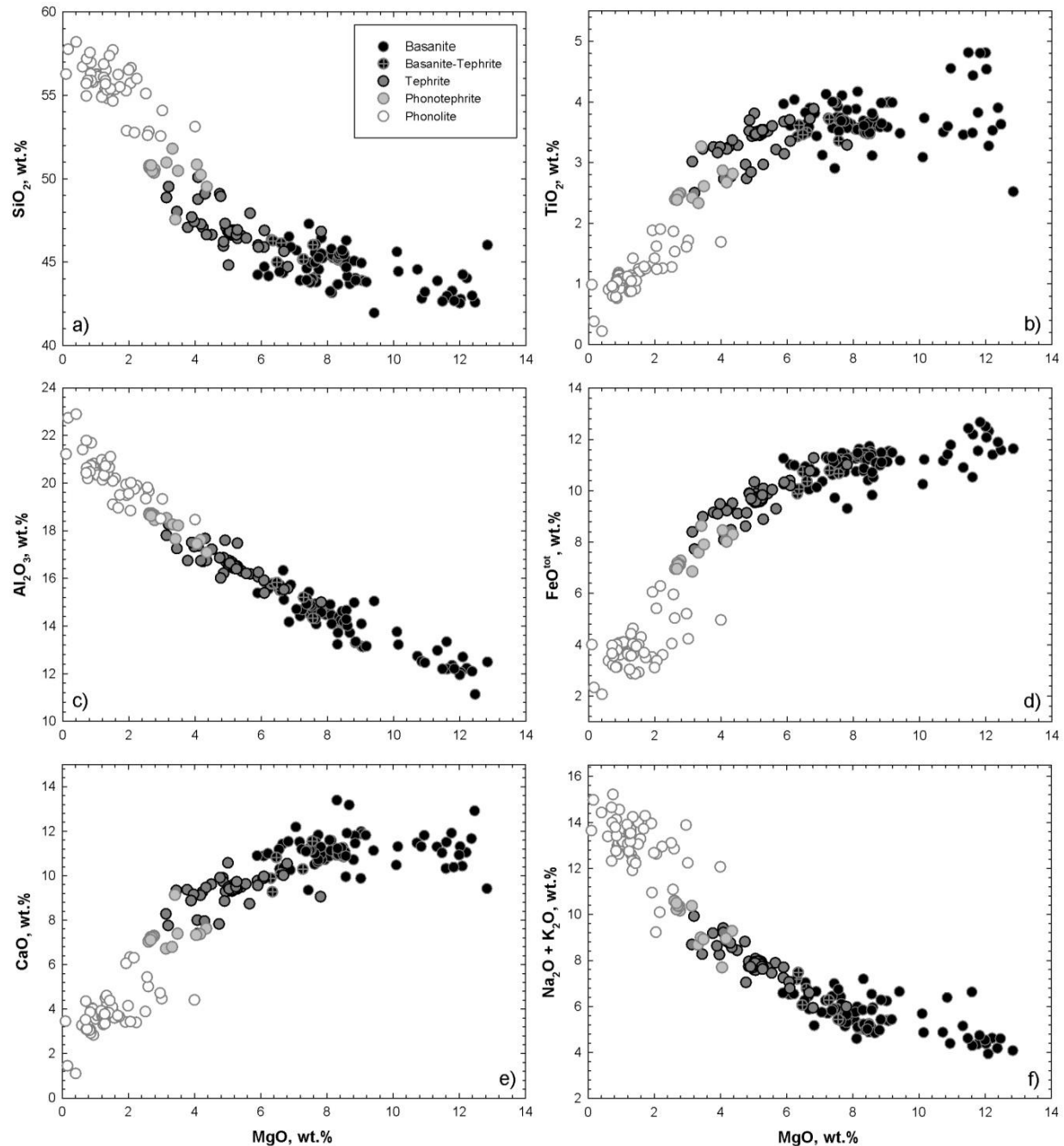


Figure 5: Variation diagrams showing Cumbre Vieja bulk rock compositions as a function of MgO content. Data source: Klügel (1997), Kaiser (1988), Praegel and Holm (2006), Hernandez-Pacheco and Valls (1982), Hernandez-Pacheco and de la Nuez (1983) and Carracedo et al. (2001).

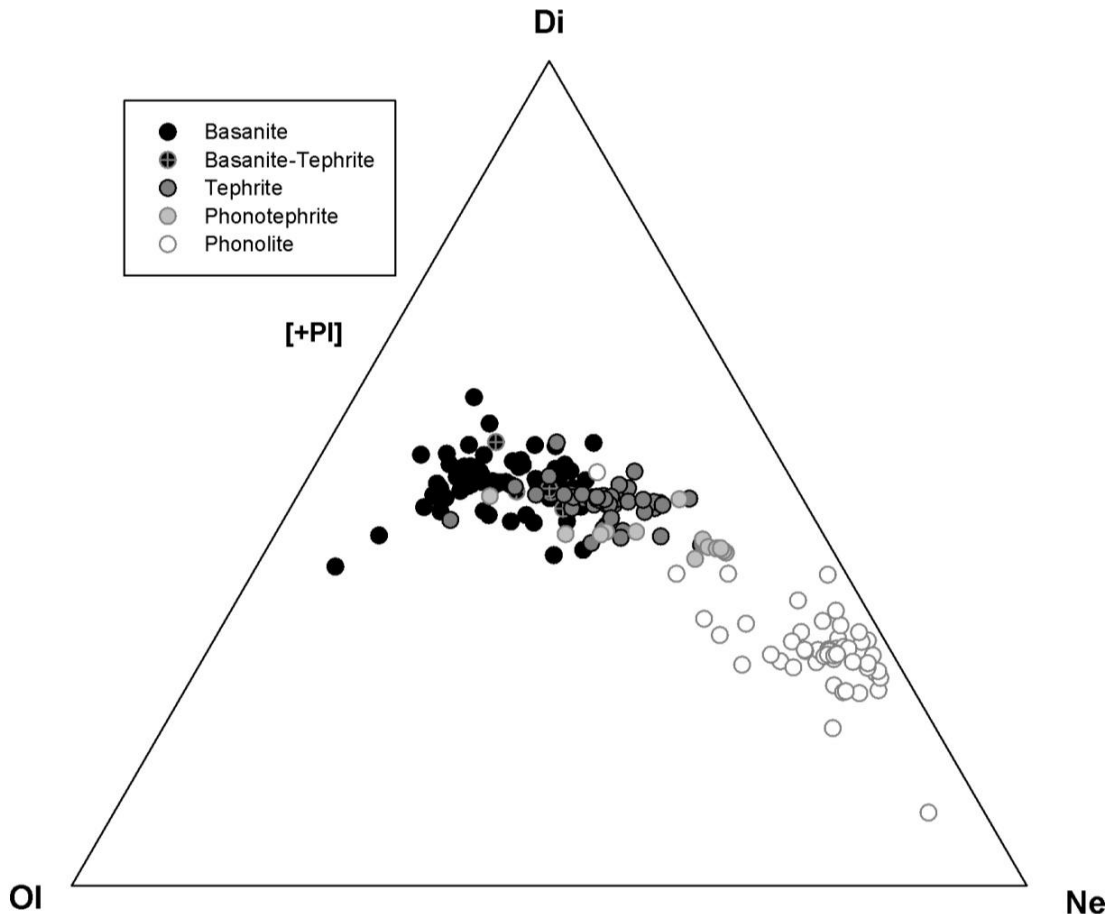


Figure 6: Pseudoternary projection of the basalt tetrahedron for alkalibasalts in the composition plane defined by nepheline (Ne), olivine (Ol), and high-calcium clinopyroxene (Di) normative components after Sack et al. (1987). Normative components used in this and subsequent figures are calculated after Sack et al. (1987). Data source: Klügel (1997), Kaiser (1988), Praegel and Holm (2006), Hernandez-Pacheco and Valls (1982), Hernandez-Pacheco and de la Nuez (1983) and Carracedo et al. (2001).

2.1 Model of magma plumbing system beneath Cumbre Vieja volcano

The experimental pressures chosen for this study (700, 550 and 400 MPa) are based on the current model of magma plumbing beneath Cumbre Vieja volcano discussed in Klügel et al. (2005) (see Figure 7). The model of the magma plumbing system is based on fluid inclusion barometry, xenoliths and clinopyroxene-barometry (Putirka et al. 1996) and includes three major intervals of magma stagnation and fractionation: (1) within the uppermost mantle (~410 – 770 MPa), (2) within the lower crust (240 – 470 MPa) and (3) at shallow levels (>200 MPa). Fluid inclusion barometry of CO₂-dominated inclusions in basanitic phenocrysts and mafic to

ultramafic xenoliths yield a major pressure range of 240-470 MPa, i.e. within the lower crust, and subordinate shallower pressures (Klügel et al., 2005). The inference of an "underplating zone" in the lower crust is consistent with massive occurrences of gabbro xenoliths from the lower oceanic crust in some Cumbre Vieja lavas. Therefore, important differentiation processes involved in the genesis of the basanite-phonolite-series of the Cumbre Vieja volcano are expected in this pressure range.

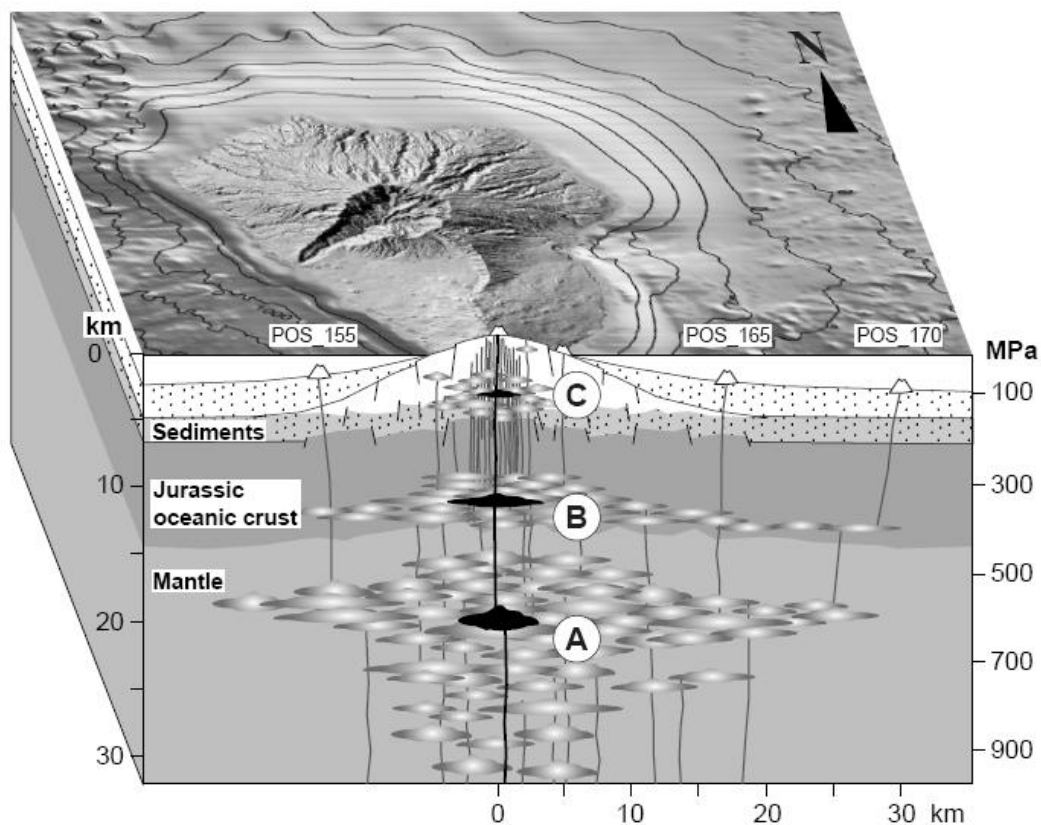


Figure 7: Model of magma plumbing beneath Cumbre Vieja volcano, La Palma (after Klügel et al. 2005). The storage system is visualized as a plexus of interconnected magma pockets (gray gradients) where fractionation occurs. The active part of a single eruption is shown in black.

2.2 Prediction of the natural LLD by thermodynamic calculations

As a prerequisite study phase equilibria simulations were conducted for both basanitic starting materials (168-1 and KLA-1-6-22) utilizing the MELTs model by Ghiorso & Sack (1995). Calculations were performed using solid phase fractionation mode, in the pressure interval from 100 to 800 MPa including both isobaric and polybaric simulations, with various H₂O contents in the melt (2-6 wt.%) at oxygen fugacities ΔFMQ to ΔFMQ+2 (log fO₂ relative to the fayalite-magnetite-quartz buffer) (see Figure 8).

Good agreement between residual melt compositions and the natural liquid line of descent (LLD) were obtained only for the stage of “basanite to tephrite” magma evolution by crystallization of Ol+Spl, followed by Ol+Cpx+Spl. The MgO-rich part of the natural trend (MgO: 14-9 wt.%) is characterized by strong MgO depletion at nearly constant SiO₂ contents and can be reproduced by 25-30% Ol+Spl crystallization at pressures between 200 and 800 MPa, hydrous conditions and log fO₂ conditions between ΔFMQ and ΔFMQ+1. The natural LLD proceeds to an inflection point at 5 wt.% MgO (tephritic melt) at which CaO, FeO and TiO₂ start to decrease and SiO₂ increases up to 58 wt.% until the magma reaches phonolitic compositions. Natural LLD with MgO contents ranging from 9 to 7.5 wt.% can be reproduced by Ol+Cpx+Mt crystallization at pressures between 200 and 800 MPa, hydrous conditions and log fO₂ conditions of ΔFMQ+1. The strong change in melt composition at lower MgO contents is explained by the appearance of kaersutite/pargasite at the liquidus of tephritic melts. At this stage (tephrite to phonolite) discrepancies between calculated melt compositions and natural Cumbre Vieja bulk rock compositions were observed. So far it has been impossible to model kaersutite or pargasite using MELT simulations mainly due to the lack of an amphibole crystallization model. Thus, the conditions of kaersutite/pargasite, clinopyroxene, magnetite and plagioclase crystallization and the effect of co-crystallization of those minerals on the melt evolution are crucial to understand the genesis of Cumbre Vieja magmas from tephrite to phonolites.

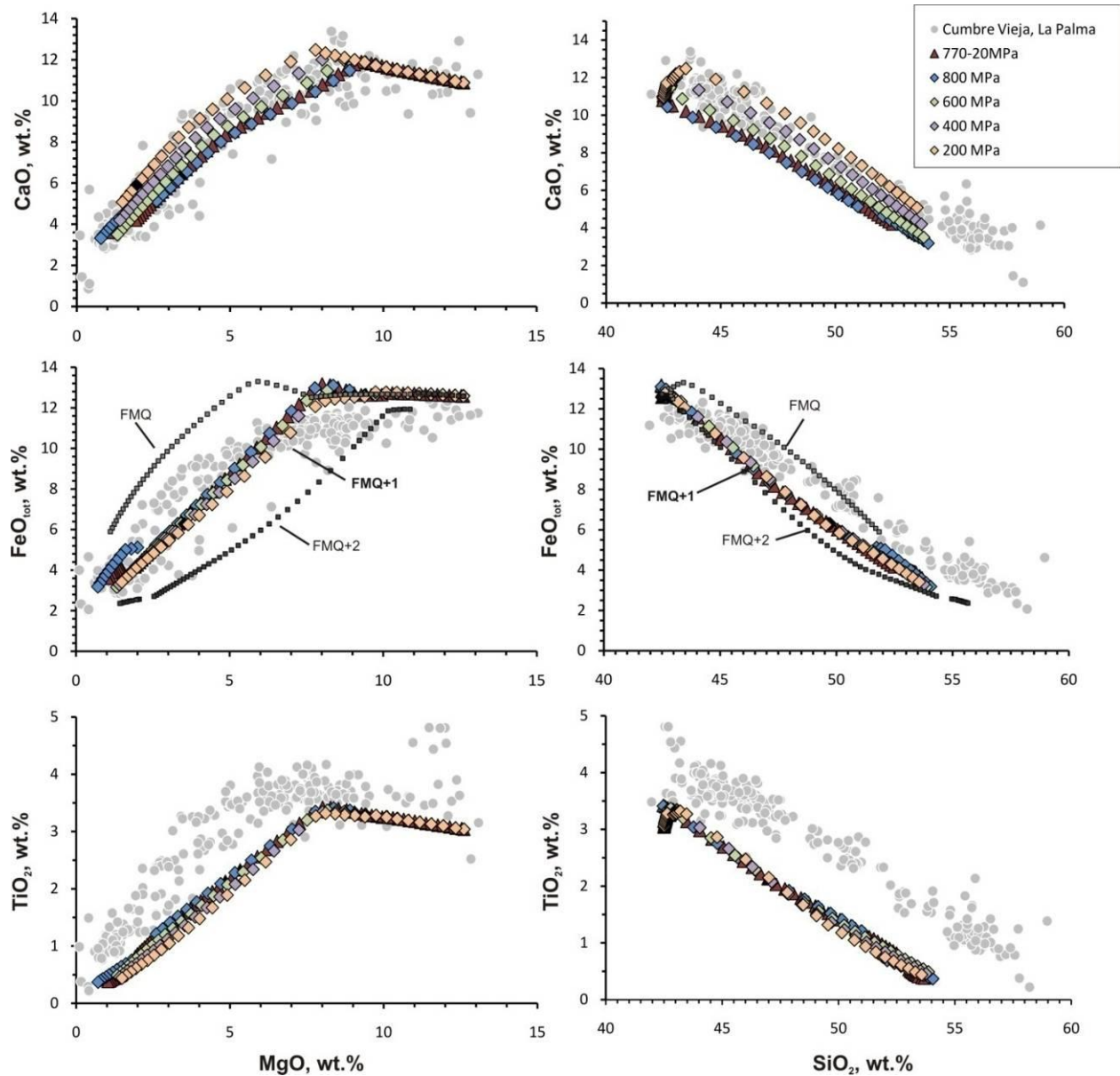


Figure 8: Comparison of natural lavas and liquid lines of descent modeled for sample 168-1 at different p-T conditions. Calculations were performed using solid phase fractionation mode, at QFM+1 oxygen buffer and 2 wt.% H₂O, in the pressure interval from 200 to 800 MPa (including both isobaric and polybaric simulations). The modeled trends follow the natural trend at high MgO contents (basanite to tephrite magma evolution), i.e. where spinel and olivine crystallize. The discrepancies at lower MgO contents (tephrite to phonolite) might be explained by the lack of amphibole in MELT simulations (Ghiorso & Sack, 1995).

3. Experimental Methods

3.1 Starting Material

Two natural basanites were used for the experimental investigation. The primitive basanite 168-1 with 13.7 wt.% MgO (Table 1) is a submarine sample dredged from the eastern flank of Cumbre Vieja at 1610-1680 m H₂O depth during POSEIDON cruise 270. This basanite contains 14.6 vol.% of olivine (Ol, 84.32±0.69 mol.%), 34.9 vol.% clinopyroxene (Cpx, Mg#77.02±4.99) and 1 vol.% spinel (Spl, Cr#0.52±0.06) as phenocrysts. The groundmass consists of Ol and Cpx microlites and glass.

The evolved basanite KLA-1-6-22 with 8.7 wt.% MgO (Table 2) is a sample from vesicular lapilli and bombs of the 1712 eruption, collected from the eastern rim of El Charco crater (UTM 221850/3162100, 1650 m above sea level). It contains roughly 8.6 vol.% of Ol (Fo83.53±0.37 mol.%), 22.1 vol.% Cpx (Mg#73.71±4.92) and 2.6 vol.% Spl (Cr#0.38±0.14) as phenocrysts and microphenocrysts. Olivine reaches 2 mm in size, Cpx is smaller and partly forms glomerocrysts. The microcrystalline groundmass is composed of glass Ol, Cpx, plagioclase (Pl) and glass. Both basanitic rock samples were ground in an agate mortar to a fine grained powder, loaded in a Pt crucible and fused twice (grinding between fusions) at 1 atm and 1600°C for 1 hour and quenched in water to a homogeneous glass. The composition of the starting material was confirmed by electron microprobe analyses. Both basanitic starting compositions are identical to the bulk rocks within the analytical error. However, FeO content of the starting glasses is slightly elevated due to oxidation of iron during the fusing process.

Table 1. Starting composition 168-1 (primitive basanite)

	starting glass	Ol core	Ol rim	Cpx	Spl in Ol	Mt
SiO₂	43.31 (± 0.26)	40.11 (± 0.28)	39.57 (± 0.04)	46.79 (± 2.58)	0.04 (± 0.02)	0.39 (± 0.29)
TiO₂	3.06 (± 0.04)	0.01 (± 0.01)	0.02 (± 0.01)	2.56 (± 1.16)	5.91 (± 2.88)	12.9 (± 1.87)
Al₂O₃	11.26 (± 0.11)	0.01 (± 0.01)	0.04 (± 0.03)	6.37 (± 1.92)	13.57 (± 2.71)	6.81 (± 0.31)
FeO^{tot}	12.91 (± 0.20)	14.38 (± 0.57)	16.28 (± 0.36)	6.78 (± 1.24)	44.17 (± 7.99)	68.63 (± 0.78)
MnO	0.18 (± 0.03)	0.21 (± 0.06)	0.26 (± 0.07)	0.1 (± 0.04)	-	0.73 (± 0.06)
MgO	13.71 (± 0.15)	44.64 (± 0.45)	42.84 (± 0.21)	12.88 (± 1.31)	9.02 (± 1.5)	4.15 (± 0.91)
CaO	11.05 (± 0.16)	0.15 (± 0.04)	0.36 (± 0.01)	22.73 (± 0.33)	0.04 (± 0.03)	0.37 (± 0.07)
Na₂O	2.74 (± 0.09)	0.06 (± 0.06)	-	0.42 (± 0.1)	0.01 (± 0.01)	0.21 (± 0.09)
K₂O	1.0 (± 0.02)	0.01 (± 0.01)	-	0.01 (± 0.01)	0.01 (± 0.01)	0.04 (± 0.02)
P₂O₅	0.61 (± 0.06)					
Cr₂O₃	0.10 (± 0.05)	0.03 (± 0.03)	0.04 (± 0.03)	0.52 (± 0.35)	23.1 (± 7.45)	0.05 (± 0.02)
Total	99.94	99.63	99.42	99.15	95.86	94.27
Mg#		84.32 (± 0.69)	81.79 (± 0.4)	77.02 (± 4.99)	0.36 (± 0.06)	0.16 (± 0.04)
En			0.39 (± 0.03)			
Wo			0.49 (± 0.01)			
Fs			0.12 (± 0.02)			
Fe³⁺#				0.28 (± 0.11)	0.76 (± 0.02)	
Cr#				0.52 (± 0.06)		

Mg# of Ol and Cpx is calculated as $100 \times \text{Mg}/(\text{Mg}+\text{Fe}^{\text{tot}})$; En is enstatite content $\text{Mg}/(\text{Mg}+\text{Fe}+\text{Ca})$ Wo is wollastonite content $\text{Ca}/(\text{Ca}+\text{Mg}+\text{Fe})$; Fs is ferrosilite content $\text{Fe}/(\text{Fe}+\text{Mg}+\text{Ca})$ Cr# of Spl is calculated as $\text{Cr}/(\text{Cr}+\text{Al})$ Mg# of Spl is calculated as $\text{Mg}/(\text{Mg}+\text{Fe}^{2+})$ Fe³⁺# of Spl is calculated as $\text{Fe}^{3+}/(\text{Fe}^{3+}+\text{Cr}+\text{Al})$

Table 2. Starting composition KLA-1-6-22 (evolved basanite)

	starting glass	Ol core	Ol rim	Cpx	Spl in Ol	Mt
SiO₂	43.26 (± 0.18)	39.98 (± 0.23)	39.47 (± 0.23)	46.5 (± 1.98)	0.04 (± 0.03)	0.06 (± 0.02)
TiO₂	3.81 (± 0.04)	0.02 (± 0.01)	0.04 (± 0.02)	2.79 (± 0.82)	10.04 (± 2.81)	15.16 (± 1.38)
Al₂O₃	13.01 (± 0.15)	0.04 (± 0.02)	0.04 (± 0.02)	6.58 (± 1.55)	12.86 (± 1.85)	5.33 (± 0.97)
FeO^{tot}	12.22 (± 0.21)	15.08 (± 0.33)	17.66 (± 0.75)	7.66 (± 1.18)	50.5 (± 3.36)	68.86 (± 2.81)
MnO	0.18 (± 0.07)	0.25 (± 0.06)	0.25 (± 0.04)	0.15 (± 0.05)	0.06 (± 0.03)	0.52 (± 0.13)
MgO	8.99 (± 0.14)	44.58 (± 0.24)	42.39 (± 0.42)	12.14 (± 1.27)	9 (± 1.34)	4.68 (± 1.24)
CaO	11.82 (± 0.17)	0.26 (± 0.04)	0.34 (± 0.03)	22.5 (± 0.32)	0.02 (± 0.02)	0.14 (± 0.13)
Na₂O	3.45 (± 0.12)	0.02 (± 0.01)	0.03 (± 0.01)	0.63 (± 0.23)	0.01 (± 0.01)	0.05 (± 0.06)
K₂O	1.48 (± 0.02)	-	-	0.01 (± 0.01)	-	0.01 (± 0.01)
P₂O₅	0.88 (± 0.04)					
Cr₂O₃	0.07 (± 0.03)	0.03 (± 0.02)	-	0.09 (± 0.09)	13.16 (± 6.99)	0.42 (± 0.1)
Total	99.16	100.26	100.25	99.05	95.68	95.23
Mg#		83.53 (± 0.37)	80.47 (± 0.8)	73.71 (± 4.92)	0.33 (± 0.03)	0.17 (± 0.04)
En				0.37 (± 0.03)		
Wo				0.5 (± 0.01)		
Fs				0.13 (± 0.02)		
Fe³⁺#					0.38 (± 0.07)	0.78 (± 0.05)
Cr#					0.38 (± 0.14)	0.05 (± 0.02)

Mg# of Ol and Cpx is calculated as $100 \times \text{Mg}/(\text{Mg}+\text{Fe}^{\text{tot}})$; En is enstatite content $\text{Mg}/(\text{Mg}+\text{Fe}+\text{Ca})$ Wo is wollastonite content $\text{Ca}/(\text{Ca}+\text{Mg}+\text{Fe})$; Fs is ferrosilite content $\text{Fe}/(\text{Fe}+\text{Mg}+\text{Ca})$ Cr# of Spl is calculated as $\text{Cr}/(\text{Cr}+\text{Al})$ Mg# of Spl is calculated as $\text{Mg}/(\text{Mg}+\text{Fe}^{2+})$ Fe³⁺# of Spl is calculated as $\text{Fe}^{3+}/(\text{Fe}^{3+}+\text{Cr}+\text{Al})$

3.2 Experimental setup

Phase equilibria experiments at 700, 550 and 400 MPa were performed in internally heated pressure vessels (IHPV), using argon as pressure medium (Berndt et al., 2002). Depending on the vessel the intrinsic redox conditions were close to FMQ+3.3 or to FMQ+3.8 at H₂O saturated conditions (Schüssler et al., 2008). Low temperature experiments with high H₂O contents in the melt (>4 wt.% H₂O in the melt) at 400 MPa were conducted in a second IHPV pressurized with a mixture of Ar and H₂ to maintain the required *fH₂* in the vessel and to perform more reduced experiments (close to FMQ+1 at H₂O saturated conditions). The *fH₂* was controlled by using a Shaw-membrane (Scaillet et al., 1995; Berndt et al., 2002), calculations of *fO₂* values are based on the equation of Schwab & Kuestner (1981). Experiments were conducted at temperatures from 1175°C to 1010°C, with 25°C interval, to cover a wide range of crystallization conditions in the fluid saturated system. The temperature was recorded by two S-type thermocouples with an uncertainty of ±5°C. All experiments were conducted in sealed Au or Au₈₀Pd₂₀ capsules filled with dry glass powder and different proportions of H₂O and silver oxalate (Ag₂C₂O₄) used as a source of CO₂. The initial fluid composition was varied from XH₂O^{fl}=0 (CO₂-rich fluid, nominally dry conditions) to XH₂O^{fl}=1 (H₂O-saturated conditions). A set of five to six capsules were heated with a ramp of 30-80°C/min up to the experimental run temperature. The experimental run duration ranged from 24 hours to five days, depending on the experimental temperature. All samples were quenched using a sample holder equipped with a rapid quench device (Berndt et al., 2002) with a cooling rate of 150°C/s. This quench rate was sufficient for runs with melt H₂O contents less than approximately 7 wt.%, but was insufficient for runs with melt H₂O contents higher than 7 wt.%, due to formation of quenched crystals. After quenching, the molar fraction of the fluid phase of each capsule was calculated by the "weight-loss" method, but this method failed for most crystallization experiments.

3.3 Fe pre-saturation of the capsule material

Most of the high temperature experiments were conducted using Au₈₀Pd₂₀ or Au capsules with a 3.2 mm outer diameter, 0.2 mm wall thickness and 15 mm in length. Experiments at log *fO₂* conditions lower than FMQ required an additional experimental pre-treatment due to the well

known problem of iron loss in noble metal capsules (e.g. Barr and Grove, 2010). Using the galvanization method the inner part of the Au₈₀Pd₂₀ tube walls were electrochemically coated with a thin layer of iron. By subsequent annealing at 900°C in a reduction furnace iron diffuses from the surface into the tube material, forming an Au-Pd-Fe alloy. These Fe-pre-saturated capsules were further used in superliquidus (T=1250-1280°C) experiments using the basanitic starting material KLA-1-6-22 to constrain the experimental conditions for iron-loss for basanitic compositions at high temperatures. Five sets of isobaric experiments at 50, 200, 400 and 700 MPa with H₂O activities ranging from nominally dry to H₂O saturated conditions have been performed. Significant iron loss (up to 22.7%) was observed only in experiments at superliquidus conditions with less than 1 wt.% of H₂O in the melt and log fO₂ close to FMQ. Therefore, in our nominally dry experiments (with corresponding redox conditions close to FMQ buffer) we used Fe pre-saturated capsules.

At subliquidus and nominally dry conditions, both Au-Pd-capsules with and without Fe-pre-saturation were used to check for possible iron loss. Iron loss up to 14% in Au-Pd container without pre-treatment was observed. At oxidizing conditions iron migration from the capsule material into the experimental charges (up to 16% iron gain) occurred using the pre-saturated capsules.

3.4 Analytical techniques

3.4.1 Electron-probe microanalysis

The composition of the natural minerals and all experimental run products were determined by a Cameca SX100 electron microprobe (Hannover laboratory). The major elements for the crystalline phases were acquired with an accelerating voltage of 15 kV and a beam current of 15 nA for minerals and 4 nA for glasses, respectively, to minimize the migration of alkalis (Hunt and Hill, 2001). Counting times for Na and K were 10s for minerals and 6s and 8s for glasses. For the other elements, the counting times were 10s for minerals and 10s for glasses. For glass measurements, the beam size was defocused to 10 µm, but depending on the degree of crystallization and the size of the melt pools the beam size was reduced to 5 or 2 µm. The H₂O content in the melt was determined by the "by difference" method (e.g., Devine et al., 1995)

using glass standards with known H₂O concentration (our own H₂O-bearing glasses from superliquidus experiments and standard glasses from Shishkina et al., 2010). The melt H₂O contents estimated by microprobe and H₂O determinations obtained for some crystal free glasses by Fourier transform infrared spectroscopy (FTIR) and/or Karl-Fischer titration (KFT) methods (see below) are identical within an error of the “by difference” method (approximately 0.5 wt.%).

3.4.2 Karl-Fischer titration

H₂O concentrations in quenched glasses of experiments conducted at 50, 400, 700 MPa and superliquidus conditions were measured by Karl-Fischer titration (KFT). Experimental runs i-1-12 and k1-12 were measured in the framework of this project by Fritzsche (2013). A detailed description of the KFT method is provided by Behrens et al. (2009). 9-17 mg of each sample was heated in a platinum crucible up to a temperature of about 1300°C, in order to measure the amount of released water from the glass structure by colorimetric titration. The results are shown in Table 3. However, it has to be mentioned that H₂O solubility in basanitic systems at high pressure is high and can be elevated up to approximately 10.5 wt.% at 700 MPa. The resulting high H₂O contents in the alkali-rich basanite lead to high NBO/T ratios and to a general difficulty to quench those glasses. Therefore, a very high quench rate is necessary to maintain glasses with a minimum amount of quench crystals. To avoid H₂O loss from the sample at ambient pressure, the H₂O contents were measured directly after the experiment.

3.4.3 Fourier transform infrared spectroscopy

To measure low H₂O concentrations of experimental products derived from experimental products conducted at 50 and 400 MPa and superliquidus conditions, doubly polished glass sections of 50–100 µm thickness (for mid-infrared measurements, MIR) and 200–300 µm thickness (for near-infrared measurements, NIR) were prepared. For analysis, a Bruker IFS88 FTIR spectrometer equipped with an IR-Scopell microscope was used to obtain absorption spectra either in the MIR or in the NIR. Spectra were recorded only in areas which were free from cracks, fluid bubbles or quench crystals. For each spectrum, 50–100 scans were performed. For the calculation of the H₂O content, evaluation of the thickness and the density of each sample were required. The thickness of each section was determined by a digital

micrometer (Mitutoyo; precision $\pm 2 \mu\text{m}$). The density of the fused anhydrous starting material was measured by weighing a single glass piece in air and in water; an average of $2.887 \pm 0.022 \text{ g/L}$ was obtained. To get the relevant parameters for the Lambert-Beer Law, knowledge on the composition dependant molar absorption coefficient is necessary. The molar absorption coefficient was determined for the investigated evolved basanitic glass composition (KLA-1-6-22). The results of the FTIR analyses of superliquidus experiments are listed in Table 3. Experimental runs i-1-12 and k1-12 were measured in the framework of this project by Fritzsche (2013).

3.4.4 Determination of Fe^{2+} and Fe^{3+}

To obtain the redox state of Fe ($\text{Fe}^{2+}/\Sigma\text{Fe}$ ratio) in experimental glasses we used a wet chemical method which is based on the colorimetric method of Wilson (1960) and was modified to minimize the amount of toxic material and to proof the reproducibility, a detailed description was published by Schuessler et al. (2008). For this method small amounts (5-7 mg) of the sample material were decomposed using hydrofluoric acid in presence of ammonium vanadate. To avoid the oxidation of Fe^{2+} during the analytical procedure, all ferrous iron is oxidized by V^{5+} , which is highly resistant to oxidation compared to Fe^{2+} , as soon as iron is released from the sample. According to the reversible reaction:



The amount of generated V^{5+} is equal to the amount of Fe^{2+} in the sample material. The equilibrium of the reaction is shifted to the right hand side under the strongly acidic ($\text{pH} < 1$) conditions during sample dissolution. After complete sample dissolution and increasing the pH value to approximately 5, Fe^{2+} is regenerated from V^{4+} which shifts the equilibrium of reaction (1) to the left-hand side. The regenerated Fe^{2+} forms a very stable, red coloured complex with 2:2' bipyridyl in the solution, which shows an intensive absorption band in the visible spectrum. Measurements of Fe^{2+} and total Fe were made on the same solution with an UV/VIS spectrometer (Zeiss Specord S10) before and after the reduction of Fe^{3+} into Fe^{2+} . Since both

Fe^{2+} and total Fe are measured in the same solution, the $\text{Fe}^{2+}/\Sigma\text{Fe}$ ratio can be directly calculated by dividing the absorbances of Fe^{2+} and total Fe. The results of the wet-chemical colorimetric iron analyses of superliquidus experiments are listed in Table 3. Experimental runs i-1-12 and k1-12 were measured in the framework of this project by Fritzsché (2013).

Table 3. Superliquidus experiments

Run	Experimental conditions										Calculated water activity		wet-chemical coloimetric		Model calculations			
	P [MPa]	T [°C]	run duration [h]	log f_{O_2} ** [bar]	Capsule material	XH ₂ O***	melt H ₂ O [wt%]	H ₂ O IR [wt.%]	?wt% H ₂ O IR	H ₂ O KFT [wt.%]	?wt% H ₂ O KFT	Fe loss/gain [wt. %]	$a_{\text{H}_2\text{O}}$	Fe ²⁺ EFe	error Fe ²⁺ EFe	Fe ²⁺ EFe		
											(Burnham)	(Moore)	(K&C)	(Moretti)				
k1*	50	1250	20	-6.00	AuPd	0.00	0.76	0.56	0.01	0.47	0.05	-0.39	0.07	0.09	0.69	0.02	0.69	0.75
k3*	50	1250	20	-5.00	AuPd	0.28	1.28	0.98	0.01	1.01	0.07	0.05	0.27	0.29	0.58	0.02	0.59	0.59
k4*	50	1250	20	-4.61	AuPd	0.47	1.40	1.33	0.02	1.34	0.06	0.10	0.43	0.46	0.49	0.02	0.55	0.52
k5*	50	1250	20	-4.20	AuPd	0.58	1.91	1.10	0.01	1.77	0.07	0.27	0.67	0.73	0.42	0.02	0.51	0.45
k6*	50	1250	20	-3.86	AuPdFe	1.00	2.04	-	-	2.22	0.06	0.30	0.94	1.07	0.41	0.02	0.47	0.39
k7*	50	1250	20	-6.37	AuPdFe	0.24	-	0.40	0.01	0.34	0.08	0.18	0.04	0.06	0.74	0.02	0.73	0.80
k8*	50	1250	20	-5.71	AuPdFe	0.06	0.40	0.40	0.01	0.59	0.06	0.72	0.10	0.13	0.72	0.02	0.67	0.71
k9*	50	1250	20	-4.90	AuPdFe	0.27	0.98	0.94	0.01	1.09	0.05	0.96	0.30	0.33	0.60	0.02	0.59	0.57
k10*	50	1250	20	-4.32	AuPdFe	0.37	1.32	-	-	1.63	0.06	1.20	0.60	0.63	0.52	0.01	0.52	0.47
k11*	50	1250	20	-	AuPdFe	0.90	-	-	-	0.60	0.07	-7.07	-	-	0.89	0.04	-	0.08
k12*	50	1250	20	-3.78	AuPdFe	1.00	-	-	-	2.33	0.07	108	1.03	1.17	0.40	0.01	0.46	0.37
i1*	400	1250	20	-6.98	AuPd	0.00	0.92	0.73	0.01	0.69	0.05	-0.78	0.04	0.04	0.76	0.02	0.79	0.76
i2*	400	1250	20	-6.67	AuPd	0.05	1.37	0.70	0.01	0.62	0.05	-0.55	0.03	0.03	0.76	0.02	0.73	0.74
i3*	400	1250	20	-5.20	AuPd	0.29	2.90	2.52	0.11	2.36	0.05	0.09	0.30	0.18	0.54	0.01	0.65	0.55
i4*	400	1250	20	-4.91	AuPd	0.38	3.71	3.11	0.13	3.00	0.06	0.10	0.42	0.25	0.50	0.03	0.62	0.50
i5*	400	1250	20	-4.39	AuPd	0.64	4.54	3.55	0.17	4.53	0.06	0.15	0.72	0.46	0.43	0.02	0.59	0.40
i6*	400	1250	20	-3.98	AuPd	1.00	5.91	4.27	0.23	6.14	0.06	0.08	1.01	0.74	0.36	0.01	0.55	0.32
i7*	400	1250	20	-6.97	AuPdFe	1.00	-	0.62	0.01	0.47	0.04	0.41	0.02	0.02	0.77	0.02	0.83	0.76
i8*	400	1250	20	-6.91	AuPdFe	0.10	0.50	0.82	0.01	0.50	0.05	0.65	0.02	0.03	0.76	0.02	0.78	0.76
i9*	400	1250	20	-5.44	AuPdFe	0.18	1.74	1.85	0.06	1.92	0.05	1.55	0.23	0.14	0.54	0.02	0.70	0.59
i10*	400	1250	20	-4.90	AuPdFe	0.21	2.35	2.79	0.12	3.03	0.06	1.69	0.44	0.25	0.46	0.02	0.67	0.49
i11*	400	1250	20	-4.50	AuPdFe	0.48	3.49	3.22	0.16	4.14	0.06	1.27	0.65	0.40	0.40	0.01	0.63	0.42
i12*	400	1250	20	-4.09	AuPdFe	0.96	4.74	3.50	0.18	5.66	0.07	1.20	0.92	0.65	0.32	0.01	0.59	0.34
N1	400	1280	12	-3.40	AuPd	1.00	-	-	-	7.47	0.08	-	1.27	1.00	0.53	0.01	0.49	0.23
LP I05	700	1280	20	-3.46	AuPd	1.00	6.28	-	-	9.16	0.13	0.25	1.18	0.77	0.31	0.01	0.53	0.35
LP I06	700	1280	20	-3.94	AuPd	0.85	5.56	-	-	6.33	0.09	0.20	0.77	0.44	0.37	0.01	0.58	0.43
LP I07	700	1280	20	-4.06	AuPd	0.52	5.37	-	-	5.72	0.10	0.12	0.68	0.38	0.40	0.01	0.59	0.45
LP I08	700	1280	20	-4.41	AuPd	0.50	5.09	-	-	4.27	0.06	0.23	0.49	0.26	0.43	0.01	0.63	0.51
LP I09	700	1280	20	-5.17	AuPd	0.01	3.91	-	-	2.18	0.07	0.14	0.20	0.11	0.57	0.02	0.70	0.64
LP I10	700	1280	20	-6.93	AuPd	0.40	0.57	-	-	0.39	0.09	-1.86	0.01	0.01	0.98	0.03	0.83	0.80
LP I11	700	1280	20	-5.96	AuPd	0.16	143	-	-	1.01	0.07	-1.25	0.06	0.04	0.74	0.01	0.77	0.73
LP I12	700	1280	20	-5.19	AuPd	0.17	172	-	-	2.14	0.08	-0.59	0.19	0.10	0.69	0.01	0.70	0.64
LP I13	700	1280	20	-4.66	AuPd	0.19	2.14	-	-	3.44	0.09	-0.71	0.37	0.19	0.62	0.01	0.65	0.56
O1	700	1280	12	-	AuPd	1.00	-	-	-	9.16	0.08	-	-	-	0.34	0.01	-	-

*Fritzsché (2013), - not determined; **Oxygen fugacity calculated from aH₂O (calculated after Moore, see text). ΔFMQ is log f_{O_2} expressed relative to the FMQ buffer;

***Mole fraction of H₂O and CO₂ in the fluid phase measured by the weight loss method.

3.5.1 Calculation of $a_{\text{H}_2\text{O}}$ and f_{O_2}

All experiments conducted in this study (superliquidus and phase equilibria experiments) were fluid-saturated, varying the $X_{\text{H}_2\text{O}}$ from 0 to 1 (nominally dry to H_2O saturated). The amount of free fluid phase was approximately 10% and the concentrations of H_2O and CO_2 in the fluid phase ($X_{\text{H}_2\text{O}}^{\text{fl}}$) were determined after the experiment by the weight loss method for each experimental run. But the uncertainty of this method is relatively high, because fluid can be trapped in vesicles or the liquid can have lost H_2O if quenching was insufficient (Moore 1998). Thus, the H_2O activity ($a_{\text{H}_2\text{O}}$) in each experiment was calculated using different solubility models, which require the determination of the H_2O concentration in the quenched glasses.

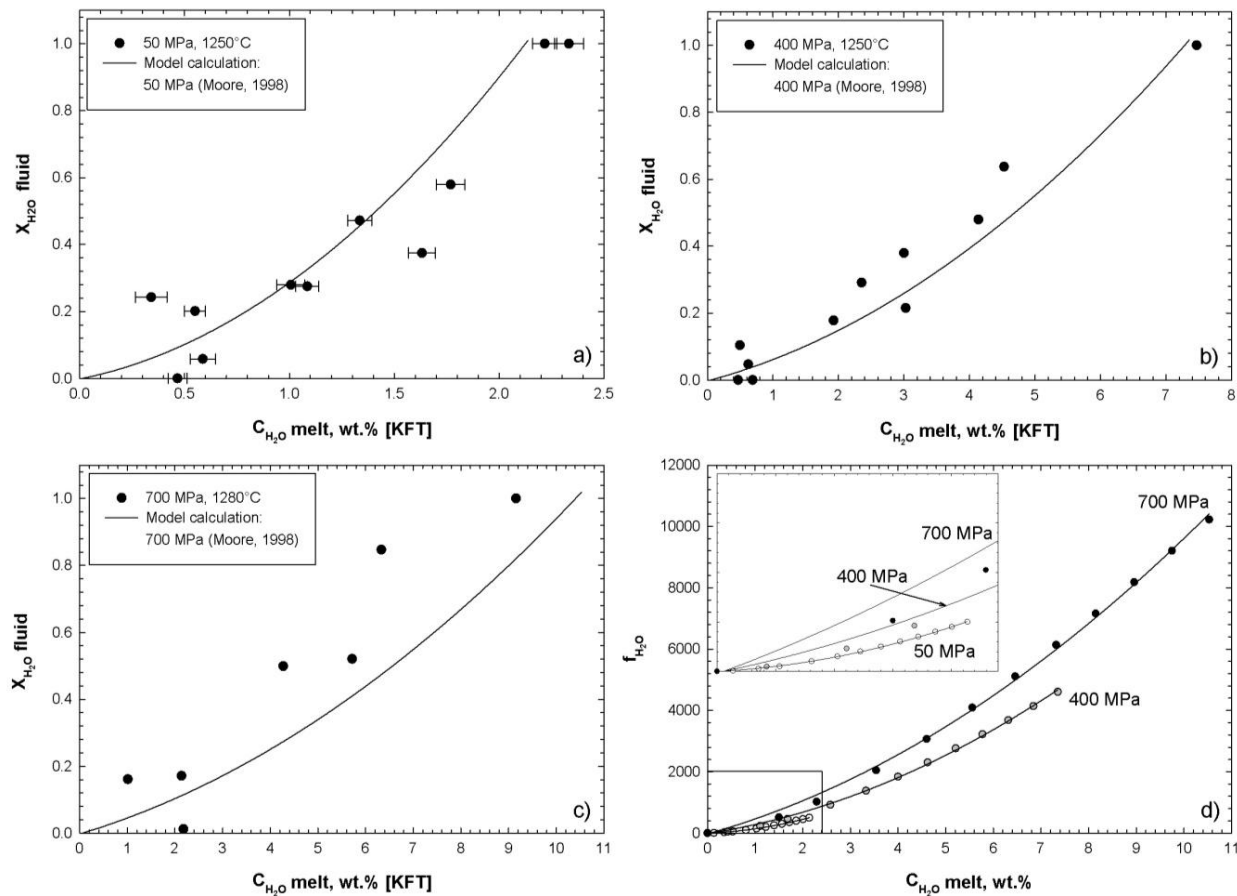


Figure 9: Molar fraction of H_2O in the fluid phase of experiments conducted at superliquidus conditions and 50 (a), 400 (b) and 700 MPa (c) as a function of the H_2O concentration in the coexisting melt (wt.%). Also plotted are model calculations after Moore (1998) for the same basanitic composition (KLA-1-6-22). (b) and (c) Error is in symbol size. (d) Calculated H_2O fugacity after Moore (1998) at given H_2O concentration in the melt for 50, 400 and 700 MPa using basanite KLA-1-6-22.

We used the KFT data of our superliquidus experiments ($X_{\text{H}_2\text{O}}$ from nominally dry to H_2O saturated conditions, at 700, 400 and 50 MPa) to test the applicability of the H_2O solubility models of Burnham (1979) and Moore (1998) for alkali-rich compositions and pressures between 50 to 700 MPa. Figure 9 shows $X_{\text{H}_2\text{O}}^{\text{fl}}$ as a function of the H_2O concentration in the melt measured by KFT for experiments conducted at 50, 400, 700 MPa and superliquidus conditions. Also plotted are the model calculations using the empiric model of Moore et al. (1998) applied for the same basanitic composition (KLA-1-6-22) and the same p-T conditions of the experimental runs. Calculated H_2O solubilities by Moore (1998) are in good agreement with the KFT data for all investigated pressures. However, KFT data for maximum solubility at 700 MPa is low due to insufficient quenching at high pressures and high H_2O concentration in the glass (discussed above). Corresponding to the quenching effect the molar fraction is elevated (discussed above). H_2O solubility calculated at 700 MPa using the model of Moore (1998) yields a reasonable value of 10.53 wt.%. In this model the H_2O fugacity ($f_{\text{H}_2\text{O}}$) is calculated by using a modified Redlich-Kwong equation of state which was shown in the Appendix of Holloway and Blank (1994). Figure 11d shows the calculated $f_{\text{H}_2\text{O}}$ as a function of the H_2O concentration in the melt for 50, 400 and 700 MPa (see Table 4 for empirical equations). We used the function to calculate the $f_{\text{H}_2\text{O}}$ and in another step $a_{\text{H}_2\text{O}}$ of experimental glasses at given temperature and pressure, with the following equation:

$$a_{\text{H}_2\text{O}} = f_{\text{H}_2\text{O}}^{\text{calc}} / f_{\text{H}_2\text{O}}^0 \quad (2)$$

$f_{\text{H}_2\text{O}}^0$ data were taken from Pitzer and Stern (1994).

Calculated H_2O activities using either the Burnham model or the calculated $f_{\text{H}_2\text{O}}$ from the Moore model applied to equation (1) are shown in Figure 10. It is well known that the model of Burnham significantly underestimates H_2O solubility at high pressure. The deviation between measured H_2O concentration in the melt and calculated $a_{\text{H}_2\text{O}}$ at H_2O saturated conditions ($a_{\text{H}_2\text{O}}=1$) are 1.2 wt.% at 400 MPa and 2.7 wt.% at 700 MPa using the Burnham model. Our application of the Moore model calculates reasonable $a_{\text{H}_2\text{O}}$ at high pressures, but slightly

overestimates the H₂O solubility at low pressures, while the model of Burnham works well at low pressures.

At known $f_{\text{H}_2\text{O}}$ and f_{H_2} , the prevailing oxygen fugacity within the capsule can be calculated according to the dissociation reaction of H₂O ($\text{H}_2 + \frac{1}{2}\text{O}_2 = \text{H}_2\text{O}$):

$$K_w = f_{\text{H}_2\text{O}} / f_{\text{H}_2} * (f_{\text{O}_2})^{0.5} \quad (3)$$

Whereas the logarithm of oxygen fugacity is given by Robie et al. (1978) as

$$\log f_{\text{O}_2} = 2\log f_{\text{H}_2\text{O}} - 2\log f_{\text{H}_2} - 2\log K_w \quad (4)$$

And f_{H_2} is either the P_{H_2} by Shaw-membrane or the P_{H_2} which corresponds to the intrinsic conditions of the internally heated pressure vessel multiplied by the H₂ fugacity coefficients of Shaw and Wones (1964).

As shown in Figure 9d the $f_{\text{H}_2\text{O}}$ increases with C_{H₂O} in the melt and the equilibrium constant of the dissociation reaction of H₂O shows that increasing $f_{\text{H}_2\text{O}}$ causes an increase of f_{O_2} (Scaillet et al., 1995). In Figure 10d measured H₂O concentrations of superliquidus experiments conducted at 50, 400, 700 MPa are plotted as a function of oxygen fugacity relative to the FMQ buffer, the data shows that with increasing H₂O content in the melt from nominally dry (0.5 wt.% of H₂O) to H₂O saturated conditions (depending on pressure) calculated oxygen fugacities vary from FMQ to \sim FMQ+3.8. Whereas the quantity FMQ is the difference between the natural logarithm of f_{O_2} of the experiment and the log f_{O_2} of the quartz–fayalite–magnetite buffer determined by Schwab and Küstner (1981).

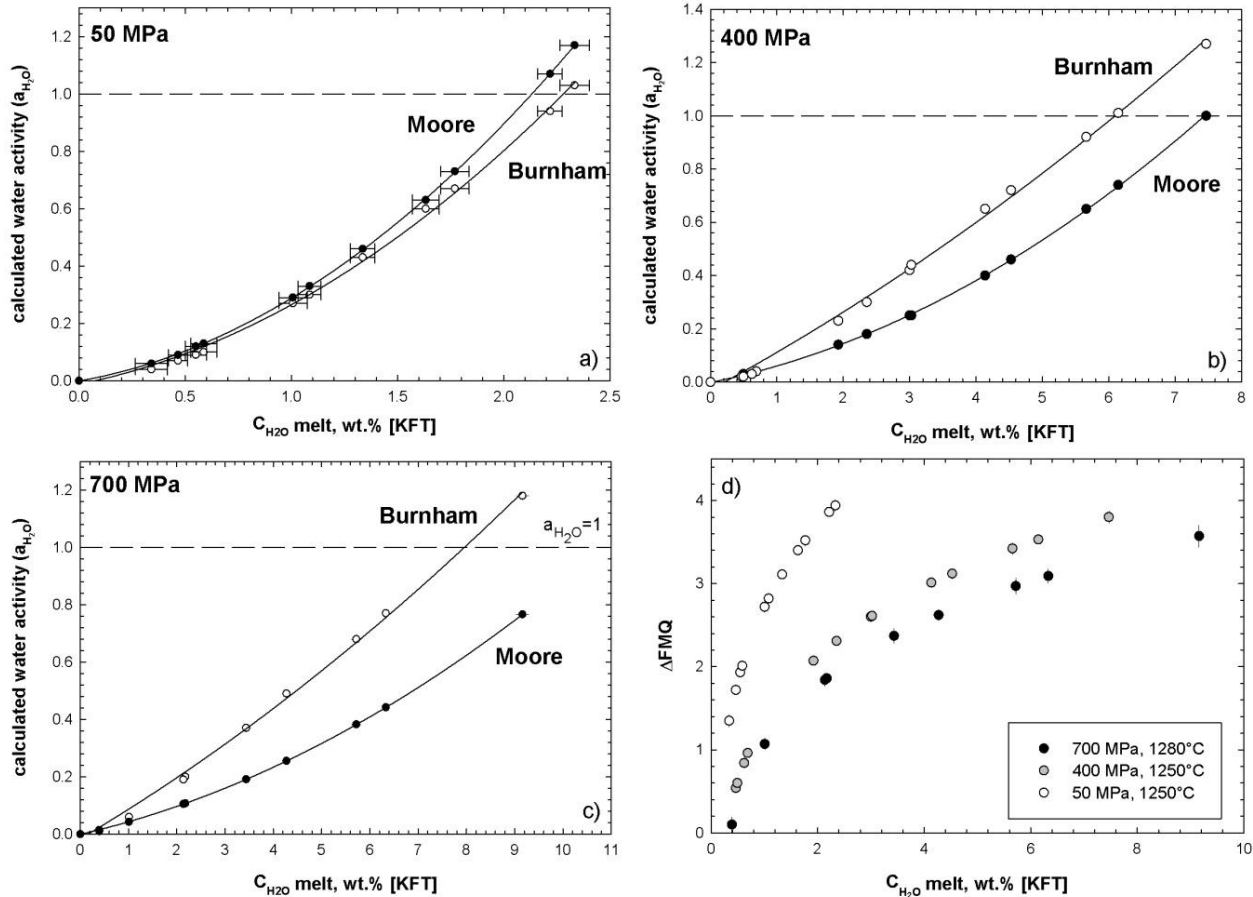


Figure 10: Calculated H_2O activity using either the model of Burnham (1979) or the model of Moore (1998) as a function of H_2O concentration in the melt for experiments conducted at 50, 400 and 700 MPa at superliquidus conditions. d): Dependence of H_2O concentration in the melt on oxygen fugacity (expressed relative to the FMQ buffer) at 50 (a), 400 (b) and 700 MPa (c) and superliquidus conditions. H_2O concentrations are measured by KFT, the error is in symbol size. Calculation of oxygen fugacity see text.

Table 4. Empirical equations for calculation of f_{H_2O} according to Moore (1998)

Pressure [MPa]	f_{H_2O}
50	$81.39 \times CH_2O\text{ melt}^2 + 62.15 \times CH_2O\text{ melt} - 0.849$
400	$54.17 \times CH_2O\text{ melt}^2 + 239.0 \times CH_2O\text{ melt} - 12.38$
550	$52.04 \times CH_2O\text{ melt}^2 + 326.2 \times CH_2O\text{ melt} - 21.07$
700	$52.88 \times CH_2O\text{ melt}^2 + 434.5 \times CH_2O\text{ melt} - 25.06$

3.5.2 Calculation of $\text{Fe}^{2+}/\Sigma\text{Fe}$ ratio in glasses

It is well known that the redox state of iron in a silicate melt is influenced by $a_{\text{H}_2\text{O}}$ and redox conditions of the system (e.g. Schuessler, 2008). So far no experimental data on nominally dry to hydrous conditions of basanitic compositions and elevated pressure exists. For estimation of $\text{Fe}^{2+}/\Sigma\text{Fe}$ ratios in experimental glasses and calculation of partition coefficients for Fe^{2+} between melt and minerals, we performed experiments at superliquidus and at nominally dry to H_2O -saturated conditions using the basanitic starting material KLA-1-6-22 at 50, 400 and 700 MPa. After the experiment the $X_{\text{H}_2\text{O}}$ of the fluid phase was determined by the weight loss method. H_2O concentrations in the melt were measured by IR, KFT and $\text{Fe}^{2+}/\Sigma\text{Fe}$ ratios by colorimetric $\text{Fe}^{2+}/\text{Fe}^{3+}$ determination. All results are summarized in Table 3. In addition the experimental charges were checked by electron microprobe for iron loss or gain (see Fe-pre-saturation) and a homogeneous distribution of iron over the whole capsule material. At 50 MPa and 1250°C the measured $\text{Fe}^{2+}/\Sigma\text{Fe}$ ratio ranges from 0.41-0.74 with decreasing H_2O concentrations in the melt from 2.22-0.34 wt.%. At 400 MPa and 1250°C the measured $\text{Fe}^{2+}/\Sigma\text{Fe}$ ratio varies from 0.36-0.77 with H_2O concentrations ranging from 7.47 to 0.47 wt.%. At 700 MPa and 1280°C the measured $\text{Fe}^{2+}/\Sigma\text{Fe}$ ratio ranges from 0.31-0.74 with decreasing H_2O concentrations in the melt from 9.16-1.01 wt.%. The dependency of the H_2O content in the experimental glasses on the $\text{Fe}^{2+}/\Sigma\text{Fe}$ ratio in the melt is shown in Figure 11a. This dependency can be used for the estimation of $\text{Fe}^{2+}/\Sigma\text{Fe}$ ratio in experimental glasses at given H_2O content and given pressure (see Table 5 for empirical equations).

In Figure 11 (b, c and d) measured $\text{Fe}^{2+}/\Sigma\text{Fe}$ ratios are shown in comparison to calculated $\text{Fe}^{2+}/\Sigma\text{Fe}$ ratio after Kress and Carmichael (1991) and Moretti (2005). At 50 MPa the $\text{Fe}^{2+}/\Sigma\text{Fe}$ ratio are in good agreement with the predictions of Kress and Carmichael (1991) and Moretti (2005). At 400 and 700 MPa the model of Kress and Carmichael (1991) predicts higher $\text{Fe}^{2+}/\Sigma\text{Fe}$ ratios (corresponding to more reduced conditions) at $\text{Fe}^{2+}/\Sigma\text{Fe}$ ratios below 0.6 which results in a strong deviation from the 1:1 correlation, while predictions of Moretti (2005) are very close to the 1:1 correlation even at high pressures.

To test the applicability of the of the Moretti model and our own calibration for $\text{Fe}^{2+}/\Sigma\text{Fe}$ ratio in the melt (based on the measured H_2O concentration and $\text{Fe}^{2+}/\Sigma\text{Fe}$ ratio of superliquidus

experiments at different pressures) on crystallization experiments (experiments at temperatures between 1175 and 1010°C) we calculated partition coefficients of ferrous iron and magnesium between olivine and melt for starting composition KLA-1-6-22 and 168-1. After Toplis et al. (2005) Kd_{ol-liq} values depend on temperature and melt composition and can vary from 0.17 to 0.40. In Figure 12 a comparison of the KD values, in which ferric iron in the coexisting melt was either calculated by the model of Moretti (2005) or by our own calibration for $Fe^{2+}/\Sigma Fe$ ratio in the melt for given pressure. Both data sets are in a good agreement of the given Kd values of Toplis et al. (2005) and close to a 1:1 correlation (see Figure 12).

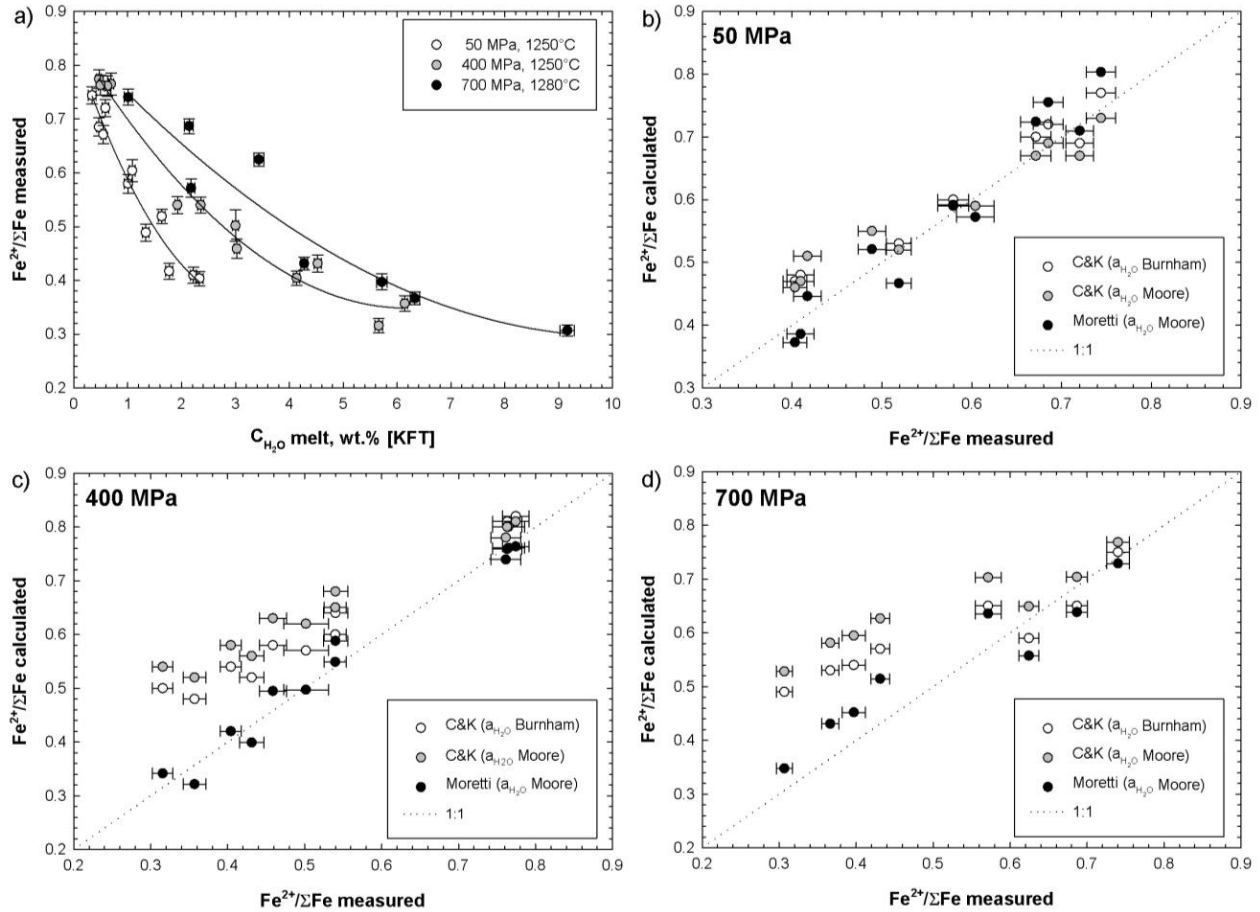


Figure 11: a) Influence of H_2O concentration in the melt on the $Fe^{2+}/\Sigma Fe$ ratio of experiments conducted at 50, 400 and 700 MPa at superliquidus conditions using the evolved basanite (KLA-1-6-22). Error of H_2O concentration is in the symbol size. Comparison between calculated and measured $Fe^{2+}/\Sigma Fe$ ratios of experiments conducted at 50 (b), 400 (c) and 700 MPa (d) at superliquidus conditions and modeled by Kress and Carmichael (1991) and Moretti (2005) using either the H_2O activity calculated by Burnham (1979) or by Moore (1998). The dashed line is a 1:1 correlation.

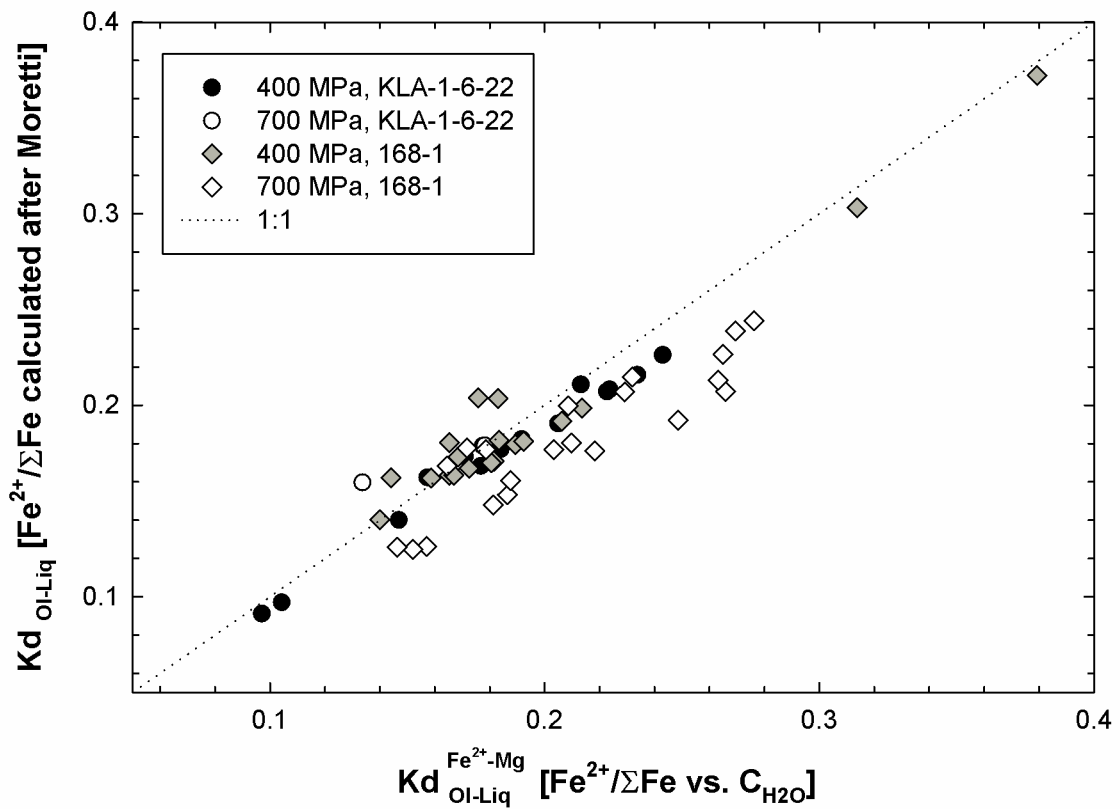


Figure 12: Comparison of partitioning coefficients of Fe^{2+} and Mg between olivine and the coexisting melt using either the model of Moretti (2005) or our own calibration for the estimation of $\text{Fe}^{2+}/\Sigma\text{Fe}$ ratio in the melt, of crystallization experiments conducted at 400 and 700 MPa using either the primitive basanite (168-1) or the evolved basanite (KLA-1-6-22) as starting material. The dashed line represents a 1:1 correlation.

Table 5. Empirical equations for calculation of $\text{Fe}^{2+}/\Sigma\text{Fe}$ in glasses

Pressure [MPa]	$\text{Fe}^{2+}/\Sigma\text{Fe}$
50	$-0.13 \times \ln(\text{CH}_2\text{O melt}) + 0.561$
400	$-0.17 \times \ln(\text{CH}_2\text{O melt}) + 0.665$
700	$-0.22 \times \ln(\text{CH}_2\text{O melt}) + 0.783$

4. Results

4.1 Phase relations

All experimental conditions and run products of phase equilibria experiments are summarized in Tables 6-10. The crystallizing phases are olivine (Ol), clinopyroxene (Cpx), amphibole (Amph), plagioclase (Pl), magnetite (Mt), spinel (Spl) and apatite (Ap). Thermodynamic parameters like pressure, temperature, H₂O activity and oxygen fugacity control the stability of different phases in a system. The redox state of the system is controlled by the experimental temperature and the H₂O activity in the capsule at given pressure and given intrinsic $f\text{O}_2$ in the vessel. To investigate the influence of each of these three thermodynamic parameters on the phase relations in a basanitic system at different pressures, the observed stability fields of the minerals were plotted as a function of temperature and H₂O content of the melt for each pressure. Dashed lines indicate the degree of crystallization, which increases as a function of decreasing aH₂O or decreasing temperature. The degree of crystallization changes dramatically with the onset of amphibole, this observation will be described in more detail description in Chapter 4.2 (phase proportions).

At 400 MPa (Figure 13a & 14a), phase stabilities were investigated in the temperature range from 1010°C to 1175°C from nominally dry to H₂O saturated conditions, keeping the $f\text{O}_2$ between FMQ to FMQ+3.8. Experiments in the temperature range of 1010-1050°C and H₂O contents in the melt >4 wt.% were performed at more reducing conditions (FMQ+1 at H₂O saturated conditions). The crystallization sequence at H₂O saturated conditions is spinel/magnetite (found as inclusion in olivine), olivine, clinopyroxene, amphibole and apatite. At oxidizing conditions magnetite is the liquidus phase for the entire range of H₂O contents in the melt. At temperatures from 1050-1010°C and high H₂O contents (>4 wt.% H₂O in the melt) and log $f\text{O}_2$ close to FMQ+1 at H₂O saturated conditions CrMg-spinel was observed instead of magnetite. Olivine was observed at 1050°C and H₂O saturated conditions up to 1175°C with decreasing H₂O content in the melt. At 1050°C and H₂O saturated conditions clinopyroxene appears on the liquidus for the primitive basanite (Figure 13a) and at 1025°C for the evolved basanite (KLA-1-6-22) (Figure 14a). At H₂O saturated conditions and temperatures of 1025°C

amphibole is stable. Amphibole stability is shifted to higher temperatures up to a peak temperature of 1075°C (at approximately 3.5 wt.% H₂O in the melt) with decreasing H₂O content in the melt. However, amphibole stability extends to H₂O contents in the melts below 1 wt.% (>0.1 X_{H₂O}). Plagioclase was only reproduced at low H₂O contents in the melt (0.1-1.13 wt.%) at temperature below 1050°C for the evolved basanite (KLA-1-6-22) (see Figure 14a) and below 1075°C for the primitive basanite (168-1) (see Figure 13a). Apatite is stable at temperatures below 1010°C at high H₂O contents in the melt and up to 1050°C at very low H₂O contents (~1 wt.%) in the melt. However, apatite crystallizes preferentially at CO₂-rich and H₂O-poor conditions (<0.2 X_{H₂O}).

Experiments at 550 MPa (Figure 14b) were conducted in the stability field of Ol+Cpx+Mt to investigate the pressure dependence of stability and proportions of these phases in pressure range from 400 MPa and 700 MPa for the evolved basanite. In comparison to experiments performed at 700 MPa the stability of olivine is shifted to lower temperature (1075°C at least) instead of approximately 1115°C at 700 MPa and low H₂O contents in the melt (see Figure 14b). Phase relations at 700 MPa for the primitive basanite (Figure 13b) are very similar to those observed at 400 MPa. However, for both basanitic starting materials the mineral stability fields are shifted to higher temperatures. The crystallization sequence of the more evolved basanite at H₂O saturated conditions changed to magnetite, clinopyroxene, olivine, amphibole and apatite (see Figure 14c). At 700 MPa, plagioclase crystallization is suppressed and no plagioclase was observed at the investigated conditions.

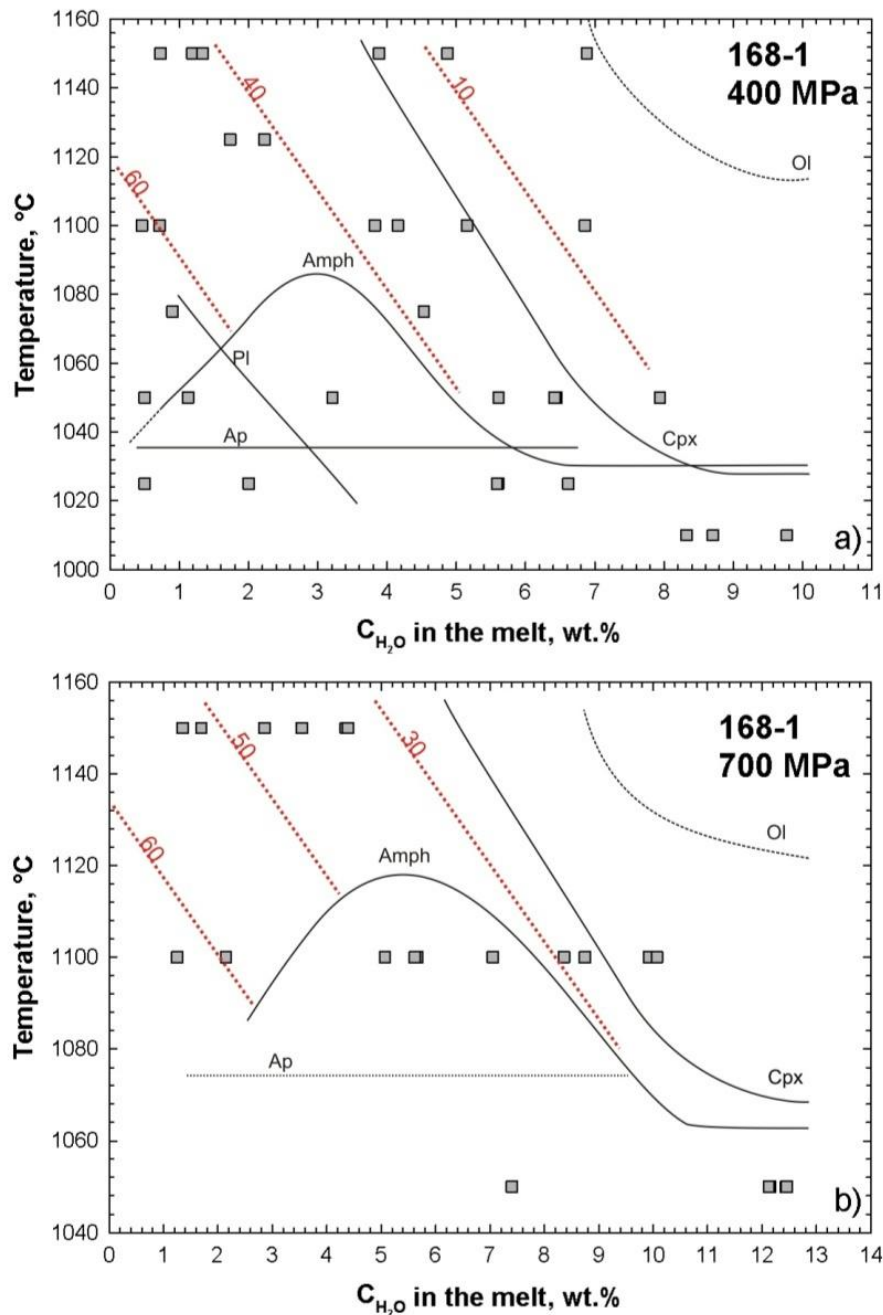


Figure 13: Phase relations of starting composition 168-1 (primitive basanite) as a function of H_2O concentration in the melt (wt.%) and temperature ($^{\circ}C$). Squares indicate experimental conditions. Shown are the stability fields of olivine (Ol), clinopyroxene (Cpx), amphibole (Amph), plagioclase (Pl) and apatite (Ap). Magnetite was stable at all investigated conditions. (a) 168-1 at 400 MPa; (b) at 700 MPa. Solid lines are observed phase boundaries, red dashed lines indicate the degree of crystallization in wt.%.

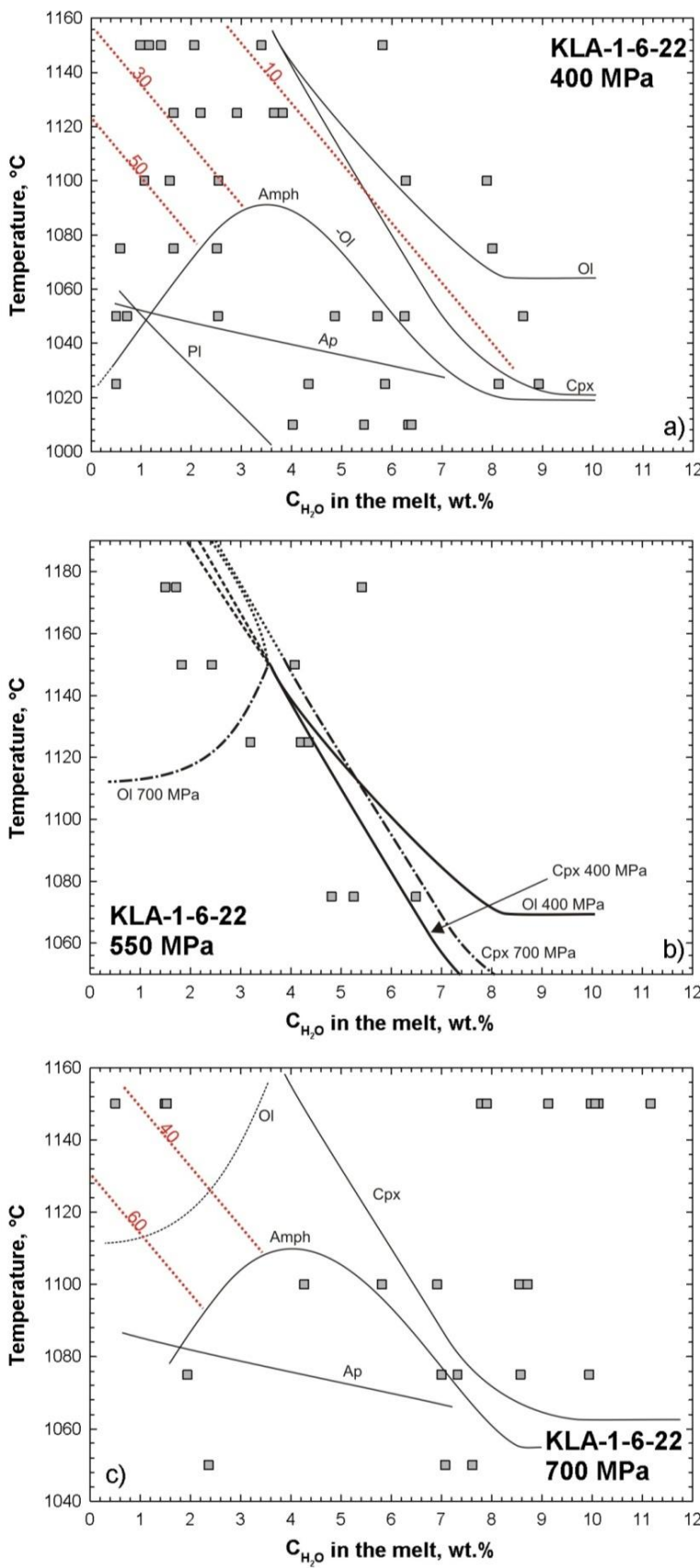


Figure 14: Phase relations of starting compositions KLA-1-6-22 (evolved basanite) as a function of H_2O concentration in melt (wt.%) and temperature ($^{\circ}\text{C}$). Squares indicate experimental conditions. Shown are the stability fields of olivine (Ol), clinopyroxene (Cpx), amphibole (Amph), plagioclase (Pl) and apatite (Ap). Magnetite was stable at all investigated conditions. (a) KLA-1-6-22 at 400 MPa; (b) at 550 MPa, Ol+Cpx+Mt+Liq phase assemblage was stable at all investigated conditions, additionally shown are the stability fields of olivine and clinopyroxene observed at 400 and 700 MPa; (c) at 700 MPa. Solid lines are observed phase boundaries, red dashed lines indicate the degree of crystallization in wt.%.

Table 6. Experimental conditions and phase relations for the primitive basanite (168-1) at 400 MPa

Run	Temperature [°C]	Duration [hours]	Capsule	Fe\$ loss/gain	melt H ₂ O [wt%]	fH ₂ O*	aH ₂ O*	log fO ₂ ** [bar]	ΔFMQ	Phase assemblage	R ²	j [%]
LP10	1050	68	Au		6.45	3778.76	0.87	-9.50	0.40	Ol(16.2), Spl(0.8), Gl(83)	0.19	17.00
LP11	1050	68	Au		6.42	3750.11	0.79	-7.19	0.32	Ol(16.5), Cpx(5), Spl(1.3), Gl(77.2)	0.19	22.80
LP12	1050	68	Au		5.61	3034.44	0.64	-7.37	0.14	Ol(17.7), Cpx(11.1), Spl(1.1), Gl(70.2)	0.18	29.90
LP30	1050	68	Au		0.50	120.66	0.03	-7.40	0.11	Ol(12.5), Cpx(36.4), Amph(14.5), Mt(6.9), Gl(29.7)	0.28	70.30
LP34	1025	73	Au		5.60	3026.69	0.64	-6.83	0.68	Ol(20.7), Cpx(11), Mt(1.8), Ap(0.1), Gl(66.4)	0.10	33.60
LP35	1025	73	Au		6.62	3940.71	0.83	-6.60	0.91	Ol(12.7), Cpx(15.3), Amph(31.9), Mt(5), Gl(35.1)	0.07	64.90
LP36	1025	73	Au		5.59	3012.36	0.63	-6.83	0.68	Ol(11.6), Cpx(13.1), Amph(39.8), Mt(4.1), Gl(31.4)	0.02	68.60
LP53	1010	96	Au		9.77	7496.55	1.58	-4.43	3.08	Ol(2.8), Cpx(8.1), Amph(61.7), Mt(7.3), Ap(0.7), Gl(19.4)	0.17	80.60
LP54	1010	96	Au		8.71	6176.00	1.30	-4.60	2.91	Ol(3.5), Cpx(8.6), Amph(61.7), Mt(6.7), Ap(0.7), Gl(18.8)	0.27	81.20
LP55	1010	96	Au		8.33	5732.61	1.21	-4.67	2.84	Ol(3.5), Cpx(9.4), Amph(61.7), Mt(6.2), Ap(0.7), Gl(18.5)	0.19	81.50
LP168	1100	34	AuPdFe		0.46	186.10	0.04	-8.20	1.04	Ol(14.8), Cpx(42.8), Mt(5.6), Gl(36.8)	0.12	63.20
LP169	1100	34	AuPd	4% loss	0.71	185.50	0.04	-8.20	1.04	Ol(13.8), Cpx(40), Mt(6.8), Gl(39.3)	0.13	60.60
LP170	1100	34	AuPd		5.15	2656.07	0.59	-5.89	3.35	Ol(11), Cpx(10.6), Mt(7.5), Gl(71)	0.08	29.10
LP171	1100	34	AuPd	6% loss	3.82	1690.98	0.38	-6.28	2.96	Ol(10.1), Cpx(16.7), Mt(7.4), Gl(65.7)	0.18	34.20
LP172	1100	34	AuPd		4.16	1916.34	0.43	-6.17	3.07	Ol(13.4), Cpx(29.6), Mt(6), Gl(51.1)	0.13	49.00
LP173	1100	34	AuPd		6.86	4176.42	0.93	-5.50	3.74	Ol(7.2), Mt(5.4), Gl(87.5)	0.42	12.60
LP180	1150	30	AuPdFe	9% gain	1.19	348.86	0.08	-7.06	1.56	Ol(15.9), Cpx(19.3), Mt(0.4), Gl(64.4)	0.14	35.60
LP181	1150	30	AuPd		0.73	189.92	0.04	-7.59	1.03	Ol(13.9), Cpx(23.4), Mt(3.2), Gl(59.4)	0.23	40.50
LP182	1150	30	AuPd		1.34	404.55	0.09	-6.93	1.69	Ol(13.9), Cpx(23.9), Mt(3.1), Gl(59)	0.16	40.90
LP183	1150	30	AuPd		3.89	1735.55	0.38	-5.66	2.96	Ol(7.7), Mt(3.2), Gl(89)	0.11	10.90
LP184	1150	30	AuPd		4.87	2435.40	0.53	-5.37	3.25	Ol(5), Mt(3.5), Gl(91.5)	0.10	8.50
LP185	1150	30	AuPd		6.88	4200.25	0.92	-4.90	3.72	Ol(1.4), Mt(2.5), Gl(96.1)	0.26	3.90
LP188	1050	68	Au		1.13	326.12	0.07	-8.35	1.55	Ol(15.9), Cpx(51.6), Amph(-3.4), Mt(6.8), Pl(-5.6), Gl(34.7)	0.23	65.30
LP189	1050	68	Au		3.21	1313.54	0.30	-7.14	2.76	Ol(12.2), Cpx(31.8), Amph(3.9), Mt(8.1), Gl(44)	0.23	56.00
LP190	1075	68	AuPd		0.90	246.18	0.06	-8.27	1.29	Ol(11), Cpx(21), Amph(30), Mt(6.8), Pl(-4.3), Gl(35.4)	0.15	64.50
LP191	1075	68	AuPd		4.53	2182.88	0.49	-6.37	3.19	Ol(15), Cpx(21.8), Mt(9.5), Gl(53.6)	0.36	46.30
LP198	1025	68	Au		0.50	120.66	0.03	-9.55	0.70	Ol(12), Cpx(48.5), Amph(25.3), Mt(2.9), Ap(1.5), Gl(9.8)	1.23	90.20
LP199	1025	68	Au		2.00	682.75	0.16	-8.04	2.21	Ol(9.5), Cpx(23.7), Amph(38.6), Mt(6.6), Ap(1.2), Gl(20.3)	0.41	79.60
LP202	1125	24	AuPd		1.73	564.49	0.12	-6.93	1.99	Ol(15.1), Cpx(24.5), Mt(2.7), Gl(57.7)	0.13	42.30
LP203	1125	24	AuPd		2.23	789.62	0.17	-6.64	2.28	Ol(13.8), Cpx(21.7), Mt(3.7), Gl(60.8)	0.09	39.20
LP216	1050	24	Au		7.94	5301.26	1.22	-5.93	3.97	Ol(10.4), Cpx(4.4), Mt(5.4), Gl(79.8)	0.23	20.20

*) fH₂O and aH₂O calculated after Moore (1998) (see text); **) Oxygen fugacity calculated from aH₂O. DFMQ is log fO₂ expressed relative to the FMQ buffer

\$) Fe loss/gain calculated by mass balance

Table 7. Experimental conditions and phase relations for the primitive basanite (168-1) at 700 MPa

Run	Temperature [°C]	Duration [hours]	Capsule	Fe\$ loss/gain	melt H ₂ O [wt%]	fH ₂ O*	a H ₂ O*	log fO ₂ ** [bar]	ΔFMQ	Phase assemblage	R ²	j [%]
LP85	1050	48	Au		12.14	13049.11	1.11	-5.66	4.03	Ol(9.7), Cpx(11.5), Mt(9.1), Gl(69.7)	0.94	30.30
LP86	1050	48	Au		12.44	13557.82	1.26	-5.62	4.07	Ol(7), Cpx(16), Amph(18.4), Mt(9.4), Gl(49.2)	0.07	50.80
LP87	1050	48	Au		12.45	13587.60	1.16	-5.62	4.07	Ol(3.7), Cpx(14.1), Amph(45.1), Mt(9.2), Gl(27.9)	0.05	72.10
LP88	1050	48	Au		12.12	13016.17	1.10	-5.66	4.03	Ol(3.6), Cpx(17.3), Amph(46.2), Mt(9.3), Ap(0.2), Gl(23.5)	0.18	76.60
LP89	1050	48	Au		7.40	6089.84	0.61	-6.32	3.37	Ol(1), Cpx(18), Amph(54.2), Mt(6.9), Ap(0.5), Gl(19.4)	0.54	80.60
LP95	1100	20	AuPd		8.74	7815.37	0.76	-5.47	3.57	Ol(6), Mt(4.3), Gl(89.8)	0.43	10.30
LP96	1100	20	AuPd		8.36	7299.45	0.71	-5.53	3.51	Ol(7.8), Mt(4.4), Gl(87.9)	0.24	12.20
LP97	1100	20	AuPd		9.92	9486.06	0.92	-5.30	3.74	Ol(9.3), Mt(5), Gl(85.7)	0.10	14.30
LP98	1100	20	AuPd		10.06	9704.61	0.95	-5.28	3.76	Ol(9.4), Cpx(12.9), Mt(6.6), Gl(71)	0.10	28.90
LP99	1100	20	AuPd		7.05	5666.88	0.55	-5.75	3.29	Ol(10.9), Cpx(31), Amph(0.7), Mt(8.3), Ap(0.4), Gl(48.7)	0.29	51.30
LP100	1100	20	AuPd		1.25	599.98	0.06	-7.70	1.34	Ol(12.1), Cpx(32.2), Mt(9.8), Gl(45.9)	0.40	54.10
LP101	1100	20	AuPd		2.15	1151.06	0.11	-7.14	1.90	Ol(11.6), Cpx(39.7), Mt(7.6), Gl(41.1)	0.14	58.90
LP102	1100	20	AuPd		5.07	3535.98	0.34	-6.16	2.88	Ol(9), Cpx(21.3), Amph(2.5), Mt(7.1), Gl(60.1)	0.03	39.90
LP103	1100	20	AuPd		5.66	4130.82	0.40	-6.03	3.01	Ol(9.6), Cpx(17.4), Amph(-0.6), Mt(6.8), Gl(66.8)	0.07	33.20
LP104	1100	20	AuPd		5.62	4085.24	0.40	-6.04	3.00	Ol(9.3), Cpx(13.1), Amph(-6.1), Mt(6.5), Gl(77.2)	0.03	22.80
LP115	1150	20	AuPd		2.86	1649.02	0.16	-6.23	2.20	Ol(12.5), Cpx(31.7), Mt(4.1), Gl(51.7)	0.24	48.30
LP116	1150	20	AuPd	2% Fe loss	3.54	2178.40	0.21	-5.99	2.44	Ol(11.6), Cpx(20.7), Mt(3.6), Gl(64.1)	0.15	35.90
LP117	1150	20	AuPd	2% Fe loss	4.35	2865.79	0.27	-5.75	2.68	Ol(11.2), Cpx(18.9), Mt(4.2), Gl(65.7)	0.21	34.30
LP118	1150	20	AuPd		4.39	2898.92	0.28	-5.74	2.69	Ol(11.3), Cpx(11.1), Mt(3), Gl(74.6)	0.07	25.40
LP154	1150	20	AuPd		1.36	661.20	0.06	-7.03	1.40	Ol(10.9), Cpx(40.7), Mt(5.3), Gl(43)	0.56	56.90
LP155	1150	20	AuPd		1.69	862.83	0.08	-6.80	1.63	Ol(11), Cpx(39.9), Mt(5.2), Gl(44)	0.12	56.10

*) fH₂O and aH₂O calculated after Moore (1998) (see text); **) Oxygen fugacity calculated from aH₂O. DFMQ is log fO₂ expressed relative to the FMQ buffer

\$) Fe loss/gain calculated by mass balance

Table 8. Experimental conditions and phase relations for the evolved basanite (KLA-1-6-22) at 400 MPa

Run	Temperature [°C]	Duration [hours]	Capsule	Fe\$ loss/gain	melt H ₂ O [wt%]	fH ₂ O*	aH ₂ O*	log fO ₂ ** [bar]	ΔFMQ	Phase assemblage	R ²	j [%]
LP13	1050	68	Au		6.25	3594.11	0.76	-7.10	0.41	Ol(4.4), Cpx(1.6), Spl(1.7), Gl(92.3)	0.20	7.70
LP14	1050	68	Au		5.71	3116.64	0.66	-7.22	0.29	Ol(4.6), Cpx(7), Mt(1.6), Gl(86.2)	0.67	13.20
LP15	1050	68	Au		4.86	2429.47	0.51	-7.44	0.07	Ol(4.1), Cpx(12.9), Amph(7), Mt(1.9), Gl(74.2)	0.10	25.90
LP32	1050	68	Au		0.50	120.66	0.03	-7.40	0.11	Ol(2.7), Cpx(48.7), Mt(9.8), Pl(0.3), Ap(0.3), Gl(38.2)	0.13	61.80
LP33	1050	68	Au		0.50	120.66	0.03	-7.40	0.11	Ol(3.8), Cpx(45.8), Mt(10.7), Pl(10.9), Ap(0), Gl(28.9)	0.41	71.22
LP38	1025	70	Au		4.34	2044.41	0.43	-6.57	0.94	Cpx(17.4), Amph(37.9), Mt(3), Ap(0.2), Gl(41.4)	0.51	58.50
LP39	1025	70	Au		5.86	3245.76	0.68	-6.17	1.34	Cpx(14.2), Amph(37.1), Mt(2.7), Gl(46.1)	0.27	54.00
LP40	1025	70	Au		8.12	5500.82	1.16	-5.71	1.80	Cpx(5.9), Amph(21.7), Mt(2.5), Gl(69.9)	0.63	30.10
LP44	1010	92	Au		6.32	3665.25	0.77	-6.16	1.35	Cpx(8), Amph(26.5), Mt(3.4), Ap(0.2), Gl(61.9)	0.03	38.10
LP45	1010	92	Au		6.39	3722.71	0.78	-6.15	1.36	Cpx(17.4), Amph(37.9), Mt(3), Ap(0.2), Gl(41.4)	0.51	58.50
LP46	1010	92	Au		5.44	2892.35	0.61	-6.37	1.14	Cpx(9.6), Amph(44.5), Mt(3.7), Ap(0.7), Gl(41.5)	0.24	58.50
LP47	1010	92	Au		4.02	1823.06	0.38	-6.77	0.74	Cpx(23.2), Amph(33), Mt(4), Ap(1.1), Gl(38.8)	0.18	61.30
LP131	1100	20	AuPd		7.89	5426.76	1.21	-5.27	3.97	Mt(3.7), Gl(96.3)	0.16	3.70
LP132	1100	20	AuPd		6.27	3631.84	0.81	-5.62	3.62	Cpx(2.3), Mt(5), Gl(92.7)	0.13	7.30
LP134	1100	20	AuPd		2.54	952.71	0.21	-6.78	2.46	Ol(2.7), Cpx(44.1), Mt(6.4), Gl(46.7)	0.20	53.20
LP135	1100	20	AuPd		1.06	302.93	0.07	-7.78	1.46	Ol(3.3), Cpx(41.1), Mt(6.5), Gl(49.1)	0.24	50.90
LP174	1150	30	AuPd		1.39	426.21	0.09	-6.88	1.74	Ol(4.3), Cpx(40.8), Mt(4.2), Gl(50.7)	0.45	49.30
LP175	1150	30	AuPdFe	16% Fe gain	2.06	707.65	0.15	-6.44	2.18	Ol(4.1), Cpx(43.8), Mt(6.1), Gl(46.1)	0.54	54.00
LP192	1075	68	AuPd		0.58	145.44	0.03	-8.73	0.83	Ol(4), Cpx(44.7), Mt(7), Gl(44.3)	0.16	55.70
LP193	1075	68	AuPd		1.65	527.36	0.12	-7.61	1.95	Ol(5), Cpx(42.7), Mt(7), Gl(45.3)	0.41	54.70
LP194	1075	68	AuPd		2.51	928.02	0.21	-7.12	2.44	Cpx(31.1), Amph(9.2), Mt(7.4), Gl(52.3)	0.26	47.70
LP195	1075	68	AuPd		8.00	5367.37	1.21	-5.59	3.97	Mt(4.4), Gl(95.6)	0.32	4.40
LP196	1025	68	Au		0.50	120.66	0.03	-9.55	0.70	Ol(3.3), Cpx(46.8), Amph(14.2), Mt(8.6), Ap(1.6), Gl(25.4)	0.20	74.50
LP197	1025	68	Au		0.50	120.66	0.03	-9.55	0.70	Cpx(25.3), Amph(41.7), Mt(6.7), Ap(2.1), Gl(24.1)	0.02	75.80
LP200	1125	24	AuPd		1.65	529.43	0.12	-6.99	1.93	Ol(5), Cpx(21.8), Mt(2.1), Gl(71.1)	0.22	28.90
LP201	1125	24	AuPd		2.19	769.81	0.17	-6.66	2.26	Ol(3.3), Cpx(17.9), Mt(2.3), Gl(76.6)	0.10	23.50
LP213	1050	24	Au		0.71	185.89	0.04	-8.84	1.06	Ol(3.3), Cpx(46.8), Mt(8), Pl(-1.2), Gl(43)	0.21	56.94
LP214	1050	24	Au		2.53	937.22	0.22	-7.43	2.47	Cpx(37.1), Amph(14.7), Mt(7.1), Ap(0), Gl(41.1)	0.22	58.93
LP215	1050	24	Au		8.61	6058.65	1.29	-5.81	4.09	Mt(4.5), Gl(95.5)	0.35	4.50
LP217	1150	24	AuPd		0.98	274.09	0.06	-7.27	1.35	Ol(3.8), Cpx(12.4), Mt(0.9), Gl(82.9)	0.69	17.10
LP218	1150	24	AuPd		1.15	335.72	0.07	-7.09	1.53	Ol(4), Cpx(13.9), Mt(1.1), Gl(80.9)	0.60	19.00
LP219	1150	24	AuPd		3.39	1422.70	0.31	-5.84	2.78	Mt(1.9), Gl(98.1)	0.71	1.90
LP220	1150	24	AuPd		5.81	3206.91	0.70	-5.13	3.49	Mt(0.8), Gl(99.2)	0.82	0.80
FC-36	1125	20	AuPd		2.91	1140.51	0.25	-6.82	2.10	Ol(4.6), Cpx(18), Mt(1.5), Gl(75.9)	0.13	24.10
FC-37	1125	20	AuPd		3.64	1576.75	0.35	-6.54	2.38	Ol(3.1), Cpx(8.1), Mt(2.1), Gl(86.7)	0.06	13.30
FC-38	1125	20	AuPd		3.82	1690.03	0.37	-6.48	2.44	Ol(2.9), Cpx(6.5), Mt(2.2), Gl(88.5)	0.10	11.60

*) fH₂O and aH₂O calculated after Moore (1998) (see text); **) Oxygen fugacity calculated from aH₂O. DFMQ is log fO₂ expressed relative to the FMQ buffer

\$) Fe loss/gain calculated by mass balance

Table 9. Experimental conditions and phase relations for the evolved basanite (KLA-1-6-22) at 550 MPa

Run	Temperature [°C]	Duration [hours]	Capsule	Fe\$ loss/gain	melt H ₂ O [wt%]	fH ₂ O*	aH ₂ O*	log fO ₂ ** [bar]	ΔFMQ	Phase assemblage	R ²	j [%]
FC-1	1175	24	AuPd	6% Fe loss	5.41	3266.05	0.45	-5.62	2.61	Ol(1.2), Cpx(7.4), 0, Mt(2.6), Gl(88.8)	0.42	11.20
FC-2	1175	24	AuPd		1.50	583.99	0.08	-7.12	1.11	Ol(2.1), Cpx(7.8), 0, Mt(1.1), Gl(89)	0.15	11.00
FC-3	1175	24	AuPd		1.71	690.39	0.10	-6.97	1.26	Ol(1.9), Cpx(3.6), 0, Mt(0.6), Gl(94)	0.07	6.10
FC-7	1150	22	AuPd	10% Fe loss	4.07	2168.60	0.30	-6.26	2.26	Ol(2.5), Cpx(11.6), Mt(1.8), Gl(84.1)	0.73	15.90
FC-8	1150	22	AuPd		1.82	744.99	0.10	-7.19	1.33	Ol(2.4), Cpx(11.7), Mt(1.8), Gl(84.1)	0.11	15.90
FC-9	1150	22	AuPd		2.42	1073.10	0.15	-6.87	1.65	Ol(2.2), Cpx(12.6), Mt(1.8), Gl(83.5)	0.10	16.60
FC-42	1125	20	AuPd		3.19	1551.64	0.22	-6.84	1.98	Ol(3.4), Cpx(33), Mt(4.7), Gl(58.9)	0.46	41.10
FC-43	1125	20	AuPd		4.20	2265.95	0.32	-6.51	2.31	Ol(0.9), Cpx(20.3), Mt(4.8), Gl(73.9)	0.17	26.00
FC-45	1075	30	AuPd		4.81	2748.32	0.40	-6.46	3.00	Cpx(20.5), Mt(8.1), Gl(71.5)	0.26	28.60
FC-46	1075	30	AuPd		5.25	3124.84	0.45	-6.35	3.11	Cpx(17.8), Mt(8.3), Gl(73.9)	0.37	26.10
FC-47	1075	30	AuPd		6.49	4289.21	0.62	-6.07	3.39	Ol(-0.2), Cpx(6.5), Mt(6.6), Gl(87.1)	0.20	12.90

*) fH₂O and aH₂O calculated after Moore (1998) (see text); **) Oxygen fugacity calculated from aH₂O. DFMQ is log fO₂ expressed relative to the FMQ buffer

\$) Fe loss/gain calculated by mass balance

Table 10. Experimental conditions and phase relations for the evolved basanite (KLA-1-6-22) at 700 MPa

Run	Temperature [°C]	Duration [hours]	Capsule	melt H ₂ O [wt%]	fH ₂ O*	aH ₂ O*	log fO ₂ ** [bar]	ΔFMQ	Phase assemblage	R ²	j [%]
LP63	1050	68	Au	7.62	6350.76	0.64	-6.28	3.41	Cpx(12.8), Amph(11.6), Mt(8.5), Gl(67)	0.33	32.90
LP65	1050	68	Au	7.07	5694.40	0.57	-6.38	3.31	Cpx(20.4), Amph(11), Mt(9.3), Gl(59.3)	0.03	40.70
LP67	1050	68	Au	2.36	1293.36	0.13	-7.67	2.02	Cpx(29), Amph(34.1), Mt(7.5), Ap(1.2), Gl(28.3)	0.09	71.80
LP68	1075	71	Au	7.32	5984.32	0.59	-6.01	3.35	Mt(3.8), Gl(96.2)	0.27	3.80
LP69	1075	71	Au	9.94	9522.49	0.94	-5.61	3.75	Mt(3.5), Gl(96.5)	0.20	3.50
LP70	1075	71	Au	8.57	7584.28	0.75	-5.81	3.55	Cpx(14.9), Mt(3.5), Gl(78.1)	0.69	21.80
LP71	1075	71	Au	7.00	5604.90	0.55	-6.07	3.29	Cpx(23.4), Amph(9.5), Mt(5.2), Gl(59.6)	0.40	40.40
LP72	1075	71	Au	1.94	1014.13	0.10	-7.56	1.80	Cpx(32.9), Amph(20.5), Mt(4.7), Ap(0.5), Gl(38.5)	0.11	61.50
LP73	1100	20	AuPd	8.72	7779.29	0.76	-5.48	3.56	Mt(2.7), Gl(97.3)	0.21	2.70
LP74	1100	20	AuPd	6.91	5506.73	0.54	-5.78	3.26	Mt(3), Gl(97)	0.20	3.00
LP75	1100	20	AuPd	8.54	7547.86	0.74	-5.50	3.54	Mt(3), Gl(97)	0.08	3.00
LP76	1100	20	AuPd	5.81	4281.62	0.42	-5.99	3.05	Cpx(10.2), Mt(4.6), Gl(85.2)	0.11	14.80
LP77	1100	20	AuPd	4.26	2786.27	0.27	-6.37	2.67	Cpx(31.7), Amph(4.5), Mt(6.6), Gl(57.3)	0.11	42.80
LP78	1150	20	AuPd	9.97	9564.64	0.91	-4.71	3.72	Mt(0.5), Gl(99.5)	0.14	0.50
LP79	1150	20	AuPd	10.13	9801.92	0.93	-4.69	3.74	Mt(1.1), Gl(98.9)	0.68	1.10
LP80	1150	20	AuPd	11.17	11422.12	1.09	-4.55	3.88	Mt(1.7), Gl(98.3)	0.54	1.70
LP81	1150	20	AuPd	10.06	9692.55	0.92	-4.70	3.73	Mt(2.5), Gl(97.5)	0.36	2.50
LP82	1150	20	AuPd	7.79	6570.22	0.63	-5.03	3.40	Cpx(8.3), Mt(2.7), Gl(89)	0.29	11.00
LP83	1150	20	AuPd	9.13	8344.59	0.79	-4.83	3.60	Mt(2.1), Gl(97.9)	0.41	2.10
LP84	1150	20	AuPd	7.90	6705.47	0.64	-5.02	3.41	Cpx(9.4), Mt(2.7), Gl(87.9)	0.33	12.10
LP150	1150	20	AuPdFe	0.50	205.41	0.02	-8.04	0.39	Ol(2.3), Cpx(41.4), Mt(3.5), Gl(52.7)	0.07	47.20
LP151	1150	20	AuPd	1.49	739.26	0.07	-6.93	1.50	Ol(1.1), Cpx(34.5), Mt(3.7), Gl(60.6)	0.08	39.30
LP152	1150	20	AuPd	1.53	761.79	0.07	-6.90	1.53	Ol(1.3), Cpx(30.7), Mt(3.7), Gl(64.3)	0.17	35.70

*) fH₂O and aH₂O calculated after Moore (1998) (see text); **) Oxygen fugacity calculated from aH₂O. DFMQ is log fO₂ expressed relative to the FMQ buffer

**) Oxygen fugacity calculated from aH₂O. ΔFMQ is log fO₂ expressed relative to the FMQ buffer

4.2 Phase proportions

4.2.1 Solid phase proportions

Proportions of all relevant phases (determined by mass balance calculations) are listed in Tables 6-10. Due to the high MgO content (13.72 wt.%) of starting material 168-1 (primitive basanite) Ol is present at all conditions investigated. Furthermore, the proportion of olivine is significantly higher in experiments using 168-1 as starting material compared to Ol proportions of starting composition KLA-1-6-22 (MgO=9.06 wt.%). Figure 15 shows phase proportions (normalized to 100% solid phase) of starting composition 168-1 at 400 MPa and 1150°C crystallizing phases at this conditions are Ol, Cpx Mt. Mt is the dominating phase at high H₂O contents in the melt. With decreasing H₂O concentration in the melt the proportion of Ol increases up to a maximum proportion of 70.7% and starts decrease with the onset of Cpx (at H₂O content in the melt of approximately 5 wt.%) down to 34.3%. Cpx proportion increases up 58.5% with decreasing H₂O content in the melt. By lowering the temperature to 1100°C the proportion of Cpx increases up to 68% and Ol proportion decreases from 57% at high H₂O contents in the melt to 23.5% at low H₂O contents in the melt. At lower temperatures Amph appears on the liquidus, the proportion of amphibole increases with decreasing H₂O concentration in the melt up to a peak proportion of 7% at 1050°C (3.21 wt.% H₂O in the melt) and of 58% at 1025°C (5.59 wt.% H₂O in the melt) and decreases afterwards with decreasing H₂O content. The fraction of olivine and Cpx are significantly lowered as a function of amphibole proportion.

Using the same starting composition at 700 MPa (Figure 16) and 1150°C Ol proportion is lower in comparison to proportions observed at 400 MPa and the same temperature and decreases from 44.5% to 19.2% with decreasing H₂O content in the melt. Cpx proportion is higher in comparison to proportions observed at 400 MPa and 1150°C and increases up to 71.5% with decreasing H₂O content in the melt. Amph appears at 1100°C on the liquidus with a peak proportion of 6.3% at 5.07 wt.% H₂O in the melt.

In experiments using the evolved basanite (KLA-1-6-22) at 400 MPa (Figure 17) and 1150°C, solid phases are Ol, Cpx Mt. Magnetite is the dominating phase at high H₂O contents in the melt. With decreasing H₂O concentration in the melt Ol and Cpx appear on the liquidus and the proportion of both phases increases up to 22.2% and 82.8%, respectively. By lowering the

temperature to 1100°C Cpx proportion increases with decreasing H₂O content in the melt up to 82.9% and Ol proportion up to 6.5%. At lower temperatures Amph becomes a stable phase, the proportion of amphibole increases with decreasing H₂O concentration in the melt up to a peak proportion of 27% at 1050°C (4.86 wt.% H₂O in the melt) and of 72.1% at 1025°C (8.12 wt.% H₂O in the melt) and decreases afterwards with decreasing H₂O content. The fraction of Ol and Cpx are significantly lowered as a function of Amph proportion at 1050°C, at 1025°C Ol is no longer a stable phase due to the high proportion of Amph.

Using the same starting material at 550 MPa and 1175°C proportions of Cpx and Ol increase as a function of H₂O concentration in the melt up to 70.9% and up to 31.2%, respectively (Figure 18). Lowering the temperature to 1150°C leads to an even higher Cpx proportion (75.9% at low H₂O contents in the melt) and a lower Ol proportion (15.1% at low H₂O contents in the melt).

Using the same starting material at 700 MPa and 1150°C we observed very high proportions of Cpx and low proportions of Ol, both phases increase as a function of H₂O concentration in the melt up to 87.8% and up to 4.9%, respectively (Figure 19). At lower temperature Ol disappears completely from the liquidus and Amph becomes a stable phase, the proportion of Amph increases with decreasing H₂O concentration in the melt up to a peak proportion of 10.5% at 1100°C (4.26 wt.% H₂O in the melt) and of 35.3% at 1075°C (1.94 wt.% H₂O in the melt) and decreases afterwards with decreasing H₂O content.

The Spl fraction is mostly influenced by temperature and H₂O concentration in the melt, but is also affected by the prevailing redox conditions. Highest Mt proportions were observed at low temperatures and high H₂O contents in the melt. However, low temperature experiments at 400 MPa were performed at more reducing conditions (FMQ at H₂O saturated conditions) for both basanitic starting materials, from this data it is evident that spinel proportion is significantly lowered at more reducing conditions at constant temperature and H₂O concentration in the melt.

Plagioclase proportions are not shown, because only in three experimental runs the size of plagioclase crystals were big enough to be measured by electron microprobe. Due to the limited dataset conclusions on proportions remain extremely uncertain. Apatite proportions also are not shown, due the small size of the crystals and analytical difficulties.

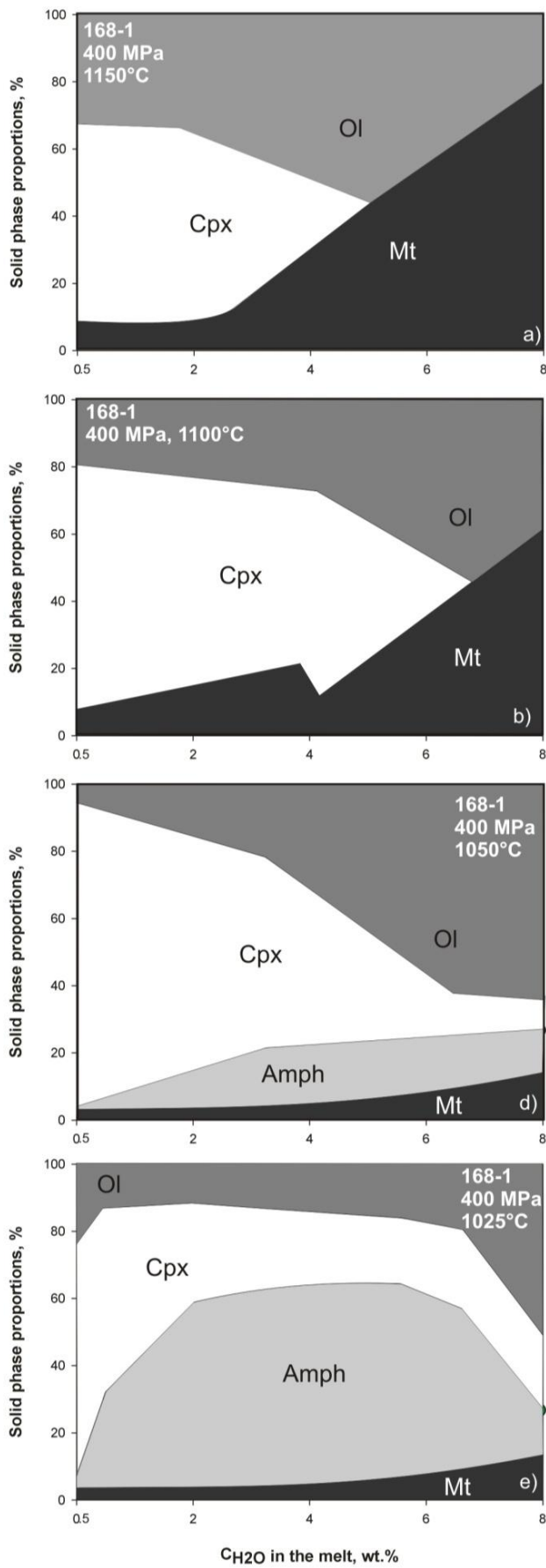


Figure 15: Calculated phase proportions (normalized to solids) using starting composition 168-1 at 400 MPa as a function of H_2O concentration in the melt at (a) 1150°C, (b) 1100°C, (c) 1050°C and (d) 1025°C. In the Ol+Cpx+Mt (1150–1100°C) phase assemblage Ol and Mt proportion decreases, Cpx proportion increases with decreasing H_2O content in the melt. At 1025°C in the Ol+Cpx+Amph+Mt phase assemblage Ol and Cpx proportions are lowered as a function of Amph proportion.

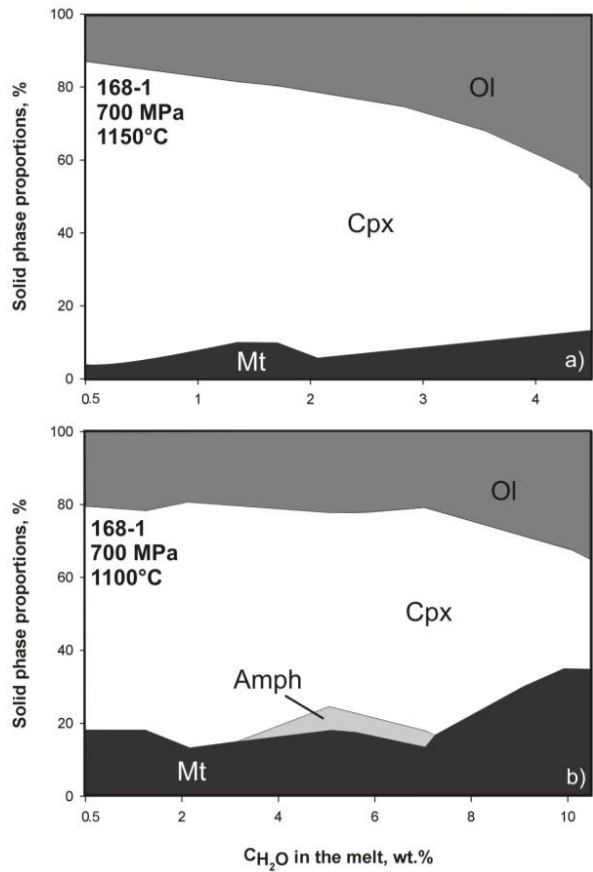


Figure 16: Calculated phase proportions (normalized to solids) using starting composition 168-1 at 700 MPa as a function of H₂O concentration in the melt at (a) 1150°C and (b) 1100°C.

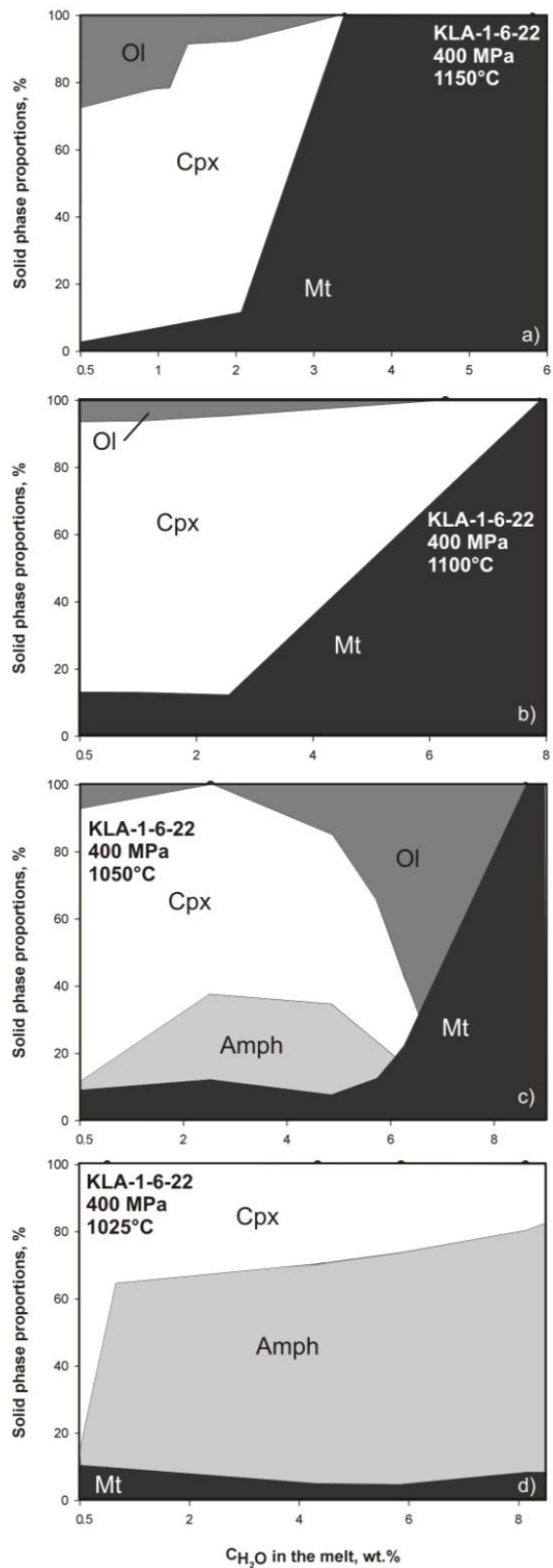


Figure 17: Calculated phase proportions (normalized to solids) using starting composition KLA-1-6-22 at 400 MPa as a function of H_2O concentration in the melt at (a) 1150°C, (b) 1100°C, (c) 1050°C and (d) 1025°C.

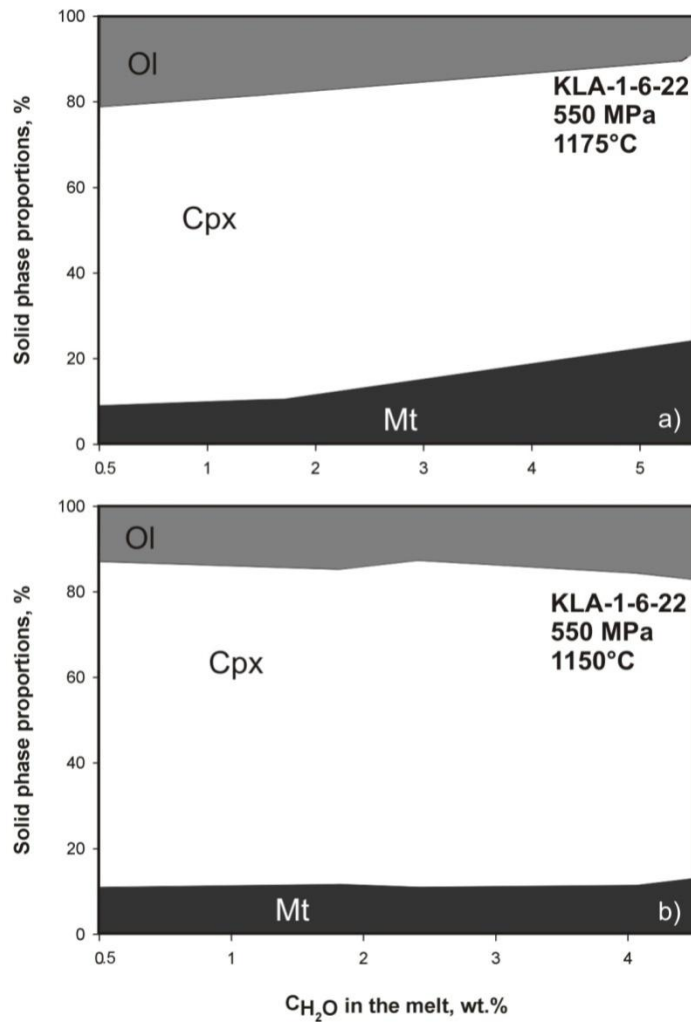


Figure 18: Calculated phase proportions (normalized to solids) using starting composition KLA-1-6-22 at 550 MPa as a function of H_2O concentration in the melt at (a) 1175°C and (b) 1150°C.

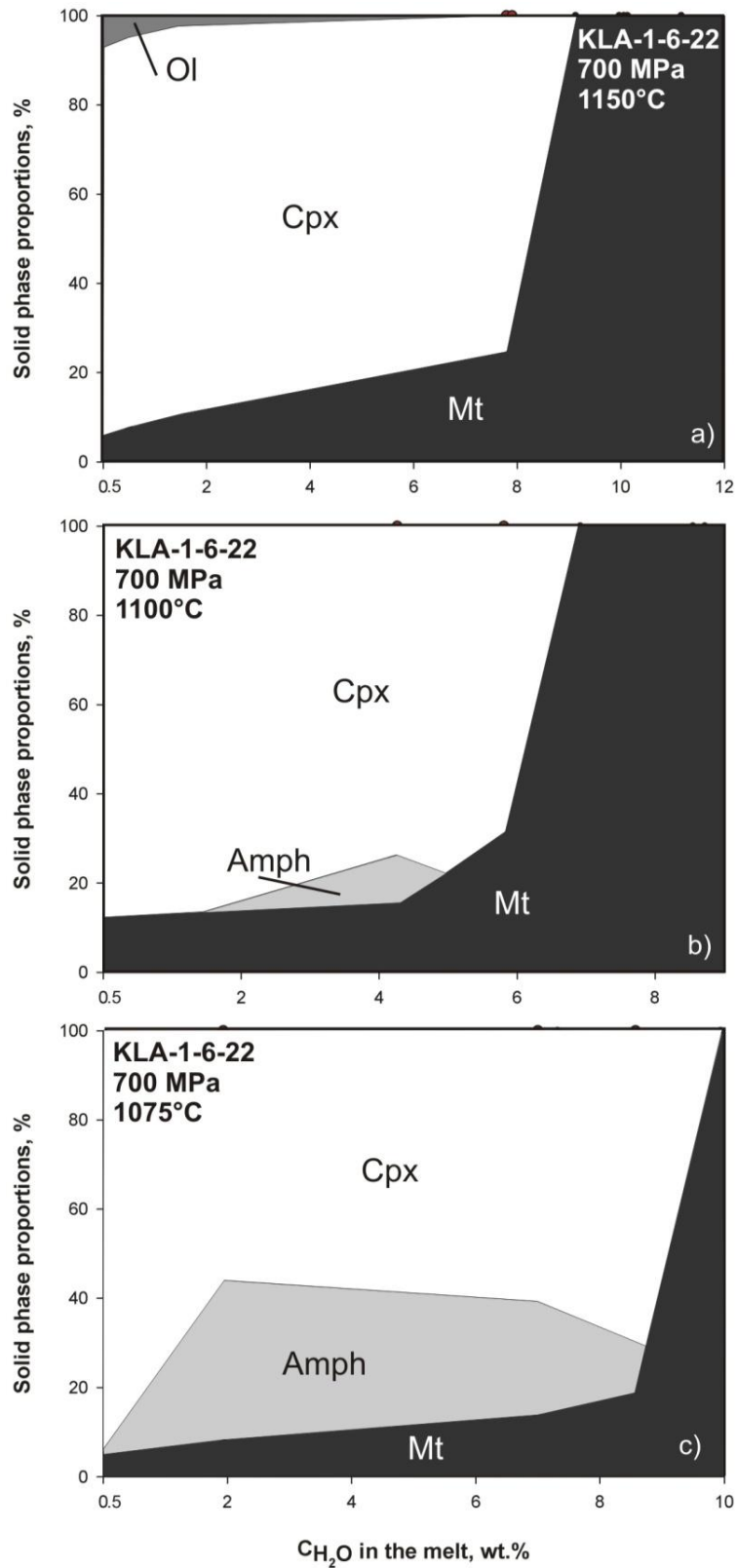


Figure 19: Calculated phase proportions (normalized to solids) using starting composition KLA-1-6-22 at 700 MPa as a function of H_2O concentration in the melt at (a) 1150°C, (b) 1100°C and (c) 1075°C.

4.2.1 Melt proportions

The melt fraction changes as a function of aH_2O and corresponding proportions of crystallizing phases. Figure 20a shows phase proportions at low H_2O activities (2.0-4.5 wt.% H_2O in the melt) and 400 MPa for sample 168-1 as function of temperature. The melt fraction continuously decreases as a function of temperature from 89.0 to 20.3 wt.% with decreasing temperature from 1150°C to 1010°C respectively. Melt fraction at high aH_2O (6.6-8.33 wt.% H_2O in the melt) (Figure 20b) systematically decreases from 96.1 wt.% to 79.8 wt.% with decreasing temperature from 1150 to 1050°C. At lower temperatures the melt fraction decreases almost very efficiently, e.g. up to 35.1 wt.% at 1025°C. This strong decrease is directly related to the appearance of amphibole on the liquidus, because with the onset of amphibole crystallization, the proportion of amphibole is very high at high aH_2O conditions. Using the same starting composition at 700 MPa (see Figure 21) we observed the identical dependence at high aH_2O conditions (7.40-8.36 wt.% H_2O in the melt). At 700 MPa and low aH_2O conditions the experimental dataset of sample 168-1 is incomplete and no direct remarks are possible.

Figure 22a and Figure 22b show phase proportions of starting composition KLA-1-6-22 at low H_2O activities (0.5-2.5 wt.% H_2O in the melt) and high aH_2O conditions (5.4-6.3 wt.% H_2O in the melt) as function of temperature at 400 MPa. We observed the similar dependencies of aH_2O on the melt fraction as for starting composition 168-1 at the same conditions. Using KLA-1-6-22 as starting material the melt fraction continuously decreases from 80.9 to 24.1 wt.% with decreasing temperature from 1150°C to 1010°C. At high aH_2O conditions (5.4-6.3 wt.% H_2O in the melt) the melt fraction (Figure 22b) systematically decreases from 99.2 wt.% to 86.2 wt.% with decreasing temperature from 1150 to 1050°C. At lower temperatures the melt fraction decreases almost immediately (to 46.1 wt.% at 1025°C) with the onset of amphibole crystallization. Using the same starting composition at 700 MPa we observed similar dependencies at low aH_2O on melt fraction (Figure 23a), as at low aH_2O conditions (1.5-4.3 wt.% H_2O in the melt) the melt fraction continuously decreases from 64.3-28.3 wt.% with decreasing temperature from 1150°C to 1050°C. But at high aH_2O conditions (7.0-7.8 wt.% H_2O in the melt) and 700 MPa (Figure 23b) Cpx is the predominant phase and the proportion of

amphibole is relatively low (9.5-11.0 wt.%), resulting in a continuous decrease of the melt fraction from 89.0 to 59.3 wt.% with decreasing temperature from 1150°C to 1050°C.

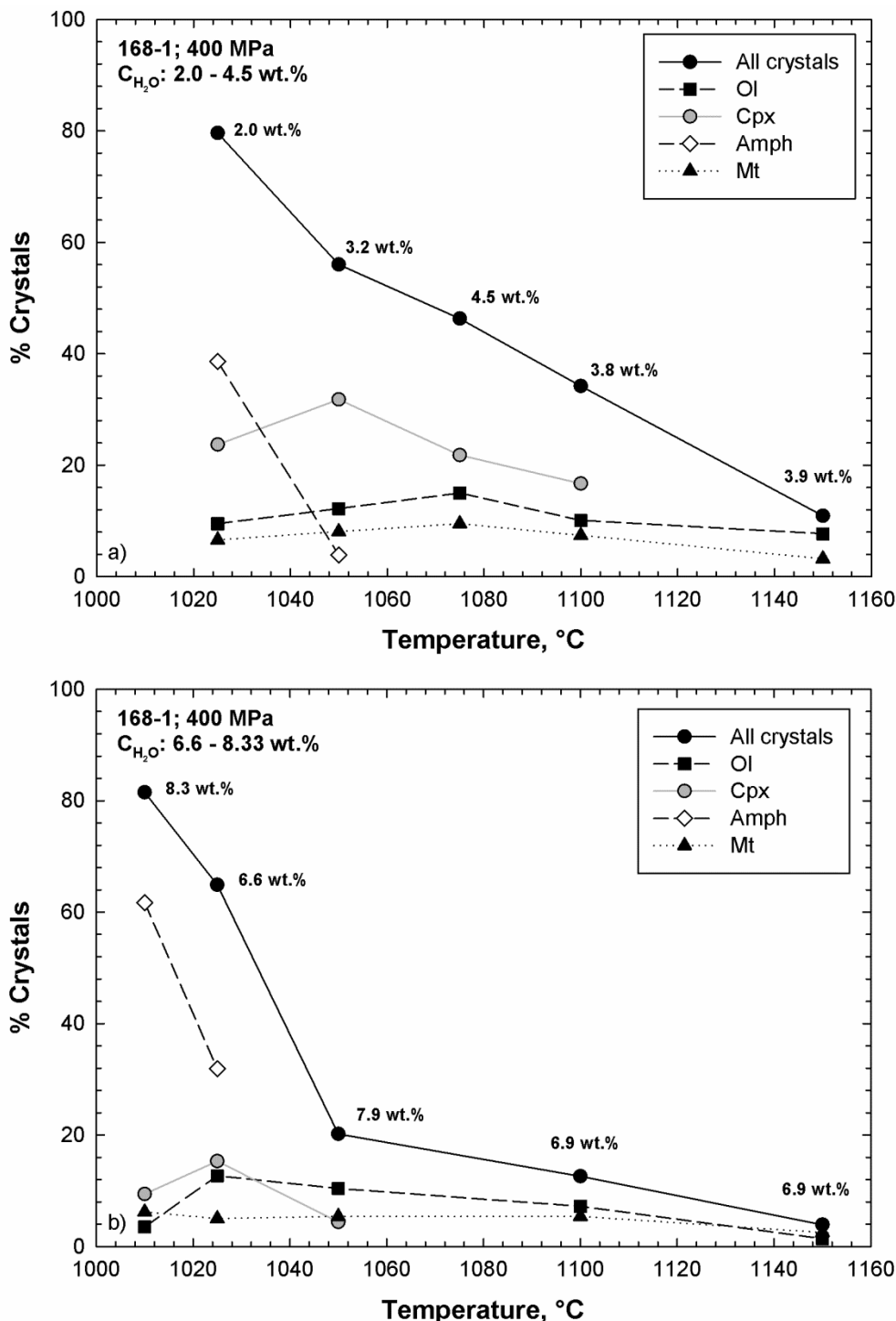


Figure 20: Calculated modal proportions (wt.%) of olivine (Ol), clinopyroxene (Cpx), amphibole (Amph) and magnetite (Mt) using starting material 168-1 at 400 MPa and (a) low H_2O concentrations (2.0-4.5 wt.%) in the melt and (b) high H_2O (6.6-8.33 wt.%) concentrations in the melt. Numbers indicate H_2O content in wt.% at constant temperature.

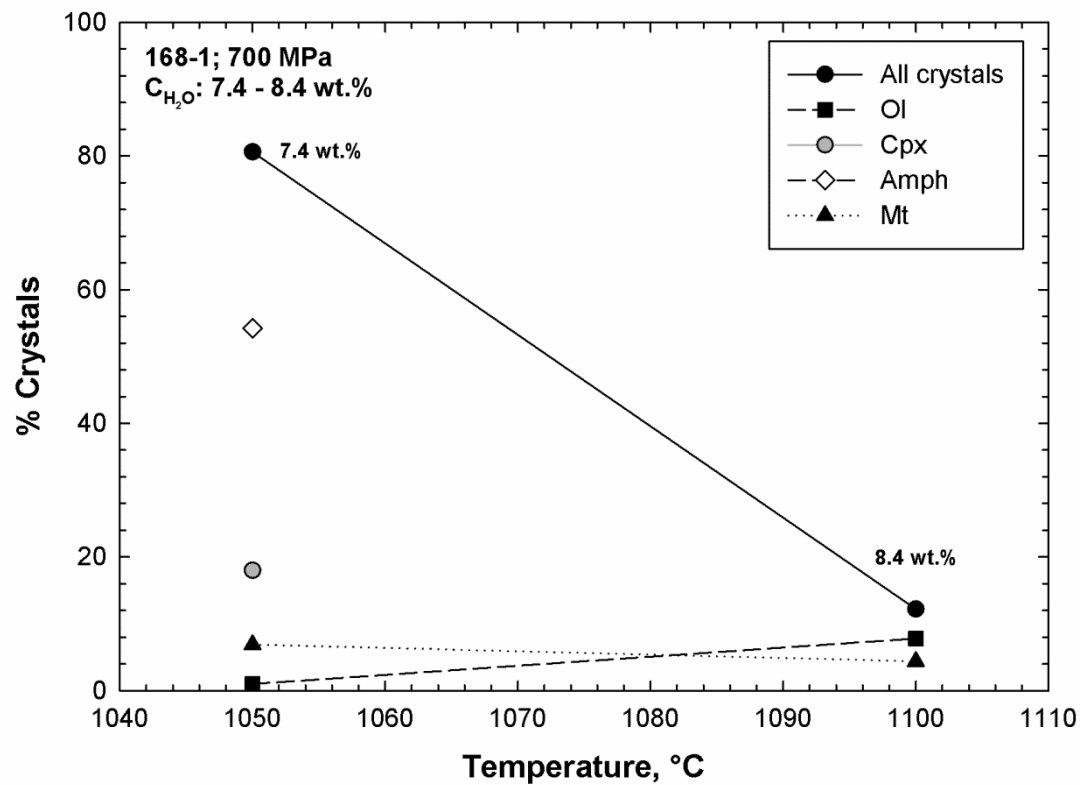


Figure 21: Calculated modal proportions (wt.%) of olivine (Ol), clinopyroxene (Cpx), amphibole (Amph) and magnetite (Mt) using starting material 168-1 at 700 MPa and high H_2O concentrations in the melt (7.4-8.4 wt.%). Numbers indicate H_2O content in wt.% at constant temperature.

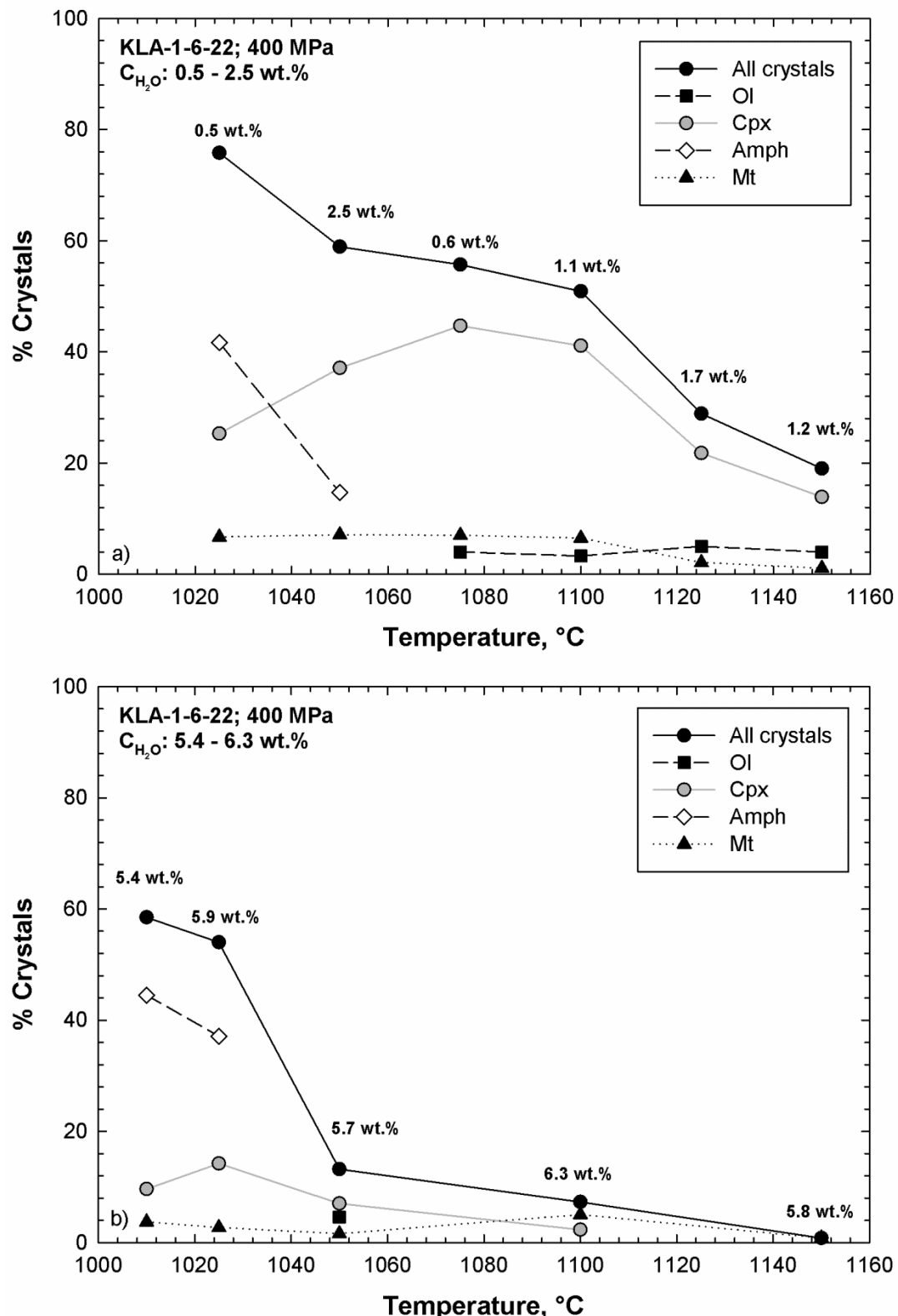


Figure 22: Calculated modal proportions (wt.%) of olivine (OI), clinopyroxene (Cpx), amphibole (Amph) and magnetite (Mt) using starting material KLA-1-6-22 at 400 MPa and (a) low H_2O concentrations (0.5-2.5 wt.%) in the melt and (b) high H_2O concentrations (5.4-6.3 wt.%) in the melt. Numbers indicate H_2O content in wt.% at constant temperature.

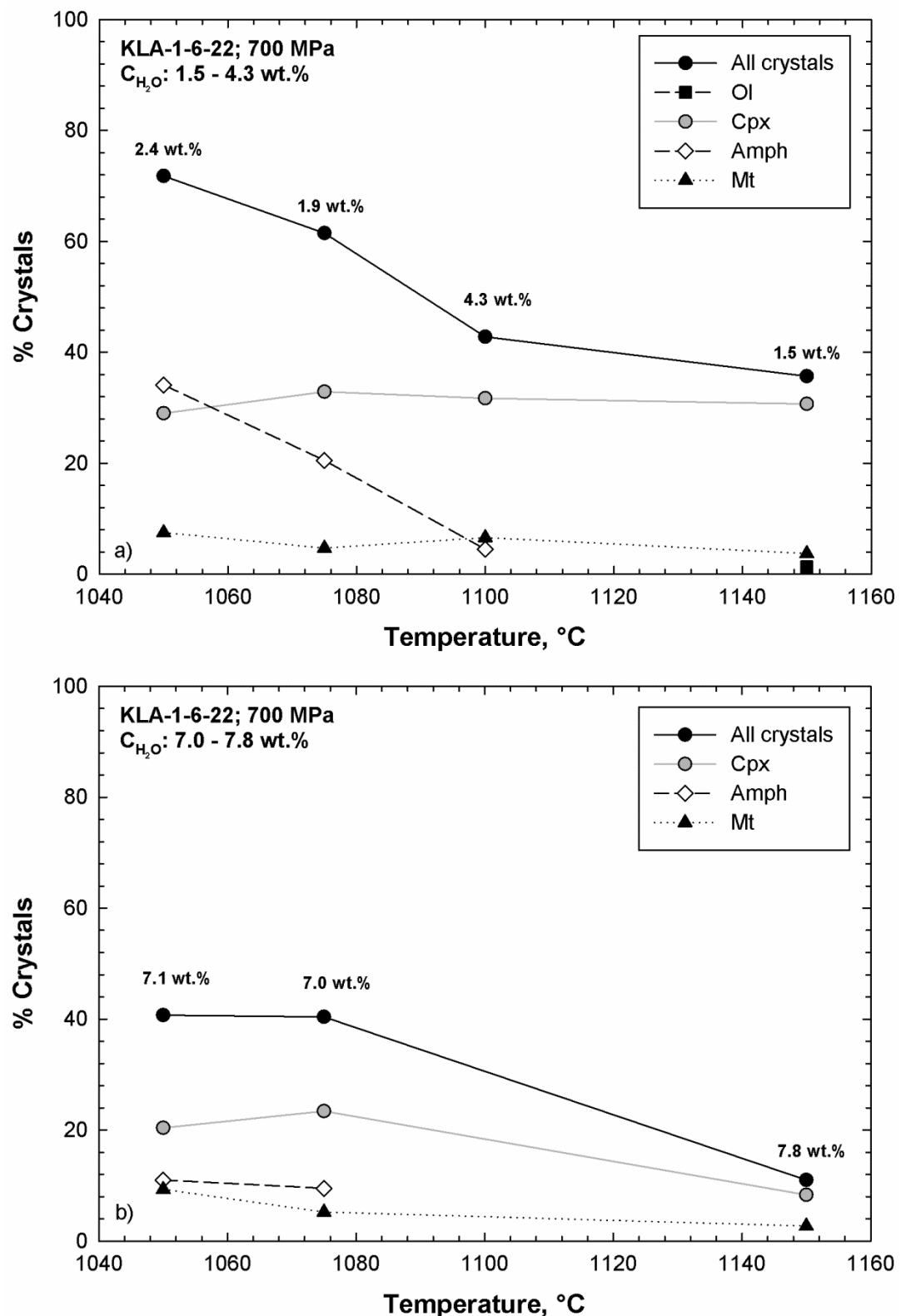


Figure 23: Calculated modal proportions (wt.%) of olivine (OI), clinopyroxene (Cpx), amphibole (Amph) and magnetite (Mt) using starting material KLA-1-6-22 at 700 MPa and (a) low H_2O concentrations (1.5-4.3 wt.%) in the melt and (b) high H_2O concentrations in the melt (7.0-7.8 wt.%). Numbers indicate H_2O content in wt.% at constant temperature.

4.3 Phase compositions

Average compositions of experimental phases determined by electron microprobe are shown in Tables 11-33.

4.3.1 Olivine

The forsterite content ($Fo=100 \times Mg/[Mg+Fe^{2+}]$) of the synthesized olivines (Tables 11-15) varies between $Fo_{74.8}$ and $Fo_{95.4}$ as a function of temperature, fO_2 and H_2O activity. The forsterite content is plotted as a function of temperature, redox conditions and H_2O activity in the melt for starting material 168-1 in Figures 24a and 24b and for KLA-1-6-22 in Figures 25a and 25b. At constant temperature the forsterite content varies as a function of H_2O activity and redox conditions (e.g. at $1100^\circ C$ from $Fo_{77.9}$ to $Fo_{94.5}$ for fO_2 conditions between $+1 < \Delta FMQ < +3.8$ and $0 < a_{H_2O} < 1$ for 168-1; at $1125^\circ C$ from $Fo_{78.2}$ to $Fo_{89.1}$ for fO_2 conditions between $+1.7 < \Delta FMQ < +2.7$ and $0 < a_{H_2O} < 0.5$ for KLA-1-6-22). Forsterite content decreases with decreasing temperature, but the effect of fO_2 conditions on the forsterite content superimposes the effect of temperature, resulting in high forsterite contents at low temperature and oxidizing conditions. At high fO_2 conditions forsterite contents are elevated for both basanitic systems, up to 95.4 mol.% for the primitive basanite (168-1) and up to 89.1 mol.% for the evolved basanite (KLA-1-6-22). This is linked to the change in $Fe^{2+}/\Sigma Fe$ ratio in the melt as a function of oxygen fugacity. High oxygen fugacities (low $Fe^{2+}/\Sigma Fe$ ratio in the melt) are characterized by strong crystallization of magnetite. The resulting decrease of iron content in the melt leads to the equilibration of olivines with high forsterite contents at low temperatures. However, high fO_2 conditions result in low $Fe^{2+}/\Sigma Fe$ ratios in the melt, resulting in low Fe^{2+} contents in the melt stabilize forsterite-rich olivine. The forsterite content is shown as a function of the magnesium number of the coexisting melt ($Mg\#^{melt}=100 \times Mg/[Mg+Fe^{2+}]$) in Figure 24c as a function of redox conditions and Figure 24d as function of H_2O activity for the primitive basanite (168-1) and in Figures 25c and 25d for the evolved basanite (KLA-1-6-22). With decreasing $Mg\#$ in the melt the forsterite content also decreases. Outliers in Figures 24c and 24d ($Fo_{76.5-77.9}$ at $Mg\#$ in the melt of 93.6-95.1 [LP53-LP55] are expected to be not in equilibrium with the coexisting melt.

The Fe^{2+} -Mg exchange distribution coefficient between olivine and melt ($Kd_{\text{Ol-Liq}}$) was calculated using the following equation:

$$Kd_{\text{Ol-Liq}} = (X_{\text{Fe}}^{\text{ol}} \cdot X_{\text{Mg}}^{\text{liq}}) / (X_{\text{Mg}}^{\text{ol}} \cdot X_{\text{Fe}}^{2+\text{liq}}) \quad (5)$$

Ferrous and ferric iron ratios in the melt were calculated using the model of Moretti (2005) (see section: Calculation of $\text{Fe}^{2+}/\Sigma\text{Fe}$ ratio in glasses). The $Kd_{\text{Ol-Liq}}$ values obtained in our study vary between 0.10-0.37 (Tables 11-15) and are plotted in Figure 24e as function of redox conditions and Figure 24f as a function of H_2O activity for the primitive basanite and in Figures 25e and 25f for the evolved basanite (KLA-1-6-22). $Kd_{\text{Ol-Liq}}$ values close to 0.3 were observed at $f\text{O}_2$ conditions below FMQ+2 independent of the $a\text{H}_2\text{O}$ for the primitive basanite and below FMQ+1 and high $a\text{H}_2\text{O}$ ($a\text{H}_2\text{O}>0.5$) for the evolved basanite. However, Kd values obtained in our study vary between 0.12-0.37 for the primitive basanite (168-1) and between 0.09-0.32 for the evolved basanite (KLA-1-6-22); deviations from the often used value of Roeder and Emslie (1970) of 0.3 ± 0.03 are related to redox conditions and subordinated to H_2O activity. Toplis (2005) described the deviations from 0.3 mainly as function of melt composition and H_2O content in the system.

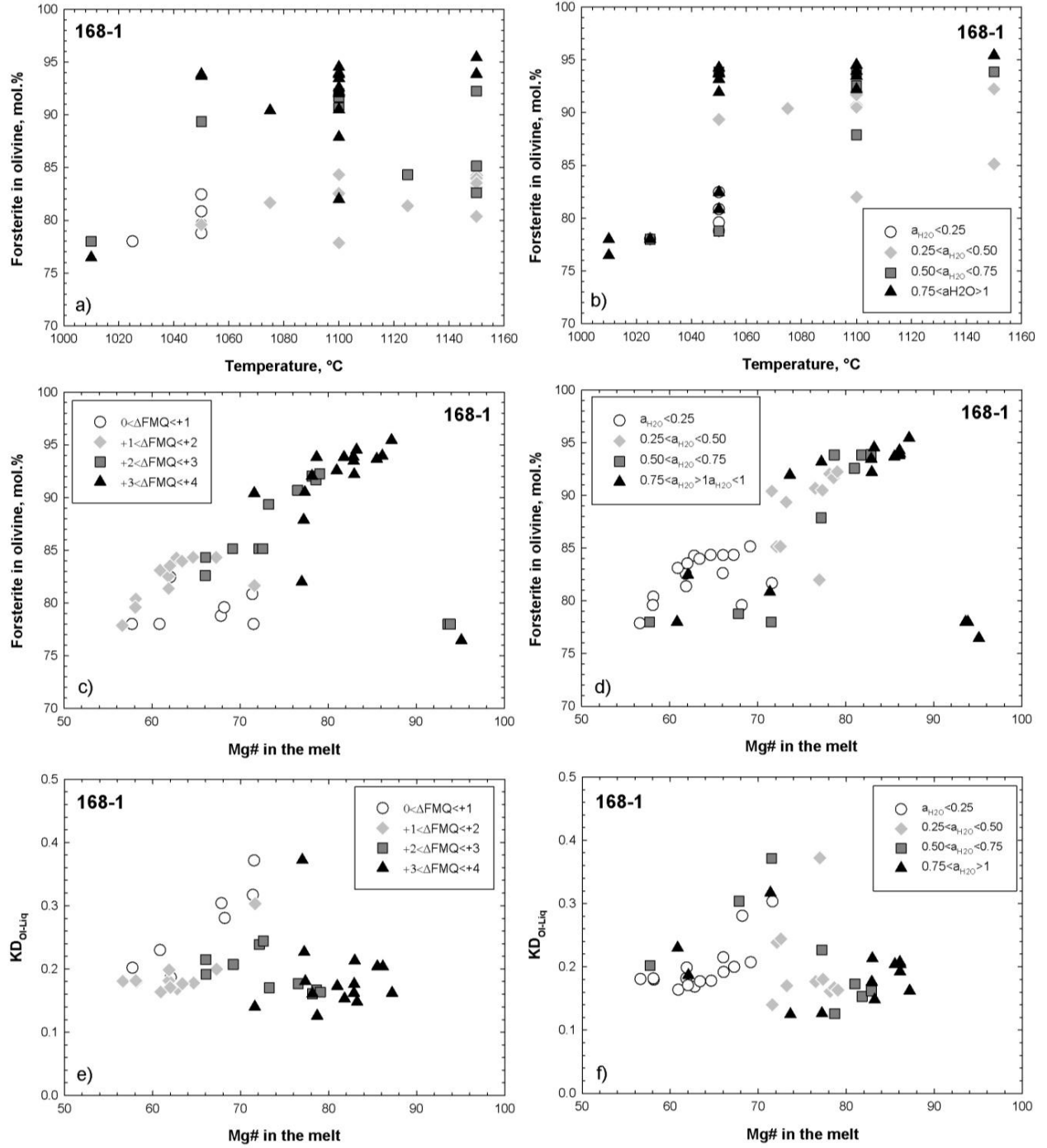


Figure 24: Olivine compositions (forsterite content) using starting composition 168-1 as function of temperature and redox conditions (a) (symbols as in Figure 9 (b)), (b) as a function of temperature and H_2O activity, (c) as a function $\text{Mg}^{\#}$ in the coexisting melt and redox conditions, (d) as a function $\text{Mg}^{\#}$ in the coexisting melt and H_2O activity, (e) partition coefficient of Fe^{2+} and Mg between olivine and melt ($KD_{\text{Ol-Liq}}$) as function of $\text{Mg}^{\#}$ in the coexisting melt and redox conditions, (f) $KD_{\text{Ol-Liq}}$ as function of $\text{Mg}^{\#}$ in the coexisting melt and H_2O activity.

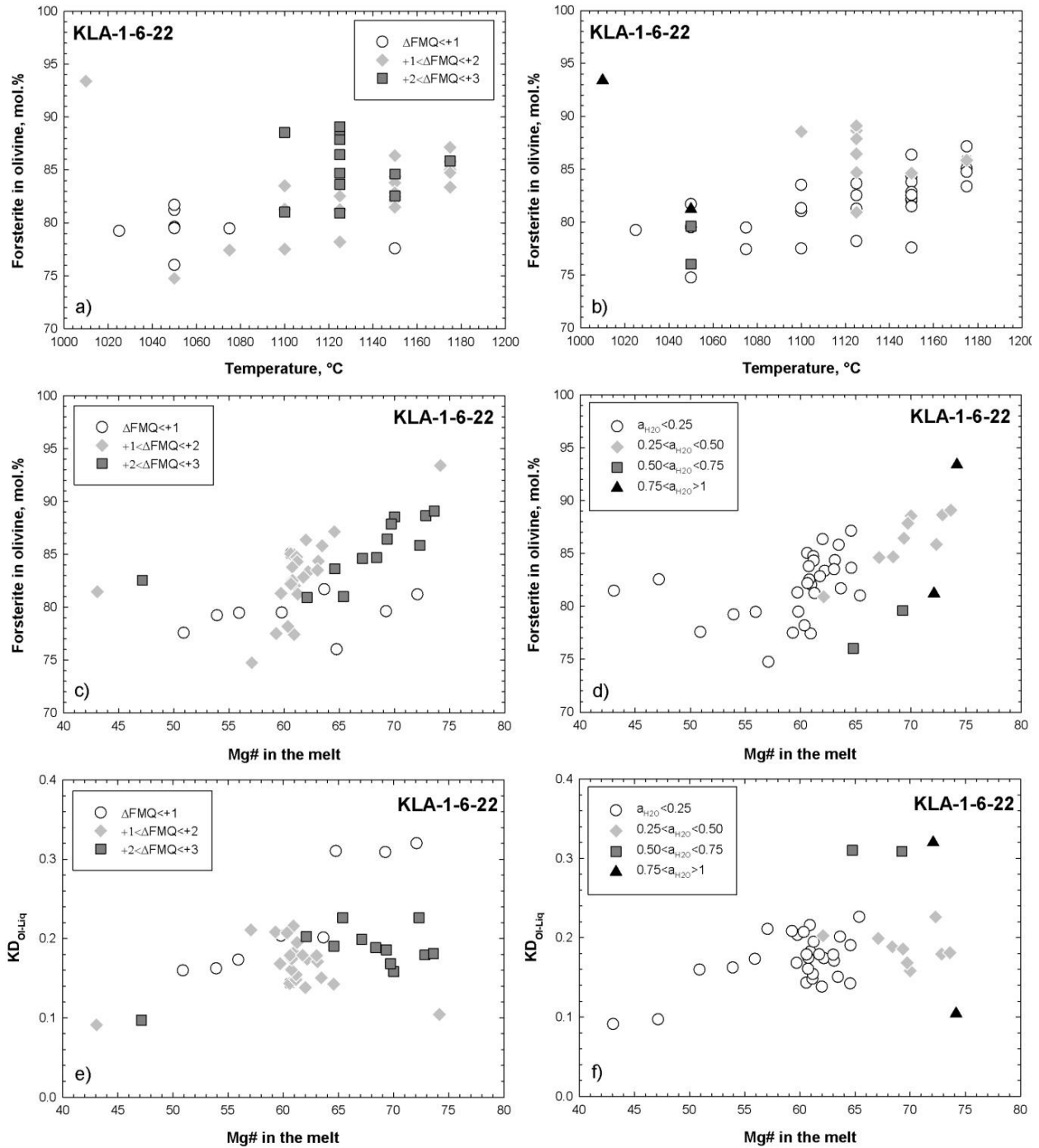


Figure 25: Olivine compositions (forsterite content) using starting composition KLA-1-6-22 as function of temperature and redox conditions (a), (b) as a function of temperature and H_2O activity, (c) as a function Mg# in the coexisting melt and redox conditions, (d) as a function Mg# in the coexisting melt and H_2O activity, (e) partitioning coefficient of Fe^{2+} and Mg between olivine and melt ($KD_{\text{Ol}-\text{Liq}}$) as function of Mg# in the coexisting melt and redox conditions, (f) $KD_{\text{Ol}-\text{Liq}}$ as function of Mg# in the coexisting melt and H_2O activity.

Table 11. Compositions of experimental olivines using starting composition 168-1 at 400 MPa

Run	Temperature [°C]	melt H ₂ O [wt%]	<i>a</i> H ₂ O	ΔFMQ	n	SiO ₂	TiO ₂	Al ₂ O ₃	FeO	MnO	MgO	CaO	Na ₂ O	K ₂ O	Cr ₂ O ₃	Total	Fo	Kd _{Ol-Liq}
LP34	1025	5.60	0.64	0.68	8	39.76 (0.28)	0.15 (0.16)	0.14 (0.29)	16.09 (0.95)	0.32 (0.07)	41.07 (1.51)	0.53 (0.45)	0.03 (0.03)	0.01 (0.01)	0.03 (0.02)	99.26	78.00	0.37
LP10	1050	6.45	0.87	0.40	5	39.69 (0.25)	0.04 (0.01)	0.02 (0.02)	16.41 (0.37)	0.28 (0.05)	45.32 (0.42)	0.4 (0.03)	-	-	-	102.16	82.45	0.19
LP11	1050	6.42	0.79	0.32	5	39.54 (0.15)	0.07 (0.03)	0.05 (0.04)	17.58 (0.25)	0.32 (0.07)	43.58 (0.23)	0.4 (0.04)	-	-	-	101.54	80.83	0.32
LP12	1050	5.61	0.64	0.14	4	39.04 (0.43)	0.12 (0.08)	0.08 (0.05)	19.17 (0.33)	0.35 (0.02)	41.84 (0.21)	0.45 (0.04)	-	-	-	101.06	78.77	0.30
LP188	1050	1.13	0.07	1.55	4	39.79 (0.68)	0.29 (0.28)	0.92 (1.2)	17.17 (0.8)	0.39 (0.04)	41.32 (3.05)	1.04 (1.35)	0.19 (0.17)	0.11 (0.14)	0.01 (0)	101.22	79.59	0.18
LP189	1050	3.21	0.30	2.76	3	40.25 (0.19)	0.07 (0.02)	0.04 (0.01)	9.84 (0.12)	0.38 (0.05)	49.82 (0.63)	0.28 (0.03)	0 (0)	0.01 (0)	0.02 (0)	100.69	89.36	0.17
LP216	1050	7.94	1.22	3.97	5	41.75 (0.1)	0.05 (0.02)	0.03 (0.02)	5.84 (0.35)	0.32 (0.04)	53.25 (0.57)	0.2 (0.03)	0.02 (0.01)	0.01 (0)	0.01 (0.02)	101.46	93.66	0.20
LP190	1075	0.90	0.06	1.29	1	38.79	0.19	0.18	16.56	0.34	43.39	0.36	0.01	0.02	-	99.84	81.66	0.30
LP191	1075	4.53	0.49	3.19	2	40.55 (0.12)	0.08 (0.01)	0.06 (0.03)	8.83 (0.02)	0.22 (0.13)	49.99 (0.94)	0.31 (0.01)	0.01 (0.01)	0.03 (0)	0.03 (0.01)	100.09	90.41	0.14
LP168	1100	0.46	0.04	1.04	7	39.19 (0.77)	0.3 (0.33)	0.64 (0.92)	17.76 (0.95)	0.35 (0.05)	40.45 (3.07)	1.85 (2.47)	0.07 (0.08)	0.03 (0.01)	0.04 (0.03)	100.64	77.86	0.18
LP169	1100	0.71	0.04	1.04	3	39.71 (0.24)	0.12 (0.04)	0.17 (0.19)	15.72 (0.18)	0.39 (0.05)	44.11 (0.52)	0.41 (0.01)	0.07 (0.06)	0.03 (0.02)	-	100.73	82.54	0.18
LP170	1100	5.15	0.59	3.35	8	41.31 (0.1)	0.09 (0.06)	0.13 (0.19)	6.76 (0.11)	0.25 (0.02)	52.34 (0.78)	0.38 (0.14)	0.07 (0.05)	0.02 (0.03)	0.02 (0.02)	101.35	92.57	0.17
LP171	1100	3.82	0.38	2.96	9	41.02 (0.28)	0.15 (0.11)	0.19 (0.19)	7.43 (0.19)	0.24 (0.03)	51.53 (1.11)	0.51 (0.51)	0.07 (0.09)	0.02 (0.02)	0.04 (0.03)	101.16	91.68	0.17
LP172	1100	4.16	0.43	3.07	8	39.53 (0.64)	0.22 (0.14)	0.57 (0.57)	15.33 (0.69)	0.35 (0.06)	43.41 (1.69)	1.03 (1.09)	0.12 (0.12)	0.03 (0.03)	0.04 (0.03)	100.59	81.99	0.37
LP173	1100	6.86	0.93	3.74	10	41.51 (0.33)	0.06 (0.03)	0.02 (0.01)	5.56 (0.31)	0.21 (0.05)	53.51 (0.44)	0.28 (0.03)	0.01 (0.01)	0.01 (0)	0.05 (0.03)	101.17	93.96	0.20
LP202	1125	1.73	0.12	1.99	5	39.33 (0.27)	0.04 (0.03)	0.08 (0.01)	16.84 (0.19)	0.33 (0.04)	43.31 (0.14)	0.39 (0.01)	0.02 (0.01)	0.02 (0)	0.04 (0.03)	100.36	81.37	0.20
LP203	1125	2.23	0.17	2.28	7	39.68 (0.27)	0.04 (0.02)	0.09 (0.01)	14.2 (0.19)	0.32 (0.03)	45.45 (0.26)	0.41 (0.05)	0.04 (0.01)	0.01 (0.01)	0.02 (0.01)	100.24	84.33	0.19
LP180	1150	1.19	0.08	1.56	10	39.44 (0.17)	0.1 (0.02)	0.11 (0.12)	17.45 (0.32)	0.32 (0.06)	42.51 (0.36)	0.58 (0.16)	0.02 (0.01)	0.01 (0.01)	0.04 (0.02)	100.55	80.37	0.18
LP181	1150	0.73	0.04	1.03	10	39.97 (0.37)	0.14 (0.1)	0.24 (0.29)	14.78 (0.35)	0.31 (0.06)	44.37 (0.92)	0.77 (0.62)	0.05 (0.05)	0.02 (0.04)	0.01 (0.02)	100.65	83.10	0.16
LP182	1150	1.34	0.09	1.69	10	40.01 (0.17)	0.08 (0.02)	0.06 (0.03)	14.88 (0.36)	0.33 (0.07)	44.77 (0.28)	0.41 (0.06)	0.03 (0.02)	0.01 (0.01)	0.04 (0.02)	100.57	83.53	0.17
LP183	1150	3.89	0.38	2.96	10	41.48 (0.5)	0.07 (0.03)	0.06 (0.04)	7.06 (0.39)	0.22 (0.06)	51.28 (0.35)	0.32 (0.03)	0.02 (0.01)	0.01 (0.01)	0.04 (0.04)	100.51	92.24	0.16
LP184	1150	4.87	0.53	3.25	10	41.99 (0.22)	0.06 (0.04)	0.04 (0.03)	5.57 (0.21)	0.2 (0.04)	52.33 (0.3)	0.26 (0.04)	0.02 (0.01)	0.01 (0.01)	0.02 (0.02)	100.48	93.86	0.16
LP185	1150	6.88	0.92	3.72	9	42.1 (0.31)	0.06 (0.02)	0.03 (0.02)	4.06 (0.26)	0.2 (0.04)	53.75 (0.4)	0.25 (0.03)	0.01 (0.01)	0 (0)	0.07 (0.03)	100.46	95.44	0.16

-, not determined

Kd_{Ol-Liq} represents Mg/Fe partitioning between olivine and silicate melt ($Kd_{Ol-Liq}^{Fe-Mg} = X_{Ol}^{Fe}/X_{Ol}^{Mg} \times X_{Liq}^{Fe}/X_{Liq}^{Mg}$)

Table 12. Compositions of experimental olivines using starting composition 168-1 at 700 MPa

Run	Pressure [MPa]	Temperature [°C]	melt H ₂ O [wt%]	<i>a</i> H ₂ O	ΔFMQ	n	SiO ₂	TiO ₂	Al ₂ O ₃	FeO	MnO	MgO	CaO	Na ₂ O	K ₂ O	Cr ₂ O ₃	Total	Fo	Kd _{Ol-Liq}
LP85	7000	1050	12.14	1.31	4.03	11	42.09 (0.33)	0.06 (0.02)	0.02 (0.02)	5.31 (0.6)	0.32 (0.08)	53.85 (0.43)	0.18 (0.02)	0.01 (0.02)	0 (0)	0.03 (0.04)	101.84	94.25	0.19
LP86	7000	1050	12.44	1.36	4.07	8	42.04 (0.46)	0.07 (0.05)	0.03 (0.03)	5.7 (0.13)	0.38 (0.04)	53.57 (0.68)	0.2 (0.03)	0.01 (0.01)	0.01 (0.01)	0.03 (0.03)	102.00	93.78	0.21
LP87	7000	1050	12.45	1.36	4.07	13	41.91 (0.21)	0.04 (0.02)	0.02 (0.02)	6.33 (0.19)	0.45 (0.08)	53.56 (0.28)	0.16 (0.02)	0.02 (0.02)	0.01 (0.01)	0.02 (0.02)	102.51	93.17	0.13
LP88	7000	1050	12.12	1.30	4.03	4	41.73 (0.4)	0.08 (0.04)	0.1 (0.13)	7.42 (0.17)	0.41 (0.03)	52.33 (0.5)	0.27 (0.14)	0.03 (0.03)	0.01 (0.01)	0.03 (0.04)	102.39	91.93	0.12
LP95	7000	1100	8.74	0.76	3.57	12	42.35 (0.29)	0.05 (0.03)	0.02 (0.02)	5.17 (0.33)	0.24 (0.05)	54.59 (0.3)	0.18 (0.03)	0.01 (0.01)	0 (0.01)	0.02 (0.02)	102.61	94.52	0.15
LP96	7000	1100	8.36	0.71	3.51	9	42 (0.15)	0.06 (0.04)	0.03 (0.02)	5.83 (0.27)	0.24 (0.04)	53.89 (0.17)	0.18 (0.02)	0.01 (0.01)	0 (0)	0.02 (0.03)	102.25	93.83	0.15
LP97	7000	1100	9.92	0.92	3.74	10	42.08 (0.2)	0.05 (0.02)	0.02 (0.01)	6.2 (0.16)	0.25 (0.03)	53.74 (0.2)	0.2 (0.02)	0.01 (0.01)	0 (0)	0.02 (0.03)	102.55	93.45	0.18
LP98	7000	1100	10.06	0.95	3.76	10	41.85 (0.31)	0.07 (0.02)	0.08 (0.09)	7.32 (0.17)	0.32 (0.05)	52.61 (0.35)	0.23 (0.07)	0.02 (0.02)	0.01 (0.01)	0.01 (0.02)	102.50	92.19	0.21
LP99	7000	1100	7.05	0.55	3.29	3	41.3 (0.08)	0.25 (0.08)	0.57 (0.32)	10.28 (0.34)	0.33 (0.17)	48.45 (1.38)	1.02 (0.66)	0.1 (0.04)	0.03 (0.01)	0 (0)	102.32	87.87	0.23
LP100	7000	1100	1.25	0.06	1.34	1	39.38	0.38	0.66	15.83	0.35	43.53	0.89	0.11	0.03	-	101.76	84.34	0.18
LP101	7000	1100	2.15	0.11	1.90	3	40.28 (1.41)	0.21 (0.14)	0.72 (0.57)	14.01 (1.13)	0.41 (0.05)	45.38 (1.16)	0.47 (0.18)	0.22 (0.22)	0.06 (0.07)	-	101.76	84.34	0.20
LP102	7000	1100	5.07	0.34	2.88	4	41.92 (0.2)	0.05 (0.01)	0.04 (0.02)	8.98 (0.49)	0.25 (0.03)	52.18 (0.29)	0.26 (0.03)	0.01 (0.01)	0.01 (0.01)	0.05 (0.02)	103.68	90.68	0.18
LP103	7000	1100	5.66	0.40	3.01	5	41.5 (0.61)	0.1 (0.05)	0.13 (0.14)	8.55 (0.46)	0.28 (0.11)	50.98 (0.83)	0.55 (0.68)	0.04 (0.04)	0.01 (0)	0.01 (0.05)	102.15	90.50	0.18
LP104	7000	1100	5.62	0.40	3.00	3	41.2 (0.12)	0.05 (0.01)	0.03 (0.01)	7.31 (0.24)	0.32 (0.09)	51.21 (0.1)	0.2 (0.01)	0.01 (0)	0 (0.01)	-	100.35	92.04	0.16
LP115	7000	1150	2.86	0.16	2.20	4	39.63 (0.29)	0.14 (0.07)	0.21 (0.23)	15.64 (0.15)	0.39 (0.01)	44.58 (0.88)	0.55 (0.37)	0.01 (0.01)	0.01 (0.01)	-	101.16	82.61	0.21
LP116	7000	1150	3.54	0.21	2.44	3	39.99 (0.22)	0.09 (0.01)	0.03 (0.03)	13.7 (0.23)	0.41 (0.06)	46.71 (0.08)	0.33 (0.04)	0.03 (0.04)	0.01 (0.01)	-	101.29	85.14	0.21
LP154	7000	1150	1.36	0.06	1.40	8	39.35 (0.13)	0.09 (0.02)	0.09 (0.06)	14.15 (0.21)	0.34 (0.04)	44.67 (0.22)	0.29 (0.04)	0.04 (0.04)	0.02 (0.01)	0.03 (0.02)	99.04	84.26	0.17
LP155	7000	1150	1.69	0.08	1.63	9	40 (0.25)	0.08 (0.02)	0.08 (0.02)	14.62 (0.22)	0.32 (0.08)	45.1 (0.19)	0.31 (0.05)	0.04 (0.03)	0.01 (0.01)	0.03 (0.01)	100.56	83.97	0.18

-, not determined

Kd_{Ol-Liq} represents Mg/Fe partitioning between olivine and silicate melt ($Kd_{Ol-Liq}^{Fe-Mg} = X_{Ol}^{Fe}/X_{Ol}^{Mg} \times X_{Liq}^{Mg}/X_{Liq}^{Fe}$)

Table 13. Compositions of experimental olivines using starting composition KLA-1-6-22 at 400 MPa

Run	Temperature [°C]	melt H ₂ O [wt%]	α H ₂ O	ΔFMQ	n	SiO ₂	TiO ₂	Al ₂ O ₃	FeO	MnO	MgO	CaO	Na ₂ O	K ₂ O	Cr ₂ O ₃	Total	Fo	Kd _{Ol-Liq}
LP13	1050	6.25	0.76	0.41	5	39.56 (0.24)	0.08 (0.02)	0.03 (0.02)	17.31 (0.35)	0.31 (0.05)	43.98 (0.35)	0.41 (0.04)	-	-	-	101.67	81.20	0.32
LP14	1050	5.71	0.66	0.29	5	39.33 (0.17)	0.08 (0.03)	0.02 (0.01)	18.58 (0.26)	0.35 (0.03)	42.61 (0.47)	0.42 (0.06)	-	-	-	101.38	79.60	0.31
LP15	1050	4.86	0.51	0.07	5	38.57 (0.47)	0.19 (0.21)	0.06 (0.06)	21.31 (0.37)	0.43 (0.04)	39.71 (0.19)	0.47 (0.08)	-	-	-	100.75	76.01	0.31
LP32	1050	0.50	0.03	0.11	4	40.74 (0.74)	0.21 (0.11)	0.65 (0.66)	15.03 (0.48)	0.44 (0.05)	41.1 (1.6)	0.73 (0.42)	0.14 (0.1)	0.13 (0.16)	0.06 (0.04)	100.55	81.69	0.20
LP33	1050	0.50	0.03	0.11	2	38.81 (0.58)	1.01 (0.16)	0.44 (0.33)	18.46 (0.94)	0.51 (0.02)	39.29 (0.11)	0.61 (0.07)	0.08 (0.04)	0.05 (0.03)	0.02 (0)	100.01	79.49	0.20
LP213	1050	0.71	0.04	1.06	3	39.92 (0.76)	0.47 (0.34)	1.45 (0.9)	18.94 (1.26)	0.49 (0.06)	37.58 (2.5)	2.49 (2.21)	0.26 (0.16)	0.14 (0.16)	0.04 (0)	101.75	74.75	0.21
LP192	1075	0.58	0.03	0.83	2	38.48 (0.29)	0.29 (0.23)	0.32 (0.36)	18.19 (0.41)	0.42 (0.05)	41.92 (0.75)	0.53 (0.18)	-	0.05 (0.05)	0.02 (0.02)	100.34	79.47	0.17
LP193	1075	1.65	0.12	1.95	2	40.07 (0.82)	0.58 (0.17)	2.63 (2.3)	16.39 (0.08)	0.4 (0.06)	37.27 (3.56)	2.01 (0.89)	0.72 (0.74)	0.34 (0.44)	-	100.40	77.42	0.22
LP134	1100	2.54	0.21	2.46	3	39.57 (0.18)	0.2 (0.05)	0.49 (0.16)	16.46 (0.07)	0.44 (0.06)	43.23 (0.42)	0.91 (0.54)	0.13 (0.08)	0.06 (0.02)	-	101.49	81.01	0.23
LP135	1100	1.06	0.07	1.46	4	38.69 (0.44)	0.2 (0.14)	0.43 (0.48)	15.1 (0.83)	0.51 (0.09)	41.87 (1.7)	1.21 (1.42)	0.06 (0.03)	0.03 (0.02)	0.07 (0.06)	98.10	81.30	0.17
LP136	1100	1.57	0.11	1.90	2	40.06 (0.02)	0.41 (0.03)	1.97 (0.26)	17.73 (0.09)	0.49 (0.06)	39.01 (0.4)	1.54 (0.04)	0.47 (0.08)	0.29 (0.07)	-	101.97	77.49	0.21
LP200	1125	1.65	0.12	1.93	5	38.95 (0.78)	0.56 (0.99)	0.38 (0.44)	17.58 (1.5)	0.38 (0.08)	40.66 (3.38)	1.76 (2.77)	0.08 (0.09)	0.04 (0.01)	0.03 (0.02)	100.40	78.18	0.21
LP201	1125	2.19	0.17	2.26	5	39.36 (0.13)	0.04 (0.03)	0.09 (0.02)	14.86 (0.12)	0.33 (0.04)	44.82 (0.21)	0.33 (0.02)	0.07 (0.06)	0.05 (0.05)	0.04 (0.03)	99.95	83.64	0.19
FC-37	1125	3.64	0.35	2.38	10	39.37 (0.22)	0.11 (0.02)	0.02 (0.02)	20.08 (0.46)	0.35 (0.06)	38.13 (0.44)	0.39 (0.03)	0.01 (0.01)	0.01 (0.01)	0.04 (0.01)	101.32	84.69	0.19
LP174	1150	1.39	0.09	1.74	12	39.38 (0.15)	0.11 (0.03)	0.1 (0.06)	16.69 (0.15)	0.28 (0.04)	43.62 (0.31)	0.56 (0.15)	0.03 (0.01)	0.01 (0.01)	0.04 (0.03)	100.77	81.47	0.09
LP175	1150	2.06	0.15	2.18	10	39.56 (0.17)	0.18 (0.14)	0.29 (0.34)	15.17 (0.36)	0.27 (0.03)	43.9 (1.19)	0.86 (0.75)	0.06 (0.05)	0.04 (0.05)	0.03 (0.02)	100.33	82.55	0.10

-, not determined

Kd_{Ol-Liq} represents Mg/Fe partitioning between olivine and silicate melt ($Kd_{Ol-Liq}^{Fe-Mg} = X_{Ol}^{Fe}/X_{Ol}^{Mg} \times X_{Liq}^{Fe}/X_{Liq}^{Mg}$)

Table 14. Compositions of experimental olivines using starting composition KLA-1-6-22 at 550 MPa

Run	Temperature [°C]	melt H ₂ O [wt%]	α H ₂ O	ΔFMQ	n	SiO ₂	TiO ₂	Al ₂ O ₃	FeO	MnO	MgO	CaO	Na ₂ O	K ₂ O	Cr ₂ O ₃	Total	Fo	Kd _{Ol-Liq}
FC-1	1175	5.41	0.45	2.61	3	37.6(4)	0.11(5)	0.1(1)	12.5(5)	0.26(4)	45.3(3)	0.44(3)	0.02(3)	-	-	96.40	85.85	0.23
FC-2	1175	1.50	0.08	1.11	3	38(1.71)	0.4(4)	0.4(5)	15(1.93)	0.28(2)	46(1.28)	-	0.03(2)	0.02(1)	-	100.36	83.36	0.17
FC-3	1175	1.71	0.10	1.26	3	39.1(2)	0.09(1)	0.05(3)	12.9(4)	0.30(5)	46.9(2)	0.48(3)	0.04(1)	-	-	99.96	85.80	0.15
FC-7	1150	4.07	0.30	2.26	4	38.4(5)	0.13(5)	0.1(1)	13.4(6)	0.08(1)	43.07(8)	0.42(4)	0.02(1)	0.01(1)	-	95.57	84.61	0.20
FC-8	1150	1.82	0.10	1.33	2	39.39(1)	0.14(7)	0.5(5)	13.6(3)	-	43.7(7)	0.6(2)	0.2(1)	0.06(6)	-	98.25	84.32	0.15
FC-9	1150	2.42	0.15	1.65	3	39.7(4)	0.09(2)	0.05(4)	14.2(2)	-	44.8(3)	0.40(2)	0.04(6)	0.01(1)	-	99.33	84.36	0.17
FC-42	1125	3.19	0.22	1.98	4	39.2(3)	0.12(3)	0.09(7)	16.9(5)	0.34(3)	43.09(5)	0.41(5)	0.04(3)	0.02(1)	-	100.14	81.24	0.19
FC-43	1125	4.20	0.32	2.31	5	40.0(3)	0.08(2)	0.04(3)	11.3(3)	0.24(4)	48.7(2)	0.34(4)	0.01(4)	0.01(1)	-	100.75	87.86	0.17
FC-47	1075	6.49	0.62	3.39	2	40.8(1)	0.06(2)	0.03(1)	8.7(4)	0.25(3)	52.2(3)	0.25(2)	0.00(4)	0.01(1)	-	102.31	90.96	0.22

-, not determined

Kd_{Ol-Liq} represents Mg/Fe partitioning between olivine and silicate melt ($Kd_{Ol-Liq}^{Fe-Mg} = X_{Ol}^{Fe}/X_{Ol}^{Mg} \times X_{Liq}^{Fe}/X_{Liq}^{Mg}$)

Table 15. Compositions of experimental olivines using starting composition KLA-1-6-22 at 700 MPa

Run	Temperature [°C]	melt H ₂ O [wt%]	α H ₂ O	ΔFMQ	n	SiO ₂	TiO ₂	Al ₂ O ₃	FeO	MnO	MgO	CaO	Na ₂ O	K ₂ O	Cr ₂ O ₃	Total	Fo	Kd _{Ol-Liq}
LP150	1150	0.50	0.02	0.39	10	38.95 (0.49)	0.17 (0.24)	0.53 (1.35)	19.74 (0.53)	0.46 (0.08)	40.34 (2.67)	0.45 (0.32)	0.16 (0.39)	0.08 (0.2)	0.03 (0.02)	100.87	77.57	0.16
LP151	1150	1.49	0.07	1.50	10	39.56 (0.16)	0.09 (0.03)	0.13 (0.12)	16.2 (0.38)	0.34 (0.06)	43.9 (0.24)	0.32 (0.06)	0.05 (0.04)	0.02 (0.02)	0.02 (0.02)	100.62	82.19	0.18
LP152	1150	1.53	0.07	1.53	11	39.9 (0.14)	0.08 (0.01)	0.07 (0.02)	15.63 (0.15)	0.35 (0.07)	44.36 (0.29)	0.31 (0.02)	0.02 (0.02)	0.01 (0)	0.03 (0.03)	100.73	82.84	0.18

-, not determined

Kd_{Ol-Liq} represents Mg/Fe partitioning between olivine and silicate melt ($Kd_{Ol-Liq}^{Fe-Mg} = X_{Ol}^{Fe}/X_{Ol}^{Mg} \times X_{Liq}^{Fe}/X_{Liq}^{Mg}$)

4.3.2 Pyroxene

The compositions of experimentally produced clinopyroxenes are listed in Tables 16-20. It is well known, that in alkali-rich systems Ti-rich clinopyroxenes show distinct sector zoning if crystal growth is too rapid to attain equilibrium (e.g. Brophy et al., 1999). In our experiments sector zoning is visible by backscattered electrons in runs conducted at high H₂O activity conditions, due to the formation of large clinopyroxene crystals (up to 100 µm). In runs conducted at low H₂O activity clinopyroxene crystals are smaller and sector zoning was not observed by backscattered electrons, but was evident by a heterogeneous distribution of elements. Different sectors in the clinopyroxene are either characterized by high Si and Mg content and accordingly low Ti, Al^{IV} and Fe and or vice versa. To overcome this unavoidable issue of chemical disequilibrium in clinopyroxenes, we collected a number of clinopyroxene analyses for each experimental run and calculated representative average compositions.

Cations per formula unit (pfu) were calculated on the basis of six oxygens and are plotted as a function of H₂O concentration in the melt and temperature in Figures 26 and 27 for the primitive basanite (168-1) conducted at 400 MPa and 700 MPa and in Figures 28, 29 and 30 for the evolved basanite (KLA-1-6-22) conducted at 400 MPa, 550 MPa and 700 MPa. A general correlation between Si, Ti, Al, Fe^{tot}, Ca and Na pfu on the H₂O content in the melt and subordinate on temperature can be observed. The Si pfu show a positive linear correlation with H₂O content in the melt. However, an opposing trend can be observed for Si pfu as a function of temperature. As Si, Ti and Al^{IV} pfu are occupying the tetraeder position in pyroxenes, a direct correlation between those elements can be observed. At high Si pfu minor Ti and Al^{IV} pfu are incorporated in the pyroxene structure and vice versa. Fe^{tot} and Na pfu decrease with increasing H₂O concentration in the melt. Ca pfu increases with increasing H₂O concentration in the melt.

Using the primitive basanite (168-1) at 400 MPa as starting material (see Figure 26) Si pfu increases with increasing H₂O content in the melt from 1.675 to 1.912, while Ti and Al^{tot} pfu decrease from 0.093 to 0.038 and 0.425 to 0.114, respectively. Highest Si pfu and corresponding low Ti and Al^{tot} pfu were observed at low temperatures (1010-1025°C) and high H₂O concentrations in the melt. Fe^{tot} pfu decreases with increasing H₂O concentration in the

melt from 0.286 to 0.151. This decrease is directly related to the increasing redox conditions and decreasing $\text{Fe}^{2+}/\Sigma\text{Fe}$ ratio with increasing H_2O content in the melt (discussed above). Due to the lower $\text{Fe}^{2+}/\Sigma\text{Fe}$ ratio in the melt and the high proportion of magnetite less Fe content is incorporated in the clinopyroxene structure. Ca pfu shows a linear increase with increasing H_2O content in the melt from 0.761 to 0.934. Na pfu decreases with increasing H_2O content in the melt from 0.104 to 0.019.

Using the same starting composition at 700 MPa (see Figure 27) Si pfu is lower in comparison to Si pfu of clinopyroxenes crystallized at 400 MPa and vary from 1.675 to 1.912. Ti and Al^{tot} decrease from 0.081 to 0.025 and from 0.420 to 0.175, respectively. Fe^{tot} and Ca pfu show no pressure sensitive behavior and are similar to those crystallized at 400 MPa varying from 0.286 to 0.173 and 0.173 to 0.286 with increasing H_2O concentration in the melt. Na pfu is elevated at given H_2O content in the melt in comparison to those crystallized at 400 MPa ranging from 0.116 to 0.032.

In Figure 28 the compositional variations of clinopyroxenes crystallized at 400 MPa using the evolved basanite as starting material (KLA-1-6-22) are shown. Si pfu increases from 1.676 to 1.883 with increasing H_2O concentration in the melt. Highest Si pfu were obtained at low temperature (1025°C and 400 MPa) and high H_2O content in the melt (8.12 wt.%). Ti and Al^{tot} pfu behave in opposing direction ranging from 0.127 to 0.042 and from 0.459 to 0.140, respectively. Fe^{tot} pfu decreases with increasing H_2O content in the melt from 0.286 to 0.160, while Ca pfu increases from 0.713 to 0.929. Na pfu decreases with increasing H_2O content in the melt from 0.137 to 0.023, while highest values were observed at low temperature.

Using the same starting composition at 550 MPa in the temperature range of olivine, clinopyroxene and spinel stability (see Figure 29) the Si pfu varies from 1.674 to 1.853, while Ti and Al^{tot} pfu decrease from 0.129 to 0.037 and 0.412 to 0.157 with increasing H_2O concentration in the melt. Fe^{tot} pfu decreases linearly with increasing H_2O content melt from 0.247 to 0.183. Ca pfu increases from 0.783 to 0.907 and Na pfu decreases from 0.034 to 0.078 with increasing H_2O content in the melt.

Using the same starting composition at 700 MPa (see Figure 30) Si pfu increases from 1.695 to 1.811, while Ti and Al^{tot} decrease from 0.091 to 0.041 and from 0.405 to 0.193, respectively.

Highest Si pfu values were observed at low temperature (1050°C) and high H₂O concentration in the melt. Fe^{tot} pfu decreases as a function of H₂O content in the melt and redox conditions from 0.277 to 0.188. Ca pfu increases from 0.779 to 0.934, while Na pfu decreases from 0.132 to 0.032 with increasing H₂O concentration in the melt.

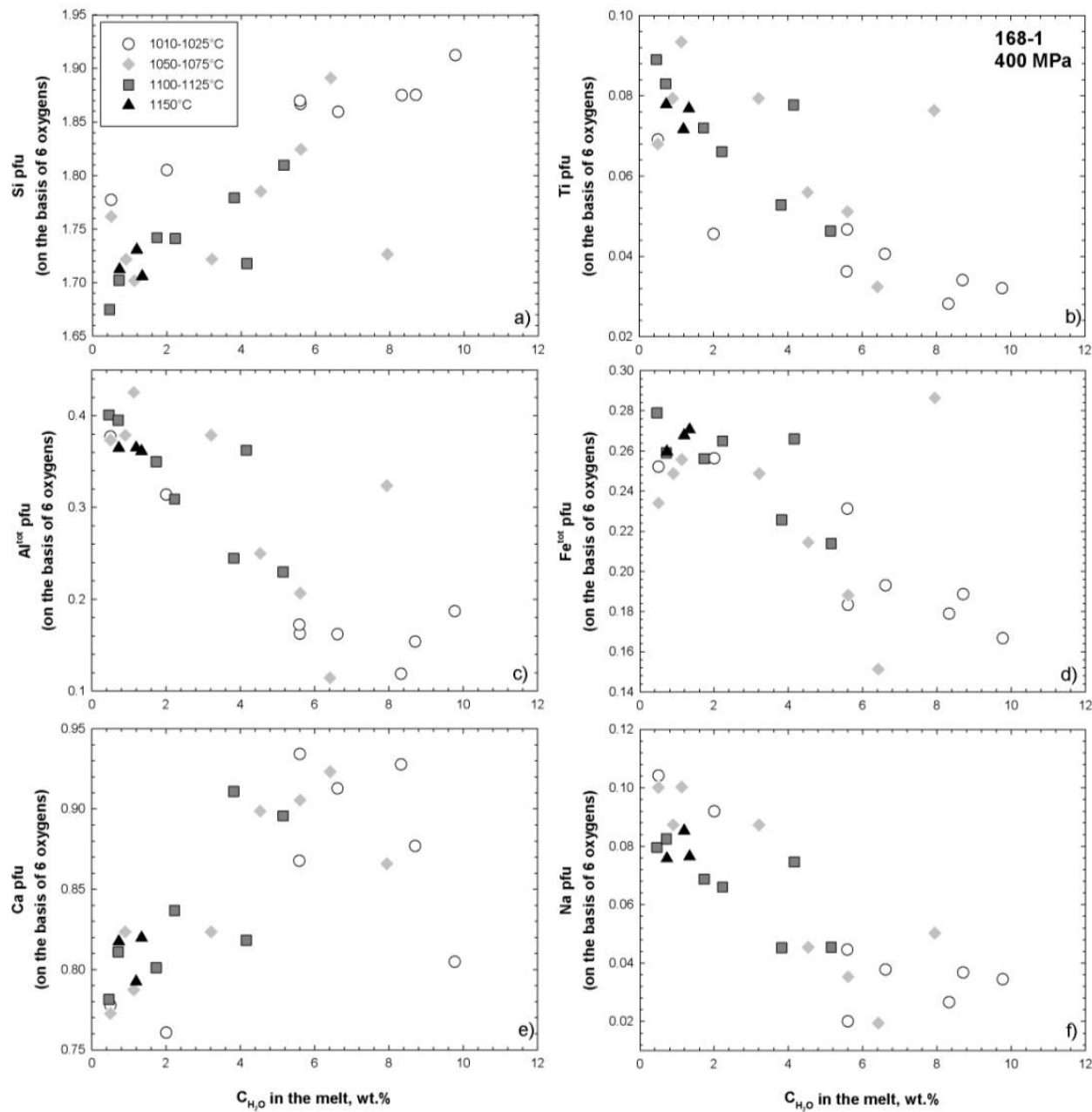


Figure 26: Variations in clinopyroxene composition using starting composition 168-1 at 400 MPa as function of H₂O concentration in the melt (wt.%) and temperature (°C). (a) Si per formula unit, (b) Ti per formula, (c) Al^{tot} per formula unit, (d) Fe^{tot} per formula unit, (e) Ca per formula unit, (f) Na per formula unit.

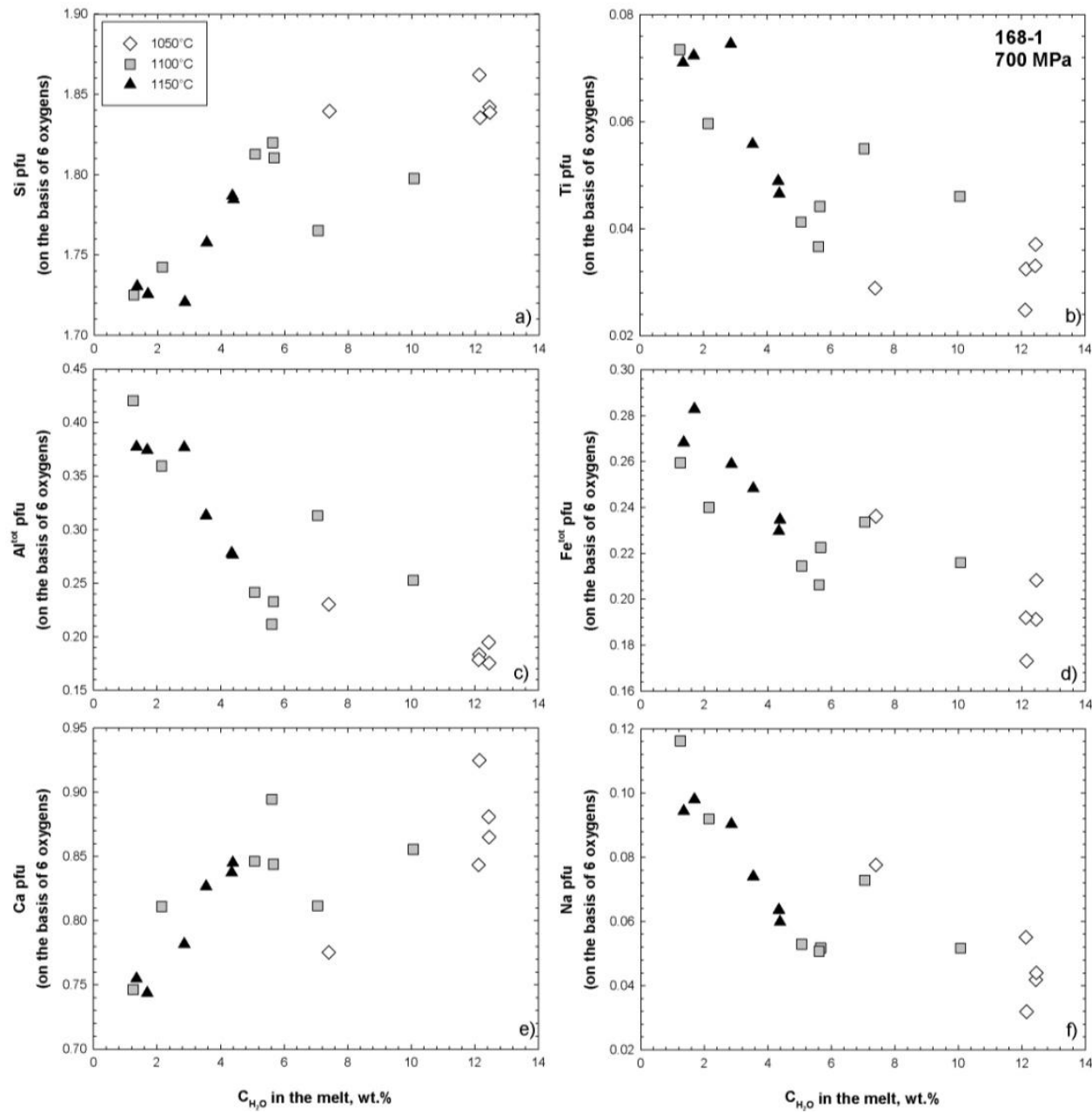


Figure 27: Variations in clinopyroxene composition using starting composition 168-1 at 700 MPa as function of H_2O concentration in the melt (wt.%) and temperature (°C). (a) Si per formula unit, (b) Ti per formula, (c) Al^{tot} per formula unit, (d) Fe^{tot} per formula unit, (e) Ca per formula unit, (f) Na per formula unit.

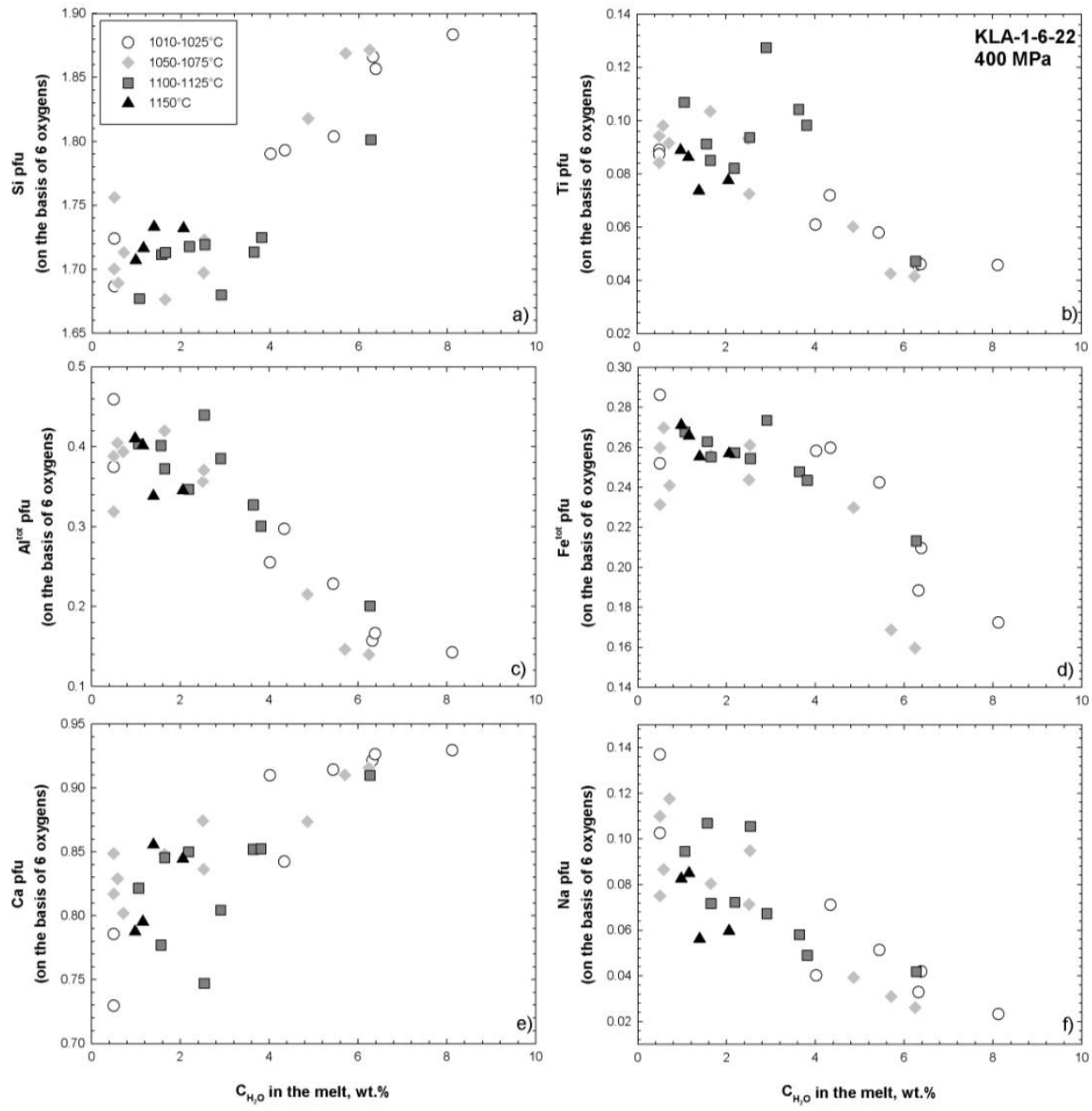


Figure 28: Variations in clinopyroxene composition using starting composition KLA-1-6-22 at 400 MPa as function of H_2O concentration in the melt (wt.%) and temperature ($^{\circ}\text{C}$). (a) Si per formula unit, (b) Ti per formula, (c) Al^{tot} per formula unit, (d) Fe^{tot} per formula unit, (e) Ca per formula unit, (f) Na per formula unit.

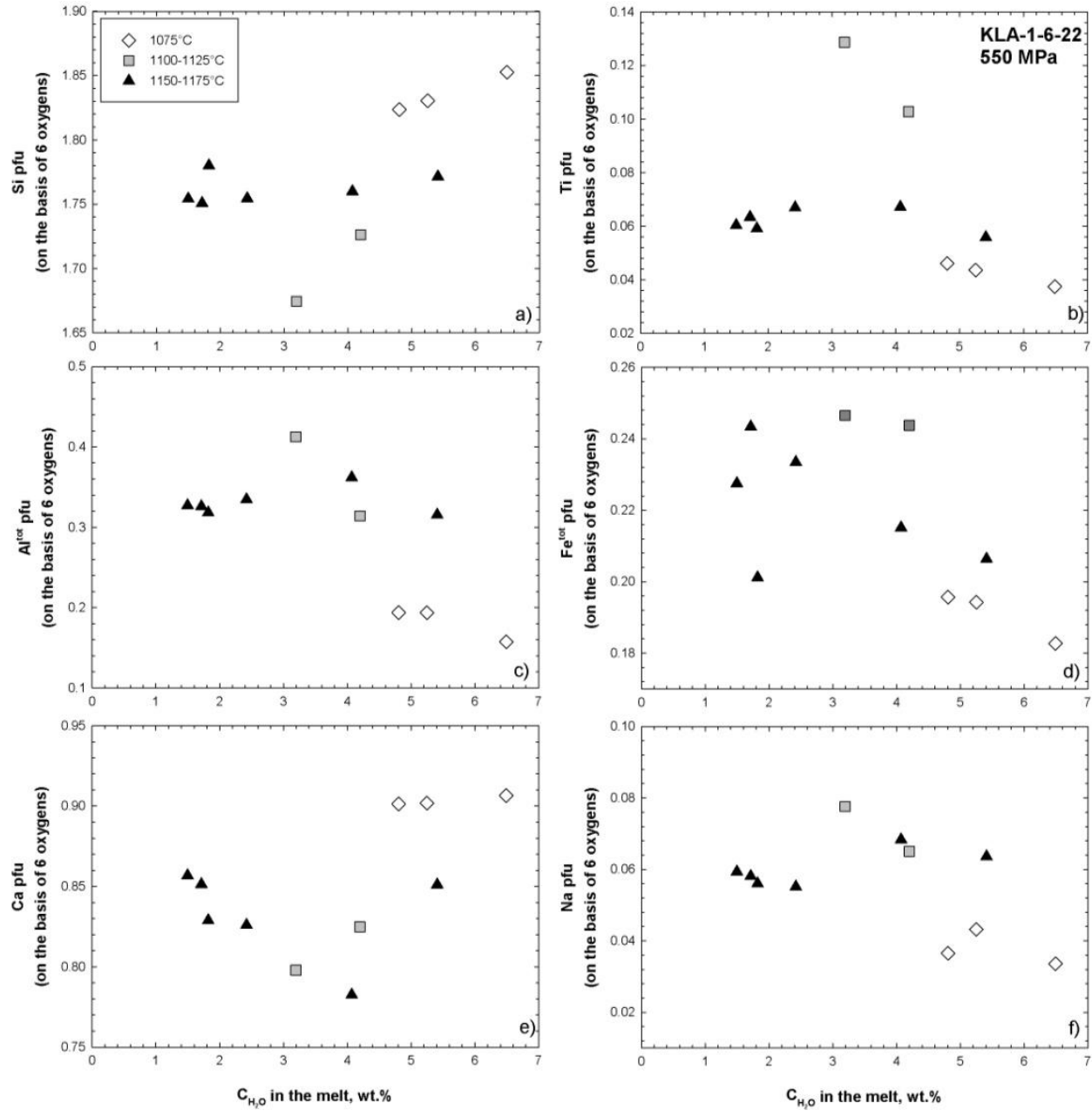


Figure 29: Variations in clinopyroxene composition using starting composition KLA-1-6-22 at 550 MPa as function of H_2O concentration in the melt (wt.%) and temperature ($^{\circ}C$). (a) Si per formula unit, (b) Ti per formula, (c) Al^{tot} per formula unit, (d) Fe^{tot} per formula unit, (e) Ca per formula unit, (f) Na per formula unit.

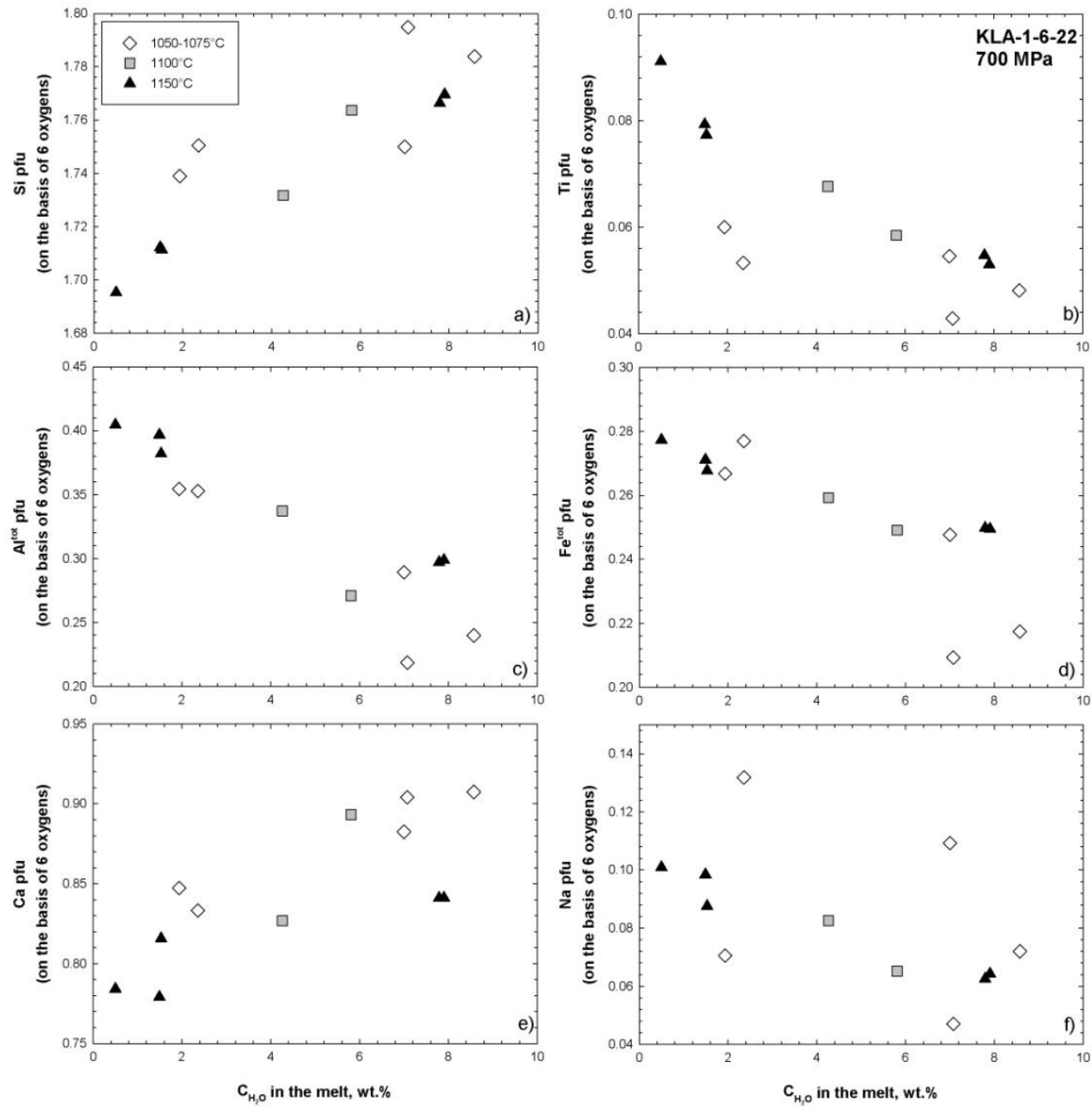


Figure 30: Variations in clinopyroxene composition using starting composition KLA-1-6-22 at 700 MPa as function of H_2O concentration in the melt (wt.%) and temperature ($^{\circ}\text{C}$). (a) Si per formula unit, (b) Ti per formula, (c) Al^{tot} per formula unit, (d) Fe^{tot} per formula unit, (e) Ca per formula unit, (f) Na per formula unit.

Table 16. Compositions of experimental clinopyroxenes using starting composition 168-1 at 400 MPa

Run	T [°C]	melt H ₂ O [wt%]	α H ₂ O	Δ FMQ	n	SiO ₂	TiO ₂	Al ₂ O ₃	FeO	MnO	MgO	CaO	Na ₂ O	K ₂ O	Cr ₂ O ₃	Total	Mg#	En	Wo	Fs	Kd _{Cpx-Liq}
LP53	1010	9.77	1.58	3.08	1	52.06 (0.05)	1.16 (0.03)	4.31 (0.24)	5.43 (0.1)	0.23 (0.01)	15.18 (0.13)	20.45 (0.09)	0.48 (0)	0.18 (0.05)	-	99.48 (0.28)	83.30	0.46	0.45	0.09	0.15
LP54	1010	8.71	1.30	2.91	5	50.56 (0.29)	1.22 (0.21)	3.52 (0.91)	6.08 (0.4)	0.18 (0.03)	15.49 (0.76)	22.07 (0.84)	0.51 (0.09)	0.09 (0.07)	0.07 (0.05)	99.78 (0.37)	81.95	0.45	0.46	0.10	0.17
LP55	1010	8.33	1.21	2.84	2	49.81 (0.91)	0.99 (0.15)	2.67 (0.45)	5.68 (0.15)	0.16 (0.07)	15.83 (0.27)	23 (0.39)	0.36 (0.1)	0.03 (0)	0.05 (0.02)	98.59 (0.04)	83.24	0.45	0.46	0.09	0.19
LP34	1025	5.60	0.64	0.68	7	50.44 (1.05)	1.68 (0.35)	3.72 (0.72)	5.92 (0.73)	0.09 (0.02)	14.37 (0.5)	23.56 (0.57)	0.28 (0.06)	0.05 (0.03)	0.12 (0.1)	100.22 (0.5)	81.22	0.42	0.49	0.10	0.22
LP35	1025	6.62	0.83	0.91	4	50.03 (0.42)	1.45 (0.19)	3.7 (0.43)	6.21 (0.14)	0.16 (0.03)	14.85 (0.06)	22.92 (0.24)	0.52 (0.06)	0.04 (0.02)	0.09 (0.02)	99.97 (0.28)	81.00	0.43	0.47	0.10	0.12
LP36	1025	5.59	0.63	0.68	5	50.11 (0.67)	1.29 (0.11)	3.91 (0.46)	7.41 (0.77)	0.16 (0.03)	14.34 (0.45)	21.7 (0.53)	0.62 (0.12)	0.12 (0.05)	0.08 (0.03)	99.74 (0.32)	77.53	0.42	0.46	0.12	0.15
LP11	1050	6.42	0.79	0.32	6	51.45 (0.47)	1.17 (0.08)	2.64 (0.24)	4.92 (0.36)	0.08 (0.04)	16.34 (0.27)	23.44 (0.29)	0.27 (0.03)	-	-	100.33 (0.49)	85.55	0.45	0.47	0.08	0.19
LP12	1050	5.61	0.64	0.14	5	49.33 (0.9)	1.84 (0.25)	4.74 (0.88)	6.08 (0.57)	0.07 (0.04)	14.98 (0.41)	22.85 (0.58)	0.49 (0.14)	-	-	100.38 (0.18)	81.45	0.43	0.47	0.10	0.24
LP198	1025	0.50	0.03	0.70	4	47.68 (1.01)	2.46 (0.16)	8.58 (0.93)	8.09 (0.28)	0.19 (0.05)	11.59 (0.8)	19.47 (1.42)	1.44 (0.21)	0.31 (0.23)	0.06 (0.01)	99.87 (0.69)	71.86	0.38	0.46	0.15	0.54
LP199	1025	2.00	0.16	2.21	2	48.92 (0.23)	1.64 (0.02)	7.22 (0.22)	8.31 (0.11)	0.22 (0.02)	13.65 (0.41)	19.24 (0.45)	1.29 (0.1)	0.25 (0.09)	-	100.77 (0.22)	74.54	0.42	0.43	0.15	0.36
LP30	1050	0.50	0.03	0.11	1	45.68	2.70	7.64	8.49	0.19	12.97	20.24	0.97	0.13	0.07	99.08	75.22	0.41	0.45	0.14	0.41
LP188	1050	1.13	0.07	1.55	7	45.6 (0.73)	3.33 (0.2)	9.67 (0.83)	8.19 (0.42)	0.18 (0.05)	11.92 (0.5)	19.69 (1.02)	1.39 (0.2)	0.26 (0.14)	0.07 (0.04)	100.31 (0.72)	72.17	0.39	0.46	0.15	0.37
LP189	1050	3.21	0.30	2.76	6	45.78 (1.19)	2.8 (0.6)	8.54 (1.77)	7.91 (0.6)	0.21 (0.04)	12.51 (1.17)	20.44 (1.29)	1.2 (0.4)	0.15 (0.15)	0.05 (0.04)	99.59 (0.48)	73.82	0.40	0.46	0.14	0.48
LP216	1050	7.94	1.22	3.97	4	44.94 (3.96)	2.64 (1.06)	7.15 (4.01)	8.91 (2.94)	0.15 (0.05)	12.61 (4.56)	21.03 (2.48)	0.68 (0.46)	0.09 (0.12)	0.03 (0.03)	98.24 (2.4)	71.61	0.39	0.46	0.15	0.63
LP191	1075	4.53	0.49	3.19	3	47.72 (0.8)	1.99 (0.33)	5.67 (0.93)	6.85 (0.78)	0.13 (0.04)	14.38 (0.55)	22.42 (0.21)	0.63 (0.07)	0.04 (0.01)	0 (0.01)	99.83 (0.58)	78.90	0.42	0.47	0.11	0.27
LP168	1100	0.46	0.04	1.04	7	44.48 (0.77)	3.14 (0.26)	9.03 (0.66)	8.86 (1.11)	0.14 (0.04)	13.52 (2.4)	19.37 (1.86)	1.09 (0.18)	0.12 (0.07)	0.1 (0.05)	99.85 (0.54)	73.13	0.42	0.43	0.15	0.35
LP169	1100	0.71	0.04	1.04	5	45.44 (0.57)	2.94 (0.26)	8.94 (0.39)	8.27 (0.19)	0.13 (0.03)	12.81 (0.69)	20.2 (0.62)	1.14 (0.13)	0.13 (0.08)	0.07 (0.03)	100.07 (0.65)	73.42	0.40	0.45	0.15	0.43
LP170	1100	5.15	0.59	3.35	7	48.47 (0.96)	1.65 (0.43)	5.22 (1.6)	6.85 (0.49)	0.08 (0.05)	14.45 (1.43)	22.39 (1.58)	0.63 (0.21)	0.06 (0.1)	0.06 (0.03)	99.86 (1.24)	79.00	0.42	0.47	0.11	0.43
LP171	1100	3.82	0.38	2.96	7	47.65 (0.46)	1.88 (0.07)	5.56 (0.24)	7.23 (0.34)	0.07 (0.04)	14.43 (0.17)	22.77 (0.27)	0.62 (0.04)	0.03 (0.01)	0.09 (0.04)	100.32 (0.45)	78.06	0.41	0.47	0.12	0.47
LP172	1100	4.16	0.43	3.07	5	45.68 (0.8)	2.75 (0.2)	8.18 (0.73)	8.46 (0.83)	0.18 (0.03)	13.09 (0.67)	20.31 (0.74)	1.02 (0.17)	0.07 (0.06)	0.07 (0.03)	99.8 (0.31)	73.39	0.40	0.45	0.15	0.52
LP202	1125	1.73	0.12	1.99	6	46.26 (0.68)	2.54 (0.21)	7.88 (0.78)	8.13 (0.32)	0.15 (0.06)	13.23 (0.84)	19.86 (0.32)	0.94 (0.08)	0.15 (0.09)	0.1 (0.02)	99.25 (0.3)	74.36	0.41	0.45	0.14	0.34
LP203	1125	2.23	0.17	2.28	8	46.42 (1.07)	2.34 (0.33)	6.99 (0.62)	8.45 (1.18)	0.19 (0.06)	13.92 (0.35)	20.82 (0.45)	0.91 (0.08)	0.06 (0.02)	0.04 (0.02)	100.13 (0.67)	74.59	0.41	0.45	0.14	0.38
LP180	1150	1.19	0.08	1.56	5	46.55 (1.18)	2.56 (0.28)	8.33 (1.09)	8.61 (0.54)	0.15 (0.05)	13.22 (1.05)	19.89 (0.49)	1.18 (0.24)	0.2 (0.14)	0.07 (0.05)	100.77 (0.31)	73.23	0.41	0.44	0.15	0.34
LP181	1150	0.73	0.04	1.03	4	45.91 (0.87)	2.77 (0.41)	8.3 (0.82)	8.33 (0.68)	0.18 (0.03)	13.42 (0.46)	20.46 (0.33)	1.05 (0.06)	0.1 (0.07)	0.08 (0.01)	100.59 (0.78)	74.18	0.41	0.45	0.14	0.39
LP182	1150	1.34	0.09	1.69	7	45.67 (0.68)	2.73 (0.17)	8.21 (0.35)	8.66 (0.54)	0.14 (0.04)	13.58 (0.26)	20.48 (0.16)	1.06 (0.05)	0.07 (0.03)	0.06 (0.03)	100.65 (0.23)	73.64	0.41	0.44	0.15	0.38

-, not determined

Mg# of Cpx is calculated as $100 \times \text{Mg}/(\text{Mg}+\text{Fe}^{\text{tot}})$ $\text{Kd}_{\text{Ol-Liq}}$ represents Mg/Fe partitioning between Cpx and silicate melt ($\text{Kd}_{\text{Cpx-Liq}} = X_{\text{Cpx}}^{\text{Fe-Mg}} / (X_{\text{Cpx}}^{\text{Fe}} / X_{\text{Liq}}^{\text{Fe}} + X_{\text{Cpx}}^{\text{Mg}} / X_{\text{Liq}}^{\text{Mg}})$

Table 17. Compositions of experimental clinopyroxenes using starting composition 168-1 at 700 MPa

Run	T [°C]	melt H ₂ O [wt%]	<i>a</i> H ₂ O	ΔFMQ	n	SiO ₂	TiO ₂	Al ₂ O ₃	FeO	MnO	MgO	CaO	Na ₂ O	K ₂ O	Cr ₂ O ₃	Total	Mg#	En	Wo	Fs	Kd _{Cpx-Liq}
LP85	1050	12.14	1.31	4.03	8	49.67 (1.11)	1.17 (0.22)	4.21 (0.72)	5.6 (0.47)	0.16 (0.04)	15.71 (0.54)	23.35 (0.43)	0.45 (0.05)	0.08 (0.07)	0.08 (0.05)	100.47 (0.69)	83.33	0.44	0.47	0.09	0.37
LP86	1050	12.44	1.36	4.07	10	49.95 (0.91)	1.19 (0.15)	4.48 (0.92)	6.2 (0.46)	0.21 (0.08)	15.52 (0.72)	22.29 (0.35)	0.59 (0.09)	0.06 (0.04)	0.07 (0.03)	100.56 (0.46)	81.69	0.44	0.46	0.10	0.41
LP87	1050	12.45	1.36	4.07	8	49.91 (0.81)	1.34 (0.25)	4.04 (0.42)	6.76 (0.68)	0.26 (0.07)	15.99 (0.39)	21.91 (0.41)	0.62 (0.04)	0.03 (0.01)	0.07 (0.04)	100.91 (0.48)	80.83	0.45	0.44	0.11	0.23
LP88	1050	12.12	1.30	4.03	7	50.83 (0.81)	0.9 (0.17)	4.14 (0.5)	6.27 (0.42)	0.37 (0.08)	16.12 (0.45)	21.48 (0.11)	0.78 (0.04)	0.04 (0.02)	0.07 (0.05)	100.98 (0.3)	82.10	0.46	0.44	0.10	0.17
LP89	1050	7.40	0.61	3.37	3	49.96 (0.59)	1.04 (0.12)	5.3 (0.39)	7.67 (0.23)	0.42 (0.04)	15.51 (0.32)	19.65 (0.22)	1.09 (0.09)	0.06 (0.04)	0.04 (0.04)	100.74 (0.48)	78.28	0.46	0.42	0.13	0.41
LP98	1100	10.06	0.95	3.76	10	48.44 (0.77)	1.65 (0.35)	5.78 (1.24)	6.96 (0.36)	0.22 (0.06)	14.92 (1.01)	21.52 (0.85)	0.72 (0.1)	0.1 (0.1)	0.05 (0.04)	100.34 (0.42)	79.26	0.44	0.45	0.11	0.43
LP99	1100	7.05	0.55	3.29	6	47.53 (0.67)	1.97 (0.24)	7.15 (0.68)	7.52 (0.46)	0.25 (0.03)	14.41 (0.52)	20.39 (0.31)	1.01 (0.03)	0.05 (0.02)	0.03 (0.03)	100.33 (0.57)	77.35	0.43	0.44	0.13	0.41
LP100	1100	1.25	0.06	1.34	1	46.42	2.65	9.04	7.77	0.21	13.06	19.44	1.41	0.08	0.10	100.18	72.83	0.41	0.44	0.15	0.48
LP101	1100	2.15	0.11	1.90	3	46.75 (0.46)	2.13 (0.13)	8.18 (0.39)	7.7 (0.1)	0.28 (0.02)	13.44 (0.18)	20.31 (0.13)	1.27 (0.1)	0.04 (0.01)	0.08 (0.02)	100.17 (0.2)	75.67	0.42	0.45	0.13	0.42
LP102	1100	5.07	0.34	2.88	5	48.86 (1.01)	1.48 (0.29)	5.52 (0.85)	6.91 (0.64)	0.17 (0.02)	15.04 (0.71)	21.29 (0.35)	0.74 (0.08)	0.03 (0.01)	0.11 (0.02)	100.14 (0.21)	79.50	0.44	0.45	0.11	0.41
LP103	1100	5.66	0.40	3.01	5	48.59 (1.21)	1.58 (0.51)	5.3 (0.82)	7.14 (0.74)	0.2 (0.02)	15.08 (0.67)	21.14 (0.6)	0.72 (0.07)	0.05 (0.02)	0.1 (0.01)	99.88 (0.39)	79.00	0.44	0.44	0.12	0.42
LP104	1100	5.62	0.40	3.00	4	49.03 (0.64)	1.31 (0.12)	4.84 (0.56)	6.65 (0.42)	0.12 (0.05)	15.15 (0.2)	22.49 (0.11)	0.71 (0.04)	0.02 (0.01)	-	100.33 (0.24)	80.25	0.43	0.46	0.11	0.41
LP115	1150	2.86	0.16	2.20	3	46.15 (0.18)	2.66 (0.12)	8.57 (0.28)	8.3 (0.2)	0.2 (0.01)	13.47 (0.22)	19.57 (0.31)	1.25 (0.09)	0.06 (0.01)	-	100.28 (0.21)	74.31	0.42	0.44	0.14	0.40
LP116	1150	3.54	0.21	2.44	5	47.17 (1.26)	1.99 (0.31)	7.13 (0.8)	7.97 (1.04)	0.22 (0.05)	14.06 (0.68)	20.7 (0.27)	1.02 (0.1)	0.03 (0.01)	0.06 (0.05)	100.36 (0.56)	75.87	0.42	0.45	0.13	0.40
LP117	1150	4.35	0.27	2.68	5	48.06 (0.61)	1.75 (0.16)	6.34 (0.5)	7.39 (0.4)	0.21 (0.07)	14.49 (0.21)	21.02 (0.43)	0.88 (0.06)	0.04 (0)	0.05 (0.03)	100.24 (0.77)	77.75	0.43	0.45	0.12	0.38
LP118	1150	4.39	0.28	2.69	5	47.86 (1.19)	1.66 (0.3)	6.29 (0.99)	7.53 (0.65)	0.16 (0.05)	14.48 (0.79)	21.15 (0.39)	0.83 (0.03)	0.04 (0.01)	0.07 (0.03)	100.05 (0.22)	77.42	0.43	0.45	0.12	0.40
LP154	1150	1.36	0.06	1.40	9	45.48 (0.92)	2.48 (0.23)	8.41 (0.45)	8.43 (0.65)	0.2 (0.06)	13.25 (0.46)	18.51 (0.33)	1.28 (0.06)	0.06 (0.03)	0.04 (0.03)	98.15 (0.33)	73.68	0.42	0.43	0.15	0.42
LP155	1150	1.69	0.08	1.63	5	46.05 (0.93)	2.57 (0.12)	8.47 (0.25)	9.03 (0.7)	0.19 (0.02)	13.52 (0.37)	18.52 (0.51)	1.35 (0.08)	0.09 (0.05)	0.09 (0.01)	99.88 (0.55)	72.74	0.42	0.42	0.16	0.44

-, not determined

Mg# of Cpx is calculated as 100 x Mg/(Mg+Fe^{tot})Kd_{Ol-Liq} represents Mg/Fe partitioning between Cpx and silicate melt (Kd_{Cpx-Liq}^{Fe-Mg}=X_{Cpx}^{Fe}/X_{Cpx}^{Mg} × X_{Liq}^{Fe}/X_{Liq}^{Mg})

Table 18. Compositions of experimental clinopyroxenes using starting composition KLA-1-6-22 at 400 MPa

Run	T [°C]	melt H ₂ O [wt%]	<i>a</i> H ₂ O	ΔFMQ	n	SiO ₂	TiO ₂	Al ₂ O ₃	FeO	MnO	MgO	CaO	Na ₂ O	K ₂ O	Cr ₂ O ₃	Total	Mg#	En	Wo	Fs	K _d cpx-liq
LP13	1050	6.25	0.76	0.41	4	50.83 (0.95)	1.5 (0.35)	3.22 (0.94)	5.18 (0.44)	0.07 (0.02)	15.92 (0.61)	23.21 (0.48)	0.37 (0.07)	-	-	100.3 (0.13)	84.56	0.45	0.47	0.08	0.21
LP14	1050	5.71	0.66	0.29	5	50.75 (0.67)	1.54 (0.18)	3.37 (0.48)	5.48 (0.28)	0.09 (0.02)	15.68 (0.3)	23.06 (0.21)	0.43 (0.05)	-	-	100.4 (0.39)	83.61	0.44	0.47	0.09	0.21
LP15	1050	4.86	0.51	0.07	1	49.05	2.16	4.93	7.42	0.21	14.33	22.00	0.55	-	-	100.64	77.50	0.42	0.46	0.12	0.27
LP38	1025	4.34	0.43	0.94	1	46.98	2.50	6.60	8.14	0.14	11.85	20.60	0.96	0.25	0.06	98.07	72.18	0.38	0.47	0.15	0.26
LP39	1025	5.86	0.68	1.34	1	46.05	3.19	8.26	8.43	0.16	13.73	17.76	1.48	0.59	0.10	99.75	74.37	0.44	0.41	0.15	0.22
LP40	1025	8.12	1.16	1.80	10	51.06 (0.94)	1.65 (0.32)	3.28 (0.75)	5.59 (0.47)	0.11 (0.04)	14.67 (0.52)	23.52 (0.34)	0.32 (0.05)	0.06 (0.03)	0.08 (0.05)	100.33 (0.63)	82.40	0.42	0.49	0.09	0.23
LP44	1010	6.32	0.77	1.35	3	50.43 (0.77)	1.65 (0.3)	3.6 (0.87)	6.09 (0.32)	0.15 (0.04)	14.6 (0.58)	23.24 (0.32)	0.46 (0.09)	0.09 (0.07)	0.06 (0)	100.36 (0.17)	81.04	0.42	0.48	0.10	0.21
LP45	1010	6.39	0.78	1.36	1	49.94	2.00	4.07	7.18	0.08	12.92	23.53	0.48	0.02	0.07	100.32	78.83	0.41	0.48	0.11	0.18
LP46	1010	5.44	0.61	1.14	1	46.05	3.19	8.26	8.43	0.16	13.73	17.76	1.48	0.59	0.10	99.75	75.40	0.39	0.48	0.13	0.19
LP47	1010	4.02	0.38	0.74	3	47.51 (0.41)	2.15 (0.1)	5.74 (0.32)	8.2 (0.08)	0.18 (0.01)	12.79 (0.14)	22.53 (0.22)	0.55 (0.22)	0.08 (0.03)	0.03 (0.03)	99.77 (0.27)	73.55	0.38	0.48	0.14	0.21
LP32	1050	0.50	0.03	0.11	8	46.57 (0.75)	3.32 (0.34)	8.3 (0.65)	7.42 (0.27)	0.2 (0.03)	11.72 (0.67)	20.75 (0.66)	1.17 (0.15)	0.2 (0.18)	0.04 (0.03)	99.7 (0.73)	72.44	0.39	0.46	0.15	0.39
LP33	1050	0.50	0.03	0.11	6	46.89 (0.93)	2.99 (0.35)	7.22 (0.81)	7.39 (0.31)	0.18 (0.05)	12.81 (0.79)	21.14 (0.47)	1.03 (0.08)	0.07 (0.02)	0.03 (0.02)	99.75 (0.39)	75.56	0.40	0.47	0.13	0.28
LP132	1100	6.27	0.81	3.62	9	48.32 (1.34)	1.68 (0.34)	4.56 (0.96)	6.84 (0.92)	0.11 (0.06)	15.33 (0.89)	22.77 (0.29)	0.58 (0.05)	0.04 (0.03)	0.06 (0.03)	100.29 (0.47)	79.99	0.43	0.46	0.11	0.44
LP134	1100	2.54	0.21	2.46	5	45.76 (0.81)	3.31 (0.17)	9.93 (1.04)	8.1 (0.29)	0.23 (0.05)	11.43 (0.98)	18.56 (2.17)	1.45 (0.28)	0.54 (0.41)	0.02 (0)	99.3 (1.1)	71.55	0.39	0.46	0.15	0.41
LP135	1100	1.06	0.07	1.46	1	44.54	3.77	9.09	8.50	0.20	12.15	20.36	1.29	0.13	-	100.03	71.80	0.38	0.46	0.15	0.40
LP136	1100	1.57	0.11	1.90	7	45.62 (1.38)	3.23 (0.5)	9.08 (0.99)	8.38 (1.25)	0.26 (0.03)	12.15 (0.79)	19.33 (1.4)	1.47 (0.32)	0.35 (0.23)	0.08 (0.07)	99.93 (0.64)	72.11	0.40	0.45	0.15	0.36
LP174	1150	1.39	0.09	1.74	9	46.12 (0.58)	2.61 (0.22)	7.63 (0.58)	8.13 (0.35)	0.12 (0.04)	12.98 (0.38)	21.24 (0.45)	0.77 (0.11)	0.07 (0.03)	0.18 (0.09)	99.85 (0.37)	74.01	0.40	0.47	0.14	0.17
LP175	1150	2.06	0.15	2.18	8	45.95 (0.52)	2.73 (0.26)	7.77 (0.7)	8.15 (0.41)	0.13 (0.04)	12.77 (0.51)	20.91 (0.62)	0.82 (0.12)	0.12 (0.07)	0.18 (0.09)	99.53 (0.19)	73.64	0.39	0.46	0.14	0.19
LP192	1075	0.58	0.03	0.83	2	44.93 (0.52)	3.47 (0.1)	9.13 (0.36)	8.58 (0.54)	0.24 (0.04)	11.81 (0.4)	20.58 (0.85)	1.19 (0.16)	0.17 (0.07)	0.09 (0.03)	100.18 (0.46)	71.03	0.38	0.47	0.15	0.39
LP193	1075	1.65	0.12	1.95	2	44.51 (0.16)	3.65 (0.13)	9.46 (0.39)	8.13 (0.16)	0.12 (0.02)	11.74 (0.24)	21.01 (0.13)	1.1 (0.01)	0.1 (0.03)	0.04 (0.03)	99.87 (0.48)	72.03	0.37	0.48	0.15	0.38
LP194	1075	2.51	0.21	2.44	3	45.03 (0.2)	3.29 (0.09)	8.02 (0.17)	7.73 (0.24)	0.2 (0.03)	12.85 (0.21)	21.65 (0.2)	0.98 (0.06)	0.07 (0.01)	0.03 (0.04)	99.83 (0.45)	74.76	0.39	0.48	0.13	0.43
LP196	1025	0.50	0.03	0.70	5	46.29 (0.67)	3.18 (0.15)	10.46 (1.12)	8.09 (0.92)	0.19 (0.04)	11.07 (0.88)	18.28 (0.67)	1.9 (0.33)	0.59 (0.23)	0.04 (0.02)	100.08 (1.37)	70.92	0.38	0.46	0.16	0.36
LP197	1025	0.50	0.03	0.70	2	44.84 (0.4)	3.09 (0.09)	8.45 (0.08)	9.1 (0.28)	0.24 (0.06)	13.43 (0.56)	19.49 (0.39)	1.41 (0.15)	0.24 (0.07)	0.02 (0.02)	100.31 (0.38)	72.45	0.41	0.43	0.16	0.29
LP200	1125	1.65	0.12	1.93	4	45.61 (1.11)	3.01 (0.32)	8.41 (0.51)	8.13 (0.95)	0.2 (0.09)	12.46 (0.04)	21.01 (0.75)	0.98 (0.1)	0.14 (0.03)	0.05 (0.04)	100 (0.24)	73.21	0.39	0.47	0.14	0.35
LP201	1125	2.19	0.17	2.26	8	45.49 (1.2)	2.89 (0.43)	7.79 (1.2)	8.15 (0.63)	0.16 (0.04)	12.91 (0.79)	21.01 (0.57)	0.99 (0.15)	0.13 (0.11)	0.06 (0.04)	99.57 (0.47)	73.85	0.40	0.46	0.14	0.37
LP213	1050	0.71	0.04	1.06	4	45.57 (0.31)	3.23 (0.11)	8.89 (0.63)	7.66 (0.3)	0.13 (0.06)	12.24 (0.44)	19.91 (0.52)	1.61 (0.24)	0.25 (0.11)	0.05 (0.02)	99.55 (0.44)	74.01	0.40	0.46	0.14	0.34
LP214	1050	2.53	0.22	2.47	4	45.53 (0.92)	2.55 (0.24)	8.31 (1.1)	8.26 (0.51)	0.19 (0.04)	12.37 (0.38)	20.63 (1.36)	1.29 (0.25)	0.19 (0.21)	-	99.32 (0.55)	72.76	0.39	0.47	0.15	0.41
LP217	1150	0.98	0.06	1.35	1	45.42	3.14	9.26	8.63	0.13	12.00	19.55	1.13	0.37	0.18	99.82	71.26	0.39	0.45	0.16	0.43
LP218	1150	1.15	0.07	1.53	1	45.78	3.06	9.09	8.48	0.07	12.09	19.79	1.17	0.32	0.08	99.93	71.77	0.39	0.46	0.15	0.41
FC-36	1125	2.91	0.25	2.10	2	46(2.62)	5(1.45)	9(1.33)	9(1.94)	-	12.6(4)	20.50(1)	0.95(9)	0.14(6)	0.05(4)	102.75	71.54	0.39	0.46	0.15	0.38
FC-37	1125	3.64	0.35	2.38	2	46.3(5)	3.7(2)	7.5(4)	8.0(3)	0.13(4)	13.3(3)	21.47(9)	0.81(7)	0.10(6)	0.11(3)	101.44	74.77	0.40	0.46	0.14	0.39
FC-38	1125	3.82	0.37	2.44	2	47(1.04)	3.5(4)	6.9(7)	7.9(7)	0.16(4)	14.1(5)	21.6(3)	0.7(1)	-	0.08(4)	101.89	76.05	0.41	0.46	0.13	0.37

-, not determined

Mg# of Cpx is calculated as 100 x Mg/(Mg+Fe^{tot})Kd_{Ol-Liq} represents Mg/Fe partitioning between Cpx and silicate melt ($Kd_{Cpx-Liq}^{Fe-Mg} = X_{Cpx}^{Fe}/X_{Cpx}^{Mg} \times X_{Liq}^{Fe}/X_{Liq}^{Mg}$)

Table 19. Compositions of experimental clinopyroxenes using starting composition KLA-1-6-22 at 550 MPa

Run	T [°C]	melt H ₂ O [wt%]	α H ₂ O	Δ FMQ	n	SiO ₂	TiO ₂	Al ₂ O ₃	FeO	MnO	MgO	CaO	Na ₂ O	K ₂ O	Cr ₂ O ₃	Total	Mg#	En	Wo	Fs	Kd _{Cpx-liq}
FC-1	1175	5.41	0.45	2.61	3	45.7(6)	1.9(2)	6.9(2)	6.4(2)	0.05(1)	13.07(6)	20.47(5)	0.8(1)	0.05(1)	0.53(9)	95.86	78.55	0.42	0.47	0.11	0.36
FC-2	1175	1.50	0.08	1.11	3	46.7(2)	2.1(2)	7.4(5)	7.2(2)	0.07(2)	13.4(6)	21.3(2)	0.81(3)	0.06(6)	0.3(1)	99.37	76.71	0.41	0.47	0.12	0.36
FC-3	1175	1.71	0.10	1.26	3	47(1.1)	2.2(3)	7.3(6)	7.7(7)	0.07(2)	13.3(5)	21.1(2)	0.80(2)	0.06(3)	0.2(2)	99.39	75.42	0.41	0.46	0.13	0.40
FC-7	1150	4.07	0.30	2.26	8	44(1.15)	2.2(3)	7.6(4)	6.4(6)	0.04(1)	12.6(5)	18.2(6)	0.9(1)	0.12(6)	0.3(1)	92.22	77.76	0.43	0.45	0.12	0.33
FC-8	1150	1.82	0.10	1.33	5	46.8(7)	2.1(2)	7.1(6)	6.3(4)	0.03(1)	13.4(5)	20.3(1)	0.76(7)	0.07(5)	0.49(8)	97.31	79.10	0.43	0.46	0.11	0.29
FC-9	1150	2.42	0.15	1.65	5	46.0(6)	2.3(2)	7.4(4)	7.3(9)	0.04(1)	13.3(3)	20.2(4)	0.75(9)	0.05(1)	0.2(2)	97.71	76.38	0.42	0.46	0.13	0.35
FC-42	1125	3.19	0.22	1.98	3	45.7(5)	4.7(4)	9.6(3)	8.1(2)	0.17(6)	12.5(3)	20.3(2)	1.09(9)	0.12(8)	0.10(3)	102.29	73.38	0.39	0.46	0.14	0.35
FC-43	1125	4.20	0.32	2.31	5	47(1.53)	3.7(6)	7.3(9)	7.9(8)	0.13(5)	13.9(9)	21.0(4)	0.9(1)	0.08(7)	0.08(3)	102.03	75.73	0.42	0.45	0.13	0.41
FC-45	1075	4.81	0.40	3.00	4	49(2.28)	1.7(6)	4(1.82)	6(1.07)	0.14(5)	15(1.37)	22.8(2)	0.5(1)	-	0.06(4)	100.73	81.25	0.44	0.46	0.10	0.39
FC-46	1075	5.25	0.45	3.11	2	49(1.54)	1.6(4)	4(1.39)	6.3(9)	0.07(6)	15(1.07)	22.7(1)	0.6(2)	0.05(3)	-	100.43	81.20	0.43	0.47	0.10	0.37
FC-47	1075	6.49	0.62	3.39	6	50(1.84)	1.3(4)	4(1.19)	5.9(9)	0.11(4)	16(1.02)	22.9(1)	0.47(5)	-	0.05(3)	100.32	82.67	0.44	0.46	0.09	0.35

-, not determined

Mg# of Cpx is calculated as $100 \times \text{Mg}/(\text{Mg}+\text{Fe}^{\text{tot}})$ Kd_{Ol-Liq} represents Mg/Fe partitioning between Cpx and silicate melt ($\text{Kd}_{\text{Cpx-Liq}}^{\text{Fe-Mg}} = X_{\text{Cpx}}^{\text{Fe}} / X_{\text{Cpx}}^{\text{Mg}} \times X_{\text{Liq}}^{\text{Fe}} / X_{\text{Liq}}^{\text{Mg}}$)

Table 20. Compositions of experimental clinopyroxenes using starting composition KLA-1-6-22 at 700 MPa

Run	T [°C]	melt H ₂ O [wt%]	α H ₂ O	ΔFMQ	n	SiO ₂	TiO ₂	Al ₂ O ₃	FeO	MnO	MgO	CaO	Na ₂ O	K ₂ O	Cr ₂ O ₃	Total	Mg#	En	Wo	Fs	K _{Cpx-Liq}
LP63	1050	7.62	0.64	3.41	6	48.57 (0.37)	1.46 (0.1)	4.38 (0.37)	6.03 (0.41)	0.07 (0.05)	15.55 (0.39)	23.37 (0.11)	0.45 (0.12)	0.01 (0)	0.06 (0.02)	99.95 (0.4)	82.13	0.44	0.47	0.09	0.36
LP65	1050	7.07	0.57	3.31	7	48.2 (0.78)	1.53 (0.11)	4.98 (0.8)	6.72 (0.4)	0.12 (0.04)	15.37 (0.95)	22.66 (0.45)	0.65 (0.18)	0.03 (0.02)	0.05 (0.02)	100.31 (0.76)	80.30	0.43	0.46	0.11	0.40
LP67	1050	2.36	0.13	2.02	7	45.89 (1.14)	1.86 (0.14)	7.85 (0.5)	8.68 (0.56)	0.21 (0.01)	11.87 (0.61)	20.39 (0.84)	1.78 (0.78)	0.1 (0.08)	0.07 (0.02)	98.69 (1.87)	70.91	0.38	0.47	0.16	0.33
LP70	1075	8.57	0.75	3.55	9	50.86 (0.41)	1.04 (0.04)	3.28 (0.23)	5.46 (0.24)	0.1 (0.03)	16.33 (0.51)	22.72 (0.21)	1.61 (1.16)	0.02 (0.01)	0.06 (0.05)	101.48 (1.33)	78.83	0.42	0.47	0.11	0.46
LP71	1075	7.00	0.55	3.29	3	50.16 (0.4)	1.09 (0.12)	3.87 (0.32)	5.91 (0.01)	0.11 (0.02)	15.5 (0.31)	22.31 (0.31)	0.86 (0.14)	0.02 (0)	0.01 (0.02)	99.84 (0.64)	75.58	0.40	0.47	0.13	0.47
LP72	1075	1.94	0.10	1.80	9	45.82 (0.81)	2.1 (0.15)	7.92 (0.41)	8.41 (0.43)	0.17 (0.03)	12.56 (0.62)	20.84 (0.47)	0.96 (0.64)	0.09 (0.1)	0.06 (0.04)	98.93 (1.43)	72.71	0.39	0.46	0.15	0.39
LP76	1100	5.81	0.42	3.05	22	49.52 (1.05)	1.44 (0.24)	4.33 (0.9)	6.42 (0.55)	0.12 (0.04)	15.2 (0.84)	22.24 (0.51)	0.75 (0.17)	0.04 (0.01)	0.07 (0.03)	100.11 (0.62)	75.46	0.40	0.47	0.13	0.51
LP77	1100	4.26	0.27	2.67	7	46.7 (0.47)	2.31 (0.17)	7.43 (0.35)	7.6 (0.27)	0.12 (0.05)	13.39 (0.35)	20.84 (0.35)	1.34 (0.2)	0.06 (0.02)	0.05 (0.04)	99.85 (0.36)	74.48	0.41	0.45	0.14	0.44
LP82	1150	7.79	0.63	3.40	9	47.45 (1.29)	1.95 (0.38)	6.77 (0.96)	8.02 (0.69)	0.21 (0.07)	14.05 (0.73)	21.09 (0.38)	0.87 (0.11)	0.03 (0.01)	0.07 (0.04)	100.52 (0.52)	75.74	0.42	0.45	0.13	0.43
LP84	1150	7.90	0.64	3.41	10	47.51 (0.74)	1.89 (0.21)	6.81 (0.9)	8.01 (0.34)	0.2 (0.07)	13.9 (0.71)	21.08 (1.14)	0.89 (0.13)	0.09 (0.17)	0.08 (0.03)	100.46 (0.78)	75.57	0.41	0.45	0.13	0.43
LP150	1150	0.50	0.02	0.39	10	45.03 (0.39)	3.22 (0.11)	9.12 (0.22)	8.81 (0.38)	0.18 (0.05)	12.46 (0.23)	19.44 (0.28)	1.38 (0.06)	0.06 (0.02)	0.05 (0.04)	99.74 (0.34)	71.60	0.40	0.45	0.16	0.32
LP151	1150	1.49	0.07	1.50	10	45.47 (0.7)	2.8 (0.26)	8.94 (0.48)	8.61 (0.41)	0.21 (0.06)	12.62 (0.4)	19.31 (0.89)	1.35 (0.2)	0.17 (0.15)	0.08 (0.03)	99.55 (0.37)	72.31	0.40	0.44	0.15	0.41
LP152	1150	1.53	0.07	1.53	8	45.62 (0.41)	2.74 (0.2)	8.64 (0.25)	8.53 (0.25)	0.19 (0.05)	12.72 (0.22)	20.29 (0.43)	1.2 (0.08)	0.06 (0.02)	0.09 (0.05)	100.08 (0.44)	72.65	0.40	0.45	0.15	0.42

-, not determined

Mg# of Cpx is calculated as $100 \times \text{Mg}/(\text{Mg}+\text{Fe}^{\text{tot}})$

$$\text{Kd}_{\text{Ol-Liq}}^{\text{Fe-Mg}} = X_{\text{Cpx}}^{\text{Fe}} / (X_{\text{Cpx}}^{\text{Mg}} \times X_{\text{Liq}}^{\text{Fe}} / X_{\text{Liq}}^{\text{Mg}})$$

4.3.3 Amphibole

Compositional variations of experimentally synthesized amphiboles are listed in Tables 21-22. For both starting compositions we observed very similar compositional changes, e.g., an increase of TiO_2 and Al_2O_3 contents with increasing temperature. TiO_2 content is also affected by the prevailing $f\text{O}_2$ condition. Highest TiO_2 contents (kaersutitic amphiboles) were observed at reducing conditions and whereas the low TiO_2 contents (magnesiohastingsitic amphibole) were observed at oxidizing conditions. Using the primitive basanite as starting material the TiO_2 content ranges between 5.77 to 1.89 wt.% (Figure 31) and between 7.82 to 2.71 wt.% using the evolved basanite as starting composition (Figure 32). This variation in TiO_2 content at oxidizing condition can be explained by high proportion of titanomagnetite in the solid phase at oxidizing conditions and low temperatures. CaO and Na_2O contents are almost constant and no remark can be made for outliers, due to unsystematic variation of these particular oxides in experimental amphiboles.

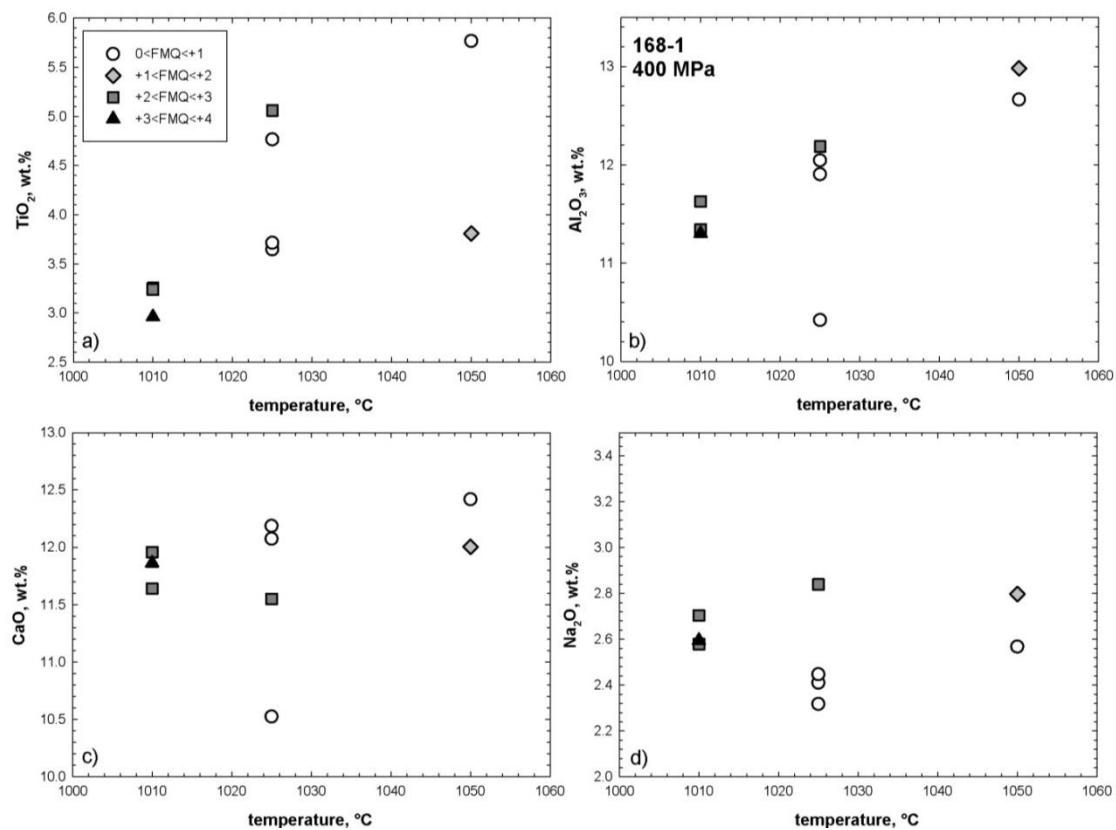


Figure 31: Effect of redox conditions and temperature ($^{\circ}\text{C}$) on amphibole composition using starting composition 168-1 at 400 MPa.

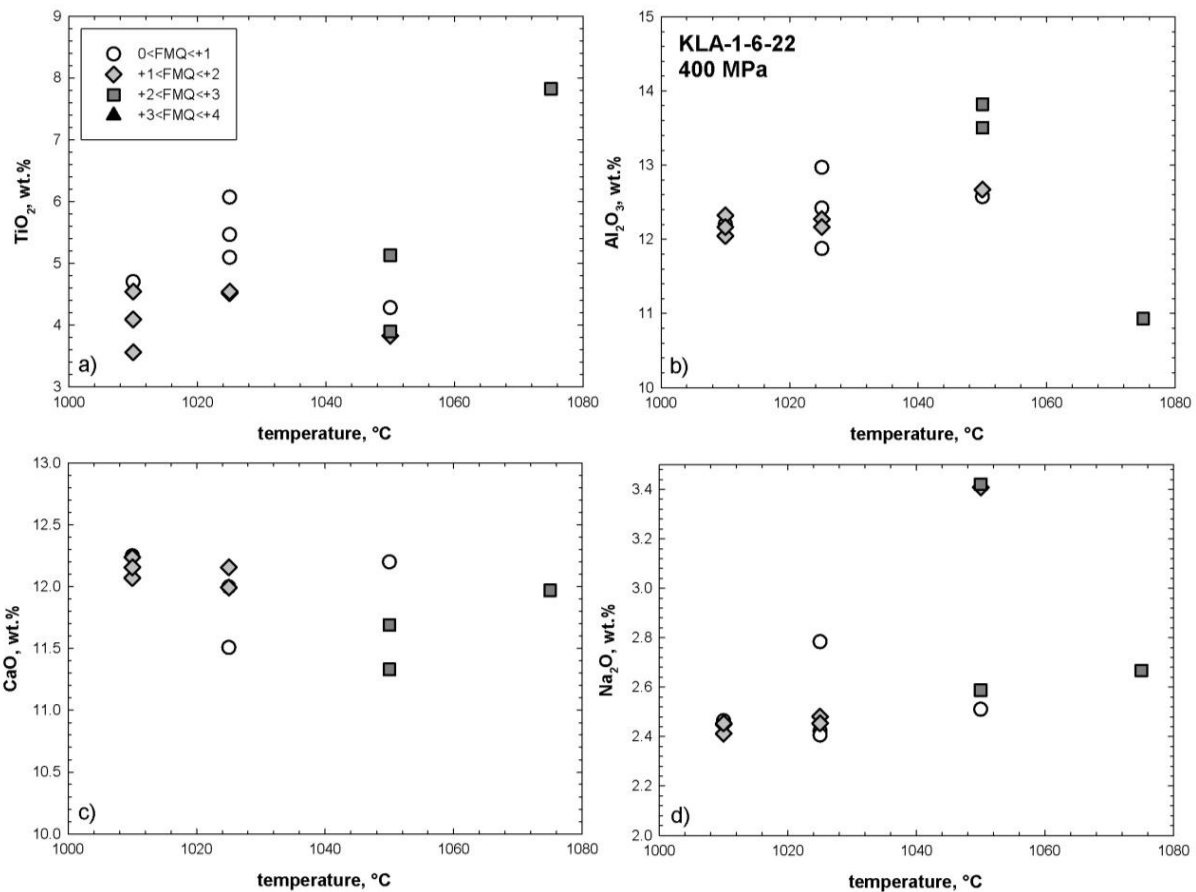


Figure 32: Effect of redox conditions and temperature ($^{\circ}\text{C}$) on amphibole composition using starting composition KLA-1-6-22 at 400 MPa.

4.3.4 Plagioclase

Only in four experimental runs we observed plagioclase crystals large enough to be measured by electron microprobe. Their average compositions are reported in Table 23. Anorthite contents vary from 39.7 to 45.8. Due to the limited dataset conclusions on the roles of thermodynamic dependencies on PI compositions cannot be evaluated.

Table 21. Compositions of experimental amphiboles using starting composition 168-1 at 400 and 700 MPa

Run	Pressure [MPa]	T [°C]	melt H ₂ O [wt%]	α H ₂ O	Δ FMQ	n	SiO ₂	TiO ₂	Al ₂ O ₃	FeO	MnO	MgO	CaO	Na ₂ O	K ₂ O	Cr ₂ O ₃	Total	Mg#
LP53	4000	1010	9.77	1.58	3.08	5	43.04 (0.61)	2.96 (0.25)	11.3 (0.54)	8.13 (0.18)	0.16 (0.02)	16.75 (0.49)	11.86 (0.4)	2.59 (0.07)	0.94 (0.09)	-	97.73	78.59
LP54	4000	1010	8.71	1.30	2.91	5	42.45 (0.18)	3.25 (0.1)	11.34 (0.12)	8.56 (0.2)	0.13 (0.07)	16.25 (0.21)	11.96 (0.17)	2.58 (0.08)	0.96 (0.02)	-	97.48	77.19
LP55	4000	1010	8.33	1.21	2.84	5	42.19 (0.51)	3.24 (0.21)	11.63 (0.11)	9.28 (0.4)	0.15 (0.06)	16.1 (0.16)	11.64 (0.08)	2.7 (0.07)	0.9 (0.03)	-	97.84	75.56
LP35	4000	1025	6.62	0.83	0.91	4	41.58 (0.4)	3.65 (0.26)	11.9 (0.41)	8.64 (0.84)	0.06 (0.04)	16.35 (0.64)	12.19 (0.16)	2.41 (0.14)	1.15 (0.04)	-	97.92	77.13
LP36	4000	1025	5.59	0.63	0.68	9	41.8 (0.67)	3.71 (0.14)	12.04 (0.49)	9.32 (0.72)	0.12 (0.03)	15.02 (1.06)	12.07 (0.39)	2.45 (0.13)	1.07 (0.05)	-	97.61	74.18
LP30	4000	1050	0.50	0.03	0.11	9	40.72 (0.59)	5.77 (0.3)	12.66 (0.41)	8.74 (0.36)	0.14 (0.04)	14.8 (0.45)	12.42 (0.7)	2.57 (0.17)	0.81 (0.06)	-	98.63	75.11
LP188	4000	1050	1.13	0.07	1.55	5	40.83 (0.45)	3.81 (0.2)	12.98 (0.24)	8.35 (0.1)	0.09 (0.04)	16.27 (0.27)	12 (0.24)	2.8 (0.06)	0.93 (0.03)	0.03 (0.03)	98.06	77.64
LP86	7000	1050	12.44	1.36	4.07	10	42.91 (0.56)	1.89 (0.13)	12.79 (0.33)	7.99 (0.14)	0.16 (0.05)	17.85 (0.16)	12.16 (0.26)	2.75 (0.04)	1.07 (0.07)	0.07 (0.05)	99.58	79.93
LP87	7000	1050	12.45	1.36	4.07	10	43.3 (0.53)	2.02 (0.2)	12.15 (0.4)	8.25 (0.29)	0.19 (0.03)	18.06 (0.15)	11.95 (0.24)	2.71 (0.08)	1.05 (0.05)	0.1 (0.04)	99.67	79.60
LP88	7000	1050	12.12	1.30	4.03	10	42.58 (0.59)	2.51 (0.25)	12.57 (0.18)	8.75 (0.69)	0.2 (0.04)	17.47 (0.27)	11.59 (0.25)	2.86 (0.13)	1 (0.05)	0.07 (0.04)	99.52	78.07
LP89	7000	1050	7.40	0.61	3.37	6	42.66 (0.51)	3.13 (0.07)	12.78 (0.35)	9.45 (0.4)	0.17 (0.07)	16.34 (0.12)	11.08 (0.29)	2.96 (0.12)	0.95 (0.04)	0.04 (0.03)	99.54	75.50
LP99	7000	1100	7.05	0.55	3.29	4	41.05 (0.29)	4.27 (0.09)	14.26 (0.15)	9.13 (0.24)	0.14 (0.04)	15.87 (0.29)	11.54 (0.26)	2.94 (0.08)	1.11 (0.04)	0.04 (0.06)	100.30	75.60
LP102	7000	1100	5.07	0.34	2.88	1	43.97	3.92	16.64	10.39	0.34	7.72	8.59	2.38	1.42	-	95.36	56.98
LP103	7000	1100	5.66	0.40	3.01	1	43.42	3.27	14.81	10.43	0.29	9.45	10.32	2.48	0.79	0.05	95.32	61.77
LP104	7000	1100	5.62	0.40	3.00	1	40.31	3.70	13.80	11.36	0.23	13.03	10.47	3.08	1.07	0.05	97.10	67.16

-, not determined

Mg# of Amph is calculated as $100 \times \text{Mg}/(\text{Mg}+\text{Fe}^{\text{tot}})$ **Table 22.** Compositions of experimental amphiboles using starting composition 168-1 at 400 and 700 MPa

Run	Pressure [MPa]	T [°C]	melt H ₂ O [wt%]	α H ₂ O	Δ FMQ	n	SiO ₂	TiO ₂	Al ₂ O ₃	FeO	MnO	MgO	CaO	Na ₂ O	K ₂ O	Cr ₂ O ₃	Total	Mg#
LP44	4000	1010	6.32	0.77	1.35	10	41.24 (0.52)	3.56 (0.2)	12.05 (0.38)	8.76 (0.55)	0.12 (0.03)	16.13 (0.93)	12.24 (0.26)	2.45 (0.12)	1.21 (0.09)	-	97.74	76.64
LP45	4000	1010	6.39	0.78	1.36	8	40.9 (0.45)	4.09 (0.28)	12.32 (0.22)	9.56 (0.4)	0.13 (0.07)	14.74 (1.13)	12.07 (0.22)	2.41 (0.07)	1.26 (0.11)	-	97.49	73.31
LP46	4000	1010	5.44	0.61	1.14	11	40.92 (0.38)	4.54 (0.16)	12.17 (0.35)	10.28 (0.39)	0.14 (0.02)	13.78 (0.63)	12.16 (0.22)	2.45 (0.14)	1.26 (0.04)	-	97.70	70.51
LP47	4000	1010	4.02	0.38	0.74	9	40.75 (0.59)	4.7 (0.21)	12.2 (0.33)	10.72 (0.65)	0.15 (0.05)	13.13 (0.6)	12.25 (0.58)	2.46 (0.14)	1.19 (0.06)	-	97.56	68.58
LP38	4000	1025	4.34	0.43	0.94	6	40.59 (0.21)	5.09 (0.13)	12.42 (0.27)	10.83 (0.44)	0.18 (0.03)	12.9 (0.88)	12 (0.27)	2.42 (0.15)	1.11 (0.05)	-	97.55	67.97
LP39	4000	1025	5.86	0.68	1.34	8	40.86 (0.35)	4.52 (0.3)	12.27 (0.26)	9.96 (0.49)	0.12 (0.05)	14 (1.02)	11.99 (0.14)	2.48 (0.08)	1.22 (0.06)	-	97.42	71.47
LP15	4000	1050	4.86	0.51	0.07	5	41.11 (0.45)	4.28 (0.19)	12.57 (0.62)	10.28 (0.74)	0.13 (0.03)	15.32 (0.54)	12.2 (0.6)	2.51 (0.09)	1.1 (0.07)	-	99.52	72.64
LP194	4000	1075	2.51	0.21	2.44	1	40.07 (0.33)	7.82 (3.75)	10.93 (3.91)	8.76 (0.1)	0.11 (0.04)	14.59 (0.2)	11.97 (0.07)	2.67 (0.05)	1.19 (0.06)	0.04 (0.04)	98.09	74.81
LP65	7000	1050	7.07	0.57	3.31	5	41.32 (0.44)	2.71 (0.22)	13.16 (0.19)	8.84 (0.13)	0.15 (0.04)	17.03 (0.79)	12.04 (0.11)	2.6 (0.14)	1.33 (0.04)	0.06 (0.01)	99.17	77.45
LP67	7000	1050	2.36	0.13	2.02	4	40.56 (0.43)	3.9 (0.04)	13.82 (0.26)	11.17 (0.35)	0.21 (0.06)	13.98 (0.08)	11.69 (0.26)	2.59 (0.32)	1.22 (0.02)	0.06 (0.05)	99.13	69.05
LP71	7000	1075	7.00	0.55	3.29	6	41.44 (0.37)	3.22 (0.09)	13.49 (0.25)	8.75 (0.18)	0.14 (0.06)	16.52 (0.34)	11.99 (0.1)	2.68 (0.25)	1.35 (0.02)	0.05 (0.03)	99.60	77.09
LP72	7000	1075	1.94	0.10	1.80	5	40.94 (0.57)	4.23 (0.33)	13.49 (0.42)	10.03 (0.29)	0.16 (0.07)	14.89 (0.47)	12.17 (0.41)	2.45 (0.56)	1.21 (0.08)	0.09 (0.02)	99.56	72.58

-, not determined

Mg# of Amph is calculated as $100 \times \text{Mg}/(\text{Mg}+\text{Fe}^{\text{tot}})$

Table 23. Compositions of experimental plagioclase

Run	Starting composition	Pressure [MPa]	T [°C]	melt H ₂ O [wt%]	<i>a</i> H ₂ O	DFMQ	<i>n</i>	SiO ₂	TiO ₂	Al ₂ O ₃	FeO	MnO	MgO	CaO	Na ₂ O	K ₂ O	Total	An	Or	Ab
LP188	168-1	4000	1050	1.13	0.07	1.55	3	55.29 (0.92)	0.72 (0.46)	24.31 (2.21)	2.35 (1.13)	0.07 (0.02)	1.35 (0.98)	7.97 (1.61)	5.91 (0.16)	1.2 (0.66)	99.15	39.65	7.13	53.22
LP190	168-1	4000	1075	0.90	0.06	1.29	3	55.07 (0.45)	0.41 (0.05)	26.03 (0.49)	1.6 (0.24)	0.03 (0.01)	1.07 (0.36)	9.05 (0.58)	5.45 (0.2)	0.71 (0.09)	99.42	45.8	4.26	49.95
LP32	KLA-1-6-22	4000	1050	0.50	0.03	0.11	6	54.77 (0.49)	1.19 (0.43)	25.5 (0.57)	1.75 (0.45)	0.03 (0.04)	0.29 (0.37)	8.81 (0.24)	5.32 (0.08)	1.23 (0.1)	98.92	44.25	7.36	48.39
LP213	KLA-1-6-22	4000	1050	0.71	0.04	1.06	4	54.66 (0.77)	0.61 (0.2)	25.85 (0.66)	1.54 (0.75)	0.07 (0.04)	0.52 (0.28)	8.46 (0.76)	5.24 (0.18)	1.6 (0.22)	98.54	42.61	9.59	47.8

An is anorthite content calculated as Ca/(Ca+Na+K)

Or is orthoclase content calculated as K/(Ca+Na+K)

Ab is albite content calculated as Na/(Ca+Na+K)

4.3.5 Spinel

The compositions of spinel, recalculated following Stormer (1983), are listed in Tables 24-28 and shown in Figures 33-37. Compositions vary from Cr-spinel to titanomagnetite as a function of redox conditions, H₂O activity and temperature. Cr-rich spinel was observed only in runs with high H₂O activity ($a_{H_2O} > 0.5$) and low redox conditions ($0 < FMQ < +1$) in equilibrium with melt and olivine. At lower H₂O activities and higher redox conditions cpx joins the phase assemblage, which also incorporates chromium, which in turn lowers the Cr/[Cr+Al] (Cr#) in spinel. In 168-1 basanite at 400 MPa, an increase in Cr# from 0.03 to ~0.21 with increasing temperature and H₂O activity can be observed (Figure 33). Higher Cr# (0.49-0.64) were observed in experiments at more reducing conditions (FMQ<+1), high H₂O activities ($a_{H_2O} > 0.5$) and spinels in equilibrium with olivine and melt. The spinel Mg# decreases as a function of temperature and decreasing H₂O content (e.g. from 0.71 to 0.23 at H₂O activities between 0.75 and 1; and from 0.64-0.20 at H₂O activities between 0.50 and 0.749), this decrease is related to the decreasing Mg# in the coexisting melt. The Fe³⁺/(Fe³⁺+Al+Cr) (Fe³⁺#) increases with decreasing temperature, increasing H₂O activity and as a function of redox conditions, e.g. at nominally dry conditions and redox conditions below FMQ+2 a decrease from 0.84 to 0.63 can be observed, which is in contrast to experiments conducted at comparable redox conditions and high H₂O activities, here the Fe³⁺# is lowered to 0.55-0.49 at 1050°C. The TiO₂ content increases with decreasing temperature as function of redox conditions and H₂O activity, e.g. in the temperature from 1150 to 1025°C at nominally dry conditions and redox conditions below FMQ+2 from 7.08 to 12.53 wt.%.

In the experimental series at 700 MPa using the same starting composition (168-1) (see Figure 34), Cr# increases from 0.04 to ~0.19 with increasing temperature and H₂O activity. The Mg# decreases as a function of temperature and decreasing H₂O content from 0.61 to 0.17 equivalent to the decreasing Mg# in the melt. The Fe³⁺# increases with decreasing temperature and increasing H₂O activity as a function of redox conditions from 0.68-0.93. The TiO₂ content increases with decreasing temperature as function of redox conditions and H₂O activity from 2.79 to 18.15 wt.%.

In using starting composition KLA-1-6-22 at 400 MPa, the Cr# increases from 0.01 to ~0.41 with increasing temperature and H₂O activity (Figure 35). Higher Cr# (0.62) were observed in

experiments with high H₂O activities ($a_{H_2O}>0.75$) and spinels in equilibrium with olivine and melt. The Mg# decreases as a function of temperature and decreasing H₂O content (e.g. from 0.49 to 0.26 at nominally dry conditions. The Fe³⁺# increases with decreasing temperature, increasing H₂O activity and as a function of redox conditions from 0.51 to 0.87. The TiO₂ content systematically increases with decreasing temperature as function of redox conditions and H₂O activity from 2.46-18.95 wt.%.

In the experimental series at 550 MPa using the same starting composition (KLA-1-6-22) experiments were conducted in the stability field of ol+cpx+spl+liq in the temperature range from 1100 to 1175°C. The Cr# decreases from 0.30 to 0.04 as a function of cpx proportion (Figure 36). The Mg# (slightly decreases as a function of temperature and decreasing H₂O content from 0.34 to 0.51. The Fe³⁺# increases with decreasing temperature, increasing H₂O activity and as a function of redox conditions from 0.42 to 0.81. The TiO₂ content increases with decreasing temperature as function of redox conditions and H₂O activity from 4.77-11.59 wt.%. At 700 MPa using starting composition KLA-1-6-22, the Cr# increases from 0.01 to ~0.41 with increasing temperature and H₂O activity (Figure 37). Higher Cr# (0.62) were observed in experiments with high H₂O activities ($a_{H_2O}>0.75$) and spinels in equilibrium with olivine and melt. The Mg# decreases as a function of temperature and decreasing H₂O content (e.g. from 0.49 to 0.26 at nominally dry conditions. The Fe³⁺# increases with decreasing temperature, increasing H₂O activity and as a function of redox conditions from 0.51 to 0.87. The TiO₂ content increases with decreasing temperature as function of redox conditions and H₂O activity from 5.10-25.93 wt.%. In the experimental series at 700 MPa, general observations are the same, but the transitions from spinel to titanomagnetite seems to be more distinct. At higher pressures the solidus is shifted to higher temperatures, which shifts the transition of spinel to titanomagnetite between 1075 and 1100°C.

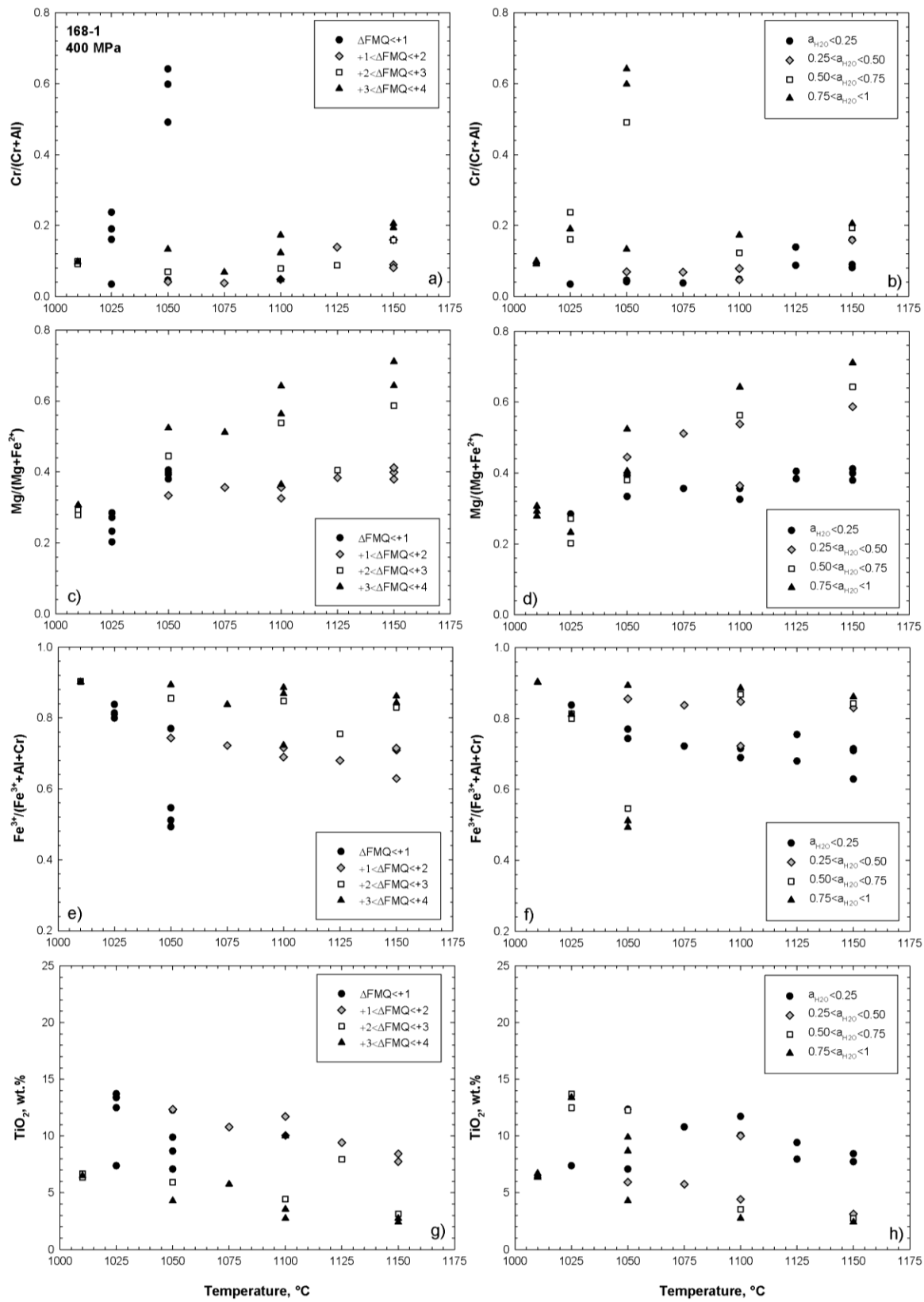


Figure 33: Variations of spinel composition as a function of temperature (°C), redox conditions and H_2O activity for sample 168-1 equilibrated at 400 MPa. (a), (b) $\text{Cr}/(\text{Cr}+\text{Al})$; (c), (d) $\text{Mg}/(\text{Mg}+\text{Fe}^{2+})$; (e), (f) $\text{Fe}^{3+}/(\text{Fe}^{3+}+\text{Al}+\text{Cr})$; (g), (h) TiO_2 (wt.%).

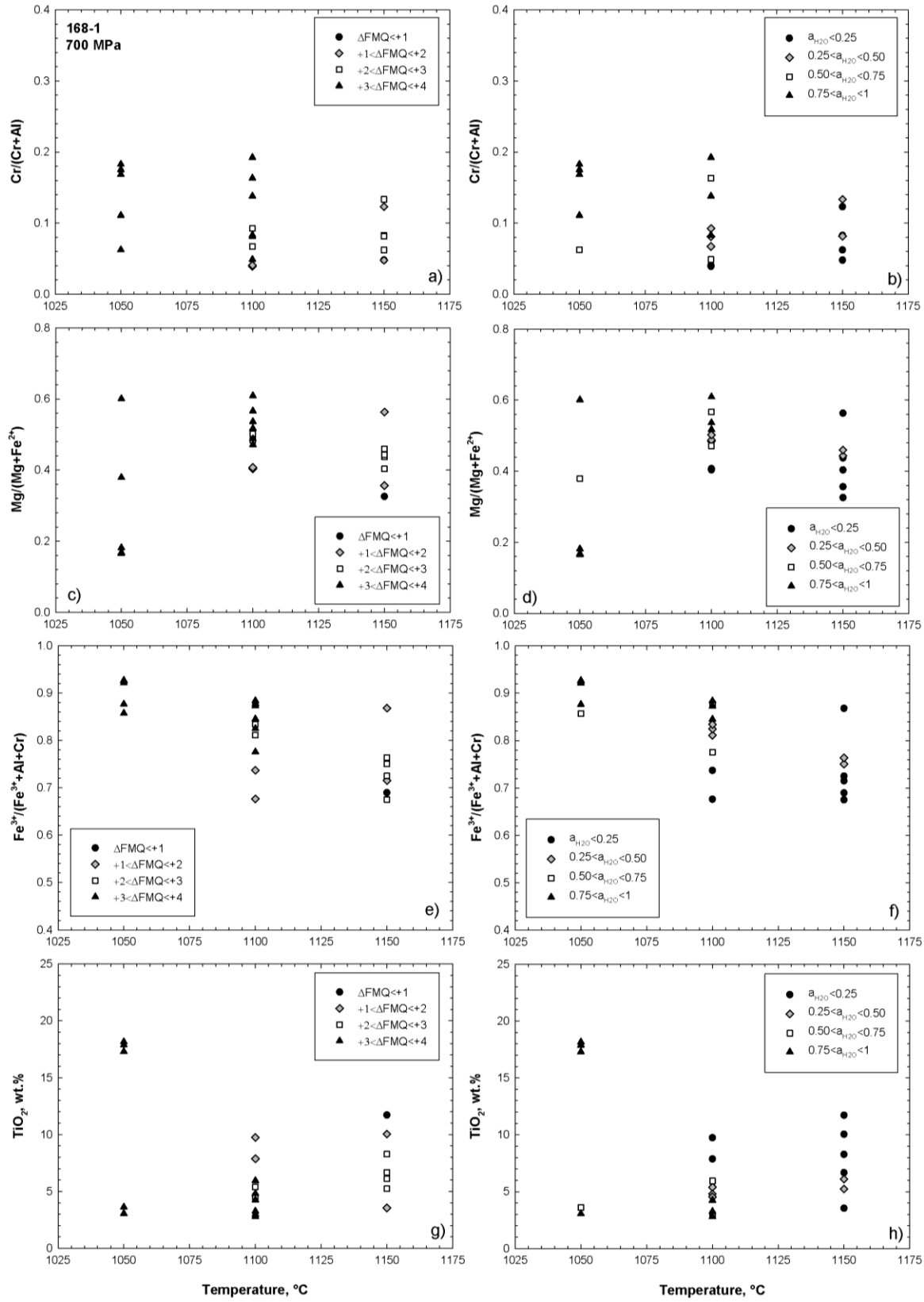


Figure 34: Variations of spinel composition as a function of temperature ($^{\circ}\text{C}$), redox conditions and H_2O activity for sample 168-1 equilibrated at 700 MPa. (a), (b) $\text{Cr}/(\text{Cr}+\text{Al})$; (c), (d) $\text{Mg}/(\text{Mg}+\text{Fe}^{2+})$; (e), (f) $\text{Fe}^{3+}/(\text{Fe}^{3+}+\text{Al}+\text{Cr})$; (g), (h) TiO_2 (wt.%).

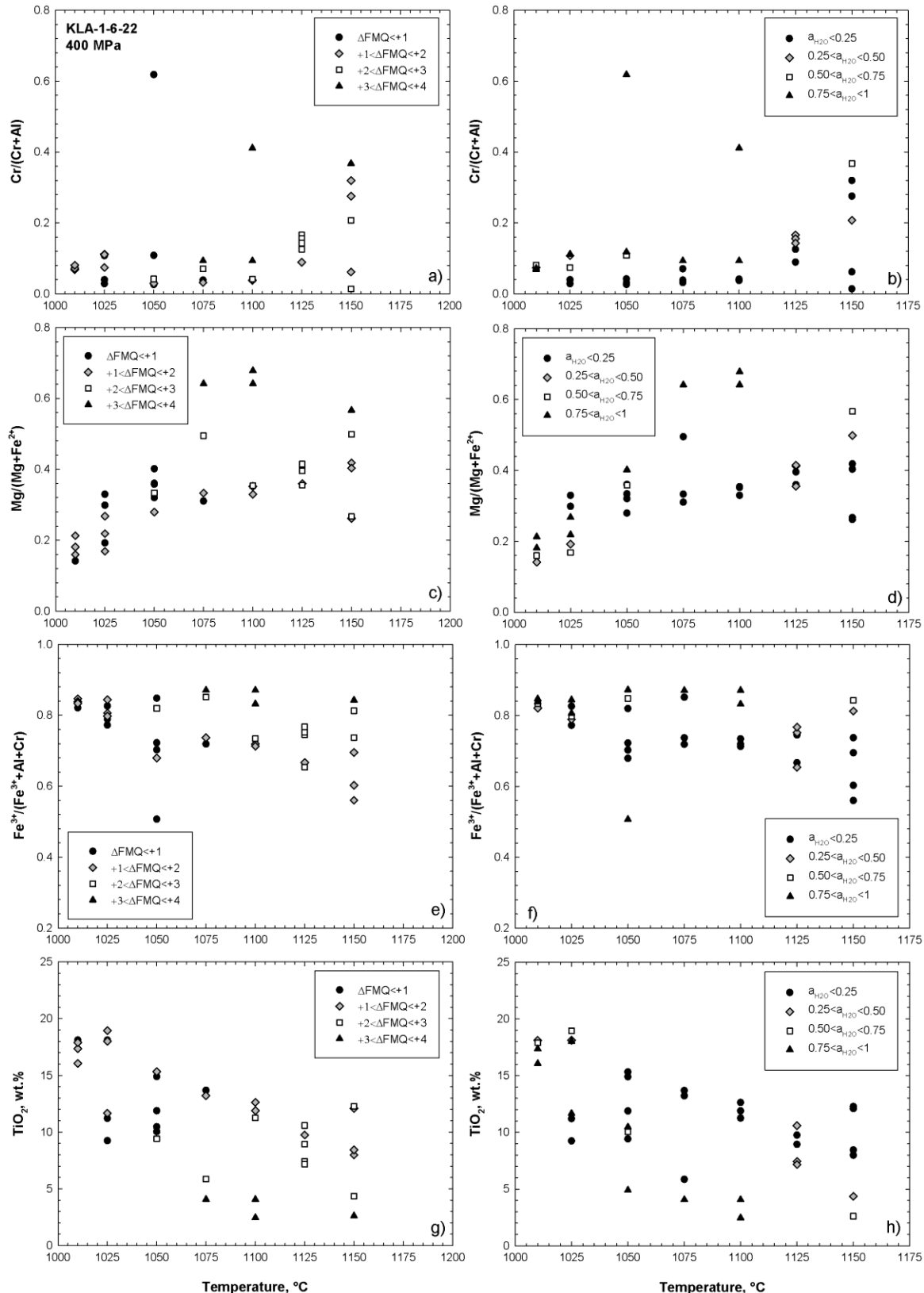


Figure 35: Variations of spinel composition as a function of temperature (°C), redox conditions and H_2O activity for sample KLA-1-6-22 equilibrated at 400 MPa. (a), (b) $\text{Cr}/(\text{Cr}+\text{Al})$; (c), (d) $\text{Mg}/(\text{Mg}+\text{Fe}^{2+})$; (e), (f) $\text{Fe}^{3+}/(\text{Fe}^{3+}+\text{Al}+\text{Cr})$; (g), (h) TiO_2 (wt.%).

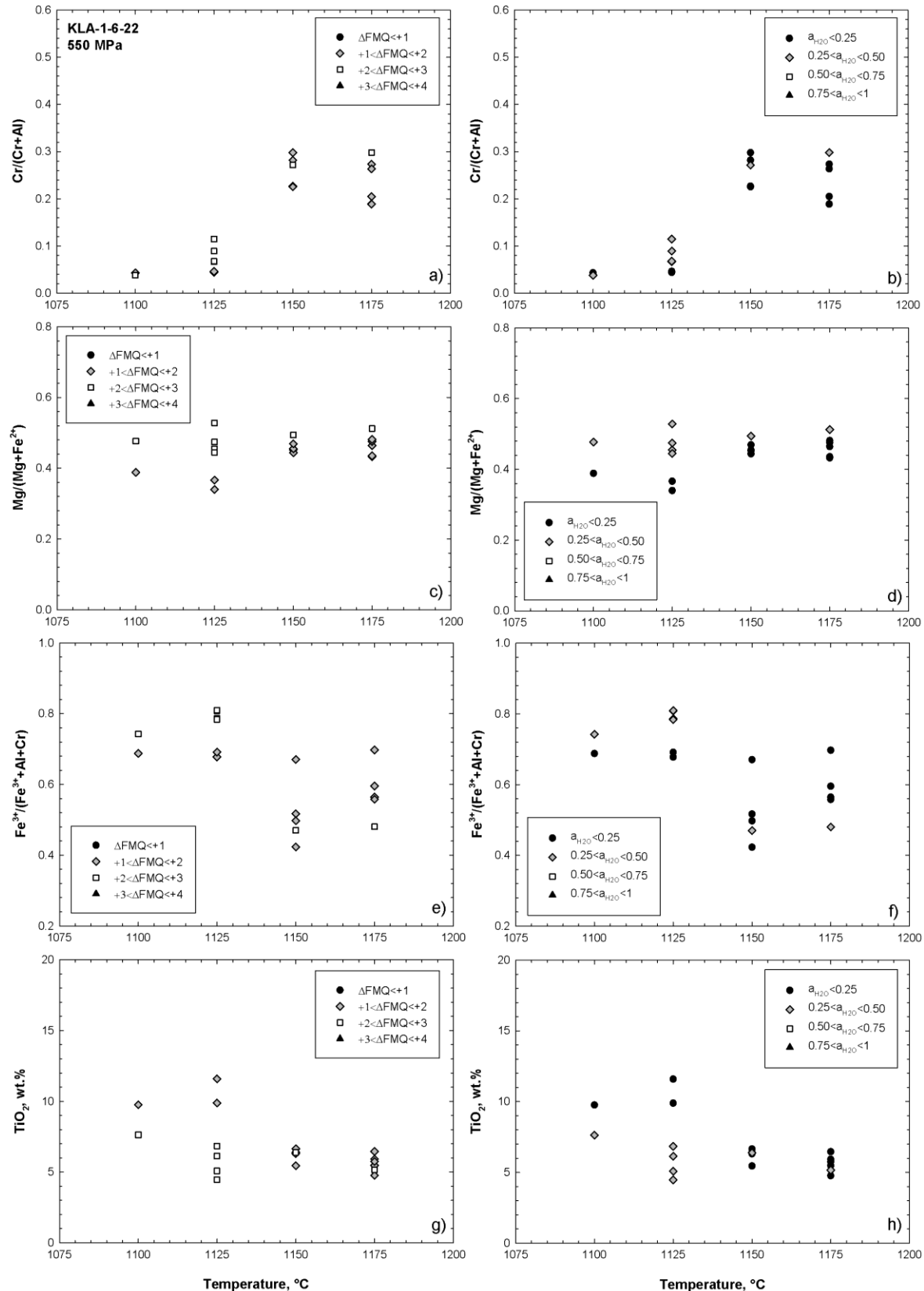


Figure 36: Variations of spinel composition as a function of temperature ($^{\circ}\text{C}$), redox conditions and H_2O activity for sample KLA-1-6-22 equilibrated at 550 MPa. (a), (b) $\text{Cr}/(\text{Cr}+\text{Al})$; (c), (d) $\text{Mg}/(\text{Mg}+\text{Fe}^{2+})$; (e), (f) $\text{Fe}^{3+}/(\text{Fe}^{3+}+\text{Al}+\text{Cr})$; (g), (h) TiO_2 (wt.%).

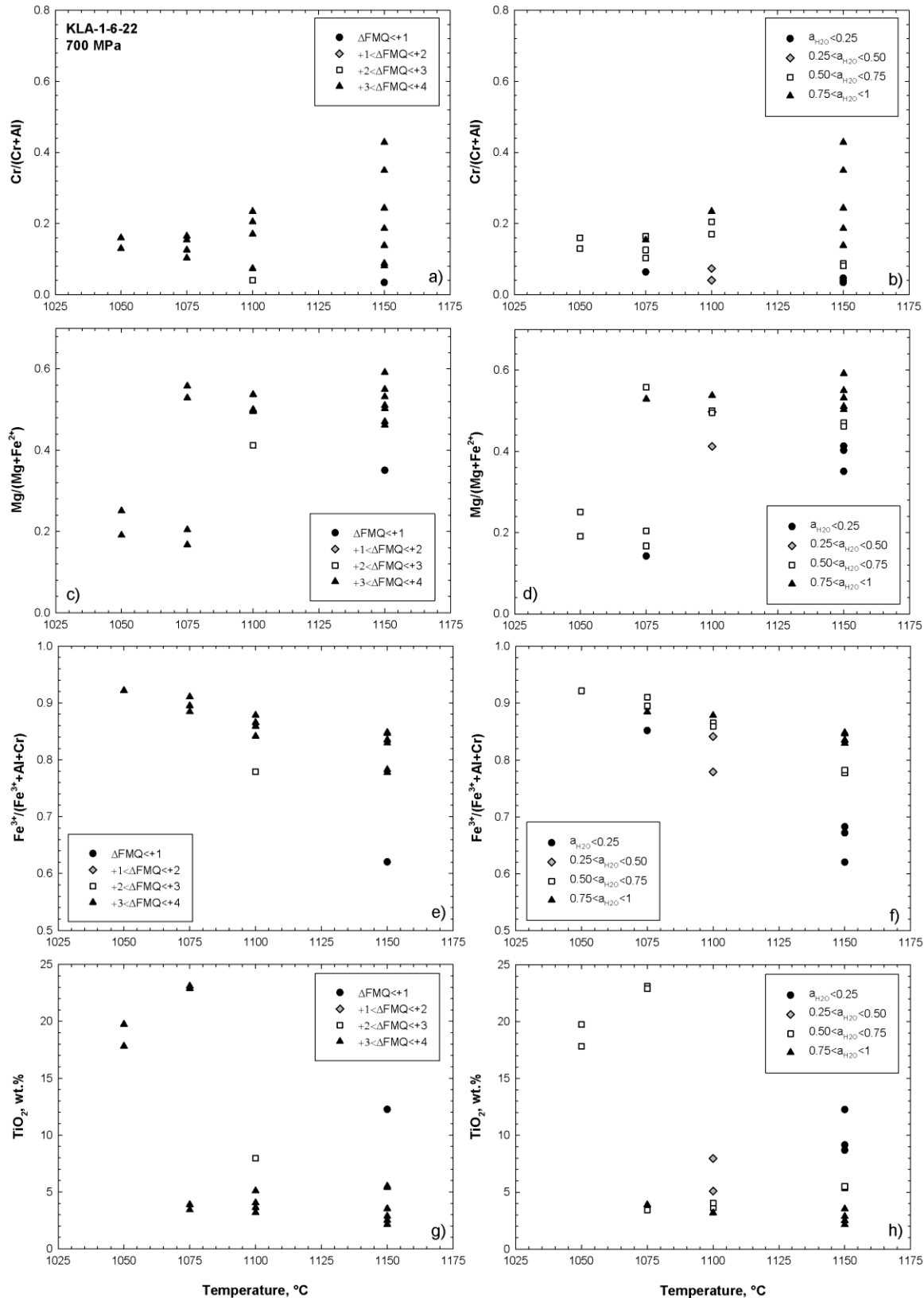


Figure 37: Variations of spinel composition as a function of temperature (°C), redox conditions and H_2O activity for sample KLA-1-6-22 equilibrated at 700 MPa. (a), (b) $\text{Cr}/(\text{Cr}+\text{Al})$; (c), (d) $\text{Mg}/(\text{Mg}+\text{Fe}^{2+})$; (e), (f) $\text{Fe}^{3+}/(\text{Fe}^{3+}+\text{Al}+\text{Cr})$; (g), (h) TiO_2 (wt.%).

Table 24. Compositions of experimental spinels using starting composition 168-1 at 400 MPa

Run	T [°C]	melt H ₂ O [wt%]	α H ₂ O	ΔFMQ	n	SiO ₂	TiO ₂	Al ₂ O ₃	FeO	MnO	MgO	CaO	Na ₂ O	K ₂ O	Cr ₂ O ₃	Total	Xusp	Cr#	Mg#	Fe ³⁺ #
LP53	1010	9.77	1.58	3.08	2	0.17 (0.05)	6.49 (0.03)	3.43 (0.04)	76.18 (0.05)	-	6.73 (0.26)	0.11 (0.02)	-	0.02 (0.01)	0.55 (0.01)	93.69	0.15	0.10	0.31	0.90
LP54	1010	8.71	1.30	2.91	4	0.18 (0.05)	6.69 (0.06)	3.34 (0.08)	76.02 (0.66)	-	6.41 (0.15)	0.13 (0.01)	0.04 (0.04)	0.02 (0.01)	0.5 (0.05)	93.32	0.16	0.09	0.29	0.90
LP55	1010	8.33	1.21	2.84	4	0.53 (0.26)	6.35 (0.05)	3.33 (0.09)	76.26 (0.83)	-	6.1 (0.14)	0.21 (0.02)	0.06 (0.05)	0.04 (0.01)	0.55 (0.03)	93.42	0.16	0.10	0.28	0.90
LP34	1025	5.60	0.64	0.68	10	0.16 (0.1)	12.49 (0.11)	4.68 (0.08)	66.35 (0.56)	0.28 (0.04)	6.65 (0.08)	0.36 (0.07)	0.04 (0.02)	0.02 (0.01)	2.17 (0.2)	93.20	0.37	0.24	0.27	0.80
LP35	1025	6.62	0.83	0.91	7	0.22 (0.12)	13.38 (0.11)	4.47 (0.06)	67.6 (0.53)	0.31 (0.04)	5.79 (0.12)	0.4 (0.07)	0.07 (0.04)	0.02 (0.01)	1.57 (0.07)	93.82	0.40	0.19	0.23	0.81
LP36	1025	5.59	0.63	0.68	7	0.27 (0.18)	13.72 (0.12)	4.43 (0.09)	67.91 (0.28)	0.34 (0.04)	5.04 (0.09)	0.36 (0.04)	0.03 (0.02)	0.03 (0.01)	1.26 (0.1)	93.39	0.42	0.16	0.20	0.81
LP10	1050	6.45	0.87	0.40	5	-	8.67 (0.04)	6.97 (0.05)	50.37 (0.4)	-	9.08 (0.14)	2.1 (1.06)	-	-	18.6 (0.22)	95.78	0.42	0.64	0.41	0.49
LP11	1050	6.42	0.79	0.32	7	-	9.89 (0.08)	7.49 (0.18)	51.05 (0.38)	-	8.74 (0.22)	4.33 (1.37)	-	-	16.63 (0.34)	98.13	0.43	0.60	0.40	0.51
LP12	1050	5.61	0.64	0.14	2	-	12.28 (0.18)	8.03 (0.4)	51.69 (1.15)	-	8.55 (0.16)	5.07 (0.92)	-	-	11.56 (0.2)	97.17	0.45	0.49	0.38	0.55
LP30	1050	0.50	0.03	0.11	9	0.55 (0.24)	7.08 (0.1)	8.02 (0.12)	63.23 (0.56)	0.36 (0.05)	8.58 (0.5)	0.39 (0.09)	0.06 (0.04)	0.04 (0.01)	0.57 (0.08)	88.88	0.20	0.05	0.39	0.77
LP188	1050	1.13	0.07	1.55	1	0.42	12.35	8.08	64.70	0.40	8.50	0.47	0.00	0.02	0.52	95.47	0.26	0.04	0.33	0.74
LP189	1050	3.21	0.30	2.76	2	0.14 (0.03)	5.94 (0.07)	5.51 (0.03)	70.96 (0.29)	0.41 (0.03)	9.72 (0.43)	0.36 (0.03)	-	0.02 (0.01)	0.62 (0.13)	93.69	0.12	0.07	0.44	0.86
LP216	1050	7.94	1.22	3.97	4	0.11 (0.07)	4.28 (0.03)	4.03 (0.03)	72.1 (0.38)	0.28 (0.04)	9.81 (0.12)	0.13 (0.04)	0.04 (0.03)	0.01 (0.02)	0.92 (0.12)	91.68	0.04	0.13	0.52	0.89
LP190	1075	0.90	0.06	1.29	2	0.7 (0.07)	10.79 (0.03)	9.16 (0.14)	63.41 (0.53)	0.42 (0.04)	8.84 (0.22)	0.46 (0.11)	0.06 (0)	0.03 (0)	0.54 (0.13)	94.41	0.33	0.04	0.36	0.72
LP191	1075	4.53	0.49	3.19	3	0.14 (0.04)	5.75 (0.04)	6.34 (0.11)	68.68 (0.27)	0.36 (0.07)	11.32 (0.18)	0.31 (0.05)	0.04 (0.03)	0.01 (0.01)	0.69 (0.04)	93.63	0.11	0.07	0.51	0.84
LP168	1100	0.46	0.04	1.04	2	0.49 (0.04)	11.72 (0.08)	9.92 (0.01)	62.87 (0.21)	0.28 (0.07)	8.2 (0.26)	0.61 (0.04)	0.08 (0.01)	0.05 (0)	0.75 (0.07)	94.97	0.47	0.05	0.33	0.69
LP169	1100	0.71	0.04	1.04	3	0.65 (0.12)	10.05 (0.09)	9.68 (0.07)	63.99 (0.25)	0.31 (0.01)	8.69 (0.03)	0.75 (0.12)	0.08 (0.07)	0.05 (0.03)	0.72 (0.04)	94.98	0.40	0.05	0.36	0.72
LP170	1100	5.15	0.59	3.35	6	0.12 (0.04)	3.54 (0.03)	5.13 (0.09)	70.41 (0.37)	0.27 (0.05)	11.68 (0.15)	0.53 (0.1)	0.1 (0.04)	0.02 (0.01)	1.07 (0.05)	92.86	0.05	0.12	0.56	0.87
LP171	1100	3.82	0.38	2.96	9	0.17 (0.07)	4.42 (0.04)	6.08 (0.1)	69.26 (0.56)	0.3 (0.07)	11.46 (0.16)	0.5 (0.06)	0.04 (0.02)	0.02 (0.01)	0.77 (0.05)	93.04	0.08	0.08	0.54	0.85
LP172	1100	4.16	0.43	3.07	3	0.55 (0.08)	10.01 (0.08)	9.45 (0.13)	63.92 (0.58)	0.33 (0.02)	8.86 (0.17)	0.68 (0.09)	0.06 (0.03)	0.03 (0.01)	0.69 (0.01)	94.59	0.30	0.05	0.36	0.72
LP173	1100	6.86	0.93	3.74	14	0.12 (0.09)	2.73 (0.06)	4.19 (0.08)	67.88 (2.28)	0.26 (0.04)	12.83 (0.19)	0.35 (0.07)	0.04 (0.02)	0.02 (0.01)	1.3 (0.09)	89.72	0.03	0.17	0.64	0.89
LP202	1125	1.73	0.12	1.99	6	0.34 (0.17)	9.42 (0.05)	10.2 (0.08)	62.04 (0.43)	0.24 (0.02)	9.27 (0.2)	0.39 (0.04)	0.06 (0.02)	0.03 (0.01)	2.46 (0.09)	94.44	0.07	0.14	0.38	0.68
LP203	1125	2.23	0.17	2.28	4	0.33 (0.32)	7.96 (0.09)	8.62 (0.09)	65.73 (0.69)	0.3 (0.05)	9.41 (0.11)	0.43 (0.15)	0.03 (0.02)	0.03 (0.01)	1.24 (0.09)	94.06	0.05	0.09	0.40	0.76
LP180	1150	1.19	0.08	1.56	3	0.3 (0.23)	8.43 (0.13)	12.25 (0.08)	61.49 (0.27)	0.18 (0.03)	9.13 (0.06)	0.4 (0.11)	0.02 (0.03)	0.02 (0)	3.48 (0.07)	95.71	0.39	0.16	0.38	0.63
LP181	1150	0.73	0.04	1.03	3	0.54 (0.28)	7.73 (0.05)	10.55 (0.13)	65.35 (0.47)	0.26 (0.09)	9.49 (0.1)	0.5 (0.06)	0.09 (0.07)	0.04 (0)	1.55 (0.01)	96.11	0.32	0.09	0.40	0.71
LP182	1150	1.34	0.09	1.69	3	0.51 (0.31)	7.74 (0.01)	10.49 (0.14)	65.29 (0.4)	0.28 (0.09)	9.81 (0.08)	0.47 (0.15)	-	0.02 (0.01)	1.38 (0.09)	96.05	0.22	0.08	0.41	0.71
LP183	1150	3.89	0.38	2.96	3	0.14 (0.02)	3.14 (0.02)	6.62 (0.13)	69.76 (0.25)	0.25 (0.07)	12.5 (0.09)	0.3 (0)	0.03 (0.01)	0.02 (0)	1.86 (0.07)	94.61	0.05	0.16	0.59	0.83
LP184	1150	4.87	0.53	3.25	3	0.1 (0)	2.73 (0)	5.95 (0.12)	69.07 (0.26)	0.21 (0.07)	13.58 (0.06)	0.22 (0.02)	0.01 (0.01)	0.02 (0.01)	2.13 (0.02)	94.02	0.04	0.19	0.64	0.84
LP185	1150	6.88	0.92	3.72	3	0.14 (0.02)	2.4 (0.01)	5.23 (0.16)	68.5 (0.35)	0.22 (0.03)	14.99 (0.22)	0.23 (0.01)	-	0.02 (0.01)	2.02 (0.06)	93.78	0.02	0.21	0.71	0.86

-, not determined

Xusp calculated after Stormer (1983)

Cr# of Spl is calculated as Cr/(Cr+Al)

Mg# of Spl is calculated as Mg/(Mg+Fe²⁺)Fe³⁺# of Spl is calculated as Fe³⁺/(Fe³⁺+Cr+Al)

Table 25. Compositions of experimental spinels using starting composition 168-1 at 700 MPa

Run	T [°C]	melt H ₂ O [wt%]	α H ₂ O	Δ FMQ	n	SiO ₂	TiO ₂	Al ₂ O ₃	FeO	MnO	MgO	CaO	Na ₂ O	K ₂ O	Cr ₂ O ₃	Total	Xusp	Cr#	Mg#	Fe ³⁺ #
LP85	1050	12.14	1.31	4.03	8	0.2 (0.12)	3.05 (0.05)	4.96 (0.08)	70.19 (0.35)	0.37 (0.05)	12.27 (0.15)	0.75 (0.09)	0.01 (0.01)	0.02 (0.01)	0.92 (0.07)	92.75	0.04	0.11	0.60	0.88
LP86	1050	12.44	1.36	4.07	4	0.06 (0.03)	2.86 (0.04)	5.32 (0.05)	71.98 (0.35)	0.43 (0.05)	11.03 (0.18)	0.44 (0.12)	0.01 (0.01)	0 (0.01)	0.71 (0.02)	91.93	0.50	0.18	0.18	0.93
LP87	1050	12.45	1.36	4.07	8	0.08 (0.02)	2.65 (0.03)	5.03 (0.06)	74.26 (0.47)	0.51 (0.04)	10.32 (0.08)	0.19 (0.07)	0.02 (0.02)	0 (0)	0.52 (0.04)	92.72	0.48	0.18	0.17	0.93
LP88	1050	12.12	1.30	4.03	5	0.15 (0.12)	18.15 (0.2)	1.37 (0.07)	66.34 (0.44)	0.16 (0.03)	4.33 (0.04)	0.7 (0.15)	0.02 (0.03)	0.02 (0.01)	0.41 (0.06)	91.67	0.51	0.17	0.17	0.92
LP89	1050	7.40	0.61	3.37	3	0.45 (0.45)	3.62 (0.03)	5.67 (0.1)	73.47 (0.63)	0.42 (0.07)	7.66 (0.13)	0.75 (0.09)	0.03 (0.03)	0.03 (0.01)	0.56 (0.03)	92.69	0.08	0.06	0.38	0.86
LP95	1100	8.74	0.76	3.57	10	0.14 (0.07)	2.79 (0.03)	4.28 (0.08)	71.06 (0.52)	0.27 (0.07)	12.52 (0.21)	0.42 (0.17)	0 (0.01)	0.01 (0.01)	1.52 (0.07)	93.02	0.04	0.19	0.61	0.88
LP96	1100	8.36	0.71	3.51	5	0.21 (0.11)	2.99 (0.02)	4.6 (0.1)	71.47 (0.66)	0.19 (0.03)	11.67 (0.17)	0.5 (0.19)	-	0.01 (0.01)	1.34 (0.1)	92.99	0.04	0.16	0.57	0.88
LP97	1100	9.92	0.92	3.74	7	0.21 (0.14)	3.27 (0.03)	4.89 (0.09)	72.04 (0.43)	0.28 (0.03)	11.16 (0.2)	0.32 (0.12)	0.03 (0.02)	0.01 (0.01)	1.17 (0.07)	93.36	0.05	0.14	0.54	0.87
LP98	1100	10.06	0.95	3.76	8	0.22 (0.1)	4.24 (0.04)	6.17 (0.12)	69.97 (0.68)	0.3 (0.05)	10.94 (0.19)	0.56 (0.12)	0.01 (0.02)	0.02 (0.01)	0.83 (0.04)	93.27	0.08	0.08	0.52	0.85
LP99	1100	7.05	0.55	3.29	7	0.19 (0.1)	5.95 (0.05)	8.98 (0.1)	66.99 (0.54)	0.36 (0.03)	10.5 (0.17)	0.59 (0.04)	0.01 (0.02)	0.02 (0.01)	0.69 (0.05)	94.26	0.13	0.05	0.47	0.78
LP100	1100	1.25	0.06	1.34	1	0.25	9.75	11.75	62.23	0.33	9.98	0.31	0.03	0.04	0.71	95.38	0.41	0.04	0.40	0.68
LP101	1100	2.15	0.11	1.90	3	0.52 (0.16)	7.88 (0.04)	9.88 (0.02)	65.64 (0.22)	0.35 (0.03)	9.63 (0.13)	0.39 (0.04)	0.04 (0.02)	0.03 (0.02)	0.62 (0.05)	94.99	0.32	0.04	0.41	0.74
LP102	1100	5.07	0.34	2.88	2	0.14 (0.01)	5.39 (0.07)	7.51 (0.05)	68.96 (0.23)	0.31 (0.02)	10.66 (0.11)	0.37 (0.02)	-	0.01 (0.01)	0.81 (0.01)	94.16	0.11	0.07	0.48	0.81
LP103	1100	5.66	0.40	3.01	2	0.54 (0.62)	4.8 (0.04)	6.91 (0.04)	70 (0.62)	0.27 (0.08)	10.76 (0.07)	0.46 (0.32)	-	0.03 (0)	0.91 (0.11)	94.70	0.10	0.08	0.49	0.82
LP104	1100	5.62	0.40	3.00	3	0.24 (0.09)	4.55 (0.04)	6.56 (0.05)	70.56 (0.65)	0.31 (0.01)	10.95 (0.11)	0.23 (0.03)	0.01 (0.01)	0.02 (0.01)	1 (0.05)	94.44	0.09	0.09	0.50	0.83
LP115	1150	2.86	0.16	2.20	2	0.25 (0.04)	8.28 (0.02)	12.22 (0.06)	63.74 (0.38)	0.28 (0.04)	9.72 (0)	0.42 (0.04)	-	0.03 (0.01)	1.21 (0.1)	96.15	0.25	0.06	0.40	0.68
LP116	1150	3.54	0.21	2.44	1	0.18	6.67	10.58	66.12	0.20	10.14	0.34	0.06	0.03	1.42	95.74	0.18	0.08	0.44	0.73
LP117	1150	4.35	0.27	2.68	2	0.25 (0.08)	6.1 (0.08)	9.57 (0.03)	66.63 (0.19)	0.24 (0.03)	10.04 (0.03)	0.33 (0.08)	0.06 (0.07)	0.02 (0)	1.27 (0.05)	94.50	0.15	0.08	0.44	0.75
LP118	1150	4.39	0.28	2.69	2	0.15 (0.01)	5.24 (0.01)	8.77 (0.04)	67.32 (0.02)	0.19 (0.04)	10.15 (0.2)	0.31 (0.07)	-	0.02 (0.02)	2.01 (0.06)	94.26	0.12	0.13	0.46	0.76
LP154	1150	1.36	0.06	1.40	5	0.34 (0.19)	7.59 (0.05)	12.92 (0.14)	58.76 (0.39)	0.31 (0.02)	10.17 (0.11)	0.38 (0.08)	0.05 (0.05)	0.02 (0.01)	0.86 (0.05)	91.39	0.24	0.05	0.36	0.72
LP155	1150	1.69	0.08	1.63	5	0.27 (0.12)	7.72 (0.07)	12.88 (0.17)	61.73 (0.44)	0.3 (0.04)	10.21 (0.13)	0.34 (0.05)	0.03 (0.01)	0.02 (0.01)	0.93 (0.06)	94.43	0.24	0.12	0.56	0.87

-, not determined

Xusp calculated after Stormer (1983)

Cr# of Spl is calculated as Cr/(Cr+Al)

Mg# of Spl is calculated as Mg/(Mg+Fe²⁺)

Fe³⁺# of Spl is calculated as Fe³⁺/(Fe³⁺+Cr+Al)

Table 26. Compositions of experimental spinels using starting composition KLA-1-6-22 at 400 MPa

Run	T [°C]	melt H ₂ O [wt%]	α H ₂ O	Δ QFM	n	SiO ₂	TiO ₂	Al ₂ O ₃	FeO	MnO	MgO	CaO	Na ₂ O	K ₂ O	Cr ₂ O ₃	Total	Xusp	Cr#	Mg#	Fe ³⁺ #
LP44	1010	6.32	0.77	1.35	9	0.18 (0.15)	16.06 (0.52)	3.67 (0.14)	67.45 (0.74)	0.4 (0.07)	5.56 (0.18)	0.31 (0.07)	0.05 (0.03)	0.03 (0.01)	0.4 (0.08)	94.10	0.46	0.07	0.21	0.85
LP45	1010	6.39	0.78	1.36	8	0.26 (0.22)	17.35 (0.14)	3.55 (0.07)	66.89 (0.43)	0.47 (0.07)	4.83 (0.13)	0.39 (0.09)	0.04 (0.02)	0.04 (0.01)	0.41 (0.05)	94.24	0.52	0.07	0.18	0.84
LP46	1010	5.44	0.61	1.14	4	0.15 (0.04)	17.9 (0.12)	3.48 (0.07)	66.9 (0.47)	0.46 (0.05)	4.27 (0.07)	0.35 (0.06)	0.02 (0.01)	0.03 (0.01)	0.46 (0.06)	94.00	0.54	0.08	0.16	0.83
LP47	1010	4.02	0.38	0.74	5	0.46 (0.18)	18.11 (0.05)	3.63 (0.1)	66.51 (0.73)	0.51 (0.05)	3.8 (0.17)	0.5 (0.03)	0.09 (0.04)	0.05 (0.02)	0.43 (0.05)	94.10	0.57	0.07	0.14	0.82
LP37	1025	8.92	1.35	1.93	9	0.16 (0.04)	18.02 (0.45)	3.99 (0.15)	64.19 (0.64)	0.38 (0.05)	5.94 (0.15)	0.29 (0.08)	0.03 (0.02)	0.03 (0.01)	0.75 (0.38)	93.78	0.54	0.11	0.22	0.81
LP38	1025	4.34	0.43	0.94	3	0.41 (0.15)	18.11 (0.13)	3.81 (0.12)	60.18 (0.52)	0.41 (0.03)	5.03 (0.13)	0.6 (0.15)	0.04 (0.03)	0.06 (0.02)	0.69 (0.06)	89.34	0.59	0.11	0.19	0.79
LP39	1025	5.86	0.68	1.34	3	0.28 (0.15)	18.95 (0.16)	4.03 (0.28)	65.01 (0.5)	0.44 (0.05)	4.64 (0.07)	0.34 (0.02)	0.03 (0.03)	0.04 (0.01)	0.48 (0.05)	94.25	0.59	0.07	0.17	0.80
LP40	1025	8.12	1.16	1.80	4	0.36 (0.27)	11.67 (1.23)	4.34 (0.29)	68.86 (0.33)	0.36 (0.06)	6.5 (0.47)	0.15 (0.08)	0.06 (0.05)	0.01 (0.01)	0.81 (0.23)	93.13	0.33	0.11	0.27	0.84
LP13	1050	6.25	0.76	0.41	5	-	10.47 (0.55)	6.98 (0.51)	49.5 (2.26)	-	8.65 (0.18)	5.11 (4.78)	-	-	16.86 (1.04)	97.56	0.42	0.62	0.40	0.51
LP14	1050	5.71	0.66	0.29	2	-	10.03 (0.22)	4.86 (0.13)	69.04 (0.17)	-	8.2 (0.54)	1.93 (0.14)	-	-	0.88 (0.02)	94.95	0.23	0.11	0.36	0.85
LP196	1025	0.50	0.03	0.70	2	0.83 (0.04)	11.21 (0.02)	7.22 (0.12)	66.37 (0.34)	0.61 (0.09)	7.36 (0.01)	0.48 (0.07)	-	0.05 (0.02)	0.32 (0.06)	94.47	0.40	0.03	0.30	0.77
LP32	1050	0.50	0.03	0.11	5	0.73 (0.24)	11.88 (0.13)	8.22 (0.19)	58.67 (0.59)	0.46 (0.05)	8.76 (0.15)	0.58 (0.08)	0.09 (0.03)	0.05 (0)	0.33 (0.07)	89.77	0.37	0.03	0.36	0.72
LP33	1050	0.50	0.03	0.11	2	0.83 (0.22)	14.9 (0.04)	7.61 (0.21)	57.54 (0.03)	0.44 (0.04)	8.3 (0.19)	0.57 (0.05)	0.18 (0.13)	0.08 (0.03)	0.36 (0)	90.80	0.49	0.03	0.32	0.70
LP213	1050	0.71	0.04	1.06	4	0.8 (0.38)	15.32 (0.14)	8.6 (0.1)	61.07 (0.42)	0.43 (0.09)	7.53 (0.24)	0.38 (0.13)	0.12 (0.06)	0.07 (0.02)	0.39 (0.04)	94.71	0.40	0.03	0.28	0.68
LP214	1050	2.53	0.22	2.47	6	0.38 (0.46)	9.41 (0.03)	5.98 (0.11)	68.07 (0.48)	0.47 (0.07)	7.88 (0.09)	0.24 (0.03)	0.06 (0.03)	0.05 (0.01)	0.39 (0.05)	92.91	0.31	0.04	0.33	0.82
LP215	1050	8.61	1.39	4.09	4	0.08 (0.05)	4.9 (0.07)	4.13 (0.09)	71.73 (0.84)	0.3 (0.04)	10.57 (0.19)	0.1 (0.02)	0.04 (0.02)	0.02 (0.01)	0.83 (0.06)	92.68	0.19	0.12	0.40	0.87
LP192	1075	0.58	0.03	0.83	1	0.30	13.68	8.49	63.90	0.40	8.09	0.46	0.00	0.03	0.51	95.87	0.42	0.04	0.31	0.72
LP193	1075	1.65	0.12	1.95	1	0.21	13.22	8.12	63.65	0.47	8.55	0.36	0.05	0.06	0.40	95.08	0.39	0.03	0.33	0.74
LP194	1075	2.51	0.21	2.44	8	0.26 (0.24)	5.86 (2.2)	5.69 (1.65)	69.4 (2.38)	0.4 (0.1)	10.93 (1.26)	0.33 (0.18)	0.04 (0.02)	0.03 (0.01)	0.65 (0.29)	93.59	0.11	0.07	0.49	0.85
LP131	1100	7.89	1.21	3.97	10	0.23 (0.3)	2.89 (0.03)	4.52 (0.08)	71.19 (0.71)	0.34 (0.06)	13.87 (0.13)	2.12 (0.76)	0.04 (0.05)	0.03 (0.01)	1.37 (0.07)	94.25	0.03	0.41	0.68	0.83
LP132	1100	6.27	0.81	3.62	11	0.16 (0.1)	4.07 (0.3)	5.48 (0.3)	70.77 (0.88)	0.33 (0.07)	13.51 (0.16)	2.15 (0.45)	0.03 (0.02)	0.03 (0.01)	0.84 (0.1)	97.35	0.05	0.09	0.64	0.87
LP134	1100	2.54	0.21	2.46	2	0.72 (0.05)	11.25 (0.07)	8.83 (0.03)	65.03 (0.2)	0.43 (0.03)	8.96 (0.02)	0.61 (0.03)	-	0.04 (0)	0.57 (0.02)	96.55	0.43	0.04	0.35	0.73
LP135	1100	1.06	0.07	1.46	2	0.36 (0)	11.9 (0.08)	9.34 (0.04)	64.63 (0.02)	0.43 (0)	9.01 (0.27)	0.43 (0)	0.04 (0.01)	0.05 (0)	0.55 (0)	96.73	0.45	0.04	0.35	0.72
LP136	1100	1.57	0.11	1.90	3	0.41 (0.15)	12.64 (0.17)	9.12 (0.03)	63.98 (0.33)	0.44 (0.07)	8.49 (0.24)	0.48 (0.02)	0.02 (0.02)	0.03 (0.01)	0.55 (0)	96.15	0.32	0.04	0.33	0.71
LP200	1125	1.65	0.12	1.93	4	0.44 (0.32)	9.76 (1.41)	11.2 (1.43)	62.68 (0.14)	0.33 (0.03)	8.83 (0.13)	0.41 (0.1)	0.06 (0.06)	0.05 (0.01)	1.64 (0.02)	95.40	0.25	0.09	0.36	0.67
LP201	1125	2.19	0.17	2.26	5	0.27 (0.07)	8.94 (0.05)	8.24 (0.08)	64.12 (1.45)	0.32 (0.05)	9.31 (0.16)	0.38 (0.05)	0.11 (0.02)	0.07 (0.05)	1.76 (0.09)	93.50	0.20	0.13	0.40	0.74
FC-36	1125	2.91	0.25	2.10	7	0.27 (0.18)	13.72 (0.12)	4.43 (0.09)	67.91 (0.28)	0.34 (0.04)	5.04 (0.09)	0.36 (0.04)	0.03 (0.02)	0.03 (0.01)	1.26 (0.1)	93.26	0.21	0.17	0.36	0.65
FC-37	1125	3.64	0.35	2.38	9	0.16 (0.04)	18.02 (0.45)	3.99 (0.15)	64.19 (0.64)	0.38 (0.05)	5.94 (0.15)	0.29 (0.08)	0.03 (0.02)	0.03 (0.01)	0.75 (0.38)	93.21	0.21	0.16	0.41	0.75
FC-38	1125	3.82	0.37	2.44	3	0.41 (0.15)	18.11 (0.13)	3.81 (0.12)	60.18 (0.52)	0.41 (0.03)	5.03 (0.13)	0.6 (0.15)	0.04 (0.03)	0.06 (0.02)	0.69 (0.06)	93.07	0.21	0.14	0.42	0.77
LP174	1150	1.39	0.09	1.74	1	0.74	8.77	11.40	58.51	0.12	8.31	1.15	0.04	0.03	5.27	95.49	0.41	0.06	0.26	0.69
LP175	1150	2.06	0.15	2.18	3	0.52 (0.16)	8.51 (0.49)	10.34 (0.34)	62.32 (1.22)	0.18 (0.08)	8.32 (0.62)	0.81 (0.08)	0.01 (0.01)	0.03 (0.01)	3.91 (0.8)	95.11	0.39	0.01	0.27	0.74

-, not determined

Xusp calculated after Stormer (1983)

Cr# of Spl is calculated as Cr/(Cr+Al)

Mg# of Spl is calculated as Mg/(Mg+Fe²⁺)

Fe³⁺# of Spl is calculated as Fe³⁺/(Fe³⁺+Cr+Al)

Table 27. Compositions of experimental spinels using starting composition KLA-1-6-22 at 550 MPa

Run	T [°C]	melt H ₂ O [wt%]	α H ₂ O	ΔFMQ	n	SiO ₂	TiO ₂	Al ₂ O ₃	FeO	MnO	MgO	CaO	Na ₂ O	K ₂ O	Cr ₂ O ₃	Total	Xusp	Cr#	Mg#	Fe ³⁺ #
FC-42	5500	1125	3.19	0.22	5	0.28(8)	11.59(8)	9.9(1)	62.2(5)	0.35(6)	8.5(2)	0.41(3)	0.02(3)	0.03(1)	0.72(6)	93.97	0.208	0.05	0.34	0.69
FC-43	5500	1125	4.20	0.32	5	0.3(3)	6.84(9)	8.0(3)	66.0(5)	0.35(5)	10.0(2)	0.4(1)	0.01(4)	0.04(1)	0.9(1)	92.76	0.209	0.07	0.44	0.78
FC-44	5500	1125	4.35	0.34	5	0.3(2)	4.47(3)	6.40(8)	59.7(1)	0.25(3)	10.3(3)	0.30(7)	0.02(2)	-	1.24(8)	82.91	0.231	0.11	0.53	0.81
FC-7	5500	1150	4.07	0.30	4	0.7(5)	6.4(1)	14.5(3)	44.8(4)	-0.08(5)	10.9(3)	0.4(2)	0.1(1)	0.04(3)	8.1(1)	85.82	0.217	0.27	0.49	0.47
FC-8	5500	1150	1.82	0.10	3	4(1.14)	6.4(2)	15.3(2)	47(1.05)	-0.03(4)	11.4(4)	1.0(2)	0.3(2)	0.14(4)	9.0(8)	93.48	0.199	0.28	0.45	0.42
FC-9	5500	1150	2.42	0.15	2	1(1.94)	6.7(2)	13.3(5)	52.0(3)	0.01(1)	10.5(3)	0.6(4)	0.1(2)	0.08(8)	8(2.28)	92.98	0.204	0.30	0.44	0.52
FC-1	5500	1175	5.41	0.45	1	0.79	5.17	14.79	46.67	-0.15	11.30	0.48	0.07	0.04	9.37	88.53	0.210	0.30	0.51	0.48
FC-2	5500	1175	1.50	0.08	1	0.19	6.45	13.33	55.69	0.05	10.77	0.27	0.01	0.02	7.48	94.26	0.201	0.27	0.46	0.56
FC-3	5500	1175	1.71	0.10	1	0.18	5.92	12.71	57.15	-0.02	10.86	0.36	-0.01	0.04	6.78	93.97	0.252	0.26	0.48	0.60

-, not determined

Xusp calculated after Stormer (1983)

Cr# of Spl is calculated as Cr/(Cr+Al)

Mg# of Spl is calculated as Mg/(Mg+Fe²⁺)Fe³⁺# of Spl is calculated as Fe³⁺/(Fe³⁺+Cr+Al)

Table 28. Compositions of experimental spinels using starting composition KLA-1-6-22 at 700 MPa

Run	T [°C]	melt H ₂ O [wt%]	α H ₂ O	Δ FMQ	n	SiO ₂	TiO ₂	Al ₂ O ₃	FeO	MnO	MgO	CaO	Na ₂ O	K ₂ O	Cr ₂ O ₃	Total	Xusp	Cr#	Mg#	Fe ³⁺ #
LP63	1050	7.62	0.64	3.41	8	0.04 (0.03)	19.44 (0.25)	1.17 (0.04)	64.08 (0.52)	0.17 (0.03)	5.92 (0.65)	0.66 (0.18)	0.17 (0.25)	0.01 (0.01)	0.29 (0.07)	95.41	0.46	0.13	0.25	0.92
LP65	1050	7.07	0.57	3.31	7	0.08 (0.04)	19.74 (0.75)	1.28 (0.05)	64.18 (0.85)	0.18 (0.04)	5.14 (0.33)	0.89 (0.19)	0.6 (0.75)	0.03 (0.01)	0.36 (0.03)	95.31	0.55	0.16	0.19	0.92
LP67	1050	2.36	0.13	2.02	5	0.4 (0.27)	21.64 (0.44)	1.56 (0.09)	62.86 (1.69)	0.23 (0.03)	3.48 (0.16)	2.6 (2.96)	0.67 (0.74)	0.05 (0.02)	0.23 (0.09)	96.07	0.63	0.09	0.13	0.90
LP68	1075	7.32	0.59	3.35	5	0.08 (0.02)	3.43 (0.03)	3.9 (0.1)	72 (0.62)	0.3 (0.07)	11.45 (0.08)	0.52 (0.09)	0.67 (0.82)	0.01 (0)	1.14 (0.09)	99.72	0.05	0.16	0.56	0.89
LP69	1075	9.94	0.94	3.75	5	0.08 (0.03)	3.89 (0.04)	4.3 (0.08)	72.37 (0.41)	0.31 (0.07)	11.08 (0.2)	0.39 (0.09)	0.04 (0.03)	0.01 (0.01)	1.17 (0.1)	99.72	0.06	0.15	0.53	0.88
LP70	1075	8.57	0.75	3.55	2	0.13 (0.01)	4.14 (0.13)	5.34 (0.05)	70.19 (0.11)	0.37 (0.01)	10.98 (0.03)	1.31 (0.39)	-	-	0.68 (0.04)	95.21	0.64	0.10	0.20	0.91
LP72	1075	1.94	0.10	1.80	3	0.08 (0.03)	25.16 (0.62)	1.57 (0.11)	59.29 (0.52)	0.25 (0.02)	4.47 (0.84)	1.02 (0.27)	-	0.06 (0.04)	0.25 (0)	93.85	0.23	0.06	0.14	0.85
LP73	1100	8.72	0.76	3.56	2	0.06 (0.01)	3.19 (0.04)	4.15 (0.05)	72.05 (0.24)	0.28 (0.04)	11.04 (0)	0.23 (0.03)	-	0.04 (0.01)	1.89 (0.08)	99.09	0.10	0.23	0.54	0.88
LP74	1100	6.91	0.54	3.26	3	0.11 (0.05)	3.63 (0.02)	4.73 (0.06)	72.7 (0.15)	0.22 (0.05)	10.52 (0.07)	0.19 (0.04)	0.02 (0.02)	0.02 (0)	1.81 (0.02)	99.97	0.12	0.20	0.50	0.87
LP75	1100	8.54	0.74	3.54	3	0.07 (0.01)	4.05 (0.05)	5.12 (0.03)	72.03 (0.66)	0.27 (0.04)	10.47 (0.35)	0.25 (0.04)	0.05 (0.01)	0.02 (0.01)	1.57 (0.04)	99.79	0.07	0.17	0.49	0.86
LP76	1100	5.81	0.42	3.05	2	0.11 (0.03)	5.1 (0.06)	6.28 (0.1)	70.34 (0.01)	0.31 (0.02)	10.89 (0.05)	0.18 (0.03)	0.1 (0.04)	0.02 (0)	0.74 (0.05)	99.71	0.10	0.07	0.50	0.84
LP77	1100	4.26	0.27	2.67	3	0.51 (0.18)	7.97 (0.04)	8.09 (0.09)	65.87 (1.07)	-	9.44 (0.18)	1.28 (0.2)	0.07 (0.04)	0.05 (0.01)	0.51 (0.01)	98.32	0.21	0.04	0.41	0.78
LP78	1150	9.97	0.91	3.72	5	0.04 (0.02)	2.15 (0.01)	4.51 (0.09)	68.65 (0.57)	0.19 (0.06)	11.88 (0.07)	0.43 (0.07)	0.01 (0.02)	0.02 (0.01)	5.04 (0.12)	98.92	0.03	0.43	0.59	0.83
LP79	1150	10.13	0.93	3.74	6	0.05 (0.03)	2.5 (0.03)	4.87 (0.08)	69.54 (0.48)	0.17 (0.05)	11.06 (0.1)	0.45 (0.08)	0.03 (0.03)	0.02 (0.01)	3.9 (0.1)	98.53	0.04	0.35	0.55	0.84
LP80	1150	11.17	1.09	3.88	6	0.1 (0.03)	2.88 (0.06)	5.17 (0.08)	70.8 (0.26)	0.22 (0.04)	10.86 (0.18)	0.36 (0.08)	0.03 (0.02)	0.01 (0.01)	2.48 (0.06)	98.88	0.05	0.24	0.53	0.85
LP81	1150	10.06	0.92	3.73	5	0.13 (0.03)	3.52 (0.04)	5.94 (0.06)	69.96 (0.51)	0.26 (0.06)	10.56 (0.14)	0.44 (0.04)	0.02 (0.04)	0.02 (0.01)	2.02 (0.07)	98.65	0.07	0.19	0.51	0.83
LP82	1150	7.79	0.63	3.40	7	0.41 (0.33)	5.37 (0.03)	8.61 (0.15)	67.26 (0.43)	0.27 (0.03)	10.34 (0.14)	0.83 (0.27)	0.02 (0.02)	0.03 (0.02)	1.23 (0.04)	99.56	0.12	0.09	0.47	0.78
LP83	1150	9.13	0.79	3.60	10	0.13 (0.07)	3.53 (0.03)	5.87 (0.1)	71.36 (0.33)	0.23 (0.03)	10.45 (0.09)	0.47 (0.06)	0.02 (0.02)	0.02 (0.01)	1.4 (0.07)	99.37	0.06	0.14	0.50	0.85
LP84	1150	7.90	0.64	3.41	6	0.24 (0.18)	5.51 (0.04)	8.41 (0.12)	67.42 (0.47)	0.29 (0.04)	10.12 (0.09)	0.62 (0.05)	0.02 (0.03)	0.02 (0.01)	1.1 (0.06)	98.92	0.13	0.08	0.46	0.78
LP150	1150	0.50	0.02	0.39	8	0.29 (0.11)	12.26 (0.06)	12.6 (0.14)	60.07 (0.36)	0.33 (0.06)	9.09 (0.14)	0.32 (0.11)	0.04 (0.01)	0.03 (0.01)	0.67 (0.05)	99.06	0.43	0.03	0.35	0.62
LP151	1150	1.49	0.07	1.50	8	0.48 (0.33)	9.16 (0.08)	11.95 (0.1)	61.9 (0.49)	0.31 (0.04)	9.84 (0.11)	0.35 (0.12)	0.03 (0.03)	0.05 (0.02)	0.73 (0.07)	98.80	0.29	0.04	0.40	0.67
LP152	1150	1.53	0.07	1.53	6	0.19 (0.03)	8.69 (0.06)	11.76 (0.17)	62.58 (0.61)	0.31 (0.04)	9.93 (0.13)	0.27 (0.06)	0.04 (0.04)	0.02 (0.01)	0.85 (0.05)	98.81	0.26	0.05	0.41	0.68

-, not determined

Xusp calculated after Stormer (1983)

Cr# of Spl is calculated as Cr/(Cr+Al)

Mg# of Spl is calculated as Mg/(Mg+Fe²⁺)Fe³⁺# of Spl is calculated as Fe³⁺/(Fe³⁺+Cr+Al)

4.3.6 Glass

All experimental residual melts are listed in Tables 29-33. Compositional variations have both basanitic starting material at all conditions investigated are shown in comparison to the natural liquid lines of descent (LLD) of the Cumbre Vieja volcano in the Appendix in Figures A2-A20. In this chapter the general influence of fO_2 , aH_2O , temperature, crystallizing phases and pressure on the residual melt composition will be presented.

4.3.7 Effect of fO_2 conditions on glass compositions

FeO , TiO_2 and SiO_2 content of residual melts are affected by the prevailing fO_2 condition. In Figure 38 experimental residual liquids are presented as function of fO_2 conditions. However, the effect of fO_2 conditions on residual melt composition with respect to FeO , TiO_2 and SiO_2 is mostly pronounced at intermediate melt compositions (MgO 5.5-2.5 wt.%) (see Figures 38a, b & c). At reducing conditions ($0 < \Delta FMQ < +1$) (white dots in Figures 38a, b & c) FeO^{tot} contents of experimental residual melts are elevated up to 2 wt.% in the range of intermediate melt compositions. SiO_2 contents of experimental liquids generated at reducing conditions resemble SiO_2 contents of the natural Cumbre Vieja lavas at the lower limit of the trend. However, TiO_2 contents show good correspondence with the natural trend. At oxidizing conditions ($+3 < \Delta FMQ < +4$) (gray squares in Figure 38) FeO^{tot} and TiO_2 contents of experimental residual melts are distinctly lower (max. deviation: FeO^{tot} : 4 wt.%; TiO_2 : 2 wt.%) as FeO^{tot} and TiO_2 contents of natural Cumbre Vieja lavas. Enrichment of SiO_2 content was observed in experimental liquids generated at oxidizing conditions with deviations from the natural trend of maximal 5 wt.%. This compositional variation in FeO , TiO_2 and SiO_2 content of experimental residual melts is directly related to the stability and proportion of magnetite. At oxidizing conditions high proportions of magnetite are stabilized and residual melts are consequently depleted in FeO , TiO_2 and enriched in SiO_2 . At reducing conditions magnetite proportions are low resulting in almost constant FeO contents in the residual melts. However, at reducing conditions kaersutitic amphibole (high TiO_2 contents up to 6.1 wt.%, see Figure 38b) are stabilized and coexisting melts are consequently depleted in TiO_2 resulting in good correspondence of TiO_2 contents between experimental melts and natural Cumbre Vieja LLD. To generate residual melts in the compositional range of natural Cumbre Vieja lavas fO_2 conditions have to be between $FMQ+1$

and FMQ+2 (see black diamonds in Figures 38d, e & f). Remarks on the effect $f\text{O}_2$ conditions on liquid compositions can be generalized as we observed the same dependency for both basanitic starting compositions at all pressures investigated.

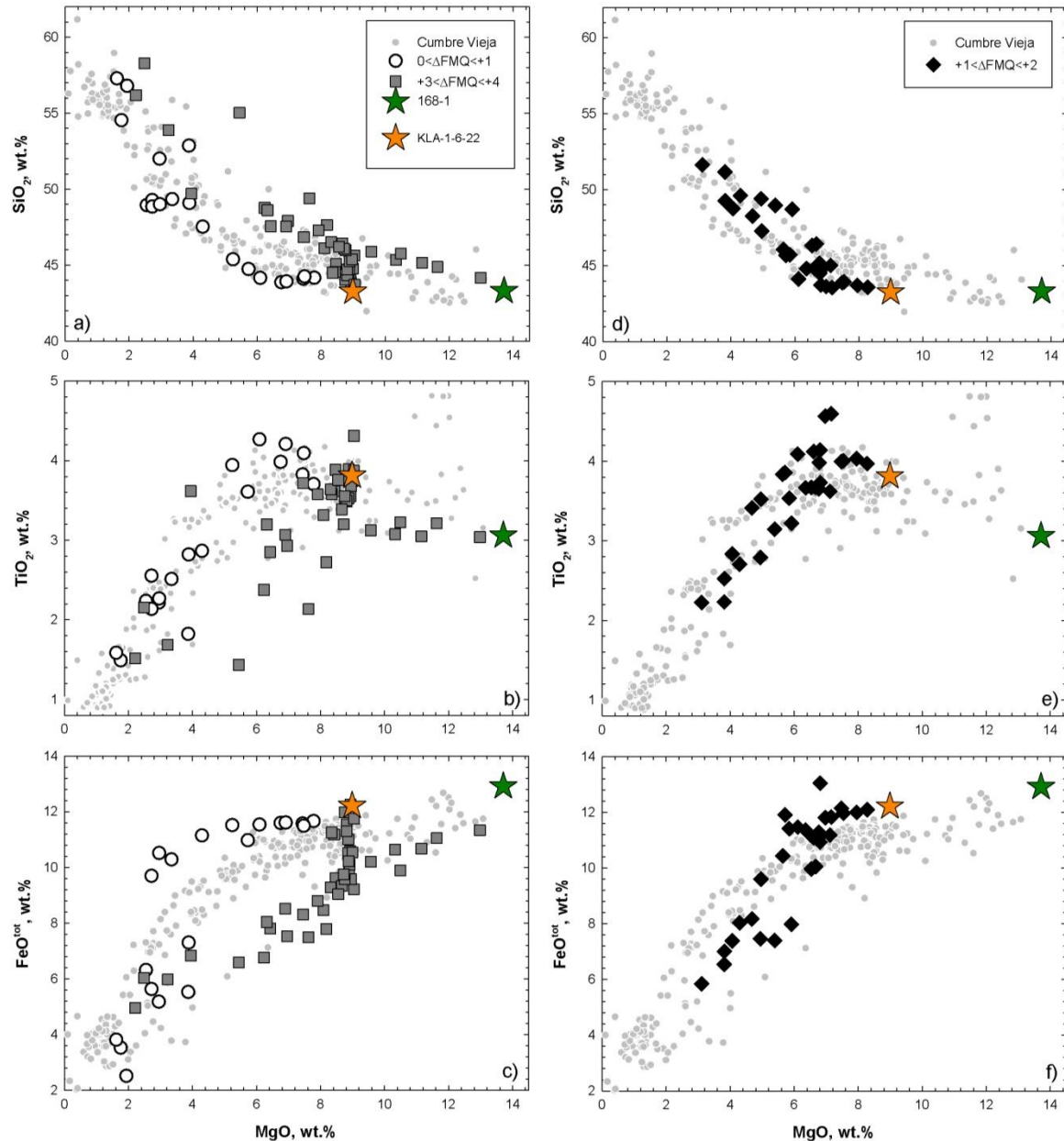


Figure 38: Effect of $f\text{O}_2$ conditions on experimental residual melts as a function of MgO content (wt.%) using both basanitic starting materials (primitive basanite: green star; evolved basanite: orange star) at all pressures investigated in comparison to natural LLD of the Cumbre Vieja volcano (CV) (all compositions are normalized to 100%). Deviations for SiO₂ (a), TiO₂ (b) and FeO^{tot} (c) content (wt.%) from the natural trend were observed at reducing conditions ($0 < \Delta\text{FMQ} < +1$) and at oxidizing conditions ($+3 < \Delta\text{FMQ} < +4$). Good correspondence between experimental residual melt compositions and natural CV LLD were observed at $f\text{O}_2$ conditions between FMQ+1 and FMQ+2 (d, e, f).

4.3.8 Effect of aH₂O and temperature on glass compositions

As shown in Sections 4.1 and 4.2 (phase relations and proportions) mineral proportions are strongly affected by the prevailing aH₂O and temperature. Consequently the composition of the residual melt is driven by temperature, aH₂O, corresponding phase assemblage and crystal proportions. In this section residual melt compositions of the same experiments that were used to demonstrate the influence of aH₂O and temperature on mineral proportions and degree of crystallization in Section 4.2.1 (Figures 20-23) are presented.

Al₂O₃ and CaO contents of residual melt compositions using the primitive basanite at 400 MPa, between 1150-1010°C, low aH₂O ($0.16 < \text{aH}_2\text{O} < 0.38$; 2.0-4.5 wt.% H₂O in the melt: white dots in Figure 39) and high aH₂O ($0.83 < \text{aH}_2\text{O} < 1$; 6.6-8.9 wt.% H₂O in the melt: black diamonds in Figure 39) are shown as function of MgO and SiO₂ content in Figure 39. Melts with high MgO contents (14-9 wt.%) show no direct dependence of aH₂O, as residual melts generated at high and low aH₂O are very close in composition with respect to Al₂O₃ and CaO content. MgO content in the residual melt at this part of the trend is linked to the proportion of crystallizing olivine, e.g. olivine proportion of 7.2 wt.% leads to a MgO depletion of 3 wt.% in the residual melt. At 1075°C and 4.5 wt.% H₂O in the melt (aH₂O: 0.49) Cpx proportion increases to up 22 wt.% and melts are consequently depleted in CaO. At MgO contents below 6 wt.% and lower temperatures (1050°C at 3.2 wt.% H₂O in the melt; 1025°C at 6.6 wt.% H₂O in the melt) amphibole appears on the liquidus. At low aH₂O Cpx predominates over Amph in the Cpx+Amph assemblage resulting in CaO depletion and more pronounced enrichment of Al₂O₃ in the residual melt. At high aH₂O amphibole predominates over Cpx and high amphibole proportions (up to 60 wt.%) are stabilized, resulting in a less extensive depletion of CaO in the residual melt. Al₂O₃ contents of those residual melts plot on the lower part of the natural trend, because generally increasing Al₂O₃ of residual melt is affected by the high proportion of Amph (Amph: e.g. 12.89 wt.% Al₂O₃ at 1050°C, 400 MPa).

We observed the same dependency of aH₂O and corresponding phase proportions on residual melt composition in experiments using the evolved basanite as starting material at 400 MPa (Figure 40). At 700 MPa Cpx predominates over Amph at low and high aH₂O resulting in residual

melts resembling the lower limit of the CaO and the upper limit of the Al_2O_3 natural trend (see Figure 41).

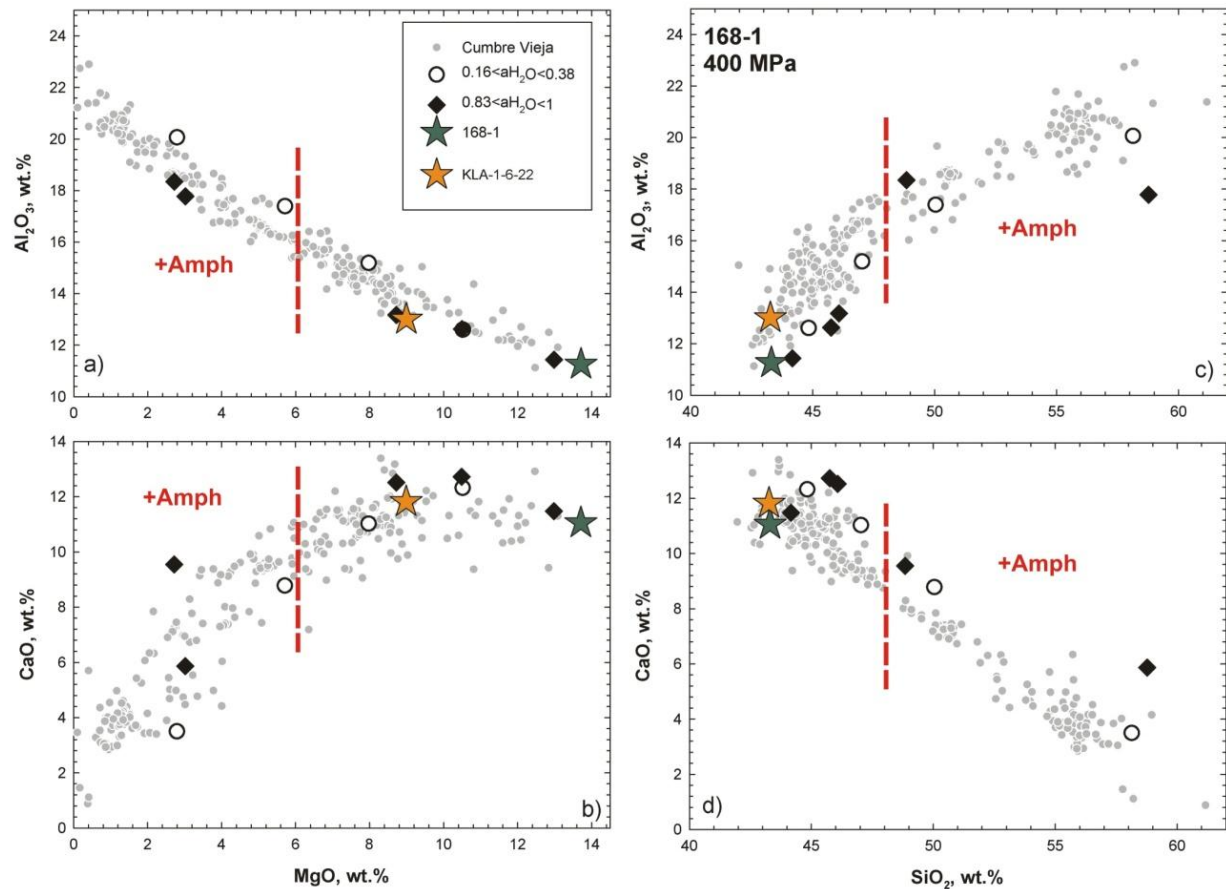


Figure 39: Effect of aH_2O on Al_2O_3 and CaO content in the residual melt composition of starting composition 168-1 (green star) at 400 MPa. The orange star indicates the starting composition of the evolved basanite (KLA-1-6-22). White dots indicate the melt evolution at low aH_2O (0.16 - 0.38 ; 2.0 - 4.5 wt.% H_2O in the melt) with decreasing temperatures from 1150°C to 1010°C . Black diamonds indicate the melt evolution at high aH_2O (0.83 - 1 ; 6.6 - 8.3 wt.% H_2O in the melt) in the same temperature range. Melts coexist with Ol+Mt ($\text{MgO}: 14$ - 9 wt.% at high aH_2O), with Ol+Cpx+Mt ($\text{MgO}: 11$ - 8 wt.% at low aH_2O) and with Ol+Cpx+Amph+Mt ($\text{Mg}: 6$ - 2 wt.%) indicated by the red dashed line.

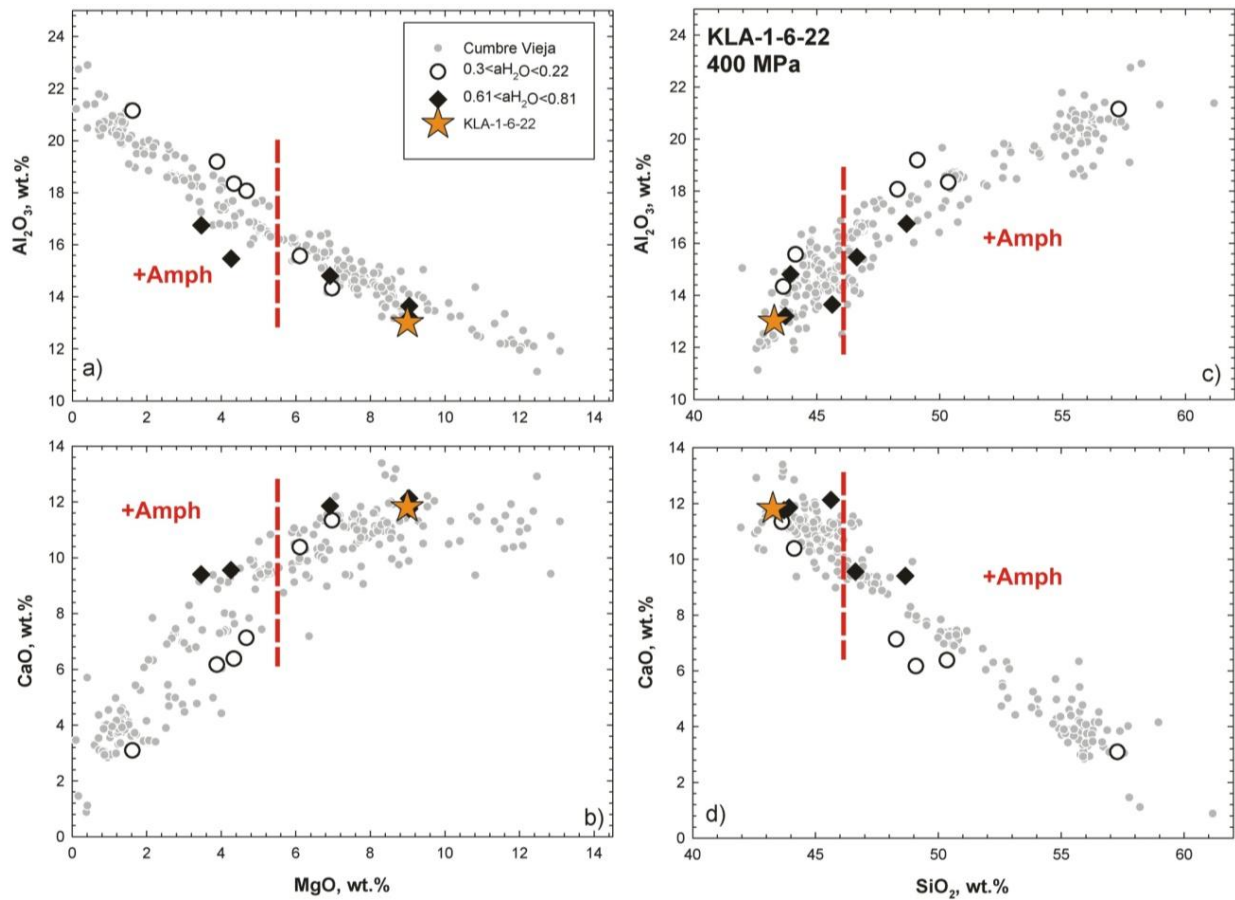


Figure 40: Effect of $a\text{H}_2\text{O}$ on Al_2O_3 and CaO content in the residual melt composition of starting composition KLA-1-6-22 (orange star) at 400 MPa. The green star indicates the starting composition of the primitive basanite (168-1). White dots indicate the melt evolution at low $a\text{H}_2\text{O}$ (0.2-0.3; 0.5-2.5 wt.% H_2O in the melt) with decreasing temperatures from 1150°C to 1010°C. Black diamonds indicate the melt evolution at high $a\text{H}_2\text{O}$ (0.6-0.8; 5.4-6.3 wt.% H_2O in the melt) in the same temperature range. At high $a\text{H}_2\text{O}$ Melts coexist with $\text{Ol}+\text{Cpx}+\text{Mt}$ (MgO : 9-7 wt.%) and with $\text{Cpx}+\text{Amph}+\text{Mt}$ (Mg : 4-3 wt.%) indicated by the red dashed line. At low $a\text{H}_2\text{O}$ Melts coexist with $\text{Ol}+\text{Cpx}+\text{Mt}$ (MgO : 7.0, 6.1, 4.7, 3.1 wt.%) and with $\text{Cpx}+\text{Amph}+\text{Mt}$ (Mg : 4.3, 1.6 wt.%).

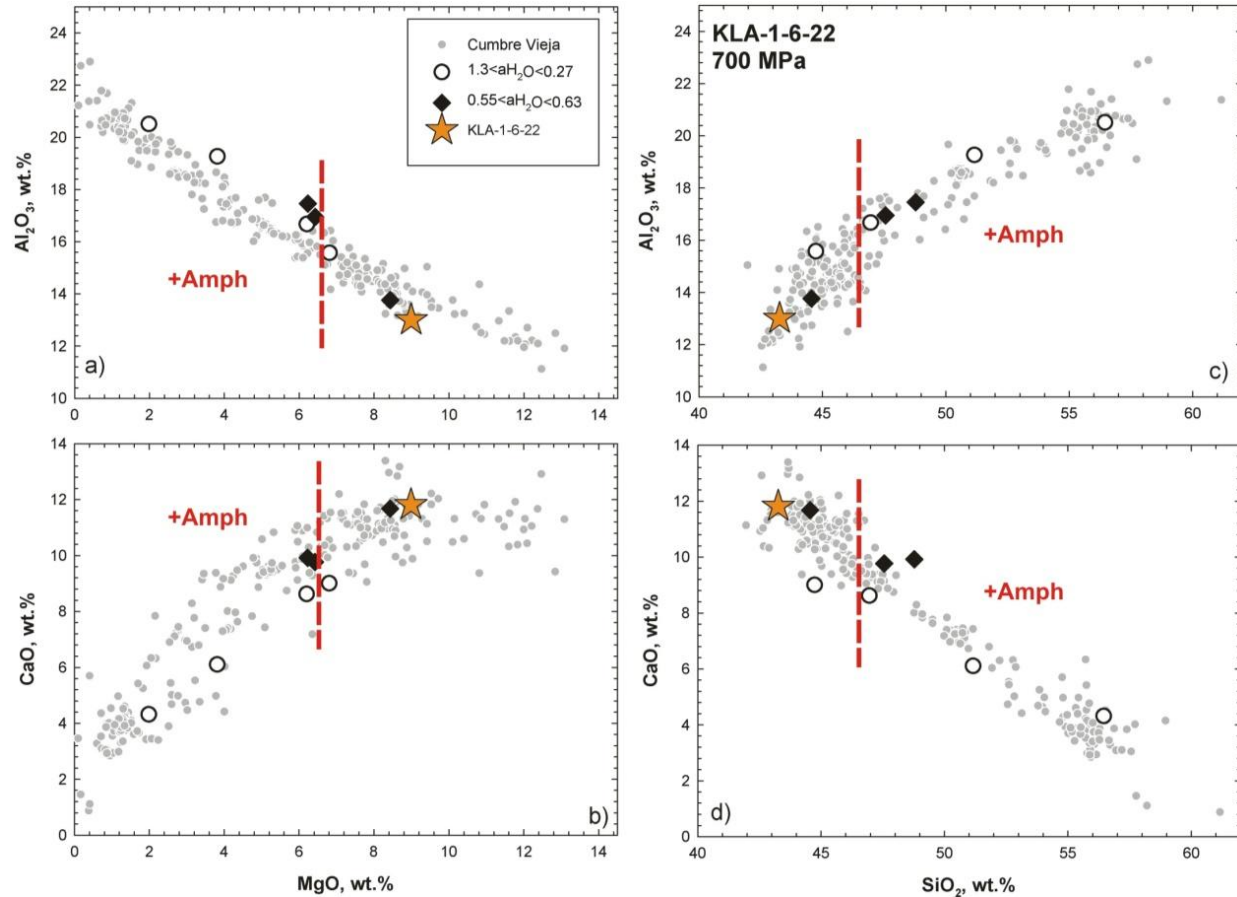


Figure 41: Effect of aH_2O on Al_2O_3 and CaO content in the residual melt composition of starting composition KLA-1-6-22 (orange star) at 700 MPa. The green star indicates the starting composition of the primitive basanite (168-1). White dots indicate the melt evolution at low aH_2O (0.13-0.27; 1.5-4.3 wt.% H_2O in the melt) with decreasing temperatures from 1150°C to 1050°C. Black diamonds indicate the melt evolution at high aH_2O (0.55-0.63; 7.0-7.8 wt.% H_2O in the melt) in the same temperature range. Melts coexist with Cpx+Mt (MgO : 9-7 wt.%) with Cpx+Amph+Mt (MgO : 7-2 wt.% at low aH_2O) and with indicated by the red dashed line.

4.3.9 Effect of mineral assemblages on glass compositions

The effect of crystallizing phases on the residual melt composition is shown in comparison to the natural liquid lines of descent (LLD) of the Cumbre Vieja volcano in the Appendix in Figures A2 (168-1 at 400 MPa), A6 (168-1 at 700 MPa), A10 (KLA-1-6-22 at 400 MPa) and A17 (KLA-1-6-22 at 700 MPa). The first part of the natural trend (~14-9 wt.% MgO) is characterized by strong MgO depletion in the melt, this part of the trend was reproduced by crystallization of olivine and spinel using the primitive basanite (168-1) at 400 and 700 MPa, temperatures of 1100-1150°C and 3.9-9.9 wt.% H_2O in the melt. High H_2O contents between 6.9 and 9.9 wt.% show elevated SiO_2 contents and result in basaltic instead of basanitic residual melts. In the natural

trend, CaO starts to decrease at approximately 8 wt.% MgO. CaO depletion at this part of the trend was reproduced by \pm OI+Cpx+Spl crystallization within experiments using both starting compositions (168-1 and KLA-1-6-22) at 400 and 700 MPa, temperatures of 1050-1150°C and 0.7-6.9 wt.% of H₂O in the melt. However, as described above the clinopyroxene proportion increases with decreasing H₂O activity and residual melts resemble natural Cumbre Vieja lavas only if the proportion Cpx is below 32 wt.%, because higher proportions of Cpx result in strong CaO depletion in the residual melt and deviations from the natural trend. Conditions with Cpx proportions below 32 wt.% were achieved at 700 and 400 MPa for the primitive basanite and 550 and 400 MPa for the evolved basanite. In the natural system, Ti-rich amphibole appears below MgO contents of approximately 5 wt.% in the bulk rock composition. Ti-rich amphibole was reproduced using both starting compositions, but only the evolved composition yielded alkali-rich residual melts. Using the evolved basanite as starting material (KLA-1-6-22) crystallization of Cpx+Amph+Mt \pm OI \pm Ap produced tephritic residual melts with H₂O contents between 3.8-6.2 wt.% H₂O and variable degrees of crystallization ($j=25.4-60.5\text{ \%}$) and phonotephritic residual melts with H₂O contents of 3.1 wt.% H₂O and $j=47.7\%$. Experiments using the primitive basanite produced the same phase assemblage at temperatures in the range of 1010-1100°C and H₂O contents in the melt spanning from 1.1-11 wt.%. However, experimentally produced residual melts show elevated SiO₂ contents and low Na₂O and K₂O values.

At 400 MPa, plagioclase joins the phase assemblage at temperatures below 1075°C and low H₂O contents (below 1wt.% H₂O), resulting in phonotephritic residual melts.

P₂O₅ of natural Cumbre Vieja lavas slowly increases with decreasing MgO content until an inflection point of approximately 1.3 wt.% P₂O₅ and 5 wt.% MgO. Phosphorus is exclusively incorporated in apatite and P₂O₅ depletion at MgO contents below 5 wt.% can be directly related to apatite crystallization. Apatite was observed at low temperatures at low xH₂O, suggesting that elevated P₂O₅ values (deviating from the natural trend) at MgO contents below 5 wt.% are due to experimental temperatures or xH₂O at which apatite is not stable.

Table 29. Compositions of experimental glasses using starting composition 168-1 at 400 MPa

Run	T [°C]	melt composition														residual melt composition			
		H ₂ O [wt%]	a H ₂ O	ΔQFM	n	SiO ₂	TiO ₂	Al ₂ O ₃	FeO	MnO	MgO	CaO	Na ₂ O	K ₂ O	P ₂ O ₅	Cr ₂ O ₃	Mg#	Fe ²⁺ /ΣFe	
LP53	1010	9.77	1.58	3.08	4	58.28 (0.54)	2.16 (0.17)	18.2 (0.13)	6.04 (0.91)	0.17 (0.07)	2.48 (0.22)	6.68 (0.2)	3.07 (0.45)	1.72 (0.12)	1.16 (0.06)	-	95.12	0.04	andesitic
LP54	1010	8.71	1.30	2.91	4	59.14 (0.71)	1.97 (0.06)	17.93 (0.29)	5.94 (0.23)	0.17 (0.07)	2.59 (0.46)	5.59 (0.27)	3.71 (0.25)	1.81 (0.14)	1.09 (0.05)	0.06 (0.03)	93.60	0.05	andesitic
LP55	1010	8.33	1.21	2.84	4	58.77 (0.61)	1.8 (0.07)	17.78 (0.31)	5.74 (0.63)	0.18 (0.02)	3.02 (0.54)	5.86 (0.28)	3.93 (0.26)	1.85 (0.13)	1.03 (0.1)	0.03 (0.03)	93.87	0.06	andesitic
LP34	1025	5.60	0.64	0.68	9	44.74 (0.48)	3.61 (0.05)	15.84 (0.24)	10.97 (0.42)	0.17 (0.04)	5.73 (0.32)	12.31 (0.47)	3.95 (0.28)	1.49 (0.33)	1.2 (0.02)	-	71.52	0.37	basanitic
LP35	1025	6.62	0.83	0.91	10	48.85 (0.82)	2.55 (0.26)	18.35 (0.33)	9.7 (0.3)	0.19 (0.03)	2.72 (0.3)	9.54 (0.38)	4.24 (0.95)	1.61 (0.21)	2.22 (0.02)	0.02 (0.23)	60.85	0.32	trachybasaltic
LP36	1025	5.59	0.63	0.68	10	49 (0.71)	2.27 (0.15)	17.33 (0.39)	10.52 (0.47)	0.2 (0.04)	2.96 (0.31)	9.11 (0.3)	5.05 (0.28)	1.8 (0.1)	1.74 (0.11)	0.02 (0.03)	57.71	0.37	trachybasaltic
LP10	1050	6.45	0.87	0.40	10	44.17 (0.34)	3.7 (0.04)	13.78 (0.16)	11.66 (0.27)	0.19 (0.04)	7.79 (0.11)	13.39 (0.16)	3.29 (0.17)	1.23 (0.04)	0.75 (0.1)	0.05 (0.04)	62.07	0.73	basanitic
LP11	1050	6.42	0.79	0.32	10	44.1 (0.13)	3.82 (0.06)	14.6 (0.12)	11.57 (0.27)	0.16 (0.05)	7.44 (0.12)	12.81 (0.13)	3.4 (0.1)	1.26 (0.02)	0.78 (0.09)	0.05 (0.05)	71.39	0.46	basanitic
LP12	1050	5.61	0.64	0.14	10	43.88 (0.19)	3.98 (0.04)	15.52 (0.16)	11.6 (0.21)	0.16 (0.05)	6.76 (0.14)	12.13 (0.14)	3.72 (0.11)	1.36 (0.03)	0.88 (0.1)	0.02 (0.06)	67.81	0.49	basanitic
LP198	1025	0.50	0.03	0.7	6	50.05 (0.52)	3.04 (0.08)	17.40 (0.04)	7.50 (0.21)	0.17 (0.04)	5.70 (0.08)	8.77 (0.11)	4.6 (0.13)	1.48 (0.1)	1.20 (0.11)	0.10 (0.02)	64.27	0.76	trachyandesitic
LP199	1025	2.00	0.16	2.21	3	49.39 (0.45)	2.32 (0.07)	17.89 (0.25)	7.60 (0.19)	0.18 (0.02)	7.61 (0.23)	5.81 (0.36)	5.35 (27)	2.60 (0.13)	1.21 (0.07)	0.04 (0.01)	64.20	0.60	trachyandesitic
LP30	1050	0.50	0.03	0.11	5	53.03 (0.35)	1.83 (0.03)	19.29 (0.23)	5.55 (0.19)	0.1 (0.02)	3.88 (0.38)	5.34 (0.26)	6.2 (0.23)	2.83 (0.1)	0.01 (0.01)	1.95 (0.12)	68.19	0.58	tephriphonolitic
LP31	1050	0.50	0.03	0.11	5	48.94 (0.34)	2.24 (0.06)	21.56 (0.28)	6.32 (0.24)	0.08 (0.03)	2.55 (0.48)	4.17 (0.25)	8.75 (0.19)	3.68 (0.11)	0 (0.01)	1.71 (0.15)	55.35	0.58	foide
LP188	1050	1.13	0.07	1.55	6	51.64 (0.53)	2.23 (0.07)	20.75 (0.08)	5.84 (0.25)	0.09 (0.04)	3.11 (0.08)	4.69 (0.12)	6.79 (0.31)	3.76 (0.13)	1.09 (0.14)	0.02 (0.01)	58.09	0.68	tephriphonolitic
LP189	1050	3.21	0.30	2.76	6	50.58 (0.34)	3.07 (0.04)	17.58 (0.11)	7.58 (0.37)	0.17 (0.01)	5.77 (0.18)	8.87 (0.21)	3.61 (0.34)	1.5 (0.08)	1.21 (0.07)	0.09 (0.08)	73.24	0.50	trachy basaltic
LP216	1050	7.94	1.22	3.97	20	46.08 (0.21)	3.20 (0.07)	13.18 (0.13)	9.76 (0.12)	0.09 (0.03)	8.72 (0.08)	12.51 (0.15)	4.31 (0.19)	1.34 (0.12)	0.77 (0.06)	0.04 (0.06)	85.53	0.27	basanitic
LP190	1075	0.90	0.06	1.29	3	49.4 (0.79)	2.32 (0.24)	17.88 (1.54)	7.61 (0.43)	0.18 (0.04)	7.62 (3.15)	5.81 (0.55)	5.35 (0.45)	2.6 (0.25)	1.21 (0.06)	0.04 (0.06)	71.62	0.71	phonotephritic
LP191	1075	4.53	0.49	3.19	5	50.21 (0.46)	3.65 (0.08)	18.09 (0.35)	6.91 (0.52)	0.23 (0.05)	3.98 (0.82)	11.58 (0.27)	3.29 (0.54)	1.01 (0.1)	1 (0.08)	0.07 (0.07)	71.60	0.41	trachybasaltic
LP168	1100	0.46	0.04	1.04	10	50.16 (0.63)	2.73 (0.07)	19.04 (0.27)	8.12 (0.29)	0.12 (0.03)	4.34 (0.33)	6.89 (0.27)	4.58 (1.95)	2.78 (0.06)	1.19 (0.11)	0.06 (0.04)	56.63	0.73	phonotephritic
LP169	1100	0.71	0.04	1.04	10	49.41 (0.39)	2.79 (0.07)	18.11 (0.69)	7.46 (0.32)	0.11 (0.04)	4.94 (0.83)	7.41 (1.44)	6.1 (0.53)	2.55 (0.27)	1.08 (0.11)	0.05 (0.05)	61.83	0.73	phonotephritic
LP170	1100	5.15	0.59	3.35	23	47.58 (0.52)	3.6 (0.3)	14.74 (2.37)	8.86 (0.52)	0.15 (0.05)	7.96 (1.43)	12.2 (1.65)	2.89 (0.27)	1.3 (0.44)	0.69 (0.19)	0.04 (0.04)	80.98	0.38	basaltic
LP171	1100	3.82	0.38	2.96	10	47.05 (0.23)	3.54 (0.06)	15.19 (0.37)	8.56 (0.27)	0.14 (0.03)	7.97 (0.24)	11.02 (0.77)	4.04 (0.22)	1.7 (0.36)	0.74 (0.06)	0.08 (0.04)	78.61	0.45	basaltic trachyandesite
LP172	1100	4.16	0.43	3.07	7	47.55 (4.04)	3.07 (0.11)	16.12 (3.64)	8.52 (0.93)	0.13 (0.03)	6.9 (2.6)	9.58 (2.95)	4.93 (1.49)	2.19 (0.7)	0.99 (0.31)	0.03 (0.02)	77.01	0.43	basanitic
LP173	1100	6.86	0.93	3.74	10	45.77 (1.06)	3.23 (0.13)	12.63 (0.62)	9.9 (0.79)	0.13 (0.04)	10.49 (1.87)	12.72 (1.78)	2.89 (1.03)	1.63 (0.48)	0.58 (0.08)	0.05 (0.01)	86.15	0.30	basaltic
LP202	1125	1.73	0.12	1.99	5	44.81 (0.16)	3.66 (0.05)	15.62 (0.19)	11.36 (0.15)	0.22 (0.07)	6.36 (0.17)	10.65 (0.15)	4.66 (0.09)	1.84 (0.03)	0.8 (0.15)	0.02 (0.02)	61.87	0.61	basanitic/tephritic
LP203	1125	2.23	0.17	2.28	8	45.42 (0.11)	3.65 (0.02)	15.49 (0.16)	10.85 (0.18)	0.14 (0.04)	6.75 (0.15)	10.67 (0.23)	4.43 (0.08)	1.78 (0.03)	0.78 (0.05)	0.05 (0.04)	66.07	0.57	basanitic/tephritic
LP180	1150	1.19	0.08	1.56	10	43.74 (0.22)	3.73 (0.04)	14.81 (0.18)	13.04 (0.29)	0.15 (0.05)	6.81 (0.15)	11.13 (0.29)	4.29 (0.16)	1.53 (0.05)	0.74 (0.08)	0.03 (0.02)	58.14	0.67	basanitic
LP181	1150	0.73	0.04	1.03	10	45.02 (0.25)	3.62 (0.05)	15.46 (0.29)	11.18 (0.2)	0.14 (0.03)	7.12 (0.18)	10.53 (0.4)	4.49 (0.24)	1.63 (0.06)	0.78 (0.13)	0.03 (0.02)	60.93	0.73	basanitic/tephritic
LP182	1150	1.34	0.09	1.69	10	45.16 (0.31)	3.65 (0.05)	15.29 (0.15)	11.29 (0.14)	0.14 (0.04)	6.76 (0.13)	10.44 (0.25)	4.73 (0.21)	1.7 (0.05)	0.8 (0.1)	0.02 (0.03)	62.01	0.65	basanitic/tephritic
LP183	1150	3.89	0.38	2.96	9	44.84 (0.27)	3.33 (0.04)	12.6 (0.12)	11.21 (0.27)	0.15 (0.03)	10.52 (0.12)	12.31 (0.17)	3.21 (0.1)	1.15 (0.02)	0.61 (0.05)	0.06 (0.05)	79.05	0.44	tephritic
LP184	1150	4.87	0.53	3.25	10	44.88 (0.19)	3.21 (0.03)	12.2 (0.08)	11.06 (0.33)	0.14 (0.04)	11.63 (0.12)	12 (0.18)	3.2 (0.16)	1.12 (0.03)	0.54 (0.09)	0.02 (0.03)	82.87	0.39	tephritic
LP185	1150	6.88	0.92	3.72	10	44.17 (0.18)	3.04 (0.03)	11.44 (0.11)	11.34 (0.23)	0.17 (0.04)	12.98 (0.18)	11.48 (0.2)	3.59 (0.15)	1.26 (0.08)	0.51 (0.1)	0.04 (0.03)	87.20	0.30	tephritic

Water content of glasses was determined using the "by difference" method (see text); n, number of analyses; FeO is the total content of iron in the melt; Fe²⁺/ΣFe calculated according to the model of Moretti (2005)

Mg# of glasses is calculated as Mg/(Mg+Fe²⁺); residual melt composition after LeMaitre et al. (1989)

Table 30. Compositions of experimental glasses using starting composition 168-1 at 700 MPa

Run	T [°C]	melt H ₂ O [wt%]	α H ₂ O	Δ QFM	n	SiO ₂	TiO ₂	Al ₂ O ₃	FeO	MnO	MgO	CaO	Na ₂ O	K ₂ O	P ₂ O ₅	Cr ₂ O ₃	Mg#	Fe ²⁺ /ΣFe	residual melt composition
LP85	1050	12.14	1.31	4.03	10	48.01 (0.7)	2.74 (0.09)	15.5 (0.19)	7.84 (0.35)	0.17 (0.05)	8.24 (0.69)	12.29 (0.94)	2.76 (0.37)	1.72 (0.27)	0.71 (0.1)	0.04 (0.02)	86.10	0.30	trachybasaltic
LP86	1050	12.44	1.36	4.07	10	49.86 (0.52)	2.15 (0.05)	16.44 (0.17)	7.56 (0.22)	0.19 (0.03)	7.69 (0.15)	10.53 (0.26)	2.88 (0.23)	1.58 (0.1)	1.07 (0.06)	0.04 (0.03)	86.09	0.29	trachybasaltic
LP87	1050	12.45	1.36	4.07	6	54.46 (0.92)	1.7 (0.12)	18.15 (0.53)	6.04 (0.49)	0.24 (0.06)	3.26 (0.96)	8.89 (0.39)	3.36 (0.74)	2.18 (0.23)	1.69 (0.16)	0.04 (0.02)	77.24	0.28	basaltic trachyandesite
LP88	1050	12.12	1.30	4.03	6	56.76 (1.07)	1.53 (0.13)	19.05 (0.49)	5 (0.51)	0.2 (0.04)	2.24 (0.5)	7.24 (0.69)	3.82 (1.25)	2.14 (0.2)	1.98 (0.14)	0.03 (0.02)	73.65	0.29	trachyandesite
LP89	1050	7.40	0.61	3.37	10	55.38 (1.29)	1.44 (0.1)	16.89 (0.96)	6.64 (1.07)	0.13 (0.02)	5.48 (0.86)	6.66 (1.25)	3.5 (1.15)	2.3 (0.24)	1.54 (0.16)	0.07 (0.02)	78.69	0.40	basaltic trachyandesite
LP95	1100	8.74	0.76	3.57	22	45.39 (0.42)	3.06 (0.05)	12.3 (0.18)	10.74 (0.3)	0.13 (0.03)	11.21 (0.22)	12.86 (0.25)	2.31 (0.19)	1.42 (0.13)	0.56 (0.08)	0.04 (0.02)	83.22	0.38	basaltic
LP96	1100	8.36	0.71	3.51	10	45.54 (0.29)	3.09 (0.07)	12.59 (0.13)	10.69 (0.31)	0.17 (0.04)	10.37 (0.25)	12.92 (0.37)	2.6 (0.26)	1.41 (0.07)	0.6 (0.07)	0.03 (0.03)	81.81	0.38	basaltic
LP97	1100	9.92	0.92	3.74	15	45.91 (0.25)	3.12 (0.05)	12.86 (0.17)	10.2 (0.21)	0.14 (0.03)	9.57 (0.08)	13.06 (0.21)	3.25 (0.22)	1.27 (0.06)	0.6 (0.09)	0.04 (0.04)	82.89	0.35	basaltic
LP98	1100	10.06	0.95	3.76	12	46.43 (0.21)	3.39 (0.04)	14.47 (0.14)	9.34 (0.25)	0.16 (0.05)	8.66 (0.21)	11.7 (0.2)	3.7 (0.42)	1.42 (0.08)	0.71 (0.1)	0.04 (0.05)	82.96	0.34	trachybasaltic
LP99	1100	7.05	0.55	3.29	20	49.26 (1.81)	3.15 (0.18)	16.99 (1.04)	7.92 (0.3)	0.16 (0.05)	6.22 (1.36)	8.89 (0.87)	3.78 (0.99)	1.7 (0.3)	1.04 (0.09)	0.03 (0.03)	77.23	0.41	trachybasaltic
LP100	1100	1.25	0.06	1.34	7	48.97 (0.36)	3.14 (0.06)	18.48 (0.44)	7.4 (0.16)	0.15 (0.05)	5.39 (0.3)	6.89 (0.74)	5.37 (0.29)	2.6 (0.14)	1.56 (0.15)	0.06 (0.01)	64.66	0.71	phonotephrite
LP101	1100	2.15	0.11	1.9	7	48.72 (0.2)	3.22 (0.06)	17.92 (0.11)	7.98 (0.16)	0.15 (0.04)	5.91 (0.19)	7.16 (0.14)	5.05 (0.17)	2.29 (0.05)	1.56 (0.13)	0.05 (0.03)	67.27	0.64	basanitic
LP102	1100	5.07	0.34	2.88	14	46.5 (0.29)	3.65 (0.05)	15.2 (0.15)	9.05 (0.15)	0.18 (0.08)	8.12 (0.15)	10.42 (0.21)	4.33 (0.21)	1.58 (0.07)	0.94 (0.1)	0.05 (0.04)	76.53	0.49	tephritic
LP103	1100	5.66	0.40	3.01	11	46.7 (0.39)	3.65 (0.07)	15.09 (0.31)	9.32 (0.21)	0.19 (0.06)	8.34 (0.4)	11.08 (0.41)	3.45 (0.41)	1.22 (0.11)	0.95 (0.11)	0.03 (0.02)	77.35	0.47	basaltic
LP104	1100	5.62	0.40	3	12	45.96 (0.27)	3.52 (0.07)	14.3 (0.1)	9.64 (0.15)	0.2 (0.05)	9.11 (0.14)	11.28 (0.15)	3.68 (0.13)	1.38 (0.05)	0.88 (0.08)	0.04 (0.03)	78.17	0.47	trachybasaltic
LP115	1150	2.86	0.16	2.2	15	45.35 (0.31)	3.71 (0.05)	15.77 (0.17)	10.64 (0.2)	0.21 (0.05)	6.92 (0.08)	9.4 (0.15)	5.01 (0.19)	1.91 (0.05)	1.06 (0.09)	0.05 (0.03)	66.04	0.60	basanitic
LP116	1150	3.54	0.21	2.44	10	44.79 (0.25)	3.7 (0.05)	14.7 (0.1)	11.22 (0.52)	0.17 (0.04)	7.89 (0.16)	10.6 (0.19)	4.31 (0.24)	1.63 (0.02)	0.95 (0.12)	0.06 (0.05)	69.16	0.56	basanitic/tephritic
LP117	1150	4.35	0.27	2.68	11	45 (0.26)	3.66 (0.07)	14.63 (0.1)	10.78 (0.32)	0.21 (0.04)	8.11 (0.11)	10.78 (0.21)	4.29 (0.25)	1.56 (0.04)	0.96 (0.08)	0.02 (0.02)	72.12	0.52	basanitic/tephritic
LP118	1150	4.39	0.28	2.69	12	44.78 (0.15)	3.55 (0.06)	13.72 (0.16)	11.36 (0.32)	0.21 (0.04)	8.73 (0.24)	11.63 (0.27)	3.83 (0.16)	1.36 (0.03)	0.82 (0.08)	0.03 (0.03)	72.57	0.52	basanitic
LP154	1150	1.36	0.06	1.4	10	46.42 (0.4)	3.67 (0.11)	16.72 (0.4)	10.05 (0.24)	0.16 (0.04)	6.67 (0.98)	7.87 (0.28)	5.24 (0.17)	2.17 (0.07)	1 (0.12)	0.03 (0.03)	62.79	0.70	basanitic
LP155	1150	1.69	0.08	1.63	9	46.32 (0.21)	3.67 (0.07)	16.43 (0.23)	9.97 (0.29)	0.16 (0.04)	6.53 (0.11)	8.28 (0.15)	5.41 (0.18)	2.19 (0.03)	1.02 (0.11)	0.01 (0.01)	63.40	0.67	basanitic

Water content of glasses was determined using the "by difference" method (see text); n, number of analyses; FeO is the total content of iron in the melt; Fe²⁺/ΣFe calculated according to the model of Moretti (2005)Mg# of glasses is calculated as Mg/(Mg+Fe²⁺); residual melt composition after LeMaitre et al. (1989)

Table 31. Compositions of experimental glasses using starting composition KLA-1-6-22 at 400 MPa

Run	T [°C]	melt H ₂ O [wt%]	α H ₂ O	Δ QFM	n	SiO ₂	TiO ₂	Al ₂ O ₃	FeO	MnO	MgO	CaO	Na ₂ O	K ₂ O	P ₂ O ₅	Cr ₂ O ₃	Mg#	Fe ²⁺ /ΣFe	residual melt composition
LP44	1010	6.32	0.77	1.35	10	46.12 (0.61)	3.56 (0.08)	15.22 (0.2)	11.51 (0.19)	0.19 (0.05)	5.89 (0.13)	10.99 (0.16)	3.4 (0.49)	1.87 (0.19)	1.22 (0.14)	0.03 (0.03)	79.03	0.24	tephritic
LP45	1010	6.39	0.78	1.36	10	47.82 (0.28)	3.41 (0.03)	16.28 (0.19)	11.26 (0.32)	0.23 (0.06)	4.32 (0.48)	10.77 (0.38)	3.32 (0.22)	1.28 (0.16)	1.25 (0.09)	0.06 (0.04)	74.17	0.24	trachybasaltic
LP46	1010	5.44	0.61	1.14	10	49.18 (0.36)	2.93 (0.05)	16.94 (0.22)	10.66 (0.4)	0.21 (0.05)	3.5 (0.42)	9.5 (0.23)	4.2 (0.21)	1.79 (0.23)	1.07 (0.13)	0.02 (0.03)	67.88	0.28	tephritic
LP47	1010	4.02	0.38	0.74	10	49.72 (0.29)	2.53 (0.04)	17.29 (0.19)	10.37 (0.23)	0.19 (0.03)	3.37 (0.14)	8.14 (0.18)	4.99 (0.24)	2.42 (0.08)	0.97 (0.17)	0.01 (0.02)	62.11	0.35	phonotephritic
LP38	1025	4.34	0.43	0.94	10	47.87 (0.28)	2.89 (0.05)	15.97 (0.15)	11.22 (0.18)	0.21 (0.04)	4.33 (0.1)	8.32 (0.17)	4.91 (0.15)	2.36 (0.06)	1.85 (0.13)	0.06 (0.03)	66.26	0.35	tephritic
LP39	1025	5.86	0.68	1.34	10	46.89 (0.35)	3.15 (0.06)	15.56 (0.27)	11.92 (0.41)	0.26 (0.05)	4.28 (0.37)	9.61 (0.24)	4.55 (0.14)	1.76 (0.22)	1.98 (0.1)	0.04 (0.03)	70.03	0.27	tephritic
LP40	1025	8.12	1.16	1.8	10	44.64 (0.33)	4 (0.04)	14.38 (0.17)	11.15 (0.21)	0.2 (0.05)	6.8 (0.4)	11.89 (0.31)	3.81 (0.37)	1.77 (0.17)	1.34 (0.12)	0.03 (0.03)	84.66	0.20	tephritic
LP37	1025	8.92	1.35	1.93	10	45.8 (0.26)	3.87 (0.04)	14.66 (0.11)	11.94 (0.35)	0.23 (0.05)	5.73 (0.32)	11.49 (0.43)	3.27 (0.16)	1.18 (0.26)	1.78 (0.12)	0.05 (0.05)	83.01	0.17	basaltic
LP13	1050	6.25	0.76	0.41	10	44.53 (0.44)	4.12 (0.04)	14.11 (0.19)	11.57 (0.19)	0.19 (0.05)	7.52 (0.15)	12.54 (0.2)	2.9 (0.62)	1.52 (0.06)	0.98 (0.07)	0.03 (0.03)	72.09	0.45	basanitic
LP14	1050	5.71	0.66	0.29	11	44.14 (0.19)	4.23 (0.05)	14.88 (0.15)	11.67 (0.24)	0.17 (0.04)	6.95 (0.12)	11.91 (0.19)	3.39 (0.09)	1.6 (0.03)	1.02 (0.04)	0.04 (0.06)	69.24	0.47	tephritic
LP15	1050	4.86	0.51	0.07	11	44.31 (0.26)	4.28 (0.06)	15.52 (0.12)	11.58 (0.24)	0.17 (0.05)	6.11 (0.08)	11.15 (0.19)	3.94 (0.12)	1.75 (0.08)	1.16 (0.09)	0.02 (0.04)	64.76	0.51	tephritic
LP196	1025	0.50	0.03	0.7	4	55.34 (0.84)	1.51 (0.17)	22.6 (0.72)	3.58 (0.38)	0.11 (0.05)	1.78 (0.57)	3.09 (0.7)	6.74 (0.74)	4.73 (0.52)	0.5 (0.09)	0.02 (0.01)	53.91	0.76	tephriphonolitic
LP197	1025	0.50	0.03	0.7	4	58.32 (0.48)	1.61 (0.06)	21.53 (0.59)	3.89 (0.16)	0.1 (0.06)	1.64 (0.18)	3.14 (0.33)	5.19 (0.41)	3.9 (0.29)	0.62 (0.24)	0.05 (0.03)	49.77	0.76	trachyanedesitic
LP32	1050	0.50	0.03	0.11	9	52 (0.58)	2.22 (0.04)	20.23 (0.27)	5.18 (0.11)	0.13 (0.02)	2.95 (0.08)	4.57 (0.52)	7.14 (0.16)	3.95 (0.04)	-	1.63 (0.19)	63.64	0.58	tephriphonolitic
LP33	1050	0.50	0.03	0.11	10	49.28 (0.23)	2.14 (0.05)	21.06 (0.16)	5.64 (0.2)	0.1 (0.07)	2.72 (0.08)	4.21 (0.07)	8.85 (0.16)	4.25 (0.06)	0.01 (0.02)	1.76 (0.12)	59.79	0.58	foideite
LP213	1050	0.71	0.04	1.06	9	49.27 (0.66)	2.53 (0.1)	19.59 (1.27)	7.01 (0.28)	0.05 (0.03)	3.82 (1.35)	6 (1.82)	6.71 (0.75)	3.46 (0.43)	1.51 (0.24)	0.06 (0.03)	57.07	0.73	phonotephritic
LP214	1050	2.53	0.22	2.47	9	50.35 (0.32)	2.96 (0.04)	18.34 (0.23)	7.05 (0.16)	0.09 (0.04)	4.34 (0.2)	6.37 (0.15)	5.97 (0.22)	2.89 (0.06)	1.61 (0.14)	0.05 (0.03)	66.66	0.55	phonotephritic
LP215	1050	8.61	1.39	4.09	20	45.63 (0.46)	3.53 (0.06)	13.05 (0.31)	9.5 (0.34)	0.1 (0.03)	8.69 (0.58)	12.42 (0.83)	4.46 (0.48)	1.61 (0.4)	0.98 (0.1)	0.05 (0.04)	86.78	0.25	trachybasaltic
LP192	1075	0.58	0.03	0.83	6	49.29 (0.33)	2.83 (0.05)	19.26 (0.14)	7.33 (0.23)	0.13 (0.05)	3.9 (0.05)	6.19 (0.17)	6.18 (0.09)	3.39 (0.05)	1.49 (0.14)	0.02 (0.01)	55.92	0.75	phonotephritic
LP193	1075	1.65	0.12	1.95	6	48.77 (0.22)	2.83 (0.04)	18.93 (0.17)	7.39 (0.11)	0.13 (0.04)	4.06 (0.13)	6.39 (0.1)	6.56 (0.17)	3.4 (0.05)	1.53 (0.11)	0.02 (0.02)	60.92	0.63	phonotephritic
LP194	1075	2.51	0.21	2.44	6	49.1 (0.47)	3.31 (0.04)	17.53 (0.14)	7.44 (0.24)	0.17 (0.06)	5.36 (0.05)	7.91 (0.19)	4.89 (0.17)	2.74 (0.18)	1.22 (0.58)	0.5 (0.92)	70.00	0.55	phonotephritic
LP195	1075	8.00	1.21	3.97	12	45.2 (0.15)	3.67 (0.06)	13.05 (0.13)	9.54 (0.14)	0.18 (0.04)	8.92 (0.23)	12.75 (0.31)	4.14 (0.22)	1.75 (0.16)	0.8 (0.09)	0.03 (0.03)	86.26	0.27	tephritic
LP131	1100	7.89	1.21	3.97	15	45.34 (0.41)	3.9 (0.05)	13.3 (0.12)	10.24 (0.17)	0.16 (0.05)	8.9 (0.19)	12.24 (0.28)	3.38 (0.15)	1.75 (0.15)	0.75 (0.05)	0.04 (0.04)	85.48	0.26	tephritic
LP132	1100	6.27	0.81	3.62	15	45.64 (0.27)	3.87 (0.04)	13.65 (0.09)	9.22 (0.13)	0.18 (0.04)	9.04 (0.07)	12.12 (0.17)	3.79 (0.13)	1.68 (0.04)	0.78 (0.07)	0.04 (0.03)	84.27	0.33	tephritic
LP134	1100	2.54	0.21	2.46	20	47.53 (0.26)	3.52 (0.06)	17.36 (0.17)	8.8 (0.19)	0.16 (0.05)	5.07 (0.07)	7.83 (0.15)	5.67 (0.29)	2.81 (0.04)	1.22 (0.09)	0.05 (0.03)	65.38	0.54	phonotephritic
LP135	1100	1.06	0.07	1.46	16	48.59 (0.26)	3.44 (0.05)	18.18 (0.16)	8.22 (0.18)	0.15 (0.05)	4.7 (0.1)	7.17 (0.12)	5.27 (0.22)	2.97 (0.06)	1.29 (0.11)	0.03 (0.04)	59.71	0.69	phonotephritic
LP136	1100	1.57	0.11	1.9	11	47.29 (0.29)	3.52 (0.05)	17.53 (0.2)	9.61 (0.19)	0.16 (0.03)	4.96 (0.15)	8 (0.31)	5.01 (0.57)	2.7 (0.07)	1.21 (0.08)	0.03 (0.02)	59.29	0.63	tephritic
LP200	1125	1.65	0.12	1.93	7	44.15 (0.16)	4.09 (0.04)	15.57 (0.17)	11.47 (0.27)	0.14 (0.03)	6.11 (0.11)	10.38 (0.17)	4.85 (0.12)	2.21 (0.04)	1.02 (0.08)	0.05 (0.02)	60.35	0.62	tephritic
LP201	1125	2.19	0.17	2.26	5	44.37 (0.35)	4.09 (0.06)	14.88 (0.06)	11.54 (0.17)	0.17 (0.05)	6.76 (0.07)	10.7 (0.14)	4.46 (0.2)	2.07 (0.03)	0.91 (0.06)	0.07 (0.03)	64.59	0.57	tephritic
FC-36	1125	2.91	0.25	2.1	10	44.22 (0.33)	4.01 (0.04)	14.96 (0.14)	12.02 (0.27)	0.23 (0.05)	6.39 (0.08)	10.84 (0.13)	4.34 (0.14)	1.98 (0.04)	-	1.02 (0.08)	62.09	0.58	tephritic
FC-37	1125	3.64	0.35	2.38	11	44.6 (0.28)	3.89 (0.05)	14.03 (0.1)	11.55 (0.22)	0.2 (0.04)	7.44 (0.12)	11.71 (0.16)	3.93 (0.16)	1.76 (0.04)	-	0.9 (0.12)	68.38	0.53	tephritic
FC-38	1125	3.82	0.37	2.44	10	44.64 (0.17)	3.88 (0.03)	14.03 (0.15)	11.48 (0.16)	0.19 (0.04)	7.57 (0.1)	11.89 (0.14)	3.74 (0.11)	1.68 (0.05)	-	0.91 (0.05)	69.34	0.52	tephritic
LP217	1150	0.98	0.06	1.35	15	43.57 (0.18)	4.60 (0.13)	14.12 (0.07)	11.83 (0.11)	0.17 (0.04)	7.15 (0.08)	11.46 (0.13)	4.037 (0.14)	2.06 (0.04)	0.95 (0.05)	0.06 (0.08)	60.82	0.69	tephritic
LP218	1150	1.15	0.07	1.53	14	43.63 (0.23)	4.57 (0.09)	14.33 (0.14)	11.81 (0.16)	0.12 (0.05)	6.97 (0.21)	11.33 (0.12)	4.14 (0.12)	2.07 (0.03)	0.99 (0.1)	0.04 (0.03)	60.95	0.67	tephritic
LP219	1150	3.39	0.31	2.78	22	44.15 (0.18)	4.2 (0.06)	13.25 (0.2)	11.01 (0.23)	0.14 (0.05)	9.18 (0.13)	11.84 (0.13)	3.46 (0.13)	1.82 (0.04)	0.86 (0.08)	-	75.70	0.48	tephritic
LP220	1150	5.81	0.70	3.49	17	43.72 (0.24)	4.31 (0.11)	13.20 (0.19)	11.75 (0.15)	0.15 (0.04)	9.04 (0.15)	11.76 (0.13)	3.27 (0.07)	1.97 (0.05)	0.79 (0.07)	0.04 (0.01)	80.07	0.34	tephritic
LP174	1150	1.39	0.09	1.74	8	46.08 (0.64)	3.79 (0.13)	18.38 (0.34)	11.65 (0.51)	0.17 (0.04)	3.21 (0.26)	6.33 (0.17)	5.85 (0.35)	3.05 (0.13)	1.47 (0.1)	0.05 (0.04)	43.08	0.65	phonotephritic
LP175	1150	2.06	0.15	2.18	8	48.2 (1.1)	3.46 (0.44)	19.33 (0.55)	9.77 (0.61)	0.15 (0.03)	2.85 (0.34)	5.88 (0.39)	5.76 (0.29)	3.17 (0.2)	1.43 (0.1)	0.01 (0.01)	47.15	0.58	phonotephritic

Water content of glasses was determined using the "by difference" method (see text); n, number of analyses; FeO is the total content of iron in the melt; Fe²⁺/ΣFe calculated according to the model of Moretti (2005)Mg# of glasses is calculated as Mg/(Mg+Fe²⁺); residual melt composition after LeMaitre et al. (1989)

Table 32. Compositions of experimental glasses using starting composition KLA-1-6-22 at 550 MPa

Run	T [°C]	melt H ₂ O [wt%]	<i>a</i> H ₂ O	ΔQFM	n	SiO ₂	TiO ₂	Al ₂ O ₃	FeO	MnO	MgO	CaO	Na ₂ O	K ₂ O	P ₂ O ₅	Mg#	Fe ²⁺ /ΣFe	residual melt composition
FC-45	1075	4.81	0.40	3	6	46.55 (0.29)	3.68 (0.05)	16.3 (0.16)	7.92 (0.15)	0.19 (0.04)	7.55 (0.1)	10.16 (0.23)	4.57 (0.15)	2.08 (0.03)	1.01 (0.06)	78.54	0.46	tephritic
FC-46	1075	5.25	0.45	3.11	6	46.83 (0.34)	3.72 (0.06)	15.83 (0.22)	8.32 (0.2)	0.24 (0.06)	7.45 (0.15)	10.55 (0.4)	4.27 (0.17)	1.85 (0.18)	0.94 (0.08)	78.26	0.44	tephritic
FC-47	1075	6.49	0.62	3.39	10	46.2 (0.19)	3.76 (0.04)	14.05 (0.16)	9.04 (0.21)	0.2 (0.06)	8.55 (0.13)	11.87 (0.12)	3.76 (0.12)	1.77 (0.03)	0.81 (0.1)	81.03	0.39	trachybasaltic
FC-42	1125	3.19	0.22	1.98	10	46.07 (0.72)	3.83 (0.05)	16.32 (0.31)	10.43 (0.24)	0.21 (0.06)	5.64 (0.16)	8.76 (0.26)	4.99 (0.27)	2.46 (0.07)	1.28 (0.11)	61.25	0.61	tephritic
FC-43	1125	4.20	0.32	2.31	8	45.69 (0.29)	3.92 (0.03)	15.07 (0.08)	10.2 (0.17)	0.21 (0.07)	7.35 (0.1)	10.31 (0.19)	4.28 (0.17)	1.99 (0.05)	0.98 (0.06)	69.72	0.56	tephritic
FC-44	1125	4.35	0.34	2.35	10	45.99 (0.56)	3.86 (0.08)	14.74 (0.14)	9.09 (0.22)	0.2 (0.03)	7.94 (0.12)	11.51 (0.14)	4.07 (0.09)	1.75 (0.04)	0.84 (0.07)	73.85	0.55	tephritic
FC-7	1150	4.07	0.30	2.26	5	44.03 (0.34)	3.97 (0.06)	14.21 (0.22)	11.68 (0.19)	0.2 (0.07)	7.54 (0.14)	11.33 (0.16)	4.26 (0.12)	1.7 (0.03)	1.08 (0.09)	67.11	0.56	tephritic
FC-8	1150	1.82	0.10	1.33	5	43.88 (0.22)	3.99 (0.05)	14.08 (0.09)	12.14 (0.22)	0.21 (0.03)	7.47 (0.16)	11.26 (0.1)	4.14 (0.1)	1.75 (0.02)	1.07 (0.08)	61.17	0.70	tephritic
FC-9	1150	2.42	0.15	1.65	5	43.94 (0.12)	4.01 (0.04)	14.05 (0.14)	11.97 (0.17)	0.2 (0.07)	7.54 (0.11)	11.19 (0.04)	4.22 (0.07)	1.74 (0.05)	1.14 (0.25)	63.11	0.66	tephritic
FC-1	1175	5.41	0.45	2.61	6	44.34 (0.19)	3.85 (0.06)	13.86 (0.1)	11.33 (0.22)	0.17 (0.06)	8.31 (0.05)	11.67 (0.11)	3.98 (0.16)	1.61 (0.03)	0.89 (0.06)	72.30	0.50	tephritic
FC-2	1175	1.50	0.08	1.11	6	43.71 (0.2)	4.03 (0.04)	13.77 (0.13)	12 (0.28)	0.18 (0.04)	7.95 (0.09)	11.62 (0.24)	4.17 (0.27)	1.7 (0.04)	0.86 (0.07)	62.18	0.72	tephritic
FC-3	1175	1.71	0.10	1.26	6	43.58 (0.21)	3.97 (0.04)	13.53 (0.11)	12.1 (0.34)	0.19 (0.07)	8.28 (0.03)	11.97 (0.09)	3.83 (0.07)	1.66 (0.04)	0.89 (0.1)	63.46	0.70	tephritic

Water content of glasses was determined using the "by difference" method (see text); n, number of analyses; FeO is the total content of iron in the melt; Fe²⁺/ΣFe calculated according to the model of Moretti (2005)

Mg# of glasses is calculated as Mg/(Mg+Fe²⁺); residual melt composition after LeMaitre et al. (1989)

Table 33. Compositions of experimental glasses using starting composition KLA-1-6-22 at 700 MPa

Run	T [°C]	melt H ₂ O [wt%]	<i>a</i> H ₂ O	ΔQFM	n	SiO ₂	TiO ₂	Al ₂ O ₃	FeO	MnO	MgO	CaO	Na ₂ O	K ₂ O	P ₂ O ₅	Cr ₂ O ₃	Mg#	Fe ²⁺ /ΣFe	residual melt composition
LP63	1050	7.62	0.64	3.41	2	48.46 (0.21)	2.96 (0.2)	16.61 (0.48)	7.61 (0.02)	0.14 (0.02)	7.04 (0.27)	11.66 (0.1)	2.45 (0.14)	1.74 (0.18)	1.31 (0.17)	-	80.37	0.40	trachybasaltic
LP65	1050	7.07	0.57	3.31	20	49.28 (0.43)	2.4 (0.06)	17.64 (0.21)	6.84 (0.17)	0.18 (0.03)	6.3 (0.12)	10.02 (0.17)	3.56 (0.22)	2.22 (0.07)	1.5 (0.13)	0.05 (0.03)	79.70	0.42	trachybasaltic
LP67	1050	2.36	0.13	2.02	10	57.3 (0.66)	1.45 (0.08)	20.82 (0.35)	4.42 (0.35)	0.12 (0.03)	2.01 (0.21)	4.37 (0.39)	4.96 (0.33)	3.5 (0.22)	1 (0.16)	0.05 (0.02)	56.31	0.63	trachyandesitic
LP68	1075	7.32	0.59	3.35	30	45.05 (0.39)	3.88 (0.08)	13.6 (0.17)	10 (0.38)	0.14 (0.04)	8.94 (0.38)	12.78 (0.29)	2.83 (0.18)	1.76 (0.2)	0.96 (0.09)	0.05 (0.04)	79.33	0.42	tephritic
LP69	1075	9.94	0.94	3.75	16	44.94 (0.31)	3.73 (0.06)	13.04 (0.2)	10.06 (0.3)	0.13 (0.03)	8.87 (0.35)	12.42 (0.4)	4.11 (0.26)	1.77 (0.28)	0.89 (0.11)	0.04 (0.02)	81.89	0.35	tephritic
LP70	1075	8.57	0.75	3.55	16	46.27 (0.23)	3.33 (0.03)	15.53 (0.14)	8.49 (0.24)	0.14 (0.04)	8.12 (0.14)	11.16 (0.11)	3.83 (0.17)	1.93 (0.03)	1.15 (0.08)	0.04 (0.02)	81.85	0.38	tephritic
LP71	1075	7.00	0.55	3.29	21	47.56 (0.3)	2.85 (0.05)	16.95 (0.18)	7.8 (0.19)	0.15 (0.03)	6.43 (0.09)	9.77 (0.14)	4.74 (0.12)	2.27 (0.03)	1.45 (0.12)	0.04 (0.03)	77.80	0.42	tephritic
LP72	1075	1.94	0.10	1.8	12	51.78 (0.3)	2.26 (0.03)	19.5 (0.21)	6.63 (0.26)	0.16 (0.06)	3.86 (0.16)	6.17 (0.19)	5.27 (0.39)	2.86 (0.18)	1.48 (0.12)	0.04 (0.03)	61.18	0.66	phonotephritic
LP73	1100	8.72	0.76	3.56	28	44.63 (0.94)	3.8 (0.12)	13.5 (0.36)	10.66 (0.29)	0.2 (0.05)	8.97 (0.41)	12.49 (0.46)	2.85 (0.3)	1.81 (0.24)	1.06 (0.12)	0.03 (0.02)	79.99	0.38	tephritic
LP74	1100	6.91	0.54	3.26	18	44.81 (0.37)	3.78 (0.05)	13.42 (0.21)	10.55 (0.31)	0.22 (0.04)	8.89 (0.33)	12.65 (0.29)	3.1 (0.33)	1.54 (0.12)	1 (0.09)	0.04 (0.02)	77.87	0.43	tephritic
LP75	1100	8.54	0.74	3.54	27	44.9 (0.46)	3.76 (0.07)	13.16 (0.22)	10.57 (0.26)	0.19 (0.07)	9.02 (0.14)	12.54 (0.27)	3.23 (0.32)	1.58 (0.08)	1.02 (0.11)	0.04 (0.03)	80.05	0.38	tephritic
LP76	1100	5.81	0.42	3.05	30	45.22 (0.22)	3.9 (0.05)	14.37 (0.14)	9.65 (0.23)	0.21 (0.04)	8.49 (0.14)	11.56 (0.15)	3.6 (0.3)	1.8 (0.08)	1.16 (0.13)	0.05 (0.03)	77.22	0.46	tephritic
LP77	1100	4.26	0.27	2.67	17	47.31 (0.58)	3.96 (0.06)	16.8 (0.28)	8.72 (0.36)	0.22 (0.04)	6.25 (0.31)	8.68 (0.43)	4.26 (1.13)	2.11 (0.22)	1.65 (0.11)	0.05 (0.02)	70.94	0.52	tephritic
LP78	1150	9.97	0.91	3.72	9	43.82 (0.24)	3.55 (0.07)	13.23 (0.17)	12.26 (0.3)	0.15 (0.05)	8.93 (0.23)	12.71 (0.48)	2.86 (0.38)	1.71 (0.18)	0.72 (0.06)	0.05 (0.04)	79.22	0.34	tephritic
LP79	1150	10.13	0.93	3.74	10	44.24 (0.62)	3.54 (0.05)	13.15 (0.21)	12.03 (0.45)	0.16 (0.04)	8.79 (0.45)	12.58 (0.45)	2.98 (0.26)	1.69 (0.26)	0.75 (0.07)	0.07 (0.03)	79.43	0.34	tephritic
LP80	1150	11.17	1.09	3.88	10	44.47 (0.29)	3.5 (0.04)	13.31 (0.12)	11.58 (0.16)	0.15 (0.03)	8.84 (0.08)	12.56 (0.15)	3.18 (0.26)	1.61 (0.05)	0.76 (0.09)	0.03 (0.02)	81.23	0.31	tephritic
LP81	1150	10.06	0.92	3.73	10	44.74 (0.24)	3.53 (0.03)	13.14 (0.09)	11.01 (0.23)	0.17 (0.03)	8.87 (0.1)	12.6 (0.15)	3.58 (0.17)	1.61 (0.03)	0.71 (0.09)	0.05 (0.03)	80.92	0.34	tephritic
LP82	1150	7.79	0.63	3.4	15	44.56 (0.23)	3.61 (0.04)	13.77 (0.16)	11.18 (0.27)	0.15 (0.04)	8.43 (0.11)	11.68 (0.16)	4.06 (0.24)	1.76 (0.03)	0.78 (0.09)	0.03 (0.02)	77.32	0.39	tephritic
LP83	1150	9.13	0.79	3.6	5	44.7 (0.29)	3.5 (0.04)	13.01 (0.13)	11.3 (0.08)	0.16 (0.06)	8.81 (0.07)	12.44 (0.18)	3.65 (0.33)	1.59 (0.05)	0.82 (0.11)	0.03 (0.03)	79.42	0.36	tephritic
LP84	1150	7.90	0.64	3.41	5	44.52 (0.16)	3.58 (0.02)	13.77 (0.12)	11.26 (0.24)	0.19 (0.04)	8.36 (0.1)	11.52 (0.16)	4.16 (0.21)	1.78 (0.03)	0.82 (0.03)	0.08 (0.07)	77.13	0.39	tephritic
LP150	1150	0.50	0.02	0.39	10	45.39 (0.37)	3.94 (0.04)	16.73 (0.11)	11.52 (0.22)	0.16 (0.03)	5.25 (0.2)	7.36 (0.25)	5.6 (0.22)	2.72 (0.03)	1.32 (0.1)	0.02 (0.02)	50.90	0.78	tephritic
LP151	1150	1.49	0.07	1.5	11	44.83 (0.29)	4.12 (0.06)	15.72 (0.19)	11.08 (0.25)	0.17 (0.03)	6.6 (0.2)	8.78 (0.25)	5.25 (0.16)	2.31 (0.05)	1.12 (0.13)	0.02 (0.02)	60.61	0.69	tephritic
LP152	1150	1.53	0.07	1.53	13	44.74 (0.28)	4.14 (0.07)	15.57 (0.2)	10.93 (0.33)	0.17 (0.05)	6.8 (0.11)	9 (0.21)	5.19 (0.23)	2.29 (0.04)	1.13 (0.08)	0.03 (0.04)	61.75	0.69	tephritic

Water content of glasses was determined using the "by difference" method (see text); n, number of analyses; FeO is the total content of iron in the melt; Fe²⁺/ΣFe calculated according to the model of Moretti (2005)Mg# of glasses is calculated as Mg/(Mg+Fe²⁺); residual melt composition after LeMaitre et al. (1989)

4.4 Experiments with tephriphonolite

In the framework of this project Wengorsch (2013) investigated the phase relations and melt evolution of a natural tephriphonolite (PF22). These experiments characterize the evolution of Cumbre Vieja lavas at the late stages of magma differentiation and are complementary to the experimental data on basanites presented in this thesis. In the following the data of Wengorsch (2013) is presented to emphasize the role of fractional crystallization in the genesis of Cumbre Vieja basanite-phonolite series and to discuss the evolution of pre-eruptive storage conditions. Below the experiments of Wengorsch (2013) are briefly presented.

The tephriphonolite PF22 (2.8 wt.% MgO) was collected in the younger volcanic series of the Cumbre Vieja rift. The outcrop is interpreted as a thephriphonolitic plug (Klügel & Hansteen unpublished) and is exposed in the crater of the 1585 eruption (UTM N28 35.028 W17 51.653). The natural rock contains 12.7 vol.% kaersutite, 2.1 vol.% clinopyroxene, 3.6 vol.% plagioclase, 0.5 vol.% oxides, 0.5 vol.% hauyne and 0.1 vol.% apatite as phenocrysts and microphenocrysts. The starting glass was produced following the procedure described in Section 3.1. The composition of the starting material was confirmed by electron microprobe analyses and listed in Table 34.

Experiments were performed in an internally heated pressure vessel at 400 and 200 MPa and temperatures between 900-1050°C. The natural mineral phase assemblage of the tephriphonolite (Cpx+Krs+Pl+Mt+Ap) in the compositional range of natural minerals, was successfully reproduced in equilibrium with a phonolitic melt at 400 MPa, 1100-950°C, 0.7-2.6 wt.% H₂O in the melt and *f*O₂ conditions of FMQ+0.2 to FMQ+1.2 (Figures 42 & 43 after Wengorsch, 2013). At 200 MPa, 1000-950°C, 0.2-1.8 wt.% H₂O in the melt and *f*O₂ conditions of FMQ+0.2 to FMQ+1.8 (Figure 44 after Wengorsch, 2013).

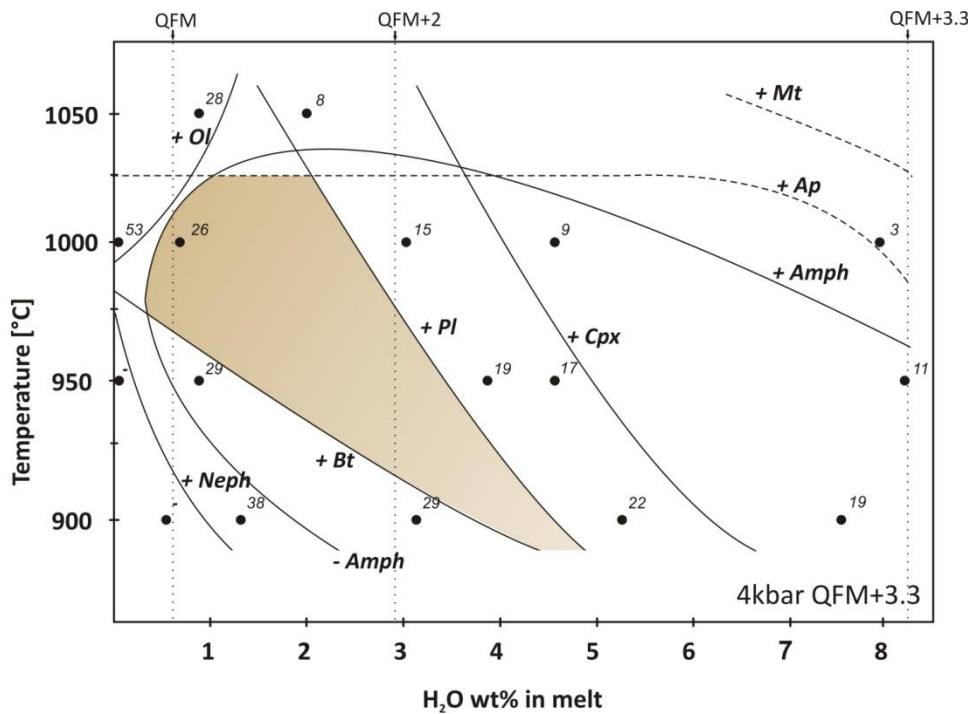


Figure 42: Phase relations for tephriphonolite PF22 as a function of H₂O content in the melt and fO₂ conditions between FMQ and FMQ+3.3 at 400 MPa after Wengorsch (2013). In this and subsequent figures the brown field indicates experimental conditions of co-crystallization of Amph+Pl+Cpx+Ap+Mt (natural phase assemblage). Dots indicate experimental conditions and numbers the crystal fraction of the particular experiment. Dashed line presents estimated stability fields and solid lines observed phase boundaries. Ol, olivine; Pl, plagioclase; Ap, apatite; Mt, magnetite; Neph, nepheline; Bt, biotite; Cpx, Clinopyroxene; Amph, amphibole.

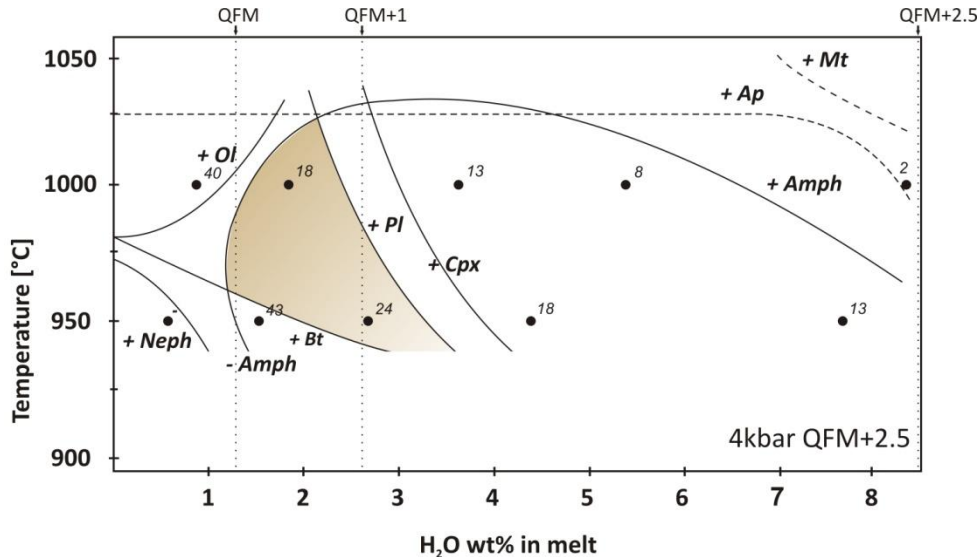


Figure 43: Phase relations for tephriphonolite PF22 as a function of H₂O content in the melt and fO₂ conditions between FMQ-1 and FMQ+2.5 at 400 MPa after Wengorsch (2013).

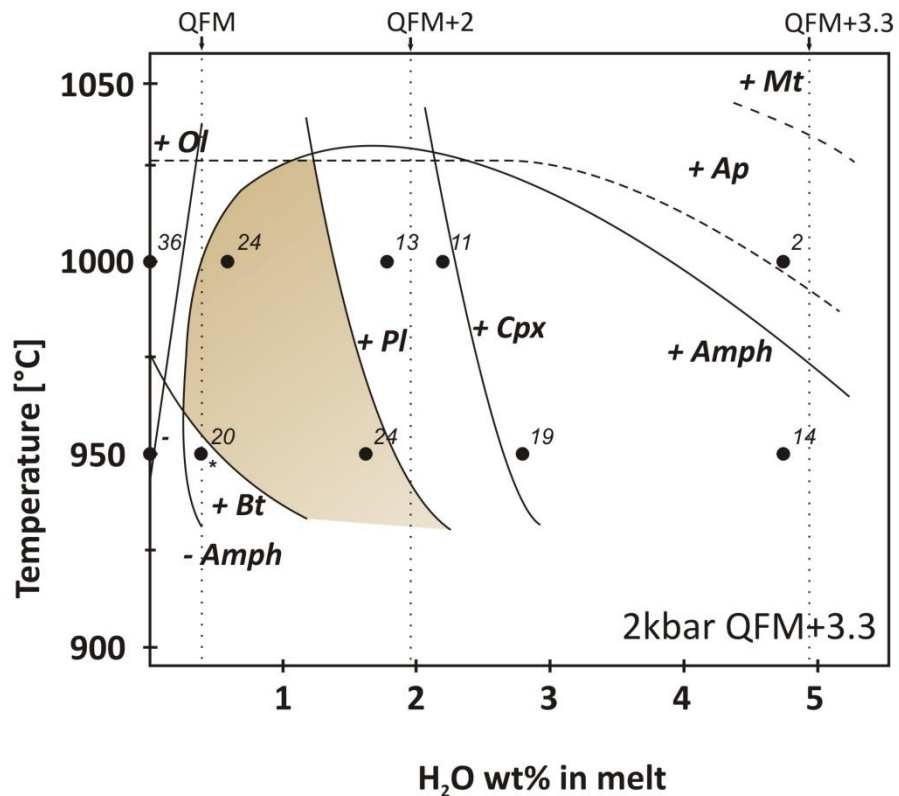


Figure 44: Phase relations for tephriphonolite PF22 as a function of H₂O content in the melt and *f*O₂ conditions between FMQ and FMQ3.3 at 200 MPa after Wengorsch (2013).

Table 34. Starting composition PF22 (tephriphonolite) Wengorsch et al. (2013)

SiO ₂	TiO ₂	Al ₂ O ₃	FeO	MnO	MgO	CaO	Na ₂ O	K ₂ O	P ₂ O ₅	Total
53.32 (0.36)	1.65 (0.07)	19.6 (0.2)	5.93 (0.06)	0.14 (0.05)	2.84 (0.02)	4.91 (0.02)	7.24 (0.17)	3.74 (0.12)	0.48 (0.05)	99.86

4.4.1 Mineral compositions

4.4.1.1 Pyroxene

In the study of Wengorsch (2013) Cpx was observed in experiments at 400 MPa, 1050-900°C, at H₂O contents in the melt between 0.5 and 5.2 wt.% and at 200 MPa, 1000-900°C, at H₂O contents in the melt between 0.5-2.8 wt.% H₂O. Cations per formula unit (pfu) were calculated on the basis of six oxygens. Cpx compositions of Wengorsch (2013) are plotted as a function of H₂O concentration in the melt and temperature for experiments conducted at 400 MPa in Figure 45 and 200 MPa in Figure 46.

Cpx data of Wengorsch (2013) show a similar dependency of decreasing Ca and increasing Si and Na pfu with decreasing H₂O content in the melt that we observed in our experiments using basanite as starting material. Decreasing the H₂O content in the melt from 4.5-0.9 wt.% at 400 MPa and e.g. 950°C leads to decreasing Si pfu increases from 1.721-1.771, increasing Ti pfu with decreasing H₂O content in the melt from 0.056-0.075 and almost constant Al pfu (0.366-0.378). Ca pfu decreases with decreasing H₂O content in the melt from 0.893-0.806 (at 950°C). Na pfu increases with decreasing H₂O content in the melt from 0.111-0.166 (at 950°C). Fe pfu increases with decreasing H₂O content in the melt from 0.290-0.324 (at 950°C).

Decreasing the H₂O content in the melt from 2.8-0.5 wt.% at 400 MPa and e.g. 950°C leads to decreasing Si pfu increases from 1.656-1.725, variable Ti pfu with decreasing H₂O content in the melt (0.063-0.077) and decreasing Al pfu from 0.433 to 0.348. Ca pfu decreases with decreasing H₂O content in the melt from 0.896-0.845 (at 950°C). Na pfu increases with decreasing H₂O content in the melt at 950°C from 0.099-0.150 (at 950°).

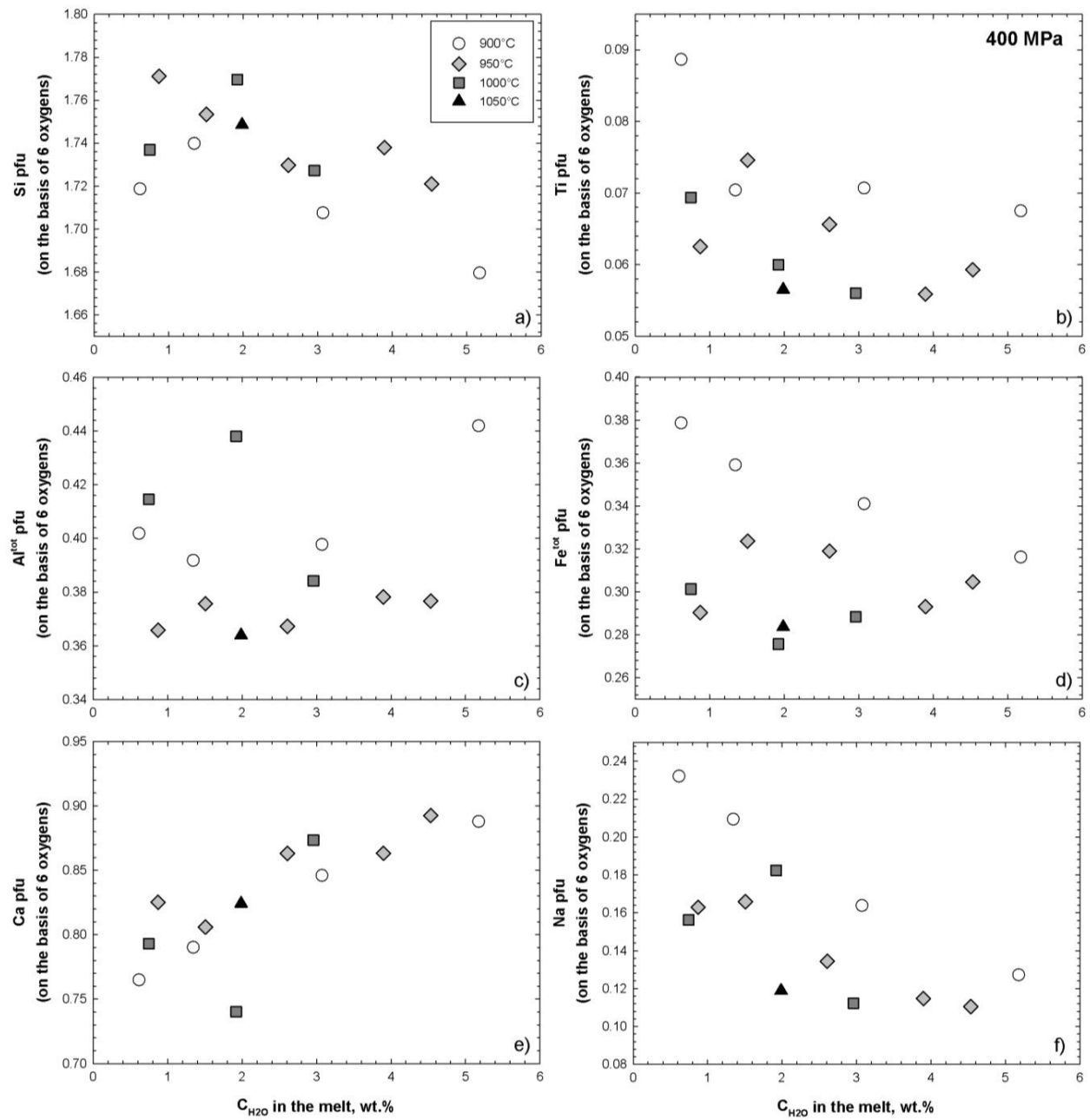


Figure 45: Variations in clinopyroxene composition using starting composition PF22 (Wengorsch, 2013) at 400 MPa as function of H_2O concentration in the melt (wt.%) and temperature ($^{\circ}\text{C}$) (unpublished data of Wengorsch, 2013).

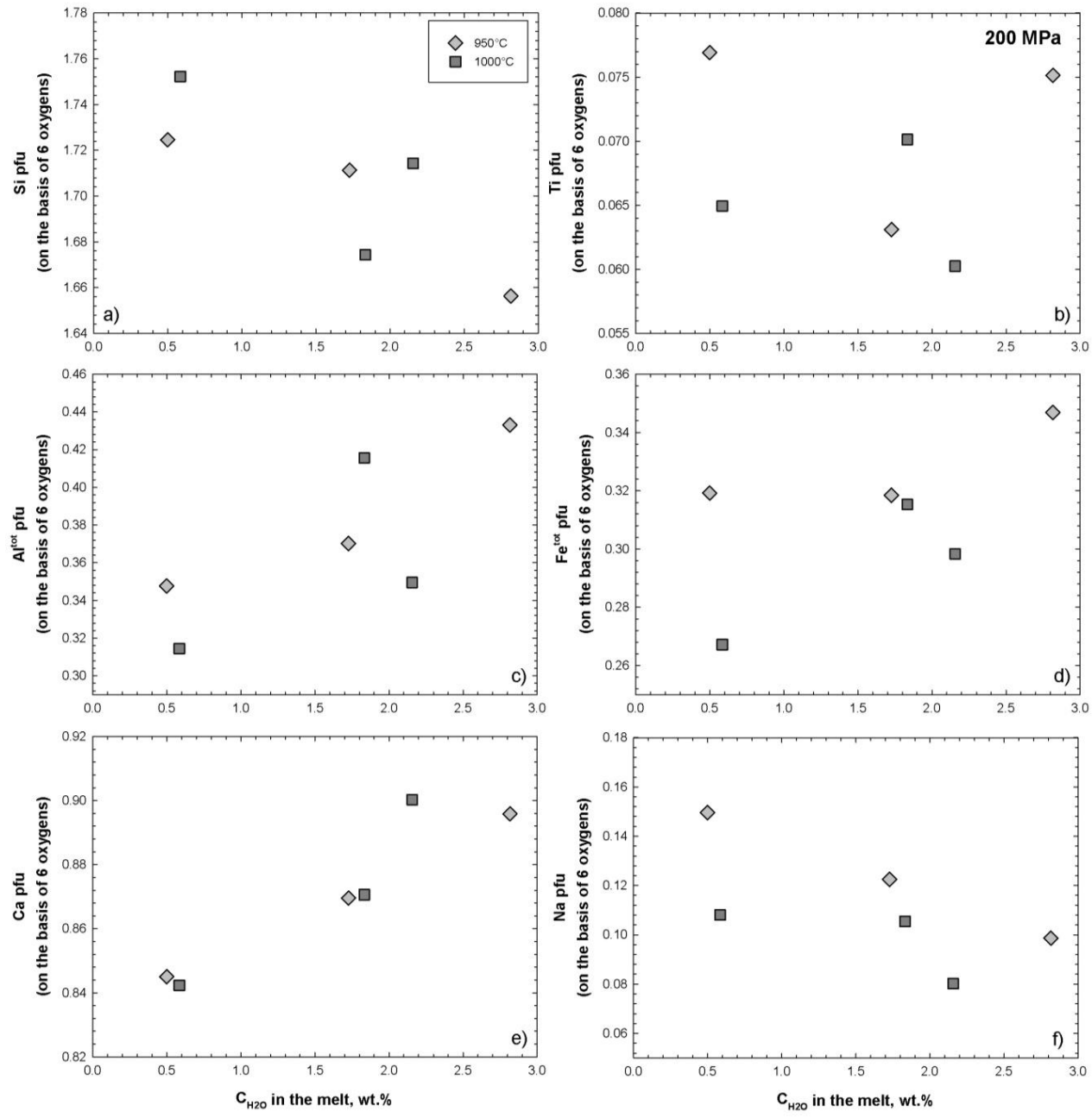


Figure 46: Variations in clinopyroxene composition using starting composition PF22 at 200 MPa as function of H_2O concentration in the melt (wt.%) and temperature ($^{\circ}\text{C}$) (unpublished data of Wengorsch, 2013).

4.4.1.2 Amphibole

In the study of Wengorsch (2013) Amph was observed in experiments at 400 MPa, 1000-900°C, at H₂O contents in the melt between 0.7 and 8.3 wt.% and at 200 MPa, 1000-950°C, at H₂O contents in the melt between 0.5-4.8 wt.% H₂O. Kaersutitic, pargasitic and magnesiohastingsitic amphibole compositions of Wengorsch (2013) are plotted as a function of *fO₂* conditions and temperature in Figure 47.

Amph data of Wengorsch (2013) shows a comparable dependency of *fO₂* conditions on Amph composition that we observed in our experiments using basanite as starting material. For example at 400 MPa, 950°C and *fO₂* conditions below FMQ+1 TiO₂ content varies between 5.1 wt.% and 6.2 wt.%, Al₂O₃ between 12.4 wt.% and 12.5 wt.%, CaO between 11.5 wt.% and 11.6 wt.%, Na₂O between 3.2 wt.% and 3.3 wt.. At the same temperature (950°C) but more oxidizing conditions (FMQ+3.29) distinctly lower TiO₂ (2.6 wt.%) and Na₂O contents (2.9 wt.%) and higher Al₂O₃ (12.9 wt.%) and CaO (12.1 wt.%) were observed. Low TiO₂ content at oxidizing condition can also be explained by the stability of high proportions of titanomagnetite at oxidizing conditions. At constant *fO₂* conditions Al₂O₃ contents increase with increasing temperature, e.g. at *fO₂* below FMQ+1 from 14.4-12.6 wt.% to 12.9-13.0 wt.% with increasing temperature from 950-1000°C. Variations in CaO and Na₂O contents depend most likely on *fO₂* conditions, but remain unclear.

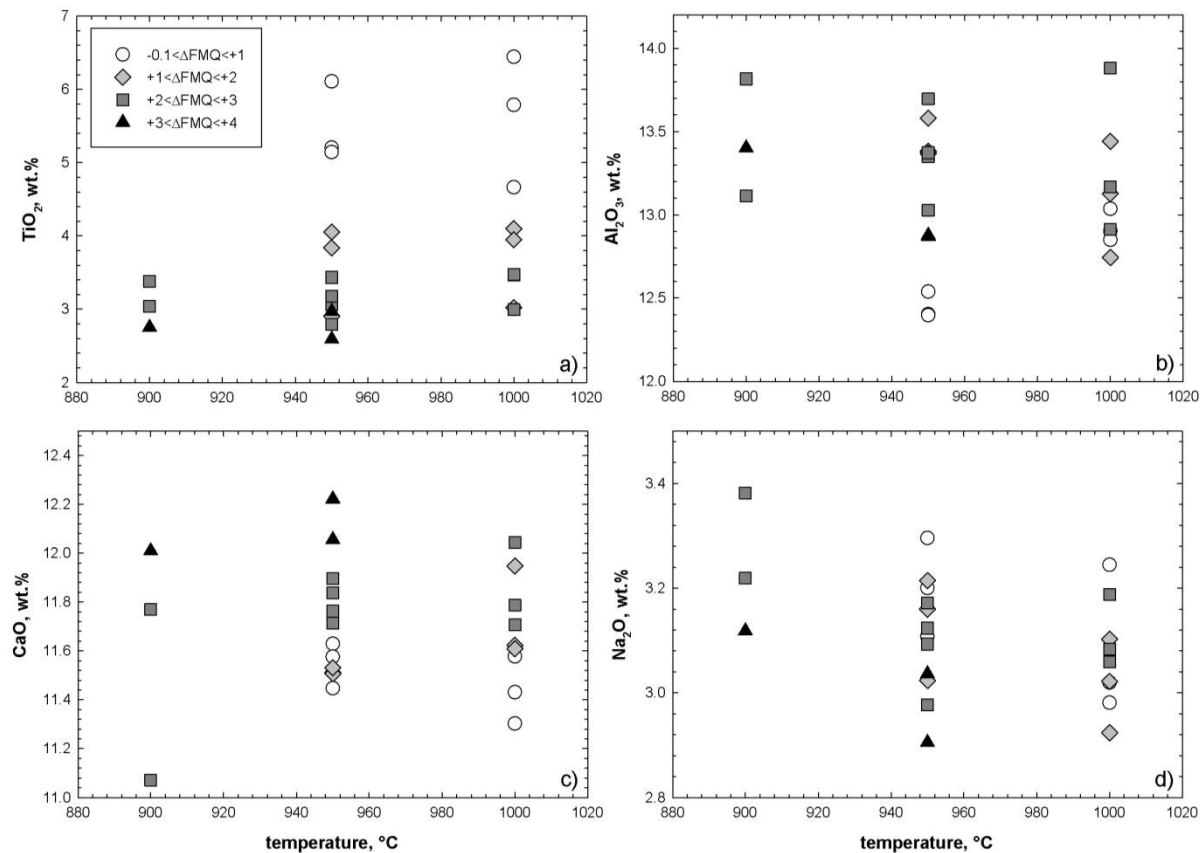


Figure 47: Effect of redox conditions and temperature ($^{\circ}\text{C}$) on amphibole composition using the tephriphonolitic starting composition at 200 and 400 MPa (unpublished data of Wengorsch, 2013).

4.4.1.3 Magnetite

In the study of Wengorsch (2013) Mt was observed at all conditions investigated, compositions are plotted as a function of $f\text{O}_2$ conditions and temperature in Figure 48.

Mt data of Wengorsch (2013) shows a comparable dependency of $f\text{O}_2$ conditions on Mg#, $\text{Fe}^{3+}\#$ and TiO_2 content of Mt that we observed in our experiments using basanite as starting material. For example at 400 MPa, $f\text{O}_2$ conditions between FMQ+1 and FMQ+2 decreasing Mg# (0.21-0.15), increasing $\text{Fe}^{3+}\#$ (0.80-0.94) and decreasing TiO_2 content (6.22-2.80 wt.%) with decreasing temperature from 1050°C to 900°C can be observed. At the same pressure but more oxidizing conditions (between FMQ+2 and FMQ+3) decreasing Mg# (0.19-0.07), increasing $\text{Fe}^{3+}\#$ (0.90-0.96) and increasing TiO_2 content (5.24-12.80 wt.%) with decreasing temperature from 1000°C to 900°C can be observed.

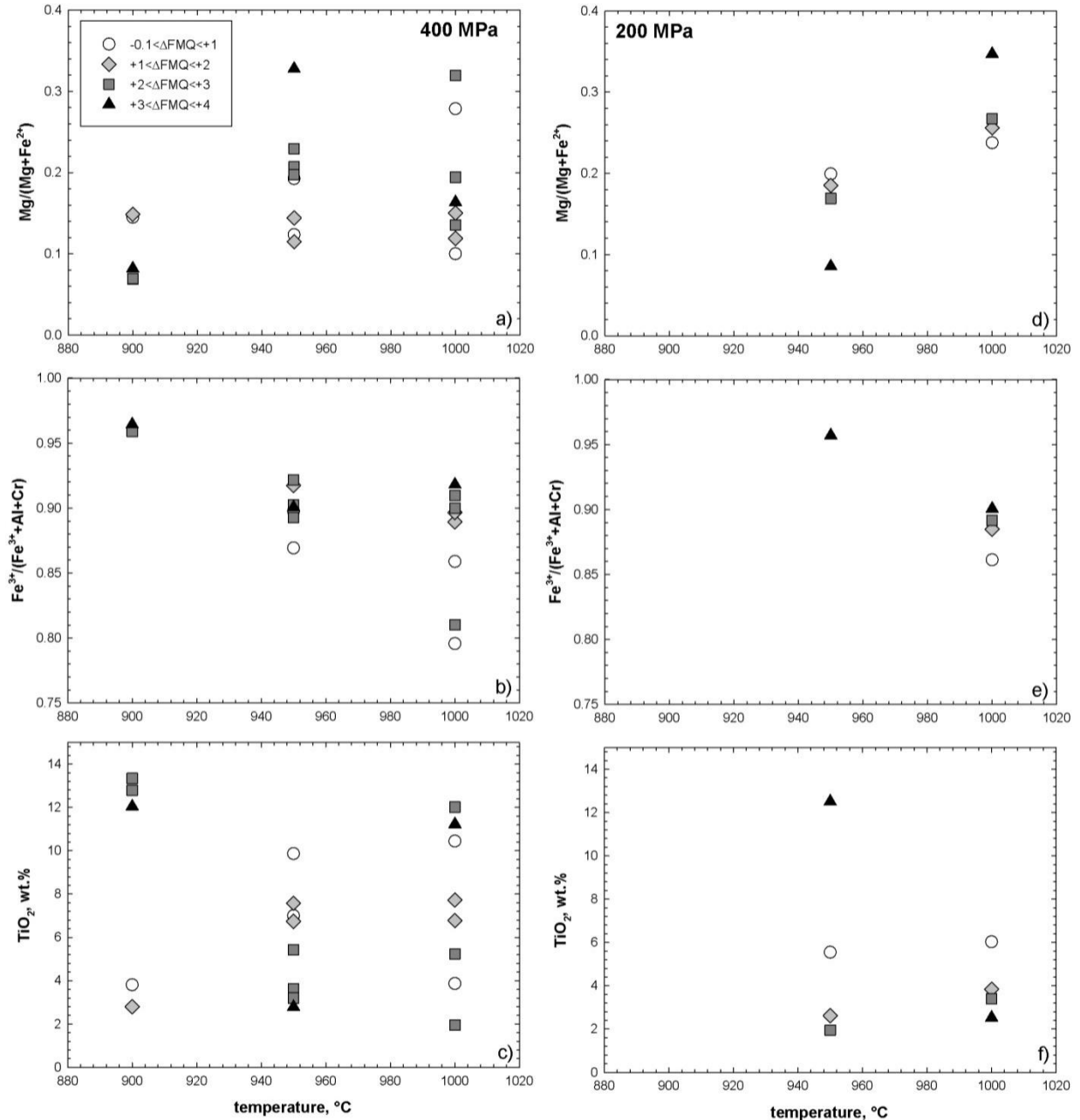


Figure 48: Effect of fO_2 on magnetite composition as a function of temperature ($^{\circ}C$) using the tephriphonolitic starting composition at 400 (a, b, c) and 200 MPa (d, e, f) (unpublished data of Wengorsch, 2013).

4.4.1.3 Glass

Residual melt compositions using tephriphonolitic starting composition PF22 used in the study of Wengorsch (2013) are shown as a function of aH_2O and fO_2 conditions in Figure 49 and Figure 50, respectively. Residual melts show systematically increasing SiO_2 , Al_2O_3 , Na_2O contents

and K₂O and decreasing TiO₂, FeO^{tot}, CaO, P₂O₅ contents with progressive crystallization (decreasing temperature). Major elements follow the natural trend of Cumbre Vieja evolved lavas. Deviating high Al₂O₃ contents (MgO: 0.38-0.95 wt.%) in the residual melt were observed at low H₂O contents in the (0.5-1.3 wt.%), those melts coexist with Pl+Ne+Cpx±Bt+Mt and were generated at 400 MPa and 950-900°C. Slightly lower Na₂O contents at high aH₂O can be related to sodium loss in the glass. Variations of SiO₂, TiO₂ and FeO^{tot} at constant MgO content can be explained by the prevailing *f*O₂ condition and corresponding Mt composition and proportion. Variations of CaO as function of aH₂O at constant MgO content can be observed and be related to the increasing Cpx proportion with decreasing aH₂O (Wengorsch, 2013).

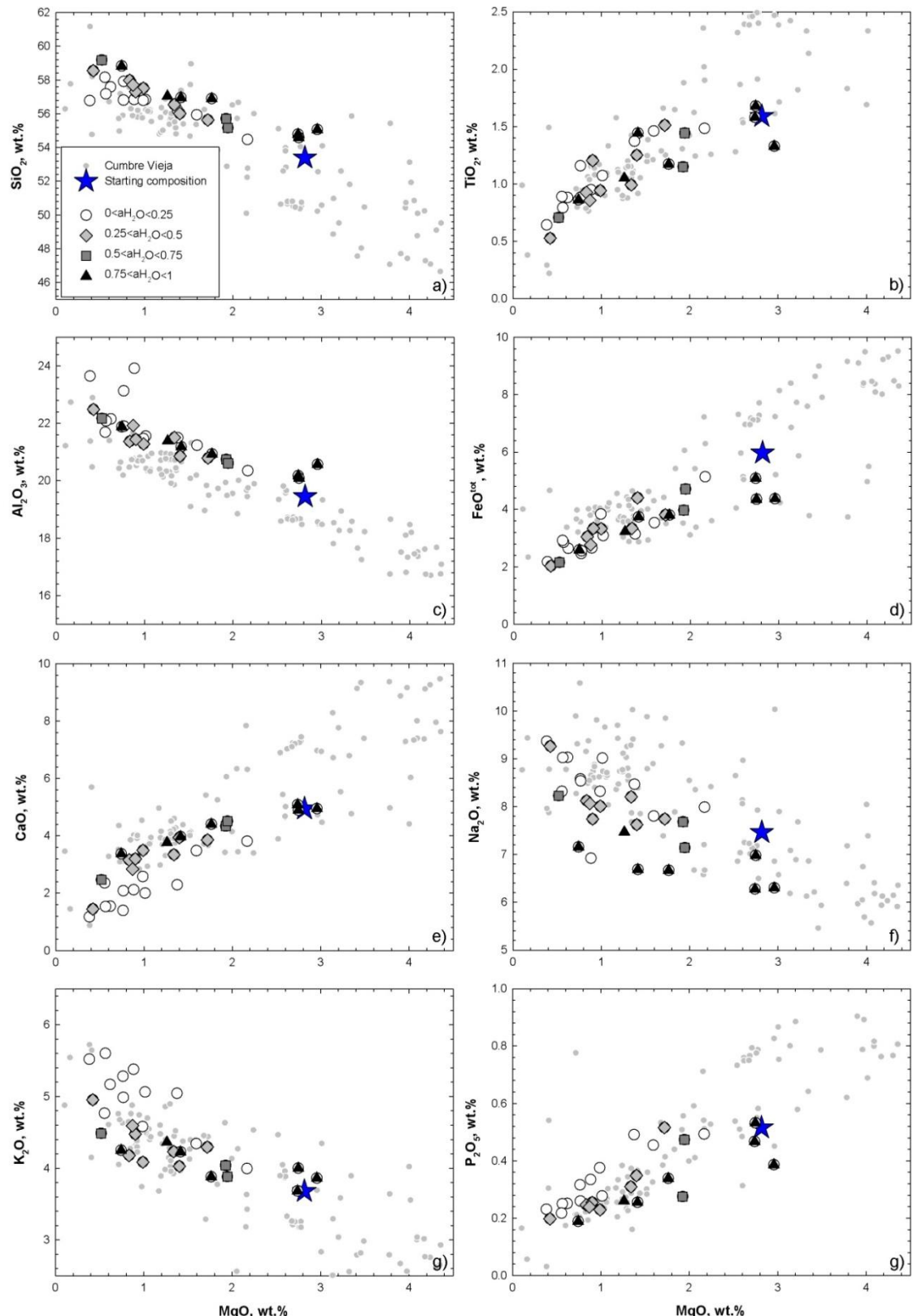


Figure 49: Effect of aH_2O on residual melt composition using the tephriphonolitic starting composition at 200 and 400 MPa (unpublished data of Wengorsch, 2013).

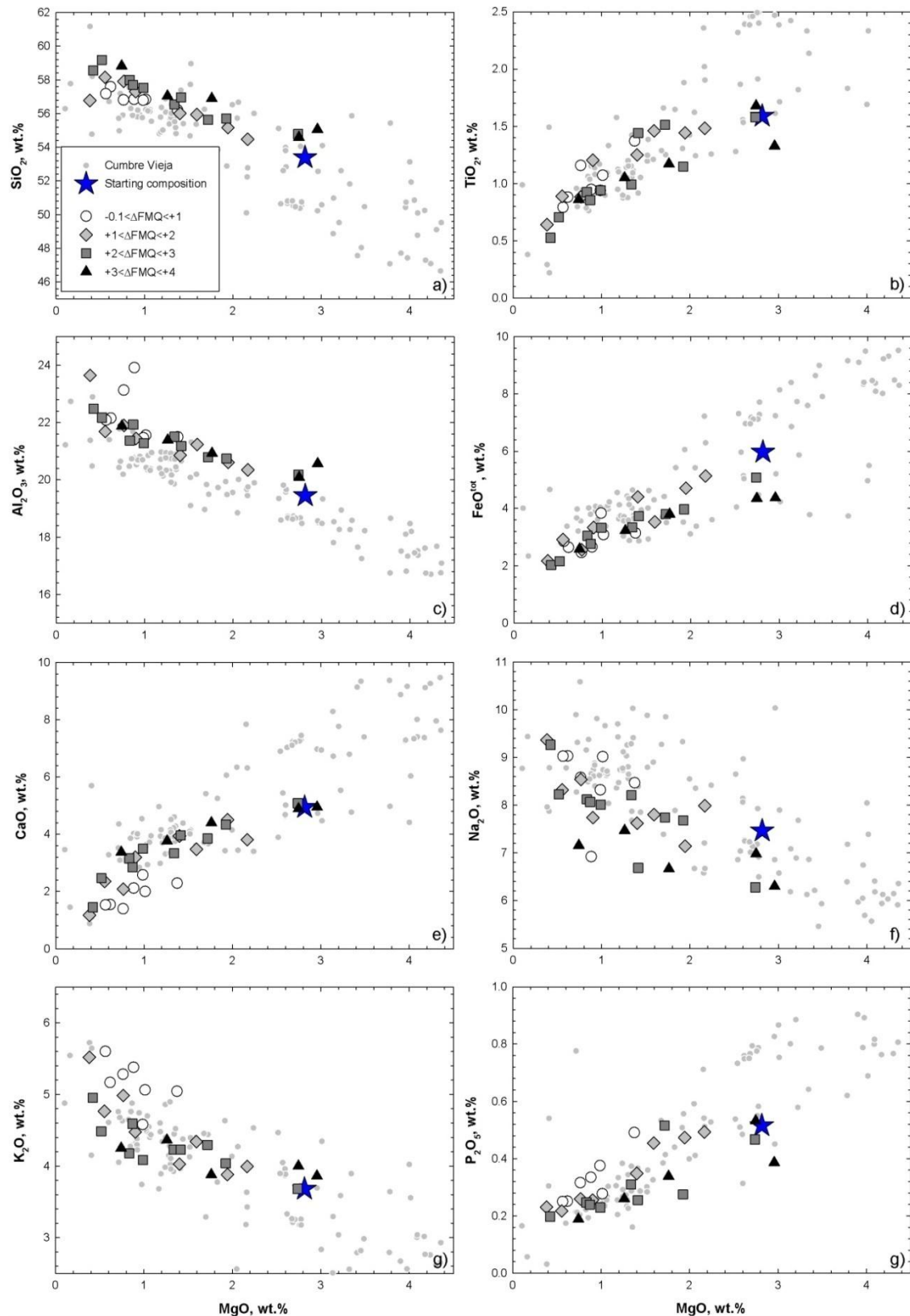


Figure 50: Effect of $f\text{O}_2$ on residual melt composition using the tephriphonolitic starting composition at 200 and 400 MPa (unpublished data of Wengorsch, 2013)

5. Discussion

5.1 Melt compositions

5.1.1. Database used in discussion

The database used for discussion includes the results of experimental investigations using starting material 168-1 (primitive basanite) and KLA-1-6-22 (evolved basanite) and PF22 (tephriphonolite used in the study of Wengorsch, 2013). All experiments were conducted in internally heated pressure vessels in the presence of a $\text{H}_2\text{O}-\text{CO}_2$ fluid ($X\text{H}_2\text{O}$ varied between 0 and 1, keeping $f\text{O}_2$ between $\sim\text{FMQ}$ and $\text{FMQ}+3.8$). Experiments using basanite were performed in the pressure range from 400 to 700 MPa and temperatures between 1010-1175°C. Wengorsch (2013) investigated the phase relations of a natural tephriphonolite (PF22) at 200 and 400 MPa and temperatures between 900-1050°C.

5.1.2 Effect of redox conditions on the liquid line of descent

Figure 51 presents compositional variations of experimental residual melts projected from the Pl apex on the pseudoternary plane OI-Di-Ne, using the projection scheme after Sack et al. (1987). This projection is very sensitive for slight changes in SiO_2 , Al_2O_3 , MgO , CaO and alkalis and discriminates between Qtz-normative and Ne-normative melts.

In Section 5.1.2 we demonstrated that oxygen fugacity controls the evolution of residual melts, as at high $f\text{O}_2$ conditions melts coexist with high proportions of magnetite and consequently are depleted in FeO^{tot} and enriched in SiO_2 . As one can see in Figure 51, at the stage of basaltic to trachybasaltic and basanitic to tephritic liquid compositions, all experimental liquids, independent of redox conditions, closely resemble natural Cumbre Vieja compositions because (a) SiO_2 enrichment is moderate at this evolutionary state and (b) the pseudoternary OI-Di-Ne plane is not sensitive to slight changes in FeO content. However, it becomes evident in the Harker diagrams (see Figure 38), that those melts deviate from the natural Cumbre Vieja lavas with respect to their FeO^{tot} content, having elevated FeO^{tot} contents under reducing and lower FeO^{tot} under oxidizing conditions. However, basanitic to tephritic melts resemble natural Cumbre Vieja lavas at $f\text{O}_2$ conditions between $\text{FMQ}+1$ and $\text{FMQ}+2$ (see Figure 38). The effect of redox conditions on LLDs (SiO_2 enrichment and FeO^{tot} deviation) is extremely pronounced at higher degrees of crystallization. Evolved melts generated at oxidizing conditions ($\text{FMQ}+3$ to

FMQ+4) trend away from natural Cumbre Vieja lavas towards Qtz-normative compositions and follow a calc-alkaline differentiation trend (black diamonds in Figure 51). In contrast, evolved tephriphonolitic to phonolitic melts produced at reduced conditions (FMQ to FMQ+2) following the Ne-normative evolutionary trend towards alkali-rich, but silica undersaturated compositions (e.g. when recalculated on the CIPW-norm basis).

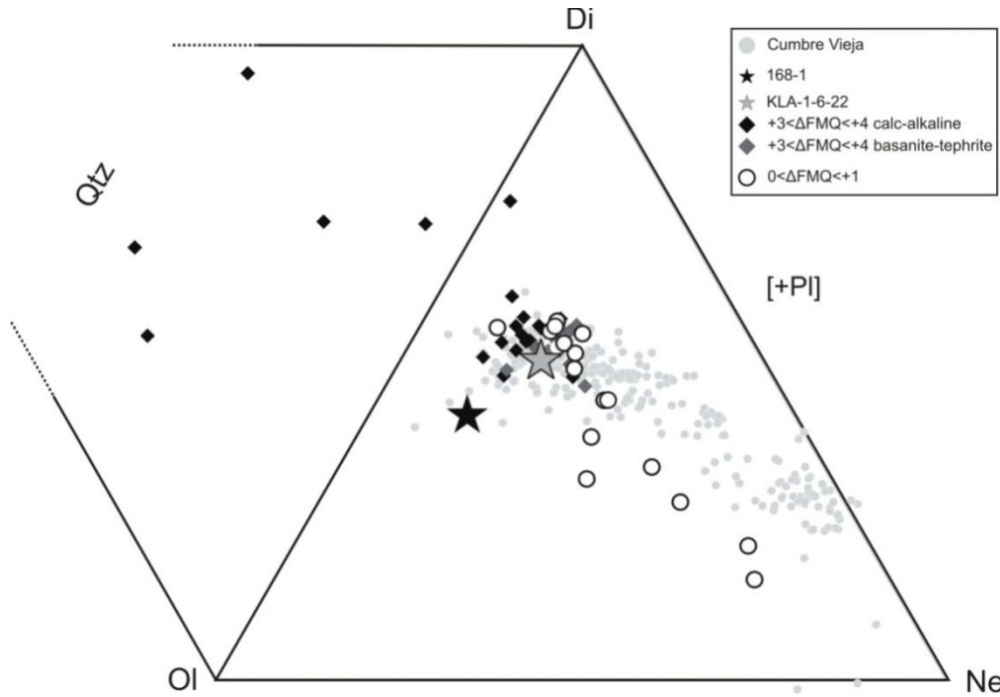


Figure 51: Effect of $f\text{O}_2$ conditions on residual melt evolution in comparison to natural Cumbre Vieja lavas (gray circles) in a pseudoternary projection from the basalt tetrahedron on the OI-Di-Ne plane (projection from PI) after Sack et al. (1987). At oxidizing conditions (FMQ+3 to FMQ+4; black diamonds) residual melts evolve towards the Qtz apex. At more reducing conditions (FMQ to FMQ+1; white circles) residual melts evolve towards the Ne-apex. The black star indicates sample 168-1 and the gray star sample KLA-1-6-22.

5.1.3 Effect of $a\text{H}_2\text{O}$ on the liquid line of descent

In Sections 4.1 and 4.2 (phase relations and proportions) we demonstrated that mineral proportions are strongly affected by the prevailing $a\text{H}_2\text{O}$ and by temperature. In Section 4.3.8 we demonstrated how residual melts evolve at high temperatures (temperatures above Amph stability) and at low temperatures (Amph stable) depending on $a\text{H}_2\text{O}$. At temperatures above Amph stability the degree of crystallization increases with decreasing H_2O in the melt and residual melts evolve continuously as a function of decreasing $a\text{H}_2\text{O}$. At low temperatures (Amph stable: at 400 MPa below 1050°C; at 700 MPa below 1100°C) residual melts evolve along two different trends: at low $a\text{H}_2\text{O}$ Cpx predominates over Amph in the Cpx+Amph assemblage

resulting in CaO depletion (plotting at the lower limit or below the natural LLD) and Al₂O₃ enrichment in the residual melt (resembling the upper limit of the natural LLD) (see Figures 39-41). At high aH₂O Amph predominates over Cpx resulting in rather high CaO contents, (plotting on the upper limit of the natural LLD), but less pronounced enrichment in Al₂O₃ in the residual melt since Amph incorporates up to 14 wt.% Al₂O₃ (see Figures 39-41). From this observation we can suggest that variations in CaO and Al₂O₃ in the residual melt can be explained by different proportions of crystallized Amph and Cpx depending on aH₂O and temperature. Tephriphonolitic melts were generated at low H₂O activities and low temperatures (1025-1050°C) by a high degree of crystallization (62 -75%) at 400 MPa. At these conditions high Cpx (36.4-51.6 wt.%) and low Amph (0-14.5 wt.%) proportions result in low CaO (3.05-5.32 wt.%) and high Al₂O₃ contents (19.22-22.28 wt.%) in the residual melt. In Figure 52 is shown that these melts deviate from the natural Cumbre Vieja lavas in the ternary pseudoternary OI-Di-Ne plane projection(projected from the Pl apex), since this projection is very sensitive for slight changes in Al₂O₃ and CaO.

The data of Wengorsch (2013) demonstrate that variations of aH₂O in evolved melts (tephriphonolitic to phonolitic) do not significantly change the residual melt composition, as all residual melts follow the same direction towards the Ne apex (Figure 52).

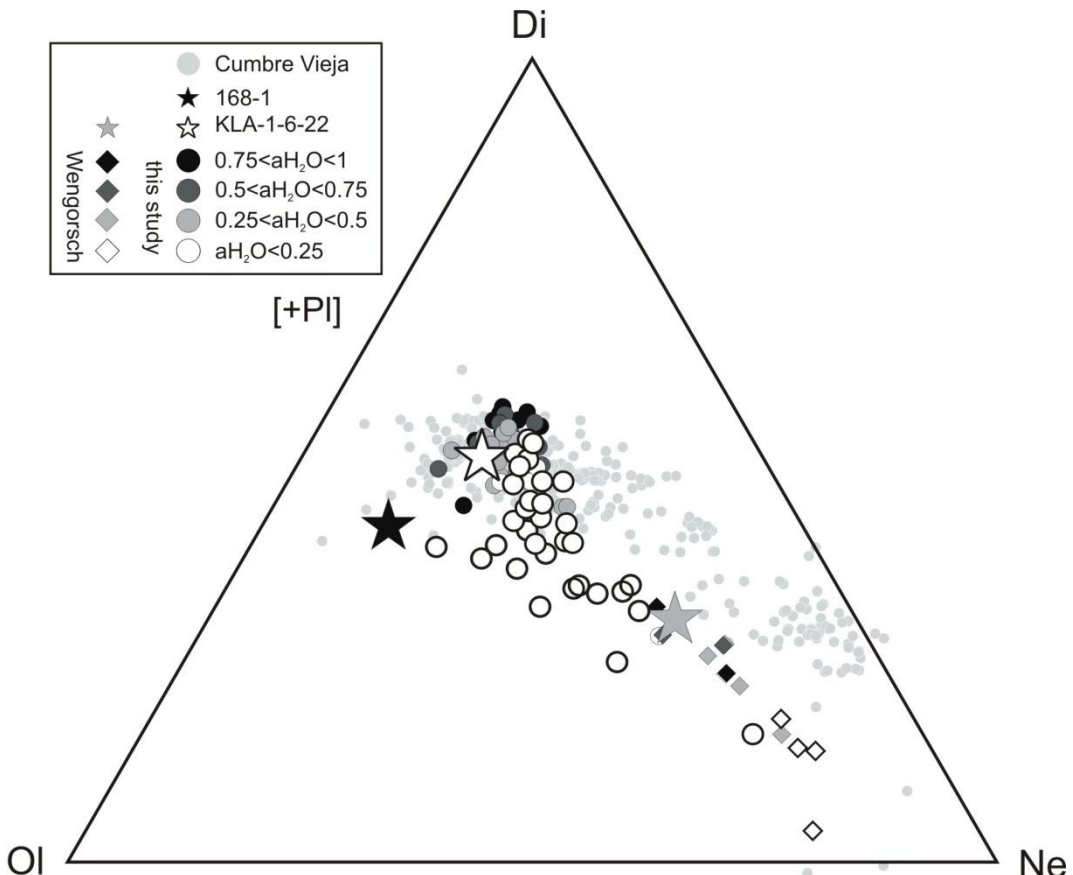


Figure 52: Effect of aH_2O on residual melt evolution in comparison to natural Cumbre Vieja lavas (gray circles) in a pseudoternary projection from the basalt tetrahedron on the Ol-Di-Ne plane after Sack et al. (1987). Evolved melts generated at low aH_2O ($aH_2O < 0.25$, white circles) deviate from the natural LLD, due to crystallization of high Cpx proportions.

5.1.4 Formation of phonolitic melts

In our experimental study tephriphonitic melts were generated at low H_2O activities (0.02-0.25; 0.5-1.13 wt% H_2O in the melt) and low temperatures (1025-1050°C) by a high degree of crystallization 61.8-74.5%. We already demonstrated that at these conditions, high Cpx and low Amph proportions were observed resulting in low CaO (3.05-5.32 wt.%) and high Al_2O_3 contents (19.22-22.28 wt.%) in the residual melts. Our experimentally generated tephriphonolitic residual melts match the tephriphonolitic starting composition of Wengorsch (2013) (Figure 53). However, this starting composition has an Al_2O_3 content of 19.60 ± 0.2 wt.% (plotting on the upper limit of the natural trend) and a CaO content of 4.91 ± 0.02 wt.% (plotting on the lower limit of the natural trend). From our observations of melt evolution with different aH_2O we can assume that the tephriphonolite PF22 (Wengorsch, 2013) was generated at low aH_2O and low

temperature. This assumption is in agreement with the results of Wengorsch (2013) since phase relations of the natural sample were reproduced at H₂O contents of 0.5-2.0 wt.% at 200 MPa, 950-1000°C and at H₂O contents of 0.5-3.1 wt.% at 400 MPa, 900-1000°C.

Experimental residual melts derived from sample PF22 (Wengorsch, 2013) evolve in the direction of the natural Montana Enrique phonolite which has a crystallinity <5%. This is contrasting with other Cumbre Vieja phonolites which have a crystallinity of 20-25%. Considering that natural Cumbre Vieja lavas shown on the ternary diagram (Figure 53) are bulk rock compositions, we can suggest that the presence of 20-25% crystals strongly shift to Di-enriched compositions on this ternary projection, and compositions of the Montana Enrique natural phonolites are closer to a "true" liquid composition. Based on our experimental investigations another explanation is that phonolites with lower Al₂O₃ and higher CaO were generated at higher aH₂O (with higher Amph and lower Cpx proportions compared to PF22). Assuming that if Wengorsch (2013) had chosen a starting composition with lower Al₂O₃ and higher CaO contents (red star in Figure 53) the residual melts would have followed the trend of crystal-rich phonolites.

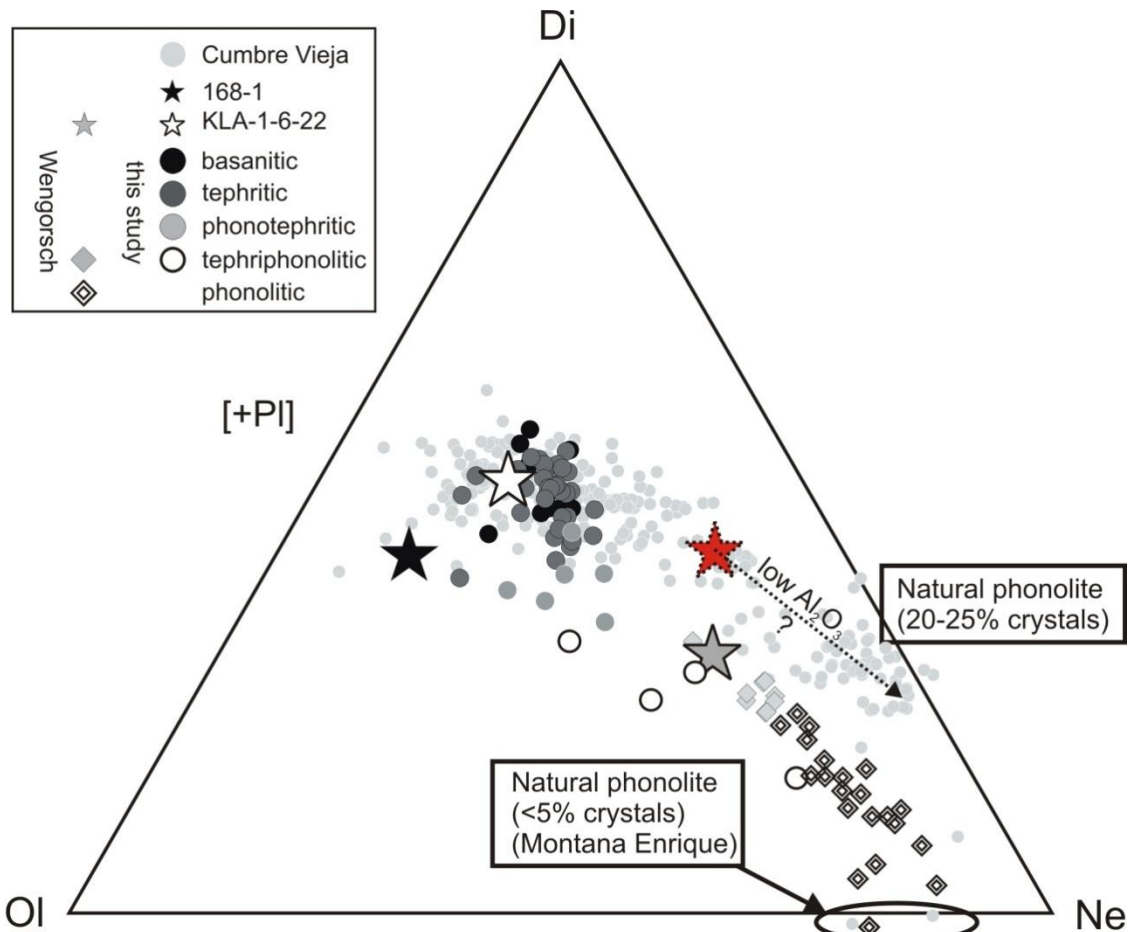


Figure 53: Residual melt composition in comparison to natural Cumbre Vieja lavas in a pseudoternary projection from the basalt tetrahedron on the OI-Di-Ne plane after Sack et al. (1987). Red star indicates a theoretical starting composition with lower Al_2O_3 and higher CaO content compared to PF22 (tephriphonolitic starting composition used in the study of Wengorsch, 2013; indicated as gray star). Residual melts generated from sample PF22 evolve towards the composition of Montana Enrique phonolite (Wengorsch 2013).

5.1.5 Effect of pressure on the liquid line of descent

Tephritic residual melts resemble the natural LLD only if the proportion of Cpx is below 32 wt.%, because crystallization of higher Cpx proportions leads to a stronger decrease in CaO in the liquid phase. Such conditions were achieved in experiments where liquids were in equilibrium with $\text{Ol}+\text{Cpx}+\text{Spl}$ mineral assemblage, at pressures between 700 and 400 MPa for the primitive basanite and between 550 and 400 MPa for the evolved basanite. Tephritic residual melts generated by $\text{Ol}+\text{Cpx}+\text{Spl}$ crystallization at 700 MPa from the evolved basanite are strongly depleted in CaO since with increasing pressure from 400 MPa to 700 MPa, e.g. at 1150°C and low aH_2O (0.02-0.25) Cpx proportions increase from 12.4-13.9 wt.% (at 400 MPa) to

41.4 wt.% (at 700 MPa). This distinct increase of Cpx proportion with pressure suggests that crystallization pressures of the evolved basanite should be below 700 MPa in order to match natural compositions.

However, it should be noted, that at 700 MPa tephritic melts saturated with Cpx+Amph+Mt (with Cpx proportions below 23.4 wt.%) also resemble natural Cumbre Vieja lavas, indicating that natural Cpx+Amph+Mt-phyric magmas can be also generated at greater depths within the magmatic conduit(s).

5.2 Mineral compositions

5.2.1 Comparison of olivine compositions

In this chapter we compare experimental to natural olivine compositions (in terms of their forsterite content) of the natural basanitic samples (168-1 and KLA-1-6-22) in order to constrain crystallization temperature and prevailing fO_2 . In our experiments using the primitive basanite we observed forsterite contents in the range of natural forsterite contents (natural: 84.3 ± 0.7 mole%; experimental: 84.0-84.3) at experimental conditions of: 400 and 700 MPa, 1100-1150°C, low H_2O contents in the melt (1.36-2.23 wt.%) at fO_2 between FMQ+1.40 and FMQ+2.28 in equilibrium with a basanitic or tephritic melt (Mg# 62.79-67.27). For the evolved basanite we observed forsterite contents resembling the forsterite content of the natural sample (natural: 83.5 ± 0.4 , experimental: 83.4-83.6) at 400 and 550 MPa, 1125-1175°C, low H_2O contents in the melt (1.50-2.19 wt.%) and fO_2 between FMQ+1.11 and FMQ+2.26 in equilibrium with tephritic melt (Mg# 62.18-64.59). Using the same starting composition at 700 MPa highest forsterite contents did not exceed 82.2-82.8 mol%, observed at 1150°C, fO_2 between FMQ+1.50 and FMQ+1.53 (H_2O content in the melt: 1.49-1.53 wt.%, in equilibrium with tephritic melts [Mg# 60.61-61.75]). To equilibrate olivines with a forsterite content in the range of natural forsterite content at 700 MPa crystallization temperatures have to be elevated up to approximately 1200°C. However, assuming that the evolved basanite (KLA-1-6-22) derived from a primitive parental magma by polybaric fractional crystallization, the slightly lower forsterite content of the natural evolved basanite compared to the natural primitive basanite can be related to magma cooling at fO_2 conditions between FMQ+1 and FMQ+2.

Comparison of natural and experimental forsterite contents allow us to constrain the crystallization temperature and redox conditions at given pressure, as forsterite contents of experimental olivines resemble their natural counterparts at high temperatures (1100-1175°C) and at similar $f\text{O}_2$ conditions (FMQ+1.11 to FMQ+2.28). However, constraints on H_2O content of the natural melts using the forsterite content of experimentally derived olivines are not straightforward. Even though H_2O contents in the melt are low for both basanitic starting materials (1.36-2.23 wt.%), but in the experimental setup H_2O activity is directly linked to $f\text{O}_2$ conditions and (as described in the results chapter) forsterite content is primarily controlled by temperature and redox conditions. Thus, according to our experimental data, olivines of sample 168-1 could have crystallized at temperatures between 1100 and 1150°C at $f\text{O}_2$ conditions between FMQ+1.40 and FMQ+2.28. Cumbre Vieja Ol of sample KLA-1-6-22 could have crystallized at slightly lower temperatures (1125°C) at 400 MPa or higher temperatures (1175°C) at 550 MPa at similar $f\text{O}_2$ conditions (FMQ+1.11 and FMQ+2.26).

5.2.2 Comparison of Cpx compositions

Figure 54 shows natural Cpx compositions of both basanites and of the tephriphonolitic starting composition used in the study of Wengorsch (2013) in comparison to experimental Cpx using starting composition 168-1 and KLA-1-6-22 at all pressures investigated (400-700 MPa). Mg# of experimental Cpx varies considerably from 85.6 to 71.6 in basanitic, from 83.6 to 71.3 in tephritic, from 74.8 to 71.0 in phonotephritic and from 75.2 to 70.9 in tephriphonolitic melts. Experimental Cpx compositions resemble natural Cpx compositions at Mg# ranging from 85 to 75 (see Figure 54), at lower Mg# experimental Cpx compositions deviate from natural Cpx compositions. Mg# below 75 of natural Cpx compositions corresponds to Cpx compositions of the natural tephriphonolite (PF22, Wengorsch, 2013) and to green-core clinopyroxenes. In Figure 54 it becomes evident that the deviation of experimental Cpx compositions from natural Cpx compositions at Mg# below 75 becomes larger with decreasing H_2O activity. At low $a\text{H}_2\text{O}$ we observed elevated Ti, Al^{tot} and Na and lower Ca and Si in comparison to natural Cpx compositions. From this observation we can suggest that deviations from natural Cpx compositions can be directly related to $a\text{H}_2\text{O}$. In our study we observed the same compositional tendencies of low Ca and Si and high Na, Ti and Al^{tot} in Cpx at low $a\text{H}_2\text{O}$ at pressures between

400 and 700 MPa and all temperatures investigated. This observation suggests that, achieving chemical equilibrium in Cpx at low H_2O activities is a general experimental problem even at run durations of a few days. This is in accordance with the frequent observation of sector zonations in Cpx from natural samples from La Palma and other places, indicating chemical disequilibria even at comparatively growth rates (Brophy et al., 1999).

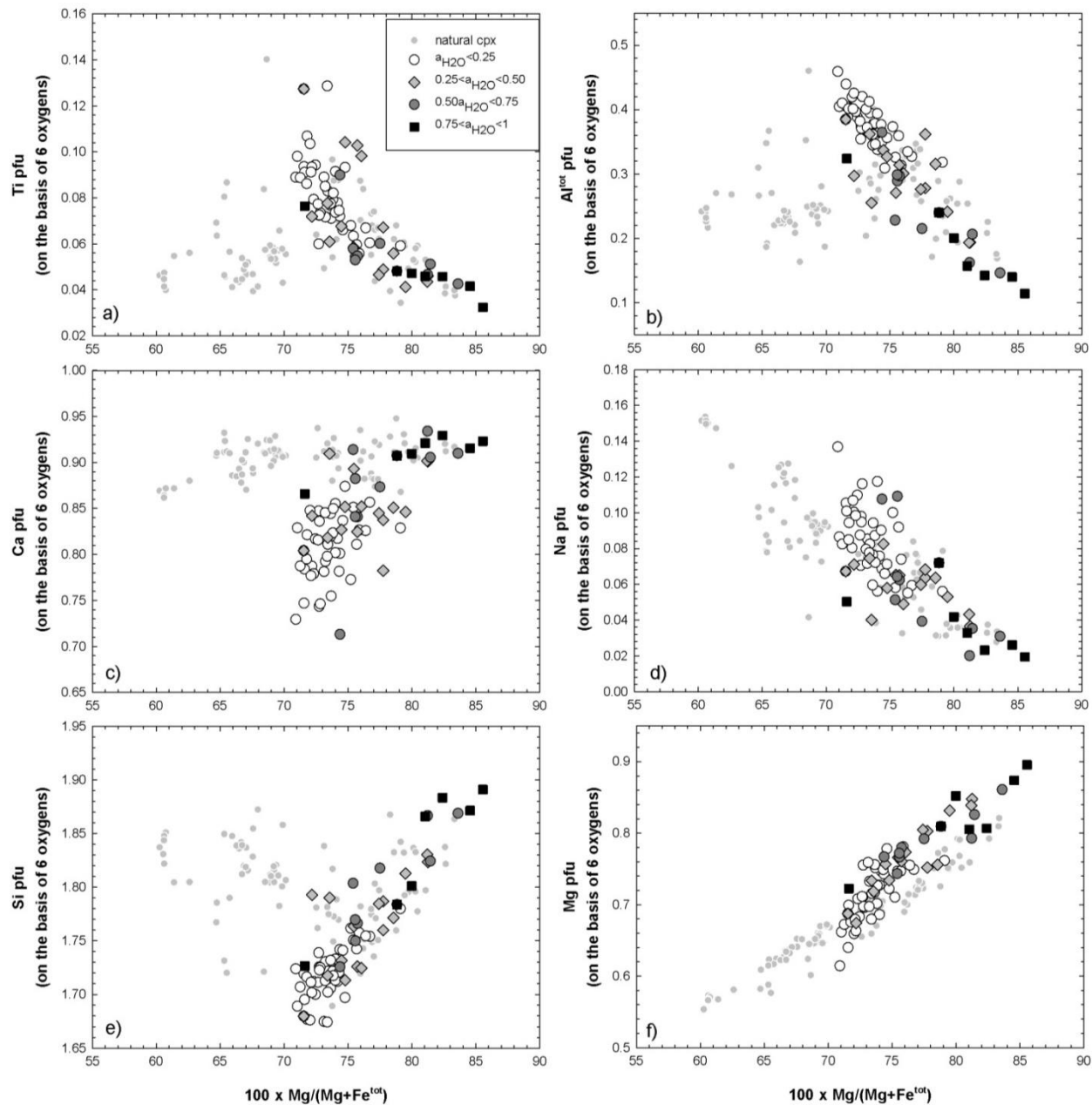


Figure 54: Experimental Cpx compositions in comparison to natural Cpx compositions of both basanitic starting materials and natural Cpx compositions of the tephriphonolitic starting material used in the study of Wengorsch (2013)

5.2.2.1 Clinopyroxene-melt barometry

Our crystallization experiments yielded Cpx-melt pairs crystallized at 400, 550 or 700 MPa, which can be used to test the applicability of the barometer of Putirka et al. (2003) for hydrous tephritic melts. Figure 55 shows that good correspondence between experimental and modeled pressures were only obtained for Cpx-melt pairs equilibrated at high $a\text{H}_2\text{O}$, where Cpx compositions demonstrated equilibrium compositions (see above). From this observation we can suggest that, calculated pressures using the Cpx-melt barometer of Putirka et al. (2003) provide reasonable results for Cpx equilibrated with the coexisting melt and can be applied for tephritic melt compositions.

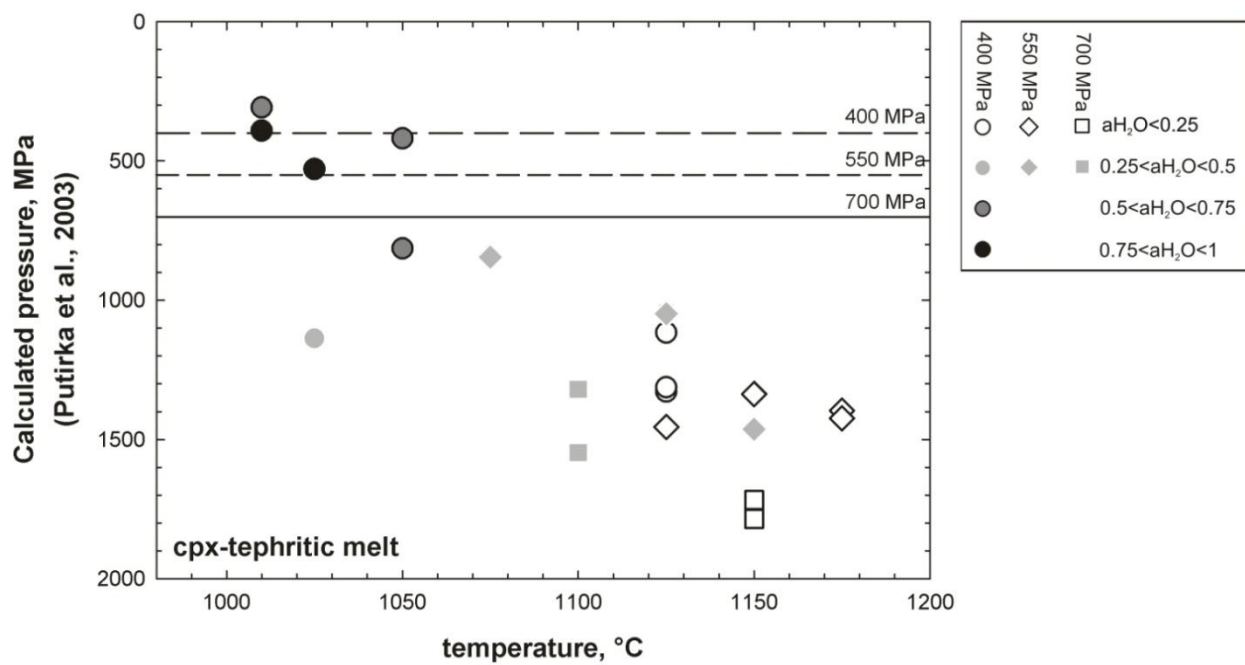


Figure 55: Calculated pressures using the cpx-melt barometer of Putirka et al. (2003) for hydrous melts, applied for experimental cpx-tephritic melt pairs crystallized at 400, 550, 700 MPa, temperatures between 1010 and 1075°C and different H_2O activities.

Cpx components were calculated following the formulation of Putirka et al. (1996, 2003) and shown as a function of H_2O content in melt and Mg# in Cpx ($100 \times \text{Mg}/(\text{Mg}+\text{Fetot})$) in Figure 56 for the primitive basanite and in Figure 57 for the evolved basanite. In general Jd, EnFs and DiHd components decrease with increasing H_2O concentration in the melt and increasing Mg^{Cpx} , while CaTi component decreases with increasing H_2O concentration in the melt and

increasing $\text{Mg}^{\#}_{\text{Cpx}}$. However, our experimental data of Cpx components show increasing scatter for all components with decreasing H_2O content in the melt at constant pressure. This strong dependence of H_2O content in the melt on Cpx components is directly related to the problem of achieving chemical equilibrium in Cpx (discussed above). At low $a\text{H}_2\text{O}$ run durations were too short to achieve chemical equilibrium, suggesting that the pressure dependence of Jd component is overprinted by this issue.

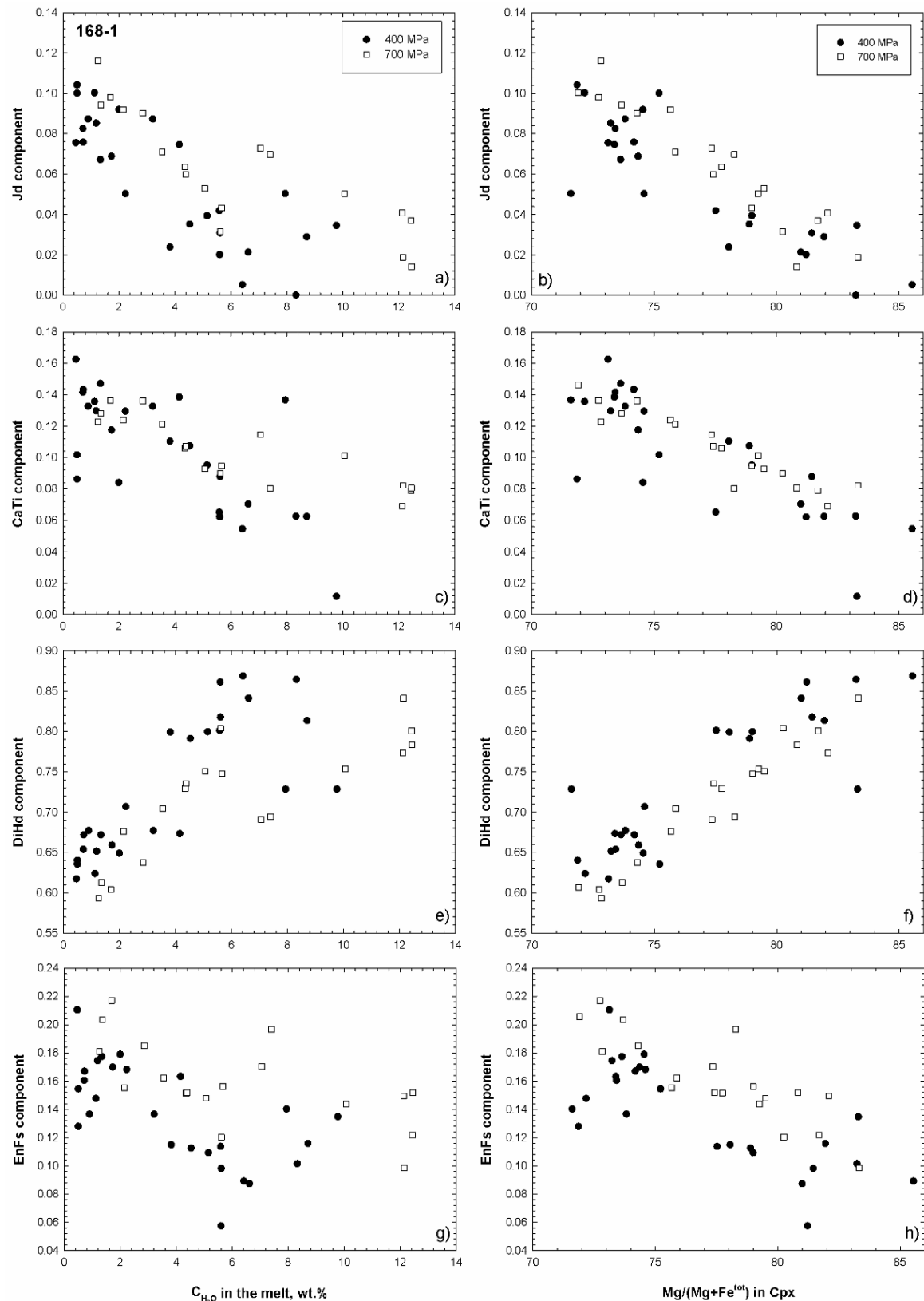


Figure 56: Variations of clinopyroxene components using starting composition 168-1 as a function of H_2O concentration in the melt or $\text{Mg}\#$ in Cpx (wt.%) and pressure.

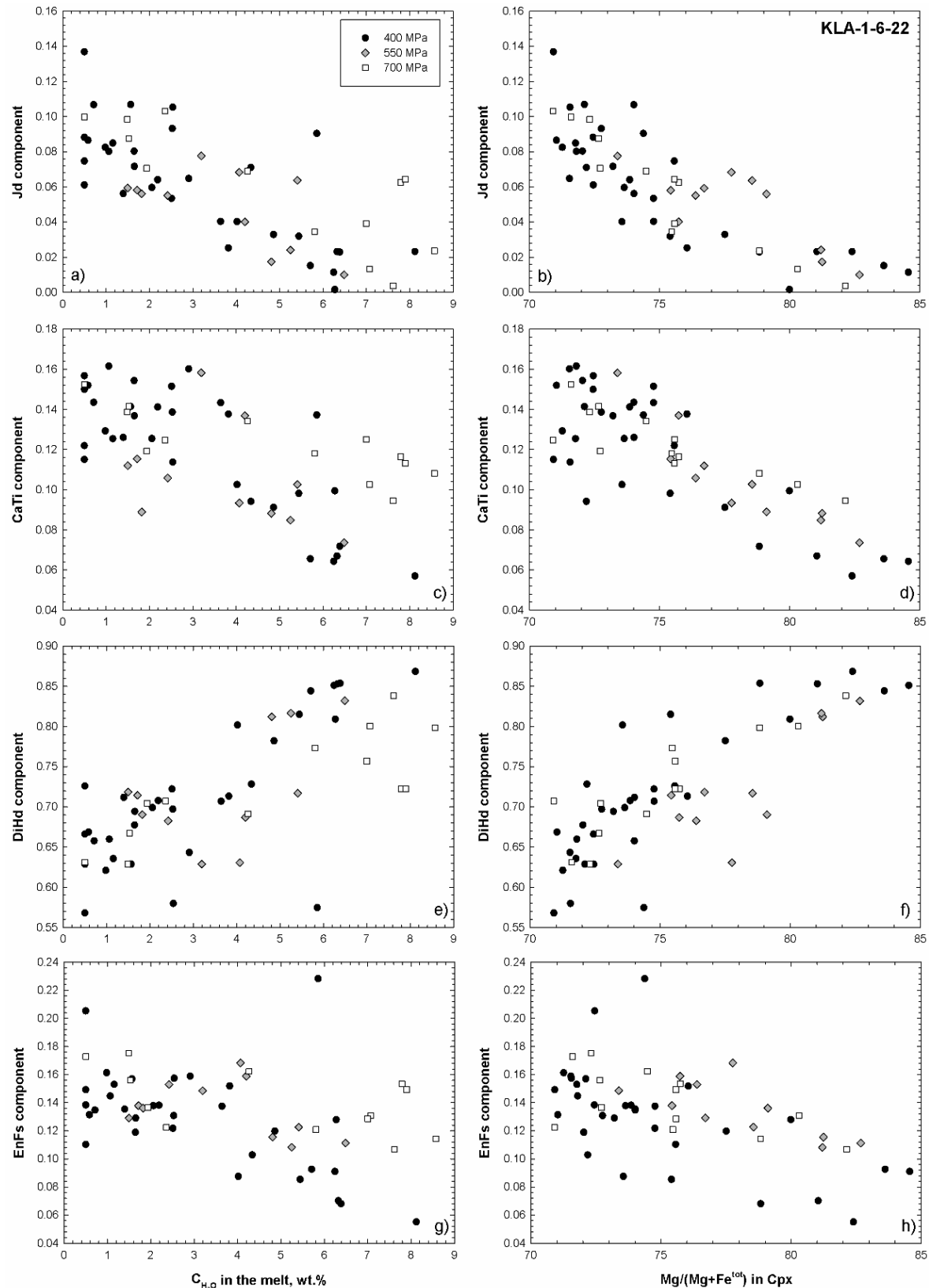


Figure 57: Variations of clinopyroxene components using starting composition KLA-1-6-22 as a function of H_2O concentration in the melt (wt.%) or $\text{Mg}\#$ in Cpx and pressure.

5.2.3 Comparison of amphibole compositions

Figures 58-60 present natural amphibole compositions in kaersutite bearing pyroxenite, tephrite and tephriphonolite (Klügel 1997 and unpublished data of Wengorsch (2013): PF22) in comparison to experimental amphibole compositions. Natural amphiboles show almost constant TiO_2 , Al_2O_3 , CaO and Na_2O contents with highly variable $\text{Mg}^{\# \text{Amp}^{\text{h}}}$ from 75 to 46 and have kaersutitic to pargasitic compositions. $\text{Mg}^{\#}$ of experimental amphiboles varies from 79.9 to 56.9. Temperature, $a\text{H}_2\text{O}$ and prevailing $f\text{O}_2$ conditions control the evolutionary state of the liquid and the $\text{Mg}^{\#}$ of the melt and also the $\text{Mg}^{\#}$ of coexisting amphibole. $\text{Mg}^{\#}$ of experimental Amph resembles natural $\text{Mg}^{\# \text{Amp}^{\text{h}}}$ at temperatures between 1010-1100°C and low $a\text{H}_2\text{O}$ (0-0.5). Using the primitive basanite a degree of crystallization of at least 50% is necessary to crystallize Amph in the range of natural $\text{Mg}^{\# \text{Amp}^{\text{h}}}$ (400 MPa: 1010-1050°C, 0.5-9.77 wt.% H_2O in the melt; 700 MPa: 1050-1100°C, 7.05-12.45 wt.% H_2O in the melt). Using the evolved basanite a degree of crystallization of at least 29% is necessary to crystallize Amph in the range of natural $\text{Mg}^{\# \text{Amp}^{\text{h}}}$ (400 MPa: 1010-1075°C, 0.5-8.12 wt.% H_2O in the melt; 700 MPa: 1050-1100°C, 1.94-7.07 wt.% H_2O in the melt). TiO_2 content generally increases with decreasing $\text{Mg}^{\# \text{Amp}^{\text{h}}}$ and decreasing temperature. However, slightly reducing conditions (FMQ to FMQ+2) and temperatures below 1050°C are necessary for appropriate TiO_2 content in amphiboles. Al_2O_3 content in experimental amphiboles increases with increasing temperature and resembles natural amphiboles at temperature between 1050-1075°C at low $a\text{H}_2\text{O}$ (0-0.5). However, we observed a contradiction for crystallization temperatures, as Al_2O_3 contents resemble natural Amph at temperatures between 1050-1075°C and TiO_2 at temperatures between 1010-1050°C. Wengorsch (2013) observed the same dependency of $f\text{O}_2$ conditions on TiO_2 contents in Amph (see Figure 61) as TiO_2 content of experimental Amph resembles natural TiO_2 content at slightly reducing conditions (FMQ to FMQ+1). However, using a tephriphonolitic starting composition Al_2O_3 contents resemble natural Al_2O_3 contents at all investigated temperatures (900-1000°C), suggesting that fractional crystallization is an important process to attain Al_2O_3 contents in the range of natural Al_2O_3 contents in Amph.

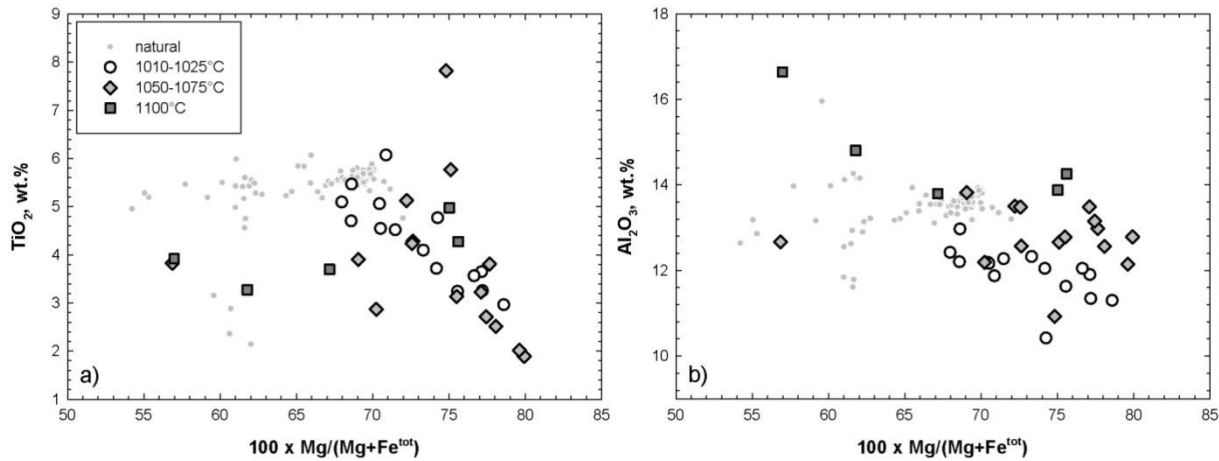


Figure 58: Effect of temperature on TiO_2 and Al_2O_3 (wt.%) content and Mg# in amphibole. Shown are natural amphibole compositions in kaersutite bearing pyroxenite, tephrite and tephriphonolite (partly from Klügel 1997; and PF22: unpublished data from Wengorsch, 2013) in comparison to experimental amphiboles using both basanitic starting compositions. TiO_2 contents of experimental Amph resemble natural TiO_2 contents at temperatures below 1050°C. Al_2O_3 contents of experimental Amph resemble natural Al_2O_3 contents at 1050-1075°C.

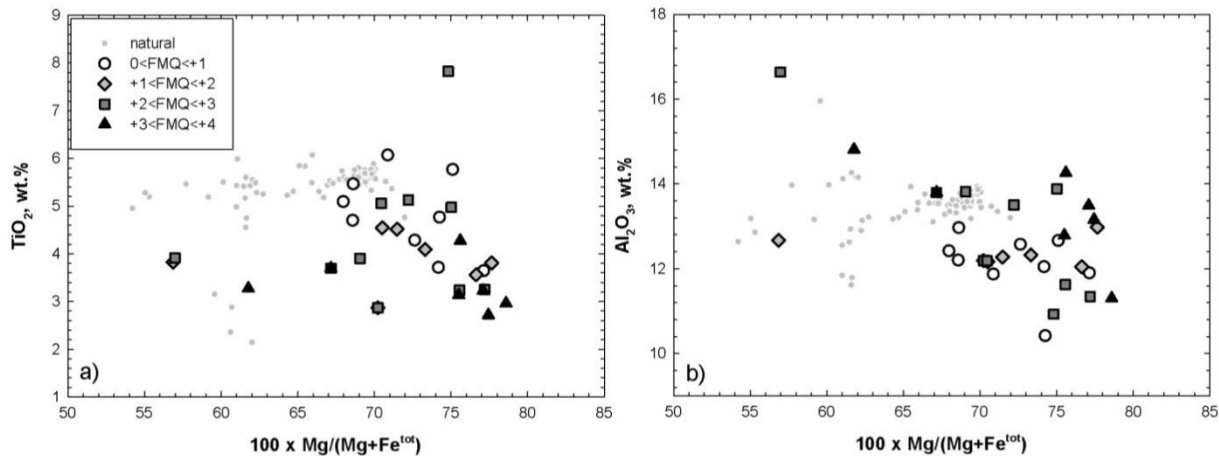


Figure 59: Effect of redox conditions on amphibole composition. TiO_2 contents of experimental Amph resemble natural TiO_2 contents at $f\text{O}_2$ conditions of FMQ to FMQ+2. Al_2O_3 contents of experimental Amph resemble natural Al_2O_3 contents at $f\text{O}_2$ conditions of FMQ+2 to FMQ+4.

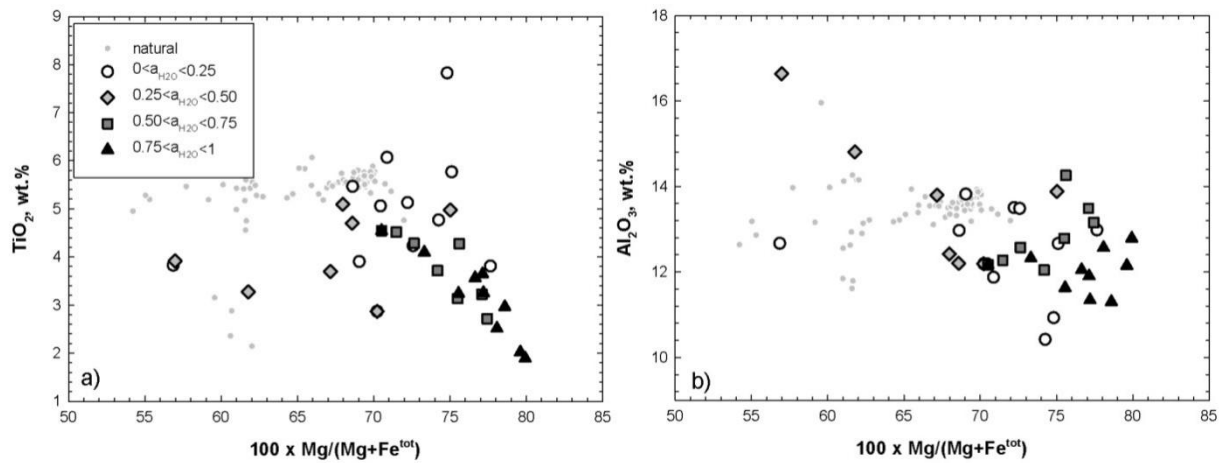


Figure 60: Effect of $a_{\text{H}_2\text{O}}$ on amphibole composition. TiO_2 and Al_2O_3 contents of experimental Amph resemble natural TiO_2 and Al_2O_3 contents at low $a_{\text{H}_2\text{O}}$ (0-0.5).

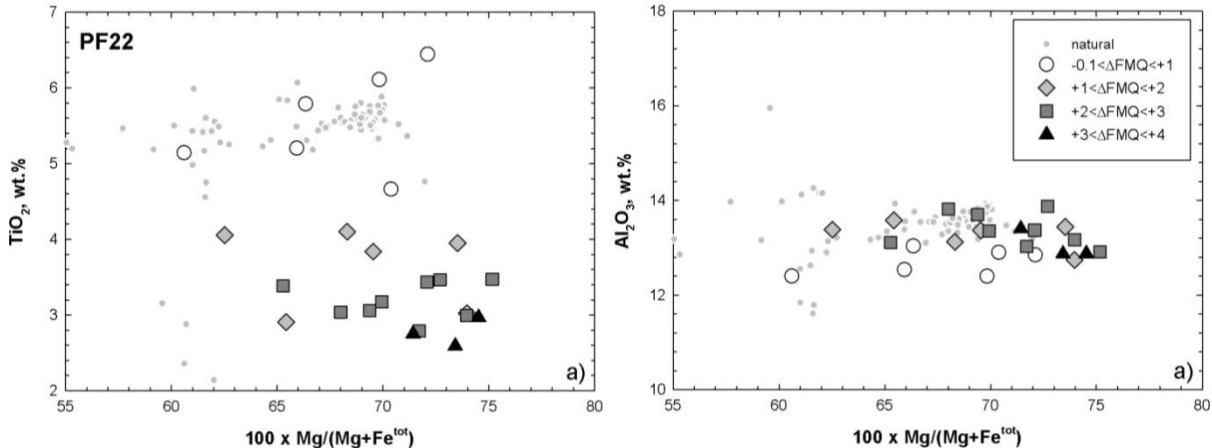


Figure 61: Effect of redox conditions on amphibole composition using a tephriphonolitic starting composition. Experimental Amph equilibrated at 400 and 200 MPa, 900-1000°C and H_2O contents in the melt between 0.5 and 8.3 wt.% (unpublished data of Wengorsch et al, 2013) resembling natural TiO_2 and Al_2O_3 contents at $f\text{O}_2$ conditions of FMQ to FMQ+1.

5.2.4 Comparison of spinel compositions

Spinel have a wide range of solid solutions and the advantage of continuous crystallization with melt evolution upon crystal fractionation (e.g. Irvine, 1965 and Barnes and Roeder, 2001). Natural compositions follow two different trends, (a) variable $\text{Cr}/(\text{Cr}+\text{Al})$ ($\text{Cr}\#$) at low $\text{Fe}^{2+}/(\text{Fe}^{2+}+\text{Mg})$ ($\text{Fe}^{2+}\#$) and (b) increasing $\text{Fe}^{3+}/(\text{Fe}^{3+}+\text{Al}+\text{Cr})$ ($\text{Fe}^{3+}\#$), $\text{Fe}^{2+}\#$ and TiO_2 at constant $\text{Cr}\#$. These compositional variations were described by Barnes and Roeder (2001) as CrAl-trend and FeTi-trend, respectively. Remarks on compositional variations of experimentally produced

spinels are based on experiments at all investigated conditions and on the unpublished data of Wengorsch (2013). Figure 62 presents conventional variation plots for spinel (e.g. Barnes and Roeder, 2001). Shown are natural spinel compositions of both natural basanitic starting compositions and magnetite compositions of natural tephriphonolite (PF22: Wengorsch, 2013) in comparison with experimentally produced spinels in equilibrium with basanitic, tephritic or phonolitic melts. Experimental spinels used for this plot equilibrated at $f\text{O}_2$ conditions between FMQ and FMQ+1, in a small temperature range (1025–1050°C) and $a\text{H}_2\text{O}$ between 0 and 0.9. Cr-rich spinel was observed at high temperature or high H_2O activity in equilibrium with basanitic melt. However, chromium content in spinel is slightly lowered with the onset of clinopyroxene crystallization. Since spinel incorporates both ferric and ferrous iron the spinel composition is strongly affected by the prevailing redox conditions. Mg and Al content in spinel is temperature dependant: at high temperatures Al- and Mg-rich spinels are stabilized which in turn lowers $\text{Fe}^{3+}\#$ and $\text{Fe}^{2+}\#$ in spinel at fixed redox conditions. Experimental Cr-rich spinels equilibrated at relatively low temperature (1050°), at high $a\text{H}_2\text{O}$ and have moderate $\text{Fe}^{3+}\#$. In order to shift the composition to lower $\text{Fe}^{3+}\#$ (natural Cr-spinel) the crystallization temperature has to be increased (above 1150°C). The FeTi-trend (Barnes and Roeder, 2001) is defined by increasing TiO_2 content with increasing $\text{Fe}^{3+}\#$ and decreasing TiO_2 content at high $\text{Fe}^{3+}\#$ values. To match natural magnetite composition (in terms of $\text{Fe}^{3+}\#$ and $\text{Fe}^{2+}\#$) in equilibrium with tephriphonolitic melts the crystallization temperature has to be decreased to reach higher $\text{Fe}^{3+}\#$ and $\text{Fe}^{2+}\#$. From our experimental data we can conclude that increasing TiO_2 content with increasing $\text{Fe}^{3+}\#$ can be related to magma cooling and decreasing TiO_2 content at high $\text{Fe}^{3+}\#$ values with progressive crystallization upon cooling.

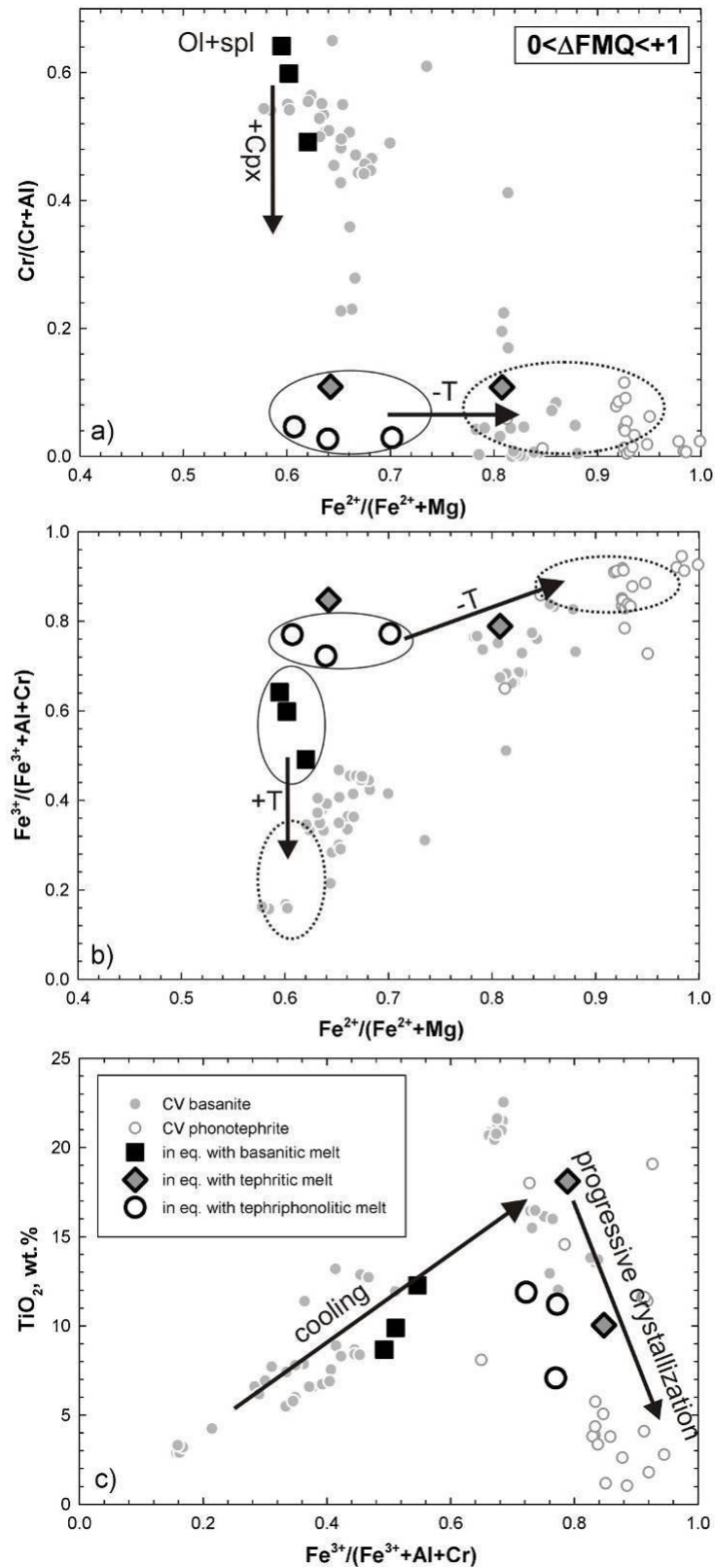


Figure 62: Effect of crystallizing phases and temperature on spinel composition. Shown are Spl compositions equilibrated at reducing conditions ($0 < \Delta\text{FMQ} < +1$) in comparison to natural spinel compositions of both natural basanitic starting compositions and magnetite compositions of natural tephriphonolite (PF22: Wengorsch, 2013).

5.3 Pre-eruptive storage conditions

5.3.1 Primitive basanite (168-1)

The natural phase assemblage (Ol+Cpx+Spl) was experimentally reproduced at 400 MPa, 1050-1150°C, 0.46-7.94 wt.% H₂O in the melt (aH₂O: 0.04-1) and fO₂ between FMQ+0.14 and FMQ+3.97, and at 700 MPa, 1100-1150°C, 1.25-2.15 wt.% H₂O in the melt (aH₂O: 0.06-0.11) and fO₂ between FMQ+1.34 and FMQ+1.90. However, Ol compositions resemble their natural counterparts at temperatures between 1100 and 1150°C at fO₂ between FMQ+1.40 and FMQ+2.28. As shown in the results, the mineral proportions of Ol (22.8-72.4% at 400 MPa; 19.2-44.5% at 700 MPa) and Cpx (67.7-72.8% at 400 MPa; 71.5-38.0% at 700 MPa) change as a function of pressure, temperature and aH₂O. The phenocryst proportions of the natural sample are 28.9% Ol and 69.1% Cpx. In our experiments similar proportions were obtained at 400 MPa at 1150°C and 1.34 wt.% H₂O in the melt (aH₂O: 0.09) (34.0% Ol, 58.4% Cpx), and at 700 MPa, 1150°C and 1.36-2.86 wt.% H₂O in the melt (aH₂O: 0.06-0.16) (19.6-25.9% Ol, 65.6-71.1 Cpx). Because Ol and Cpx proportions observed at 700 MPa are closer to natural proportions, our best estimate for the pre-eruptive crystallization conditions of sample 168-1 is 700 MPa, 1150°C, and a H₂O content between 1.3 and 2.9 wt.%.

5.3.2 Evolved basanite (KLA-1-6-22)

The natural phase assemblage (Ol+Cpx+Spl) was reproduced at 400 MPa, 1050-1150°C, 0.58-6.25 wt.% H₂O in the melt (aH₂O: 0.03-0.76) and fO₂ conditions between FMQ+0.29 to FMQ+2.46, at 550 MPa, 1075-1175°C, 1.50-6.49 wt.% H₂O in the melt (aH₂O: 0.08-0.62) and fO₂ conditions between FMQ+1.11 to FMQ+3.39 and at 700 MPa, 1150°C, 0.5-1.53 wt.% H₂O in the melt (aH₂O: 0.02-0.07) and fO₂ conditions between FMQ+0.39 to FMQ+1.53. However, Ol compositions resemble their natural counterparts at 400 and 550 MPa, 1125- 1175°C, low H₂O contents in the melt (1.50-2.19 wt.%) and fO₂ conditions between FMQ+1.11 and FMQ+2.26. As shown in the results, the mineral proportions of Ol (5.1-57.1% at 400 MPa; 3.5-31.2% at 550 MPa; 2.8-4.9% at 700 MPa) and Cpx (82.9-20.8% at 400 MPa; 80.3-50.4% at 550 MPa; 87.8-86.0% at 700 MPa) change as a function of pressure, temperature and aH₂O. In the natural sample we observed 25.8% Ol and 66.4% Cpx. In our experiments we observed Ol and Cpx proportions close to the proportions of the natural sample at 400 MPa at 1150°C and 0.98-1.15

wt.% H₂O in the melt (aH₂O: 0.07-0.09) (22.2-21.1% Ol, 72.5-73.2% Cpx), and at 550 MPa, 1175°C and 1.17 wt.% H₂O in the melt (aH₂O: 0.10) (31.2% Ol, 59.0% Cpx).

Because Ol and Cpx proportions observed at 400 MPa are closer to natural proportions, our best estimate for the pre-eruptive crystallization conditions of sample KLA-1-6-22 is 400 MPa, 1150 °C, and a H₂O content between 1.0 and 1.2 wt.%.

5.3.3 Tephriphonolite (PF22; Wengorsch, 2013)

Pre-eruptive storage conditions of the natural tephriphonolite PF22 were investigated by Wengorsch (2013). The natural phase assemblage (Krs+Cpx+Pl+Mt+Ap+Hyn) was reproduced at 200 MPa, 950-1000°C, 0.5-2.0 wt.% H₂O in the melt and *fO*₂ conditions of FMQ to FMQ+1.8, and at 400 MPa, 900-1000°C and 0.5-3.1 wt% H₂O in the melt and *fO*₂ conditions of FMQ to FMQ+2.2. At those conditions calculated crystal fraction is about 20% and resembles the natural crystal fraction. The compositional range of natural minerals was reproduced in equilibrium with a phonolitic melt at 400 and 200 MPa, 1000°C and 0.6-0.7 wt.% H₂O in the melt (Wengorsch et al, 2013).

Table 35. Pre-storage conditions of various studies

Author	Location, Starting composition	Pressure [MPa]	Temperature [°C]	melt H ₂ O [wt%]	fO ₂	Natural phase assemblage
Bernd et al. (2001)	Lower Laacher See, Phonolite	200	720-860°C	6.00	FMQ+07 - FMQ+2.7	Sa+Amph+Cpx+Mt+Hyn+Ttn
Harms et al. (2004)	Lower Laacher See, Phonolite	115-145	750-760	5-6		Sa+Amph+Cpx+Mt+Hyn+Ttn
Freise et al. (2003)	Kerguelen, Tephriphonolite	200-250	800	4-6	FMQ+07 - FMQ+1.7	CPx+Krs+Sa+Bt+Fe-Ti oxides
Andujar et al. (2008)	Tenerife El Abrigo, Phonolite	130±50	825±25	3±1	FMQ+07±1	Sa+Bt+Mt+Ttn+Ap+Hyn
Andujar et al. (2010)	Tenerife Teide, Phonolite	150±50	900±20	3±0.5	FMQ	Fsp+Cpx+Mt
Sacillet et al. (2008)	Vesuvius, Phonolite	50-350	785-977	0-7	FMQ+1.7	±Ne+Lct+Cpx+Fsp±Amph
Moussallam et al. (2013)	Erebus, Phonolite	below 200	950±25	below 0.5	FMQ-1 - FMQ	Fsp+Ttn+Ol+Cpx+Ap

Sa, sanidine; Amph, amphibole; Mt, magnetite; Hyn, Häufige; Ttn, Titanite; Cpx, clinopyroxene; Bt, biotite; Ap, apatite, Fsp, feldspar; Ne, nepheline; Lct, leucite

ΔFMQ is log fO₂ expressed relative to the FMQ buffer

5.4 Open versus closed system fractionation

The role of fractional crystallization in the genesis of Cumbre Vieja basanite-phonolite series was investigated by conducting experiments using three starting compositions. These represent different stages of magma evolution from a primitive basanite (sample 168-1) with 14 wt% MgO, and an evolved basanite (KLA1-6-22) with 9 wt% MgO, to a tephriphonolite (PF22; Wengorsch, 2013) with 3 wt% MgO. Residual melts of the primitive basanite are close to the bulk composition of the evolved basanite after crystallization of 11.3 wt.% Ol, 11.1 wt.% Cpx and 3.0 wt.% Mt at 700 MPa, 1150°C and 4.0 wt% H₂O in the melt. Tephriphonolite is the final liquid composition (melt fraction between 25.4 and 38.2 wt.%) of the primitive and the evolved basanite coexisting with Ol+Cpx+Pl±Amph+Mt±Ap at 400 MPa, 1050°C and a melt H₂O content of 0.7-1.1wt%. These melts resemble starting material PF22 (tephriphonolite, Wengorsch, 2013) for all major elements. The natural mineral assemblage of this tephriphonolite (Cpx+Krs+Pl+Mt+Ap) in the natural compositional range was reproduced in equilibrium with a phonolitic melt at 400 and 200 MPa, 1000°C and 0.6-0.7 wt.% H₂O in the melt (Wengorsch et al, 2013). Our experimental results indicate that single-step differentiation (equilibrium crystallization) from basanites to phonotephrites is possible in a pressure range from at least 400 to 700 MPa. At 700 MPa Pl crystallization in basanites is suppressed, indicating that tephriphonolitic or phonolitic melts (including Pl as a stable phase) can only be generated at lower pressures in a closed system.

It should be noted that closed system crystallization is not a likely scenario for natural magmas evolving in a reservoir over a prolonged period of time. More likely is crystallization in an open system where solid phases are removed from the residual liquids. These liquids evolve upon fractional crystallization along the liquid line of descent, which was not simulated in our experimental study. Phase relations and phase proportions change significantly with the evolution of liquids to more evolved compositions. One crucial phase to generate phonolitic melts is Pl. In our experiments, using a basanitic starting material, Pl was stable only at 400 MPa, 1025-1075°C at low aH₂O (0.03-0.07; 0.5-1.13 wt.%). Wengorsch (2013) showed that when using a tephriphonolitic starting composition Pl is stable at 200 to 400 MPa, 900-1050°C

and 0.5-3.07 wt.% H₂O in the melt. These observations suggest that the appearance of plagioclase does not depend only on pressure but also on the starting composition. It is thus possible that in an open system the formation of evolved liquids (tephriphonolitic or phonolitic composition, including PI as a stable phase) is also possible at high pressures (above 400 MPa). Based on our experimental data we conclude that genesis of tephriphonolitic and phonolitic Cumbre Viejas magmas can occur up to pressures of 400 MPa at least, which is in contrast to the relatively low pre-eruptive storage pressures of phonolites from comparable systems (e.g. >200-250 MPa for Kerguelen (Freise et al., 2003) and 130 MPa for El Abrigo, Tenerife (Andujar et al., 2008) (see Table 35 for more details). This indicates that the genesis of evolved melts is not restricted to low pressures. However, emphasis should be given on the fact that melt evolution can occur at the same pressure by fractional crystallization and lateral migration of more evolved melts and that primitive and evolved rocks can be generated at the same depth. Most pre-eruptive storage conditions inferred for phonolite melts indicate relatively low pressures (115-145 MPa for Laacher See, Eifel (Harms et al. 2004; Berndt et al. 2001), >200-250 MPa for Kerguelen (Freise et al., 2003), 130 MPa for El Abrigo, Tenerife (Andujar et al., 2008), 150±50 MPa for last eruption of Teide, Tenerife (Andujar et al., 2008), 140-200 MPa for Campania, Campi Flegrei (Fabbrizio and Carroll, 2008), 50-350 MPa for Vesuvius (Scaillet et al., 2008)), but recent data indicate that phonolites can be generated at pressures up to 1000 MPa (Grant et al. 2013). At La Palma the possibility of formation of phonolitic melts at high pressures in an open system is also supported by (a) lacking Eu anomalies in some phonolites (Johansen et al., 2005), which may indicate limited PI fractionation and pressures in excess of ~500 MPa (Fisk et al., 1988), and (b) the presence of green cores in cpx that crystallized at 410-770 MPa and appear to be in chemical equilibrium with phonolitic melts (Klügel et al., 2000). On the other hand, the formation of evolved melts and their upward migration at pressures between 240 and 470 MPa is supported by fluid inclusion data indicating significant magma ponding beneath Cumbre Vieja volcano within the lower crust (Klügel et al., 2000). Upon cooling and crystal fractionation of the ponded magmas evolved melts are expected to form, which may eventually ascend and erupt. Such a scenario is in accordance with a well-mixed population of mantle peridotite, MORB-type gabbro, and ultramafic cumulate xenoliths in a tephriphonolite

plug on Cumbre Vieja, where reaction rims and zonations of the peridotites combined with fluid inclusion barometry indicate prolonged residence of the xenoliths in a lower crustal reservoir (Klügel and Hansteen 1998).

6. Conclusions

Our experimental results indicate that differentiation from a primitive basanite to evolved liquids is possible by isobaric equilibrium crystallization. Mineral proportions of magnetite, amphibole and clinopyroxene (depending on temperature, pressure, oxygen fugacity and H₂O activity) are crucial to reproduce the natural Cumbre Vieja liquid line of descent. Tephrite and phonotephrite can derive directly from a basanite in the investigated pressure range from 400 to 700 MPa. However, tephritic residual melts resemble the natural liquid line of descent only if the proportion of clinopyroxene is below 32 wt.%. H₂O activity and oxygen fugacity are important factors controlling phase compositions and phase stabilities. It has been demonstrated that slightly reducing conditions of FMQ+1 to FMQ+2 are necessary:

- to generate alkalic, silica undersaturated melts (higher oxygen fugacity results in extensive magnetite crystallization leading to Qtz-normative residual liquids instead of Ne-normative),
- for appropriate FeO content in residual melts,
- for appropriate forsterite content of fractionated olivine,
- for crystallization of kaersutitic/pargasitic amphibole,
- for appropriate proportion and composition of spinel.

It has been demonstrated that H₂O activity controls the proportion of amphibole and clinopyroxene. At low H₂O activity and high temperature clinopyroxene predominates over amphibole in the clinopyroxene +amphibole assemblage, resulting in CaO depletion and relative enrichment in Al₂O₃ in the residual melt. At high H₂O activity and low temperature amphibole predominates over clinopyroxene, resulting in depletion of CaO and less pronounced Al₂O₃ enrichment. Natural variations of CaO and Al₂O₃ in evolved rocks at given SiO₂ contents can

thus be explained by different proportions of amphibole and clinopyroxene, which in turn depend on H₂O activity and temperature. However, kaersutitic amphibole can be stable at very low water contents in the melt (<1 wt.% H₂O^m), in contrast to calc-alkaline hornblende-bearing systems (4 wt.% H₂O).

Constraints on temperatures of basanitic melts could be made by comparing forsterite content of natural olivine phenocrysts to forsterite content of experimental olivines. According to our experimental data, crystallization temperatures of Cumbre Vieja olivine could be estimated to e.g. 1100-1150°C at 400 MPa.

Constraints on temperature for more evolved melt compositions (MgO below 5 wt.%) can be made by comparing P₂O₅ content of experimental residual melts to P₂O₅ content of natural bulk rock compositions. Phosphorus is exclusively incorporated in apatite, therefore P₂O₅ depletion in the residual melt at MgO contents below 5 wt.% indicates apatite crystallization. Apatite was observed at low temperatures (e.g. at 400 MPa: below 1050°C) at low XH₂O. This suggests that elevated P₂O₅ content at MgO contents below 5 wt.% correspond to temperatures above apatite stability at given pressure.

We tested the performance of the clinopyroxene-melt barometer of Putirka et al. (2003) and have demonstrated that clinopyroxene equilibrated with tephritic melt show good correspondence between experimental and calculated pressures. This confirms that the clinopyroxene-melt barometer of Putirka et al. (2003) yields correct results for clinopyroxene equilibrated with tephritic or basanitic melts. Therefore, we can support the model of magma plumbing beneath Cumbre Vieja volcano of Klügel et al. (2005) with our experimental investigations.

Experimental results indicate that single-step differentiation (equilibrium crystallization) from basanites to phonotephrites is possible in a pressure range from at least 400 to 700 MPa. Tephriphonolitic or phonolitic residual melts were generated at pressures below 400 MPa. At 700 MPa plagioclase crystallization in basanites is suppressed, indicating that tephriphonolitic or phonolitic melts including plagioclase as a stable phase can only be generated at lower pressures in a closed system. However, in an open system the genesis of evolved melts is not

restricted to pressures below 400 MPa exclusively, because phase stabilities and proportions strongly depend on the parental melt composition. The evolution from basanite to evolved melts can occur at the same pressure level by fractional crystallization.

7. References

- Ablay GJ, Carroll MR, Palmer MR, Marti J, Sparks RSJ (1998) Basanite-phonolite lineages of the Teide-Pico Viejo volcanic complex, Tenerife, Canary Islands. *J. Petrol.* 39: 905-936
- Ablay GJ, Ernst GGJ, Marti J, Sparks RSJ (1995) The ~2 ka subplinian eruption of Montaña Blanca, Tenerife. *Bull. Volcanol.* 57: 337-355
- Andújar J, Costa F, Martí J, Wolff JA, Carroll MR (2008) Experimental constraints on pre-eruptive conditions of phonolitic magma from the caldera-forming El Abrigo eruption, Tenerife (Canary Islands). *Chem. Geol.* 257: 173-191
- Andújar, J., Costa, F., and Martí, J., (2010) Magma storage conditions of the last eruption of Teide volcano (Canary Islands, Spain): Bulletin of Volcanology, v. 72, p. 381-395
- Barnes, S.J., and Roeder, P.L., (2001) The range of spinel compositions in terrestrial mafic and ultramafic rocks: *Journal of Petrology*, v. 42, p. 2279-2302
- Barr, J.A., and Grove, T.L., (2010) AuPdFe ternary solution model and applications to understanding the fO₂ of hydrous, high-pressure experiments: *Contributions to Mineralogy and Petrology*, v. 160, p. 631-643
- Behrens H, Stuke A (2003) Quantification of H₂O contents in silicate glasses using IR spectroscopy - a calibration based on hydrous glasses analyzed by Karl-Fischer titration. *Glass Science Technology* 76: 176-189
- Behrens, H., Misiti, V., Freda, C., Vetere, F., Botcharnikov, R.E., and Scarlato, P., (2009) Solubility of H₂O and CO₂ in ultrapotassic melts at 1200 and 1250 degrees C and pressure from 50 to 500 MPa: *American Mineralogist*, v. 94, p. 105-120
- Berndt J, Holtz F, Koepke J (2001) Experimental constraints on storage conditions in the chemically zoned phonolitic magma chamber of the Laacher See volcano. *Contrib. Mineral. Petrol.* 140: 469-486
- Berndt J, Liebske C, Holtz F, Freise M, Nowak M, Ziegenbein D, Hurkuck W, Koepke J (2002). A combined rapid-quench and H₂-membrane setup for internally heated pressure vessels: Description and application for water solubility in basaltic melts. *Am. Mineral.* 87: 1717-1726
- Berndt J, Koepke J, Holtz F (2005) An experimental investigation of the influence of water and oxygen fugacity on differentiation of MORB at 200 MPa. *J. Petrol.* 46: 135-167
- Bourdon B, Zindler A, Wörner G (1994) Evolution of the Laacher See magma chamber: Evidence from SIMS and TIMS measurements of U-Th disequilibria in minerals and glasses. *Earth Planet. Sci. Lett.* 126: 75-90
- Brophy, J. G., Whittington, C. S. & Park, Y. R. (1999) Sector-zoned augite megacrysts in Aleutian high alumina basalts: implications for the conditions of basalt crystallization and the generation of calc-alkaline series magmas. *Contrib. Mineral. Petrol.* 135, 277-290
- Burnham WC (1979) The importance of volatile constituents. In: Yoder HS Jr (ed) *The evolution of the igneous rocks*. Princeton University Press, Princeton, pp 439-482
- Carey S, Sigurdsson H (1987) Temporal variations in column height and magma discharge rate during the 79 A.D. eruption of Vesuvius. *Geol Soc Am Bull* 99: 303-314
- Carracedo, J.C., Day, S.J., Guillou, H., and Pérez Torrado, F.J., (1999) Giant quaternary landslides in the evolution of La Palma and El Hierro, Canary Islands: *Journal of Volcanology and Geothermal Research*, v. 94, p. 169-190
- Carracedo JC, Badiola ER, Guillou H, de La Nuez J, Pérez Torrado FJ (2001) Geology and volcanology of La Palma and El Hierro, Western Canaries. *Estudios Geol.* 57: 175-273

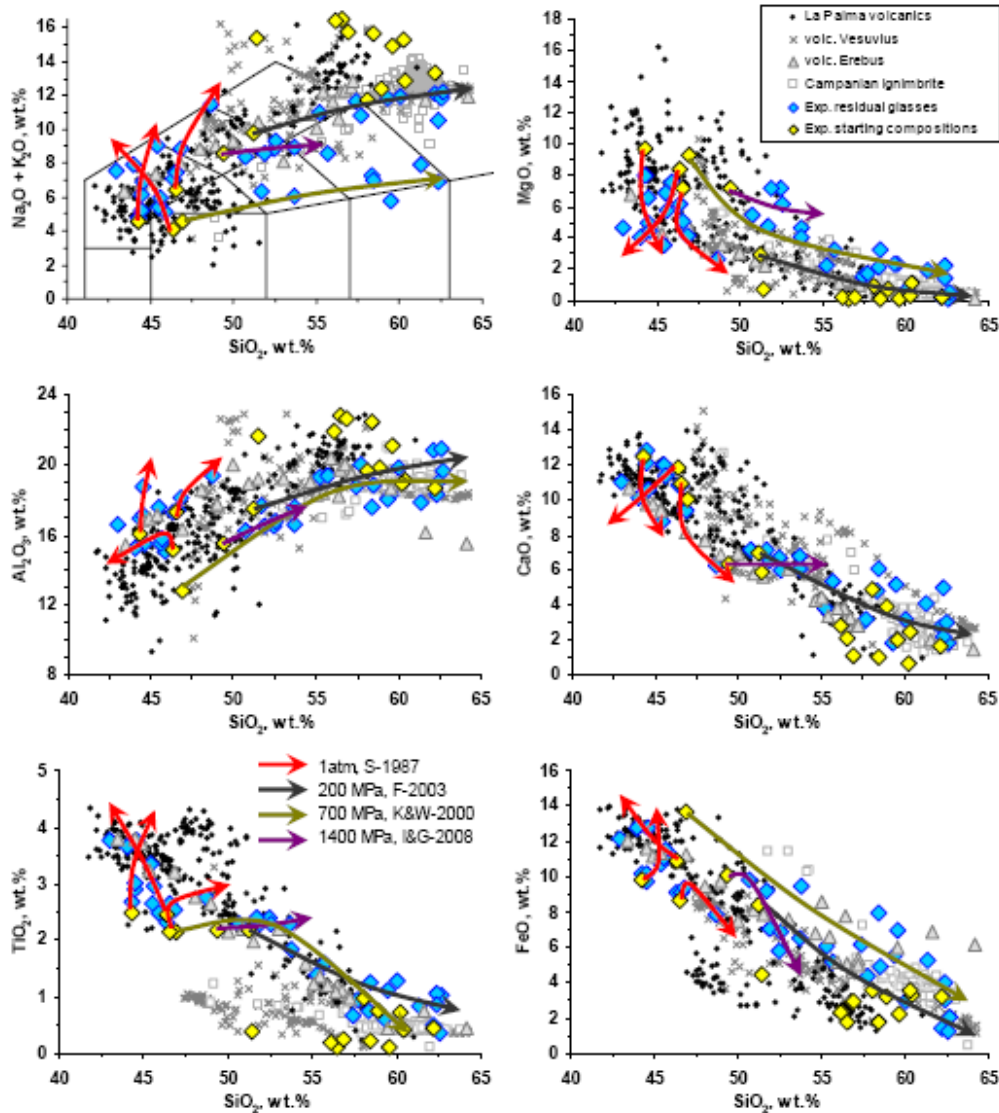
- Day SJ, Carracedo JC, Guillou H, Gravestock P (1999) Recent structural evolution of the Cumbre Vieja volcano, La Palma, Canary Islands: volcanic rift zone reconfiguration as a precursor to volcano flank instability? *J. Volcanol. Geotherm. Res.* 94: 135-167
- Devine, J.D., Gardner, J.E., Brack, H.P., Layne, G.D., and Rutherford, M.J., (1995) Comparison of microanalytical methods for estimating H₂O contents of silicic volcanic glasses: *American Mineralogist*, v. 80, p. 319-328
- Elliott TR (1991) Element Fractionation in the Petrogenesis of Ocean Island Basalts. Ph.D. thesis, The Open University, Milton Keynes
- Fabbrizio A, Carroll MR (2008) Experimental constraints on the differentiation process and pre-eruptive conditions in the magmatic system of Phlegraean Fields (Naples, Italy). *J. Volcanol. Geotherm. Res.* 171: 88-102
- Fisk MR, Upton BGJ, Ford CE, White WM (1988) Geochemical and experimental study of the genesis of magmas of Réunion Island, Indian Ocean. *J. Geophys. Res.* 93: 4933-4950
- Freise M, Holtz F, Koepke J, Scoates J, Leyrit H (2003) Experimental constraints on the storage conditions of phonolites from the Kerguelen Archipelago. *Contrib. Mineral. Petrol.* 145: 659-672
- Fritzsche, F. (2013) Einfluss des Wassergehaltes auf den Oxidationszustand von Eisen in basaltischen Schmelzen. Unpublished B.Sc. Thesis, Leibniz Universität Hannover, Germany
- Galipp K (2005) Geochemical and petrological evolution of La Palma (Canary Islands) and its rift zone during the last 1.0 Ma. Unpubl. Ph.D. thesis, Universität Bremen, Germany
- Galipp K, Klügel A, Hansteen TH (2006) Changing depths of magma fractionation and stagnation during the evolution of an oceanic island volcano: La Palma (Canary Islands). *J. Volcanol. Geotherm. Res.* 155: 285-306
- Grant, T.B., Milke, R., Pandey, S., and Jahnke, H., (2013) The Heldburg Phonolite, Central Germany: Reactions between phonolite and xenocrysts from the upper mantle and lower crust: *Lithos*, v. 182, p. 86-101
- Hansteen TH, Klügel A, Schmincke HU (1998) Multi-stage magma ascent beneath the Canary Islands: evidence from fluid inclusions. *Contrib. Mineral. Petrol.* 132: 48-64
- Harms E, Gardner JE, Schmincke HU (2004) Phase equilibria of the Lower Laacher See Tephra (East Eifel, Germany): constraints on pre-eruptive storage conditions of a phonolitic magma reservoir. *J. Volcanol. Geotherm. Res.* 134: 135-148
- Hawkesworth CJ, Blake S, Evans P, Hughes R, Macdonald R, Thomas LE, Turner SP, Zellmer G (2000) Time scales of crystal fractionation in magma chambers--integrating physical, isotopic and geochemical perspectives. *J. Petrol.* 41: 991-1006
- Hay DE, Wendlandt RF (1995) The origin of Kenya rift plateau-type flood phonolites: Results of high-pressure/high-temperature experiments in the systems phonolite-H₂O and phonolite-H₂O-CO₂. *J. Geophys. Res.* 100(B1): 401-410
- Hay DE, Wendlandt RF, Keller GR (1995) Origin of Kenya Rift Plateau-type flood phonolites: Integrated petrologic and geophysical constraints on the evolution of the crust and upper mantle beneath the Kenya Rift. *J. Geophys. Res.* 100(B6): 10549-10557
- Hernández-Pacheco A, De la Nuez J (1983) Las extrusiones sálicas del Sur de la Isla de La Palma (Canarias). *Estud. Geol.* 39: 3-30
- Hernández-Pacheco A, Valls MC (1982) The historic eruptions of La Palma Island (Canarias). *Arquipelago, Rev. Univ. Azores, Ser. C. Nat.* 3: 83-94
- Hoernle, K., (1998) Geochemistry of Jurassic Oceanic Crust beneath Gran Canaria (Canary Islands): Implications for Crustal Recycling and Assimilation: *Journal of Petrology*, v. 39, p. 859-880
- Holloway, J.R., and Blank, J.G., (1994) Application of experimental results to COH species in natural melts: *Reviews in Mineralogy and Geochemistry*, v. 30, p. 187-230

- Hunt, J.B., and Hill, P.G., (2001) Tephrological implications of beam size—sample-size effects in electron microprobe analysis of glass shards: *Journal of Quaternary Science*, v. 16, p. 105-117
- Irvine, T. N. (1965). Chromian spinel as a petrogenetic indicator. Part I. Theory. *Canadian Journal of Earth Sciences* 2, 648–672
- Irving AJ, Green DH (2008) Phase Relationships of Hydrous Alkalic Magmas at High Pressures: Production of Nepheline Hawaïitic to Mugearitic Liquids by Amphibole-Dominated Fractional Crystallization Within the Lithospheric Mantle. *J. Petrol.* 49: 741-756
- Irving AJ, Price RC (1981) Geochemistry and evolution of Iherzolite-bearing phonolitic lavas from Nigeria, Australia, East Germany and New Zealand. *Geochim. Cosmochim. Acta* 45: 1309-1320
- Johansen TS, Hauff F, Hoernle K, Klügel A, Kokfelt TF (2005) Basanite to phonolite differentiation within 1550-1750 yr: U-Th-Ra isotopic evidence from the A.D. 1585 eruption on La Palma, Canary Islands. *Geology* 33: 897-900
- Kaiser C (1988) The 1949 eruption of Volcan San Juan, La Palma, Canary Islands: Petrology and lava flow dynamics, diploma thesis, Universität Bochum, Germany
- Kaszuba JP, Wendlandt RF (2000) Effect of carbon dioxide on dehydration melting reactions and melt compositions in the lower crust and the origin of alkaline rocks. *J. Petrol.* 41: 363-386
- Kelly PJ, Kyle PR, Dunbar NW, Sims KWW (2008) Geochemistry and mineralogy of the phonolite lava lake, Erebus volcano, Antarctica: 1972-2004 and comparison with older lavas. *J. Volcanol. Geotherm. Res.* 177: 589-605
- Klimm K, Holtz F, Johannes W, King PL (2003) Fractionation of metaluminous A-type granites: an experimental study of the Wangrah Suite, Lachlan Fold Belt, Australia. *Precamb. Res.* 124: 327-341
- Klügel A (1997) Ascent rates of magmas and genesis, transport, and reactions of mantle and crustal xenoliths of the 1949 eruption on La Palma (Canary Islands). Ph.D. thesis, University of Kiel, 209 p.
- Klügel A, Hansteen TH, Schmincke HU (1997) Rates of magma ascent and depths of magma reservoirs beneath La Palma (Canary Islands). *Terra Nova* 9: 117-121
- Klügel A (1998) Reactions between mantle xenoliths and host magma beneath La Palma (Canary Islands): constraints on magma ascent rates and crustal reservoirs. *Contrib Mineral Petrol* 131: 237-257
- Klügel A, Hansteen TH (1998): Petrologic evolution of a peridotite-, cumulate- and MORB-gabbro-bearing tephriphonolite on La Palma (Canary Islands). *Eos Trans. AGU, Fall Meet. Suppl.*, Abstract V11A-13
- Klügel A, Schmincke HU, White JDL, Hoernle KA (1999) Chronology and volcanology of the 1949 multi-vent rift-zone eruption on La Palma (Canary Islands). *J Volcanol Geotherm Res* 94: 267-282
- Klügel A, Hoernle KA, Schmincke HU, White JDL (2000) The chemically zoned 1949 eruption on La Palma (Canary Islands): Petrologic evolution and magma supply dynamics of a rift-zone eruption. *J Geophys Res* 105 (B3): 5997-6016
- Klügel A (2001) Comment on "Silicic melts produced by reaction between peridotite and infiltrating basaltic melts: ion probe data on glasses and minerals in veined xenoliths from La Palma, Canary Islands" by Wulff-Pedersen et al. *Contrib Mineral Petrol* 141: 505-510
- Klügel A, Hansteen TH, Galipp K (2005) Magma storage and underplating beneath Cumbre Vieja volcano, La Palma (Canary Islands). *Earth Planet Sci Lett* 236, 211-226
- Kress, V.C., and Carmichael, I.S.E., (1991) The Compressibility of Silicate Liquids Containing Fe₂O₃ and the Effect of Composition, Temperature, Oxygen Fugacity and Pressure on Their Redox States: Contributions to Mineralogy and Petrology, v. 108, p. 82-92
- Kunzmann T (1999) The Evolution of Phonolitic Melts by Fractional Crystallization: An Experimental Study. *Eos Trans. AGU*, 80(46), Fall Meet. Suppl., 1090, Abstract V12C-08
- LeMaitre RW, Bateman P, Dudek A, Keller J, Lameyre J, Le Bas MJ, Sabine PA, Schmid R, Sorensen H, Streckeisen A, Wooley AR, Zanettin B (1989) A Classification of Igneous Rocks and Glossary of Terms

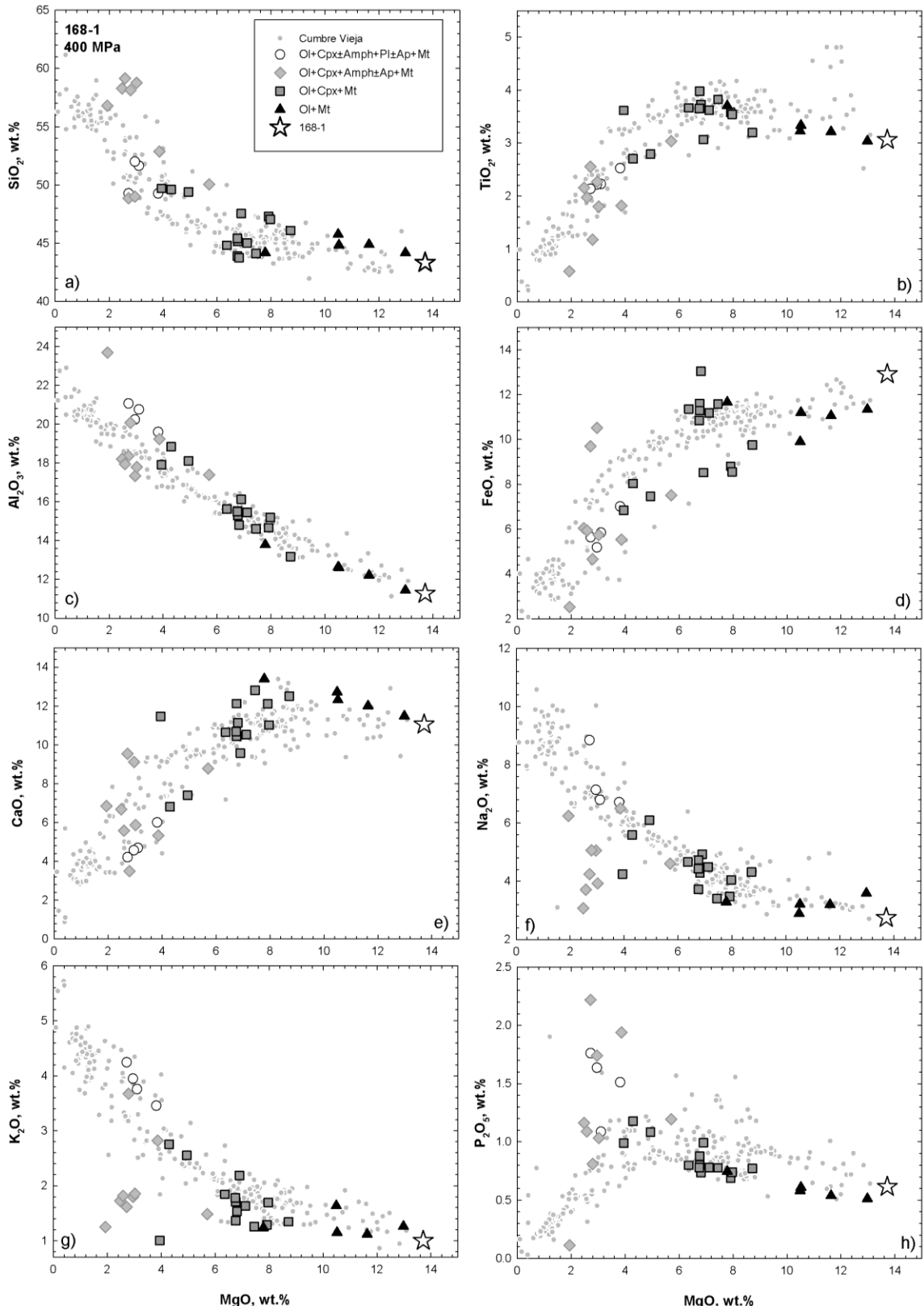
- Recommendations of the International Union of Geological Sciences Subcommission on the Systematics of Igneous Rocks, vol. Blackwell Scientific Publications, Oxford, p 193
- LeRoex AP, Cliff RA, Adair BJI (1990) Tristan da Cunha, South Atlantic: Geochemistry and Petrogenesis of a Basanite-Phonolite Lava Series. *J. Petrol.* 31: 779-812
- Marziano GI, Schmidt BC, Dolfi D (2007) Equilibrium and disequilibrium degassing of a phonolitic melt (Vesuvius AD 79 "white pumice") simulated by decompression experiments. *J. Volcanol. Geotherm. Res.* 161: 151-164
- Melluso L, Morra V, Riziky H, Veloson J, Lustrino M, Del gatto L, Modeste V (2007) Petrogenesis of a basanite-tephrite-phonolite volcanic suite in the Bobaomby (Cap d'Ambre) peninsula, northern Madagascar. *Journal of African Earth Sciences* 49: 29-42
- Mitchell-Thomé RC (1970) Geology of the Middle Atlantic, vol 12. Bornträger, Berlin
- Moore, G., Vennemann, T., and Carmichael, I., (1998) An empirical model for the solubility of H₂O in magmas to 3 kilobars: *American Mineralogist*, v. 83, p. 36-42
- Moretti, R., (2005) Polymerisation, basicity, oxidation state and their role in ionic modelling of silicate melts: *Annals of Geophysics*
- Moussallam, Y., Oppenheimer, C., Scaillet, B., and Kyle, P.R., (2013) Experimental Phase-equilibrium Constraints on the Phonolite Magmatic System of Erebus Volcano, Antarctica: *Journal of Petrology*
- Neumann ER, Sørensen VB, Simonsen SL, Johnsen K (2000) Gabbroic xenoliths from La Palma, Tenerife and Lanzarote, Canary Islands: evidence for reactions between mafic alkaline Canary Islands melts and old oceanic crust. *J. Volcanol. Geotherm. Res.* 103: 313-342
- Parat, F., Holtz, F., René, M., and Almeev, R., (2010) Experimental constraints on ultrapotassic magmatism from the Bohemian Massif (durbachite series, Czech Republic): Contributions to Mineralogy and Petrology, v. 159, p. 331-347 Pitzer, K.S., and Stern, S.M., 1994, Equations of state valid continuously from zero to extreme pressures for H₂O and CO₂: *The Journal of chemical physics*, v. 101, p. 3111-3116
- Praegel NO (1986) The petrology and geochemistry of Volcán Teneguía, La Palma, Canary Islands. Ph.D. thesis, Univ. Copenhagen, Denmark
- Praegel NO, Holm PM (2006) Lithospheric contributions to high-MgO basanites from the Cumbre Vieja Volcano, La Palma, Canary Islands and evidence for temporal variation in plume influence. *J. Volcanol. Geotherm. Res.* 149: 213-239
- Price RC, Chappell BW (1975) Fractional Crystallisation and the Petrology of Dunedin Volcano. *Contrib. Mineral. Petrol.* 53: 157-182
- Price RC, Johnson RW, Gray CM, Frey FA (1985) Geochemistry of phonolites and trachytes from the summit region of Mt. Kenya. *Contrib. Mineral. Petrol.* 89: 394-409
- Putirka K, Johnson M, Kinzler R, Longhi J, Walker D (1996) Thermobarometry of mafic igneous rocks based on clinopyroxene-liquid equilibria, 0-30 kbar. *Contrib. Mineral. Petrol.* 123: 92-108
- Putirka KD, Mikaelian H, Ryerson F, Shaw H (2003) New clinopyroxene-liquid thermobarometers for mafic, evolved, and volatile-bearing lava compositions, with applications to lavas from Tibet and the Snake River Plain, Idaho. *Am. Mineral.* 88: 1542-1554
- Reagan MK, Turner S, Legg M, Sims KWW, Hards VL (2008) 238U- and 232Th-decay series constraints on the timescales of crystal fractionation to produce the phonolite erupted in 2004 near Tristan da Cunha, South Atlantic Ocean. *Geochim. Cosmochim. Acta* 72: 4367-4378
- Robie R.A., Hemingway B.S., Fisher J.R. (1978) Thermodynamic properties of minerals and related substances at 298.15K and 1 bar (10^5 Pascals) pressure and at higher temperatures . *U.S. Geol. Surv. Bull.* 1452 (1978), p. 456
- Roeder, P., and Emslie, R., (1970) Olivine-liquid equilibrium: Contributions to Mineralogy and Petrology, v. 29, p. 275-289

- Sack RO, Walker D, Carmichael ISE (1987) Experimental petrology of alkalic lavas: constraints on cotectics of multiple saturation in natural basic liquids. *Contrib. Mineral. Petrol.* 96: 1-23
- Scaillet, B., Pichavant, M., and Roux, J., (1995) Experimental crystallization of leucogranite magmas: *Journal of Petrology*, v. 36, p. 663-705
- Scaillet B, Pichavant M, Cioni R (2008) Upward migration of Vesuvius magma chamber over the past 20,000 years. *Nature* 455: 216-219
- Schmidt B, Behrens H (2008) Water solubility in phonolite melts: Influence of melt composition and temperature. *Chem. Geol.* 256: 259-268
- Schmincke HU (1976) Geology of the Canary Islands. In: Kunkel G (ed) Biogeography and ecology of the Canary Islands, vol. Junk BV, The Hague, pp 67-184
- Schmincke HU (1977) Eifel-Vulkanismus östlich des Gebietes Rieden-Mayen. *Fortschritt Min Bh* 55: 1-31
- Schmincke HU (2008) The Quaternary Volcanic Fields of the East and West Eifel (Germany). In: Ritter JRR, Christensen UR (eds) Mantle Plumes, Springer, Berlin Heidelberg, pp 241-322
- Schmincke, H.U., Klügel, A., Hansteen, T.H., Hoernle, K., and Van den Bogaard, P., (1998) Samples from the Jurassic ocean crust beneath Gran Canaria, La Palma and Lanzarote (Canary Islands): Earth and Planetary Science Letters, v. 163, p. 343-360
- Schuessler, J.A., Botcharnikov, R.E., Behrens, H., Misiti, V., and Freda, C., (2008), Amorphous Materials: Properties, structure, and Durability Oxidation state of iron in hydrous phono-tephritic melts: *American Mineralogist*, v. 93, p. 1493-1504
- Schwab, R.G. and Küstner, D. (1981) The equilibrium fugacities of important oxygen buffers in technology and petrology. *Neues Jahrbuch für Mineralogie*, 140, 112–142
- Shaw, H.R., and Wones, D.R., (1964) Fugacity coefficients for hydrogen gas between 0 degrees and 1000 degrees C, for pressures to 3000 atm: *American Journal of Science*, v. 262, p. 918-929
- Shishkina, T., Botcharnikov, R., Holtz, F., Almeev, R., and Portnyagin, M.V., (2010) Solubility of H₂O-and CO₂-bearing fluids in tholeiitic basalts at pressures up to 500 MPa: *Chemical Geology*, v. 277, p. 115-125
- Stormer, J.C., (1983) The effects of recalculation on estimates of temperature and oxygen fugacity from analyses of multicomponent iron-titanium oxides: *American Mineralogist*, v. 68, p. 586-594
- Toplis, M., (2005) The thermodynamics of iron and magnesium partitioning between olivine and liquid: criteria for assessing and predicting equilibrium in natural and experimental systems: *Contributions to Mineralogy and Petrology*, v. 149, p. 22-39
- Villiger S, Ulmer P, Muntener O (2007) Equilibrium and Fractional Crystallization Experiments at 0.7 GPa; the Effect of Pressure on Phase Relations and Liquid Compositions of Tholeiitic Magmas. *J. Petrol.* 48: 159-184
- Weis D, Frey FA, Leyrit H, Gautier I (1993) Kerguelen Archipelago revisited: geochemical and isotopic study of the Southeast Province lavas. *Earth Planet Sci Lett* 118: 101-119
- Wengorsch, T. (2013) Experimental Constraints on the Storage Conditions of a Tephriphonolite from the Cumbre Vieja Volcano (La Palma, Canary Islands) at 200 and 400MPa. Unpublished Master thesis, Leibniz Universität Hannover, Germany
- Wilson, A.d. (1960) The micro-determination of ferrous iron in silicate minerals by a volumetric and colorimetric method. *Analyst*, 85, 823–827
- Wörner G, Schmincke HU (1984) Petrogenesis of the Zoned Laacher See Tephra. *J. Petrol.* 25:836-851
- Wolff JA, Turbeville BN (1985) Recent pyroclastic deposits on Brava, Cape Verde Islands. *Eos Trans. AGU*, 66(46), Fall Meet. Suppl., 1152, Abstract V52A-07
- Wulff-Pedersen E, Neumann ER, Jensen BJ (1996) The upper mantle under La Palma, Canary Islands: formation of Si-K-Na-rich melt and its importance as a metasomatic agent. *Contrib. Mineral. Petrol.* 125:113-139

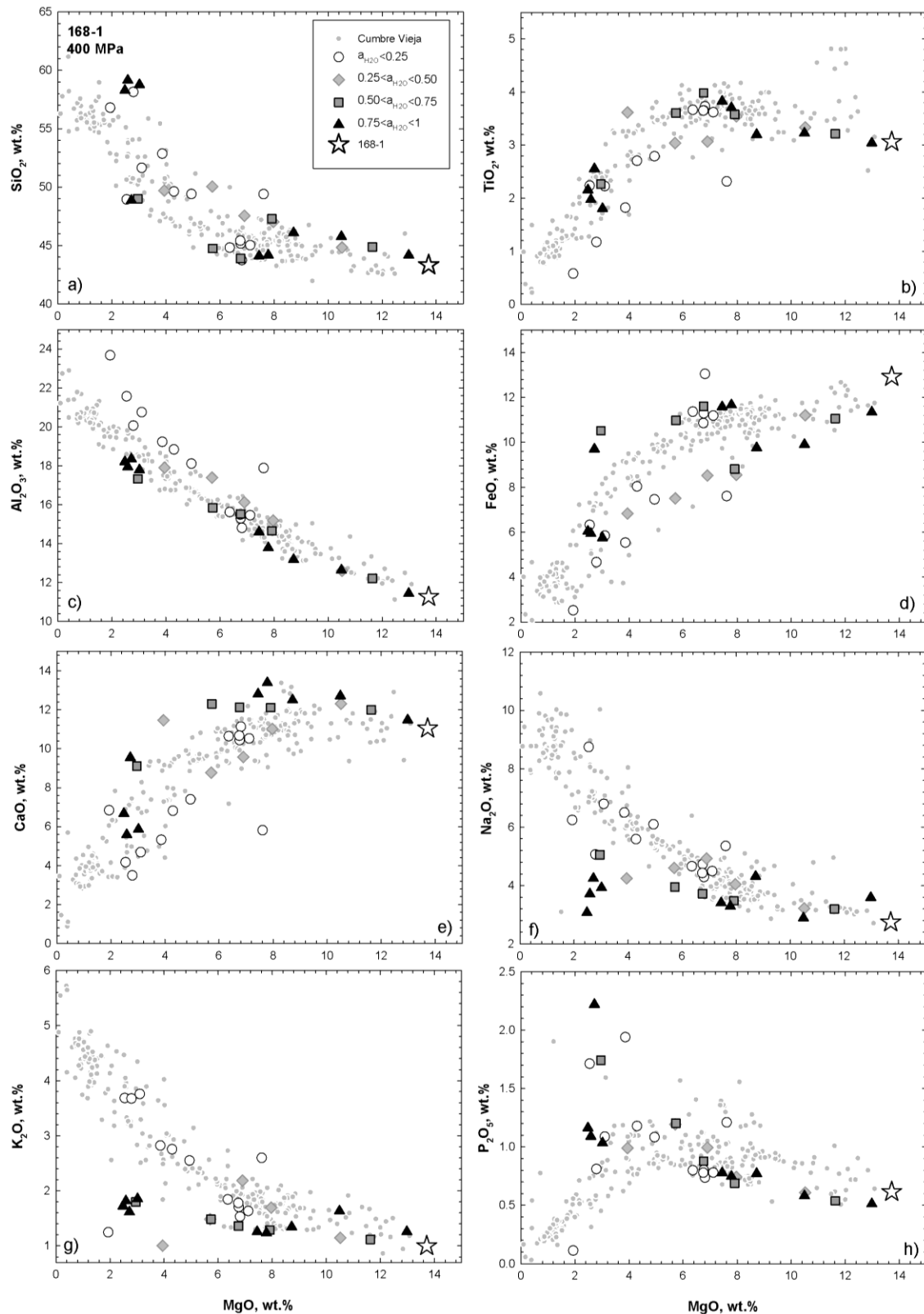
Appendix



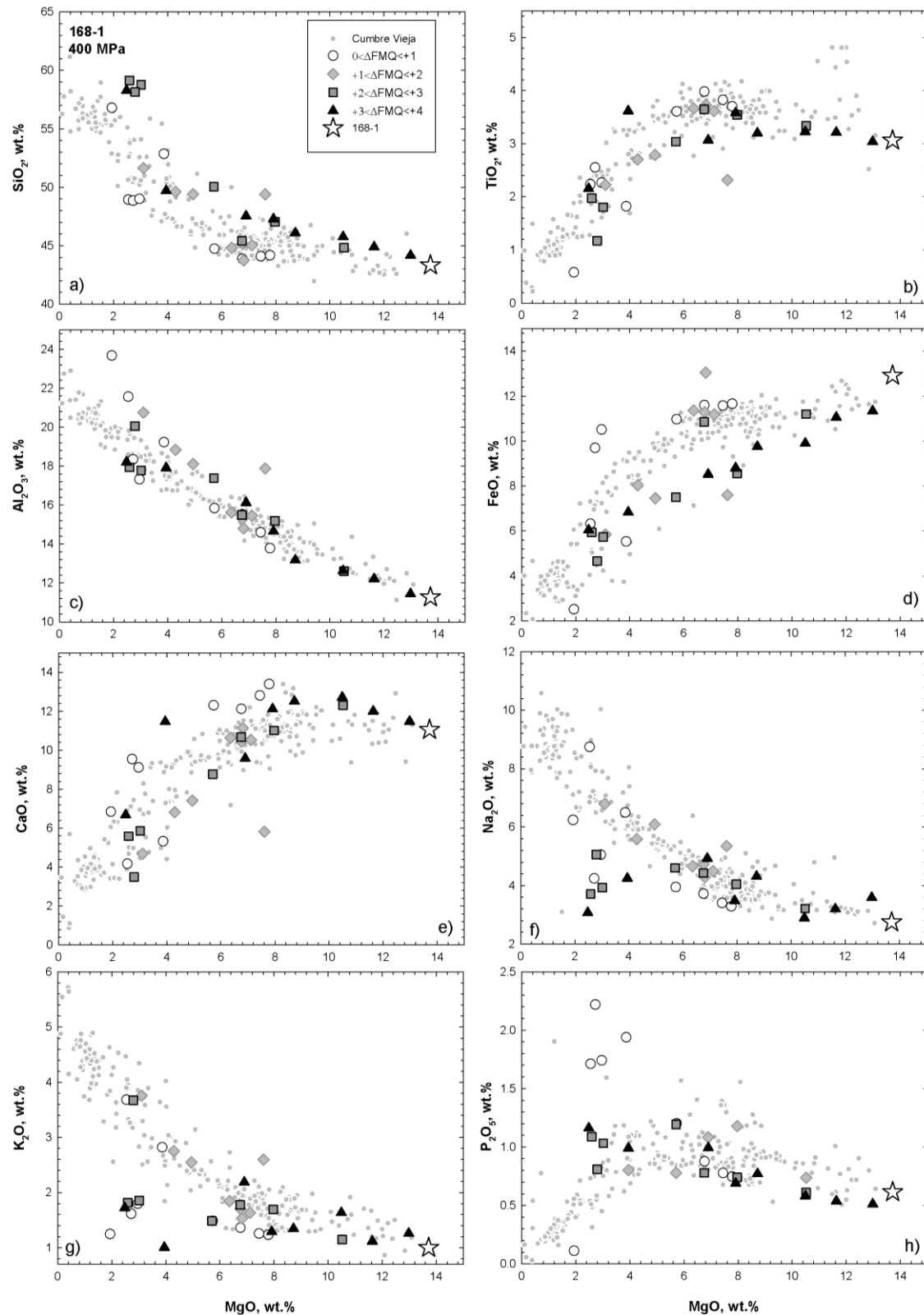
A 51: A systematic comparison of experimentally produced liquids (blue diamonds) and La Palma whole rock compositions (black circles) was performed to highlight the experimental isobaric liquid lines of descent versus compositional trend representative for natural basanite phonolite volcanic series. In addition, samples from Vesuvius (grey crosses), Erebus (grey triangles) and Campi Flegrei (grey squares) are given to show the wide compositional range of natural phonolites. Yellow diamonds represent compositions of starting materials used in experiments. Two set of experimental studies are shown on the plots: (a) experiments aimed to constrain pre-eruptive storage conditions of phonolite magmas, where phonolites themselves were used as star2815ing materials (Berndt et al. 2001; Freise et al. 2003; Andujar et al. 2008; Fabbrizio and Carroll, 2008; Scaillet et al., 2008.). Since phonolites are already evolved products, the experimental residual melts produced in these experiments are not shown. It is noteworthy that due to slight differences in composition, none of experimentally investigated phonolite can be a good representative of La Palma phonolite. (b) The second set is represented by experiments where more primitive tephri-phonolites to basanites (or alkali basalts) were used as starting materials. For these experiments both starting compositions and residual melt compositions are shown, and in addition the liquid lines of descent are highlighted by arrows: 1 atm trend from the study of Sack et al., 1987 (red arrows, S- 1987), 200 MPa from Freise et al. 2003 (gray, F-2003), 700 MPa from Kaszuba & Wendlandt, 2000 (green, K&W-2000) and 1.4 GPa from Irving & Green, 2008 (violet, I&G-2008). None of the study can be directly applied to La Palma volcanic suite due to the differences in composition of starting material (especially SiO_2 , TiO_2) or due to the PT-conditions used in experiments.



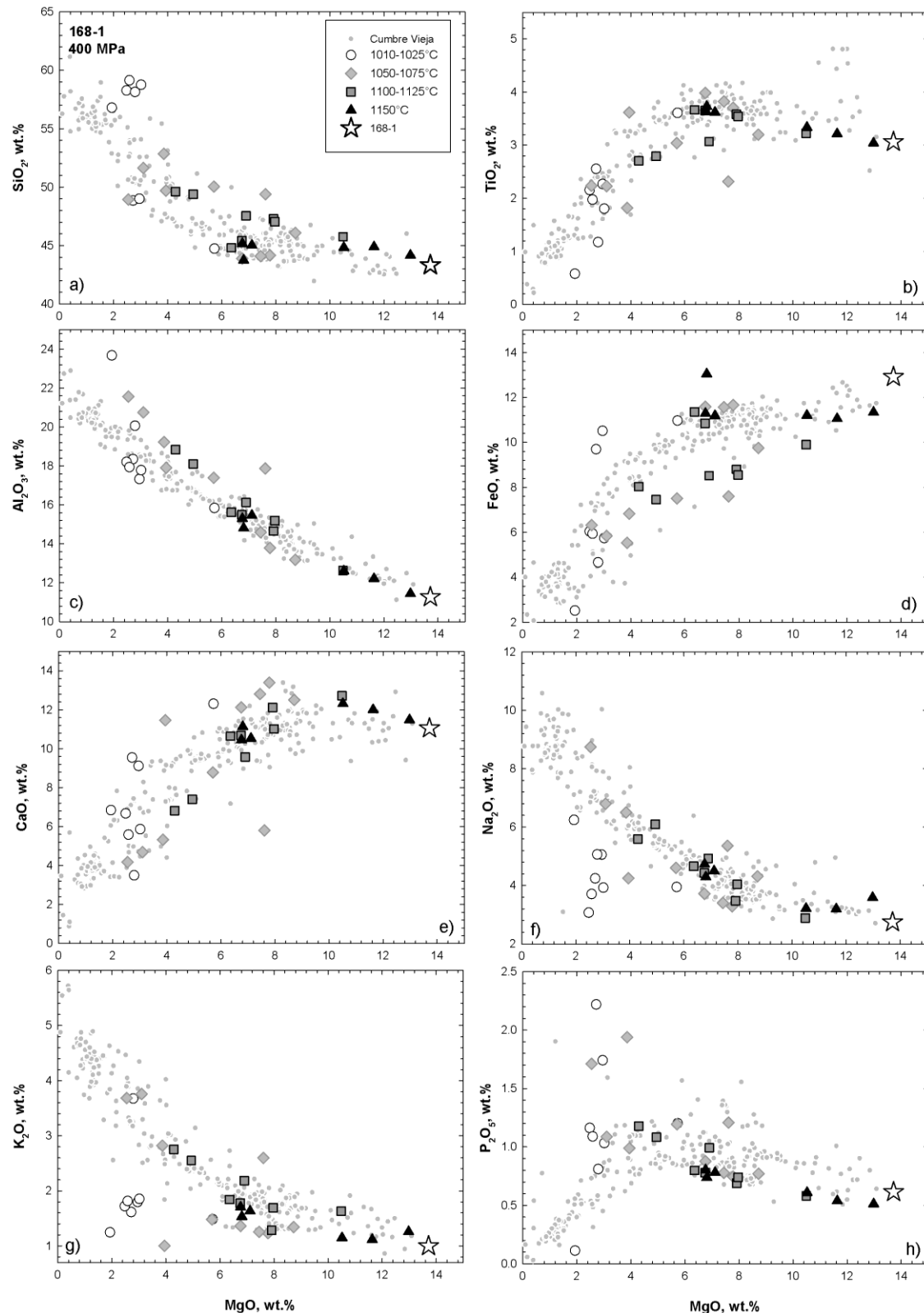
A 52: Effect of crystallizing phases on the compositional evolution of experimental residual melts as a function of MgO content (wt.%) using sample 168-1 at 400 MPa in comparison to natural LLD of the Cumbre Vieja volcano (all compositions are normalized to 100%). (a) SiO₂, (b) TiO₂, (c) Al₂O₃, (d) FeO, (e) CaO, (f) Na₂O, (g) K₂O, (h) P₂O₅.



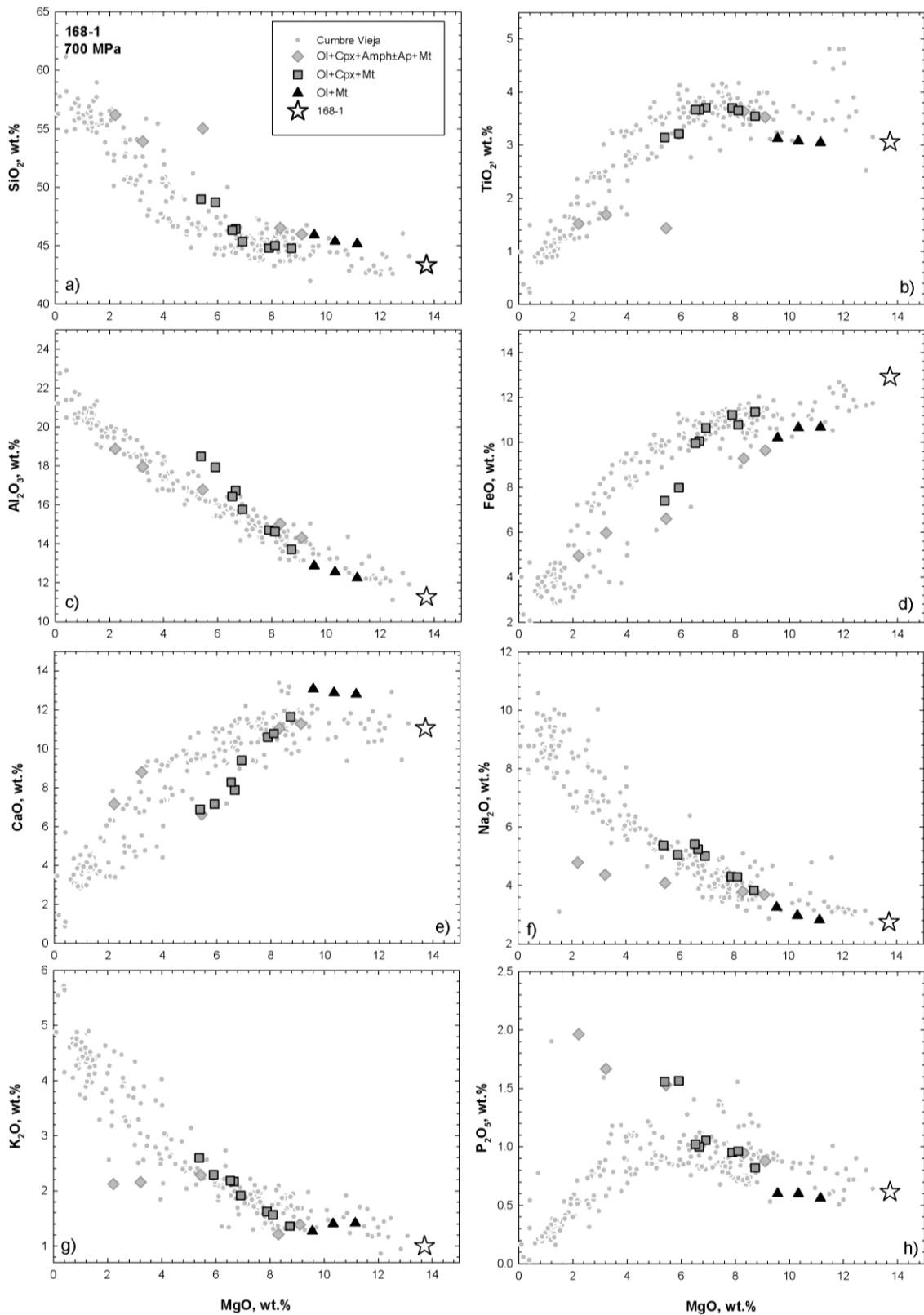
A 53: Effect of $a_{\text{H}_2\text{O}}$ on the compositional evolution of experimental residual melts as a function of MgO content (wt.%) using sample 168-1 at 400 MPa in comparison to natural LLD of the Cumbre Vieja volcano (all compositions are normalized to 100%).



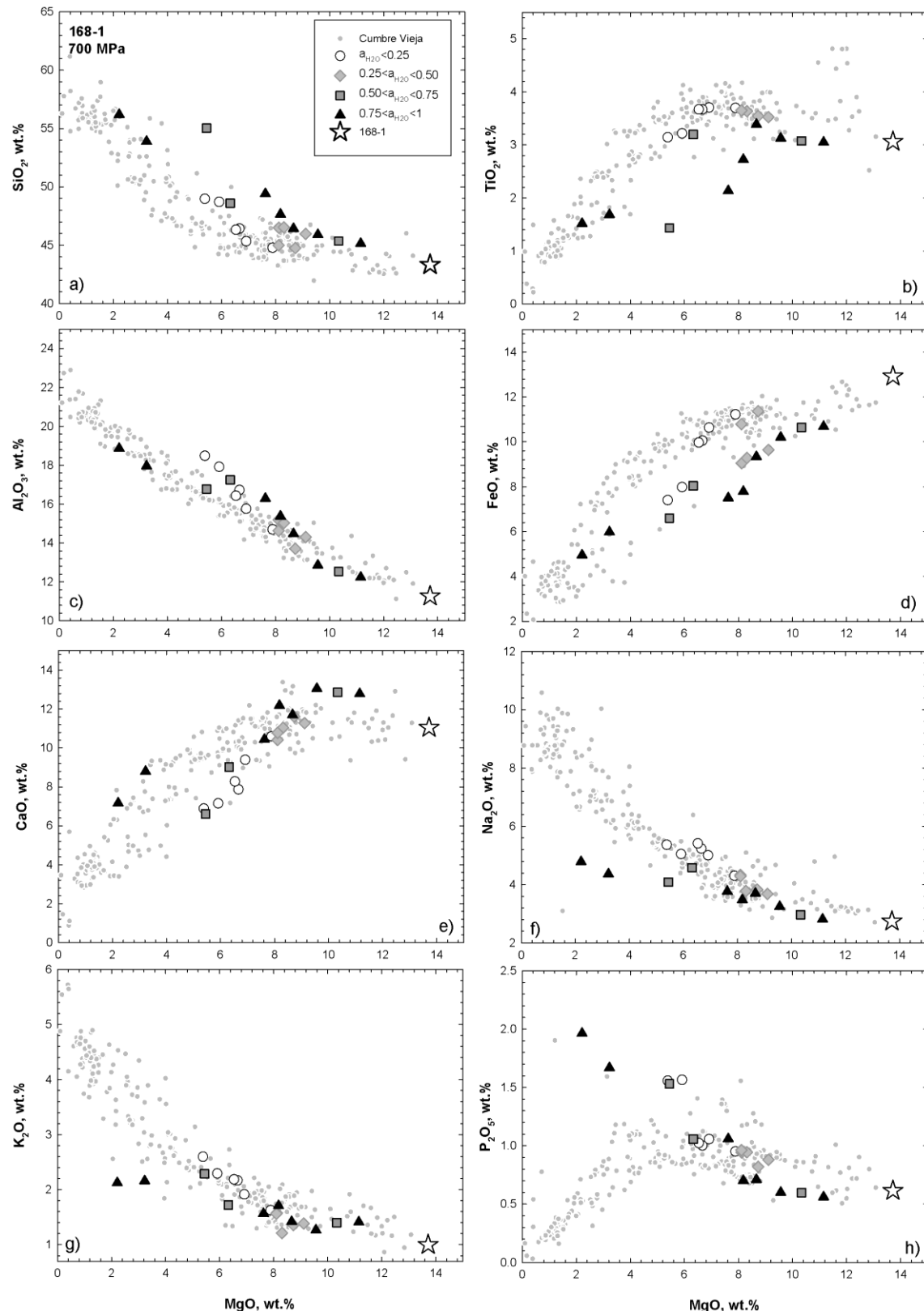
A 54: Effect of $f\text{O}_2$ on the compositional evolution of experimental residual melts as a function of MgO content (wt.%) using sample 168-1 at 400 MPa in comparison to natural LLD of the Cumbre Vieja volcano (all compositions are normalized to 100%).



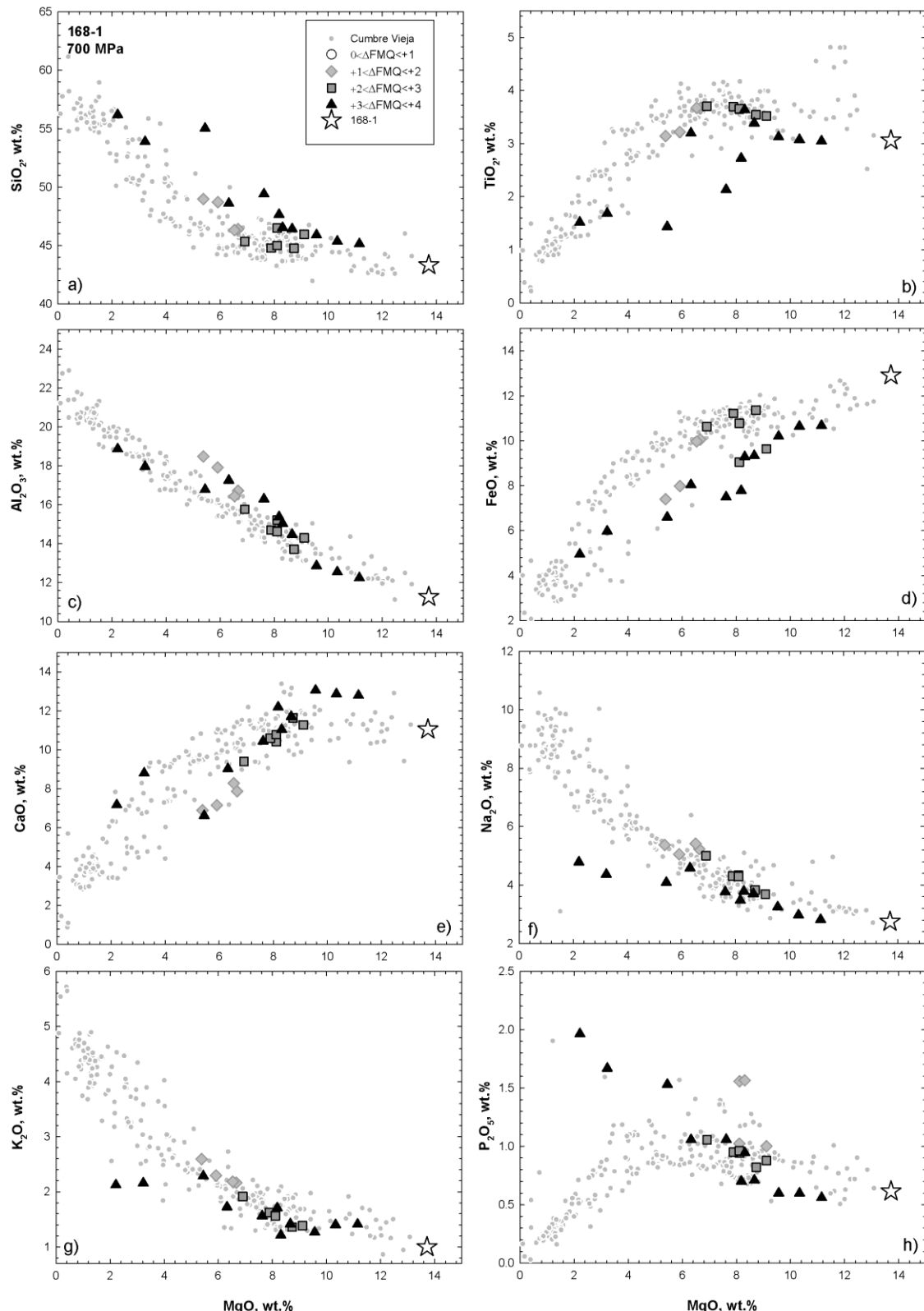
A 55: Effect of temperature ($^{\circ}\text{C}$) on the compositional evolution of experimental residual melts as a function of MgO content (wt.%) using sample 168-1 at 400 MPa in comparison to natural LLD of the Cumbre Vieja volcano (all compositions are normalized to 100%).



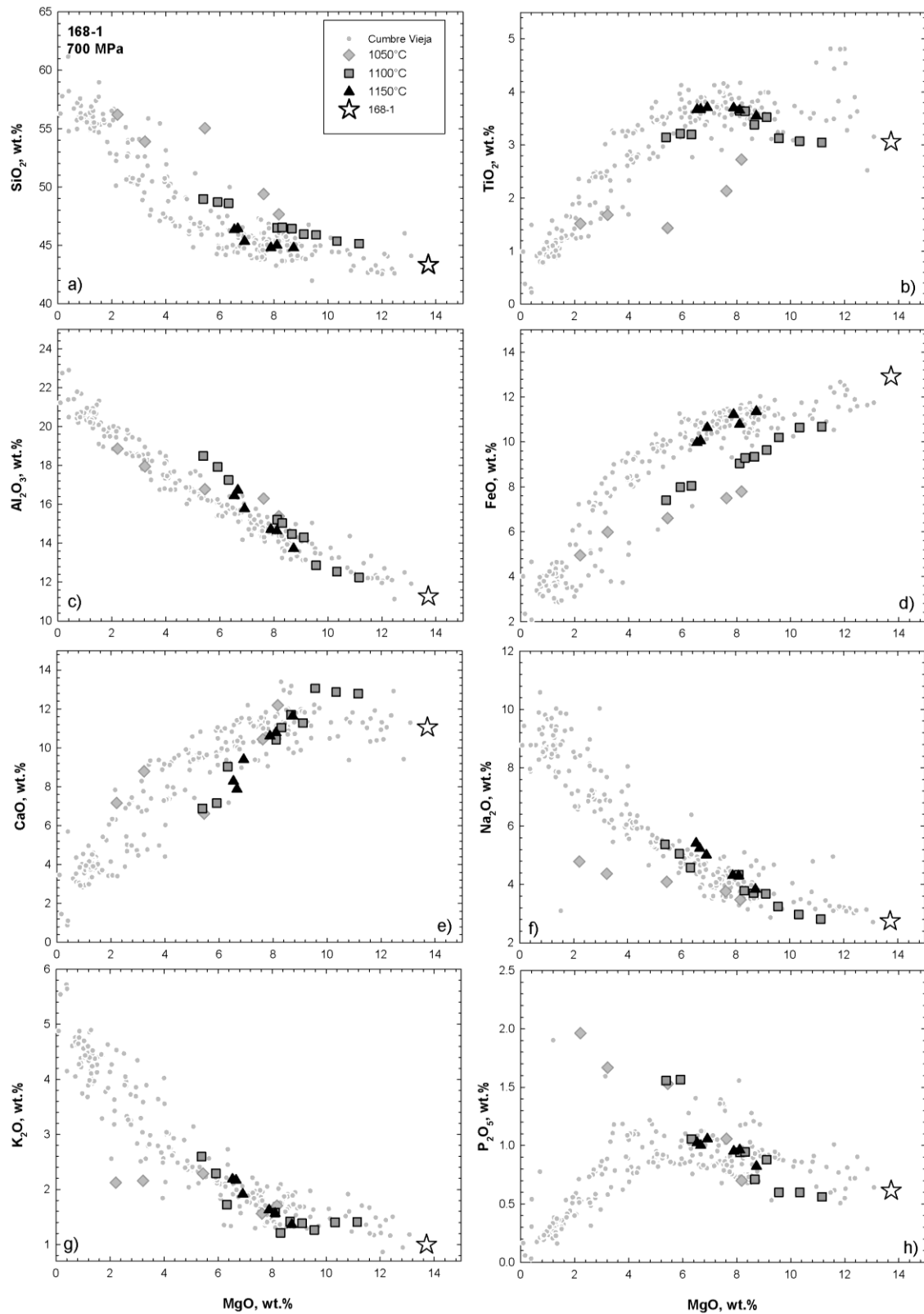
A 56: Effect of crystallizing phases on the compositional evolution of experimental residual melts as a function of MgO content (wt.%) using sample 168-1 at 700 MPa in comparison to natural LLD of the Cumbre Vieja volcano (all compositions are normalized to 100%).



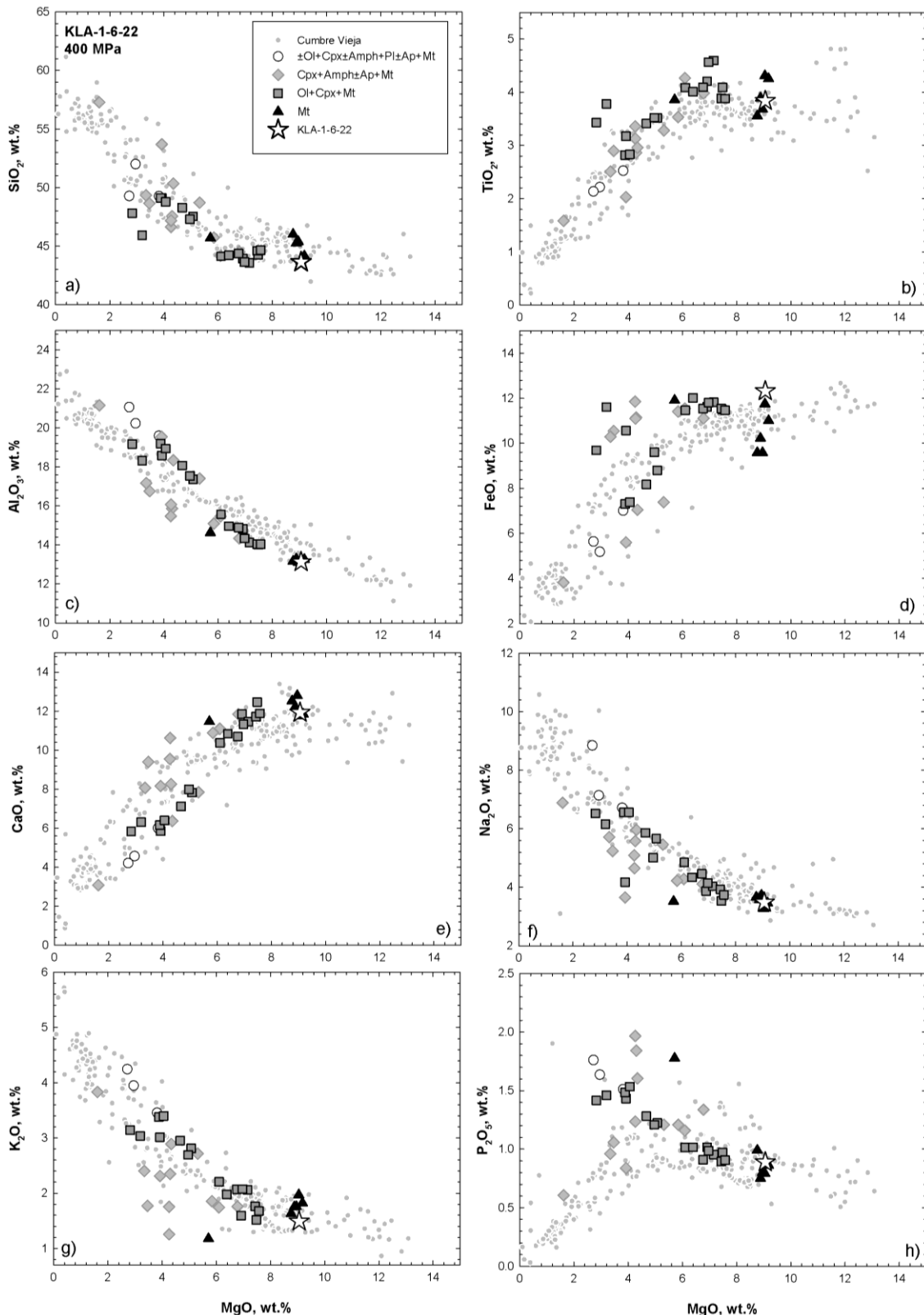
A 57: Effect of $a_{\text{H}_2\text{O}}$ on the compositional evolution of experimental residual melts as a function of MgO content (wt.%) using sample 168-1 at 700 MPa in comparison to natural LLD of the Cumbre Vieja volcano (all compositions are normalized to 100%).



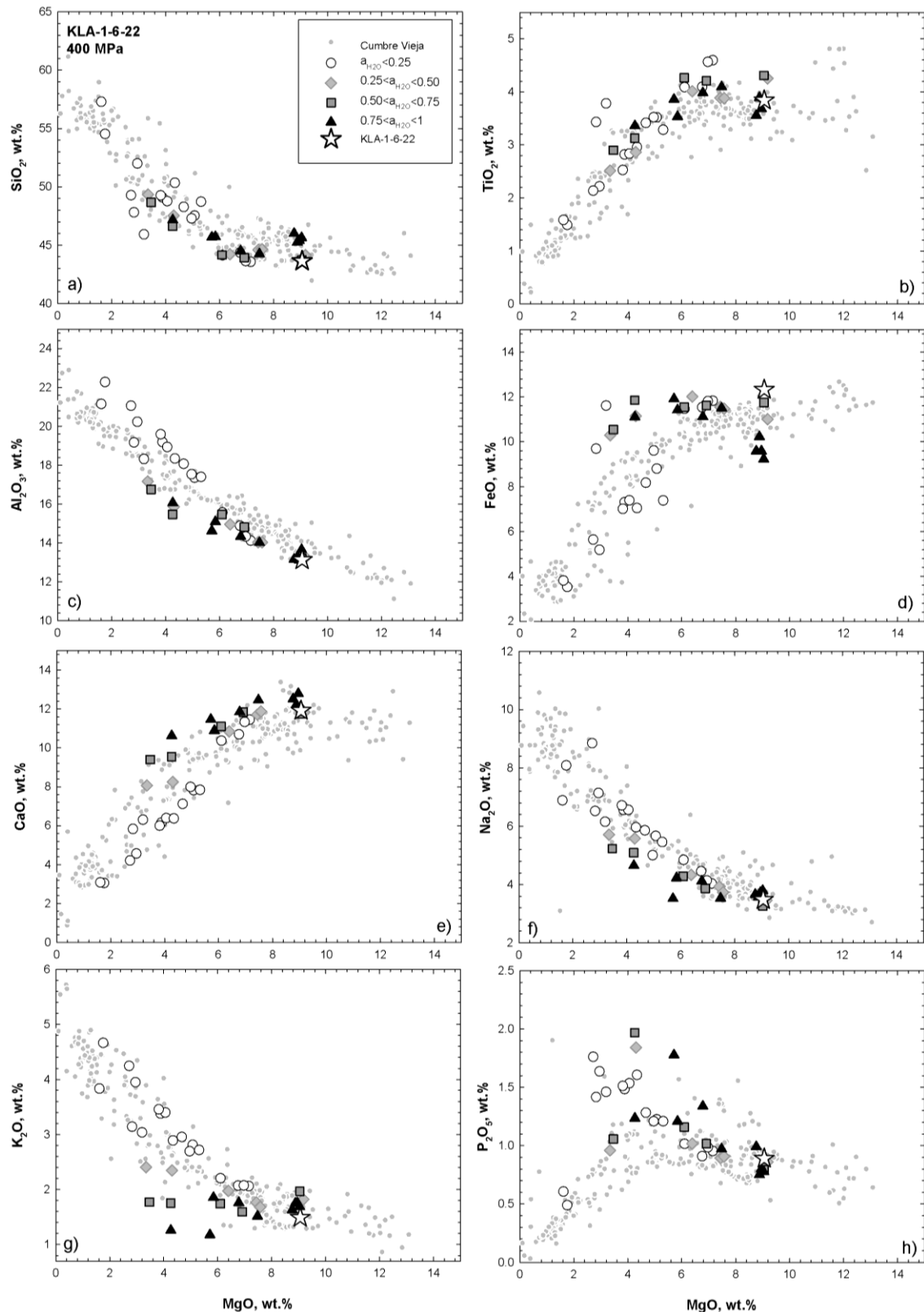
A 58: Effect of $f\text{O}_2$ on the compositional evolution of experimental residual melts as a function of MgO content (wt.%) using sample 168-1 at 700 MPa in comparison to natural LLD of the Cumbre Vieja volcano (all compositions are normalized to 100%).



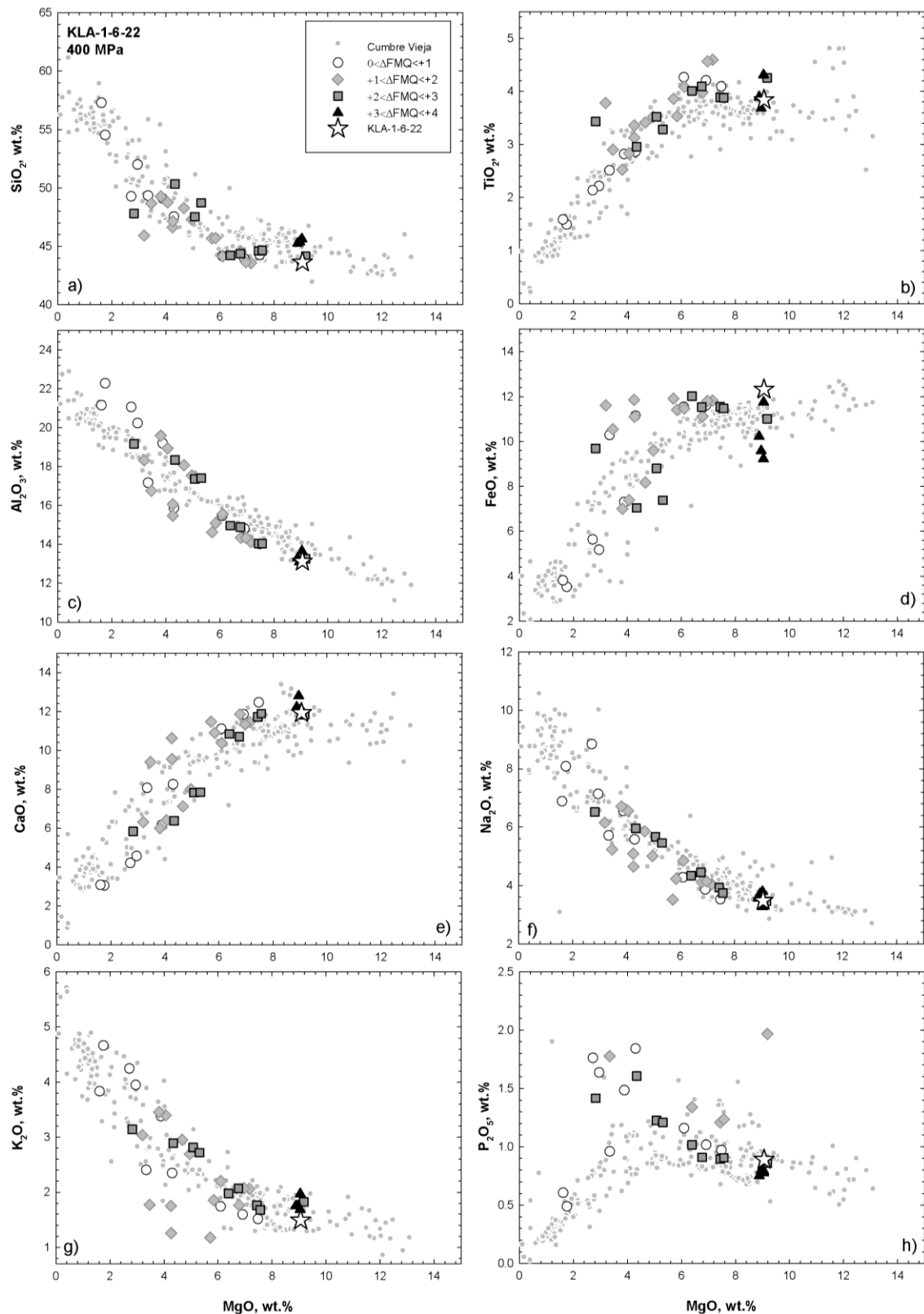
A 59: Effect of temperature ($^{\circ}\text{C}$) on the compositional evolution of experimental residual melts as a function of MgO content (wt.%) using sample 168-1 at 700 MPa in comparison to natural LLD of the Cumbre Vieja volcano (all compositions are normalized to 100%).



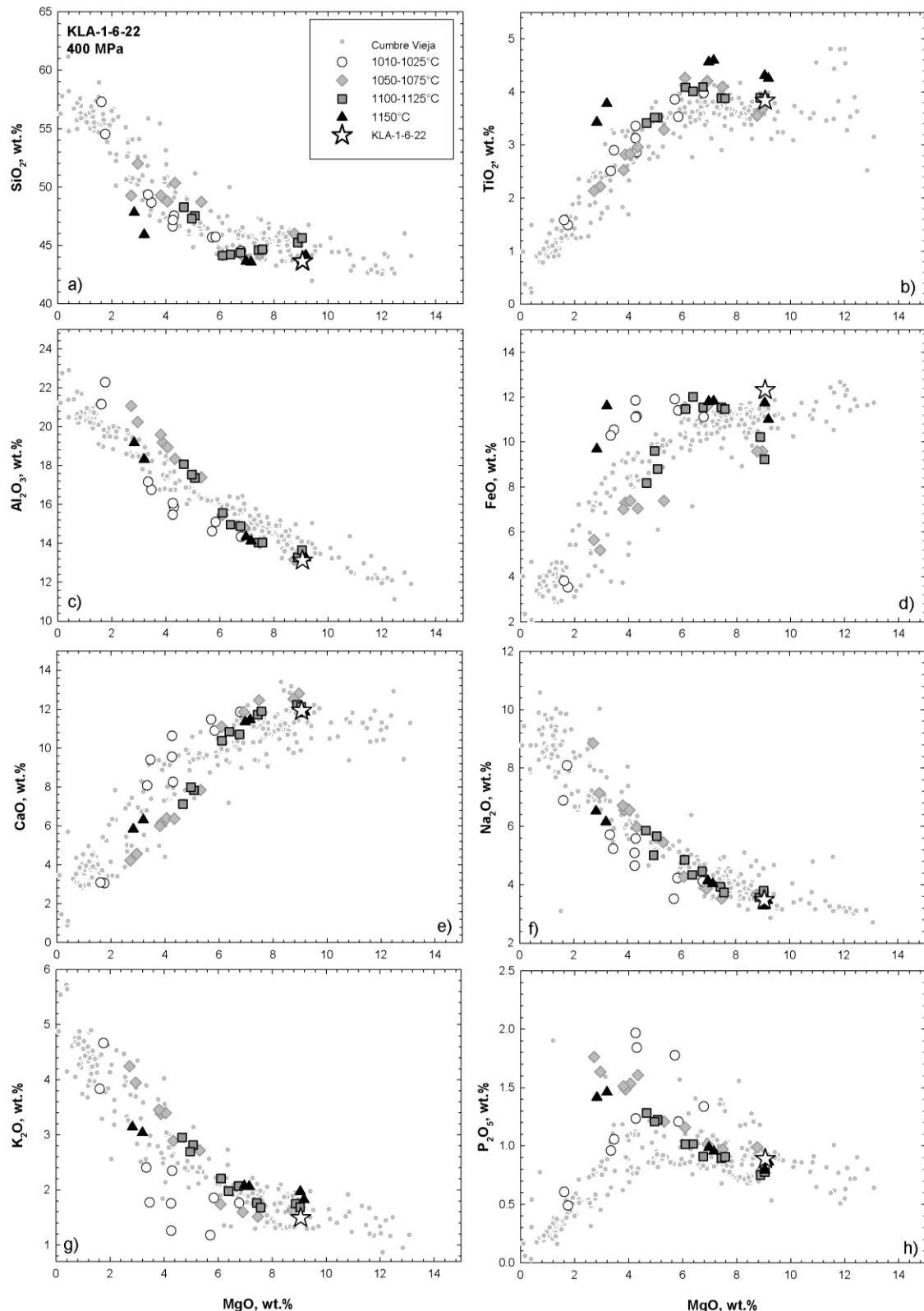
A 60: Effect of crystallizing phases on the compositional evolution of experimental residual melts as a function of MgO content (wt.%) using sample KLA-1-6-22 at 400 MPa in comparison to natural LLD of the Cumbre Vieja volcano (all compositions are normalized to 100%).



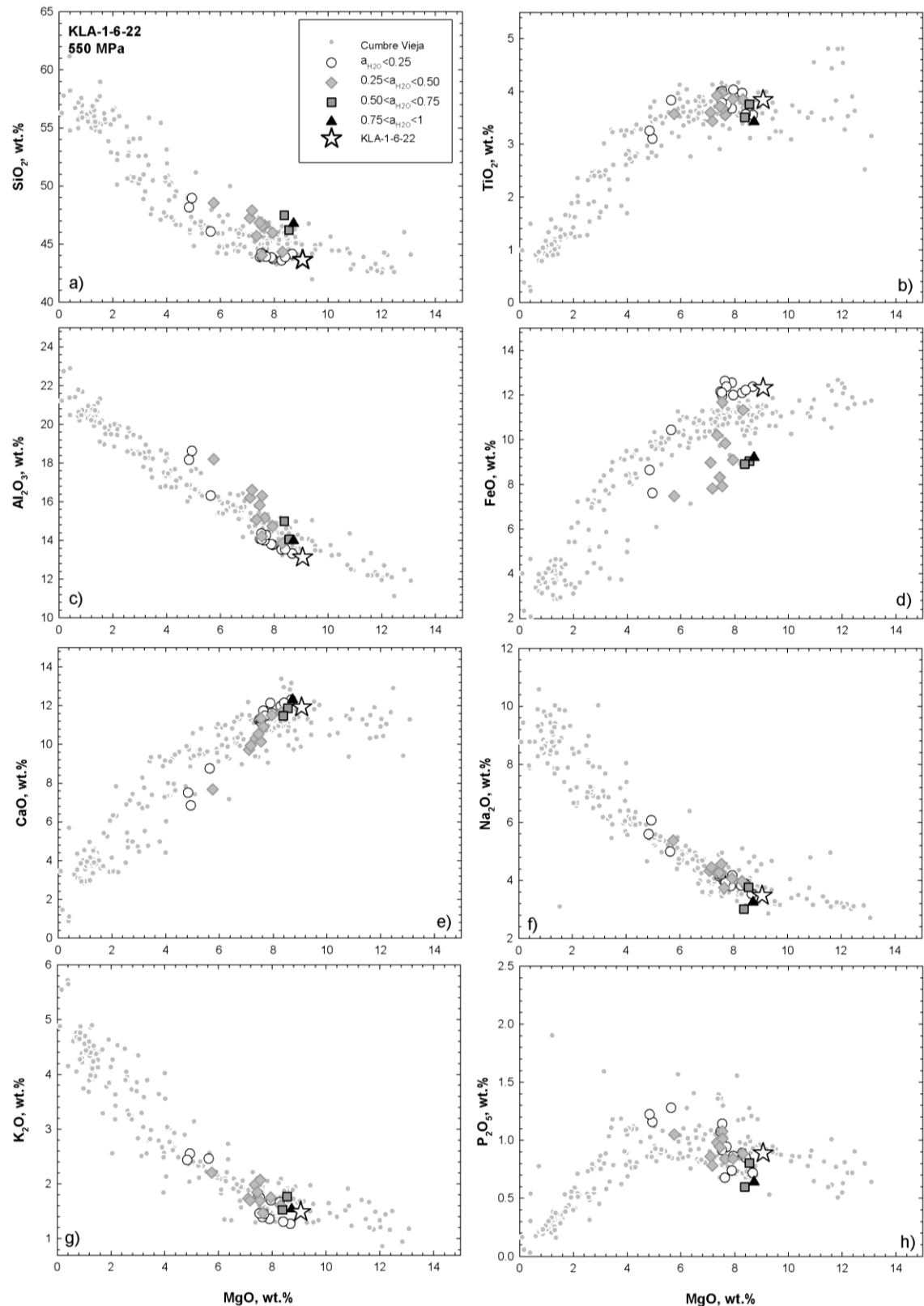
A 61: Effect of $a_{\text{H}_2\text{O}}$ on the compositional evolution of experimental residual melts as a function of MgO content (wt.%) using sample KLA-1-6-22 at 400 MPa in comparison to natural LLD of the Cumbre Vieja volcano (all compositions are normalized to 100%).



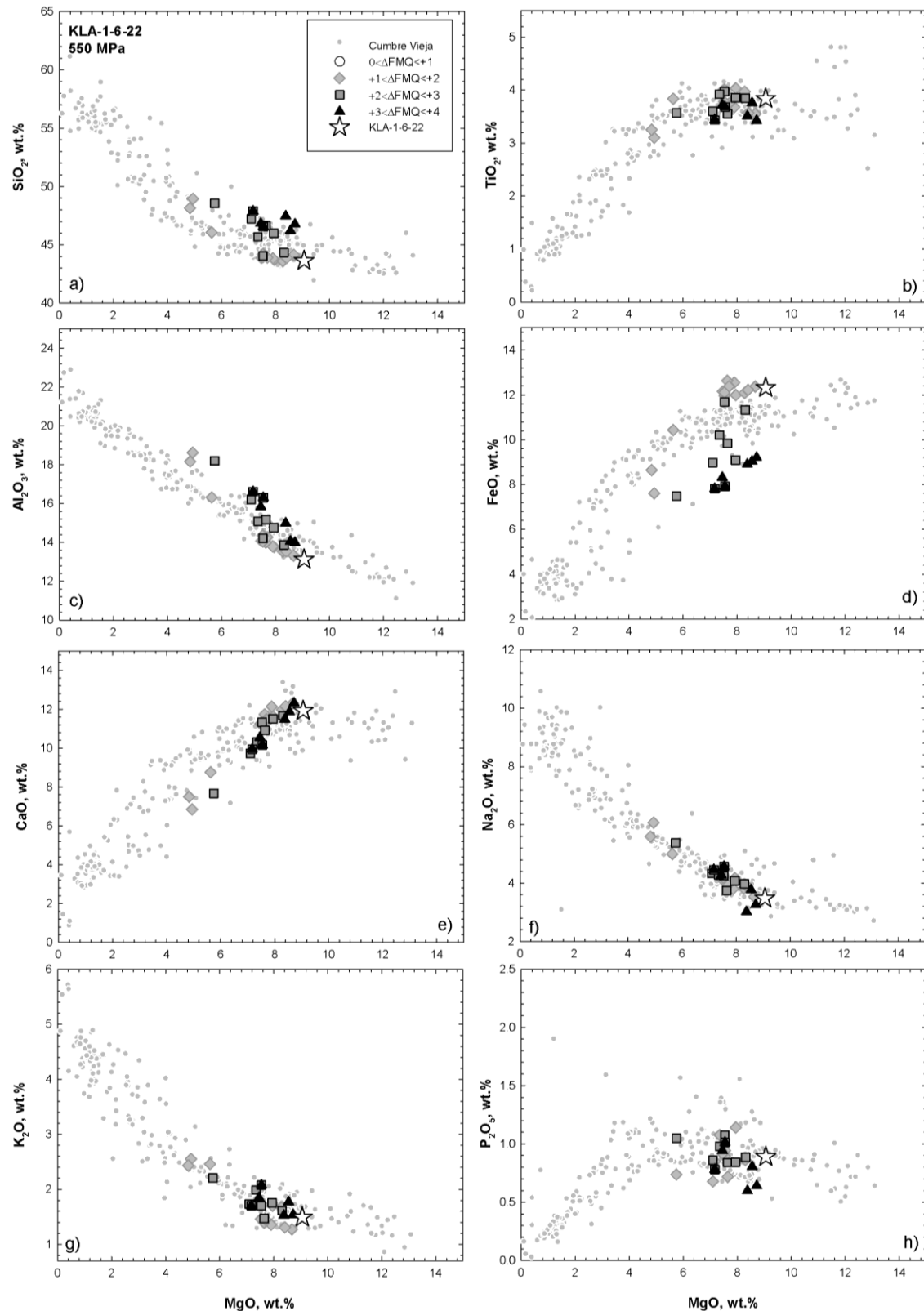
A 62: Effect of fO_2 on the compositional evolution of experimental residual melts as a function of MgO content (wt.%) and redox conditions using sample KLA-1-6-22 at 400 MPa in comparison to natural LLD of the Cumbre Vieja volcano (all compositions are normalized to 100%).



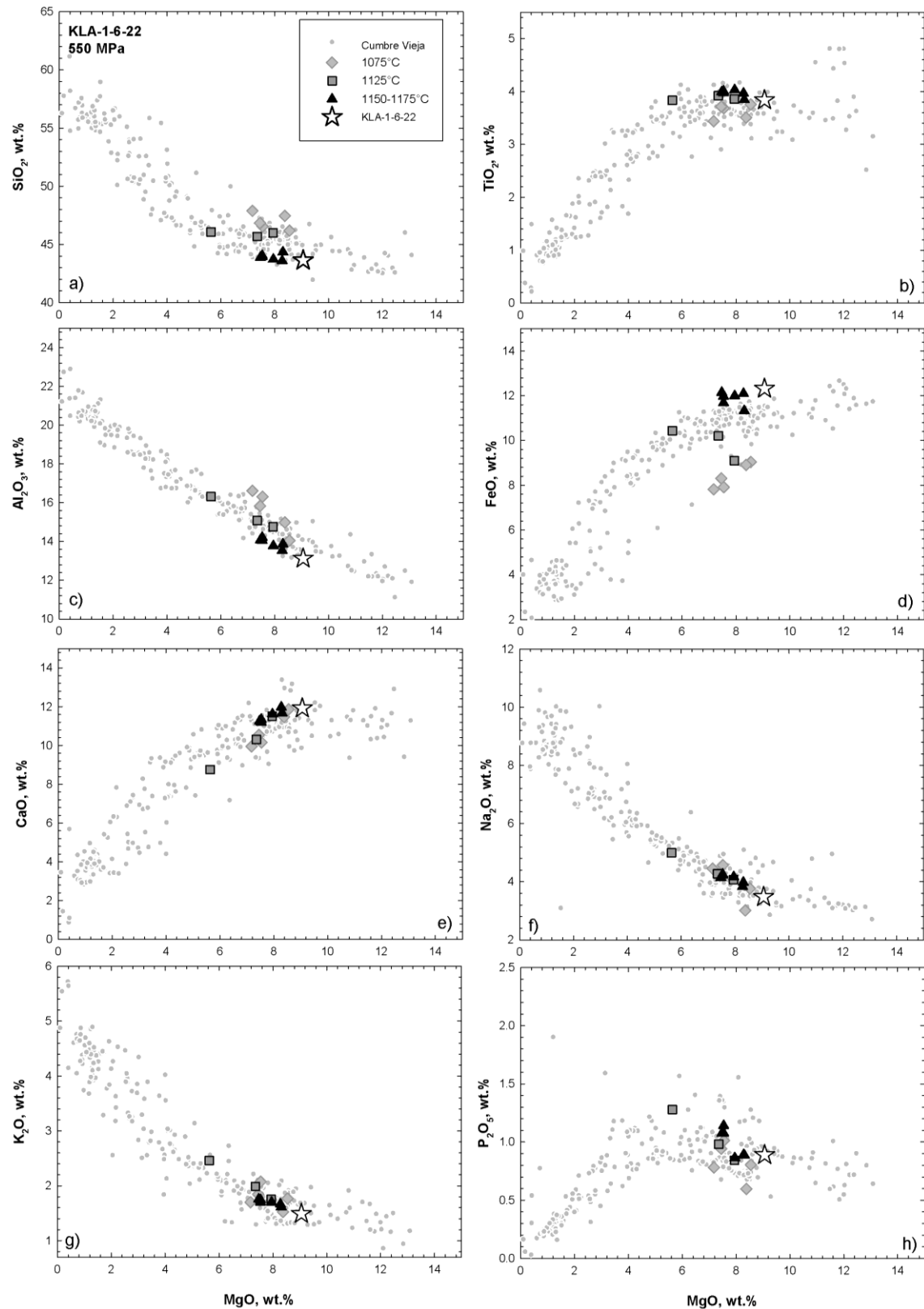
A 63: Effect of temperature (°C) on the compositional evolution of experimental residual melts as a function of MgO content (wt.%) using sample KLA-1-6-22 at 400 MPa in comparison to natural LLD of the Cumbe Vieja volcano (all compositions are normalized to 100%).



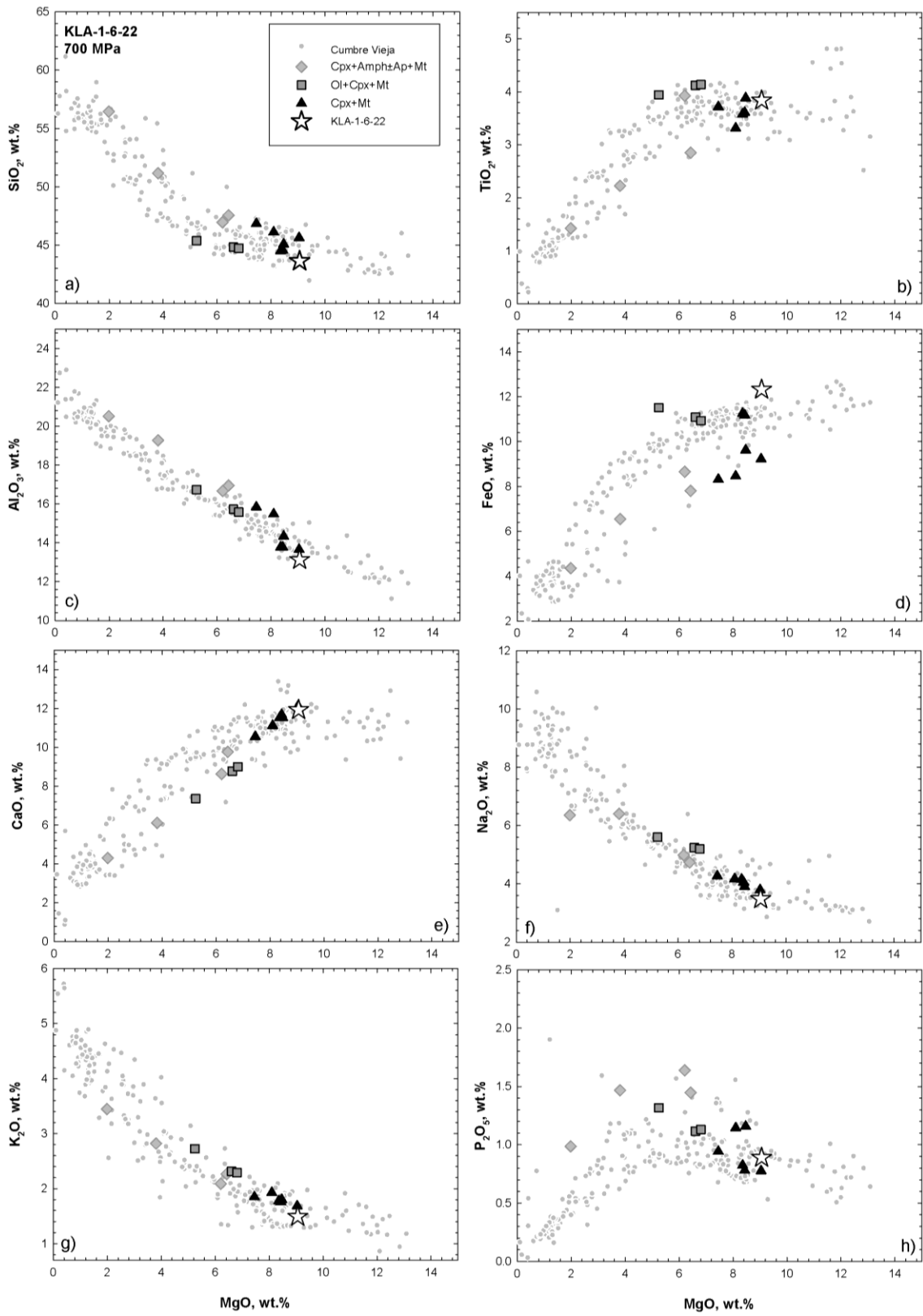
A 64: Effect of $a_{\text{H}_2\text{O}}$ on the compositional evolution of experimental residual melts in equilibrium with $\text{Ol}+\text{Cpx}+\text{Mt}$ as a function of MgO content (wt.%) using sample KLA-1-6-22 at 550 MPa in comparison to natural LLD of the Cumbre Vieja volcano (all compositions are normalized to 100%).



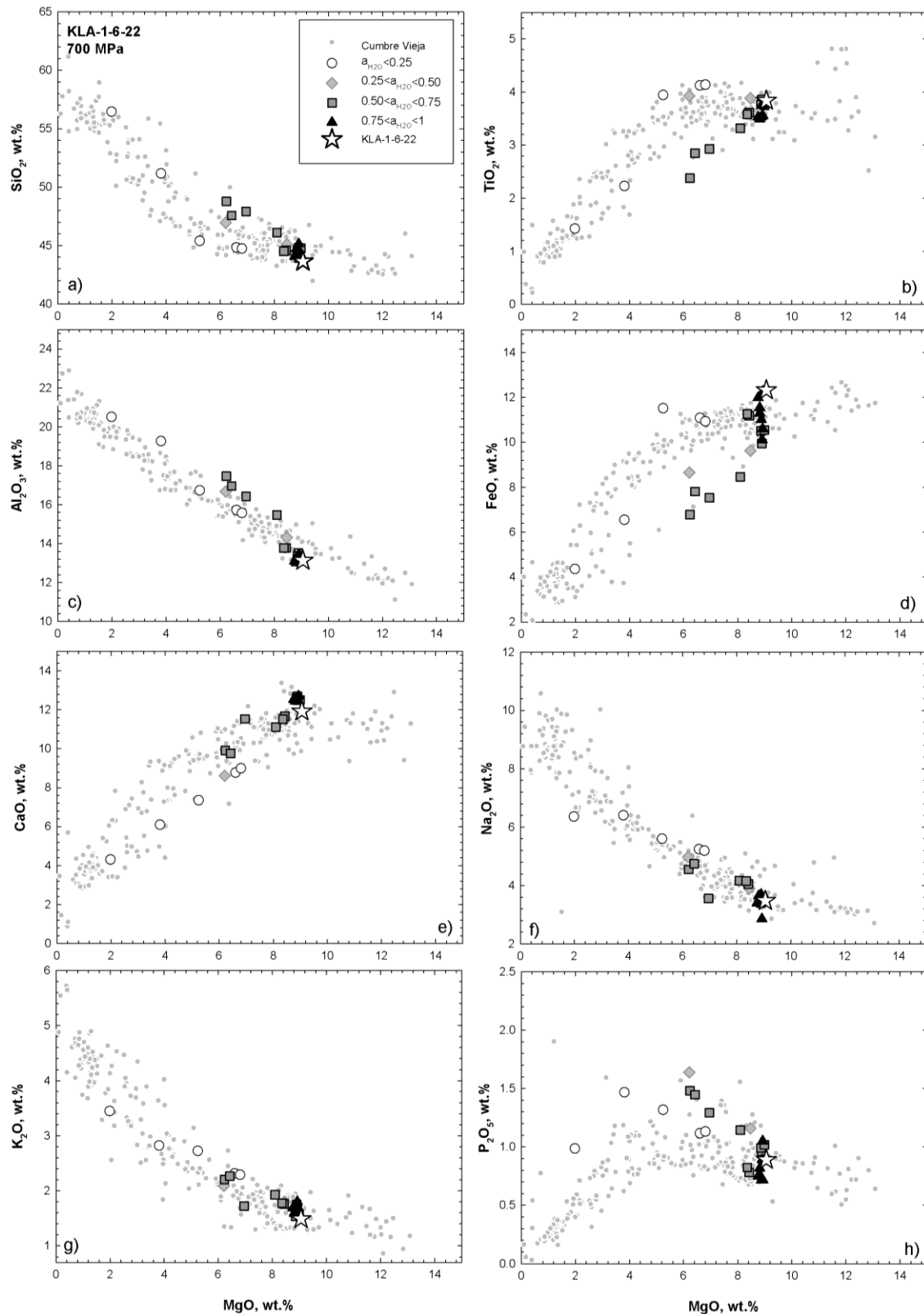
A 65: Effect of $f\text{O}_2$ on the compositional evolution of experimental residual melts in equilibrium with $\text{Ol}+\text{Cpx}+\text{Mt}$ as a function of MgO content (wt.%) using sample KLA-1-6-22 at 550 MPa in comparison to natural LLD of the Cumbre Vieja volcano (all compositions are normalized to 100%).



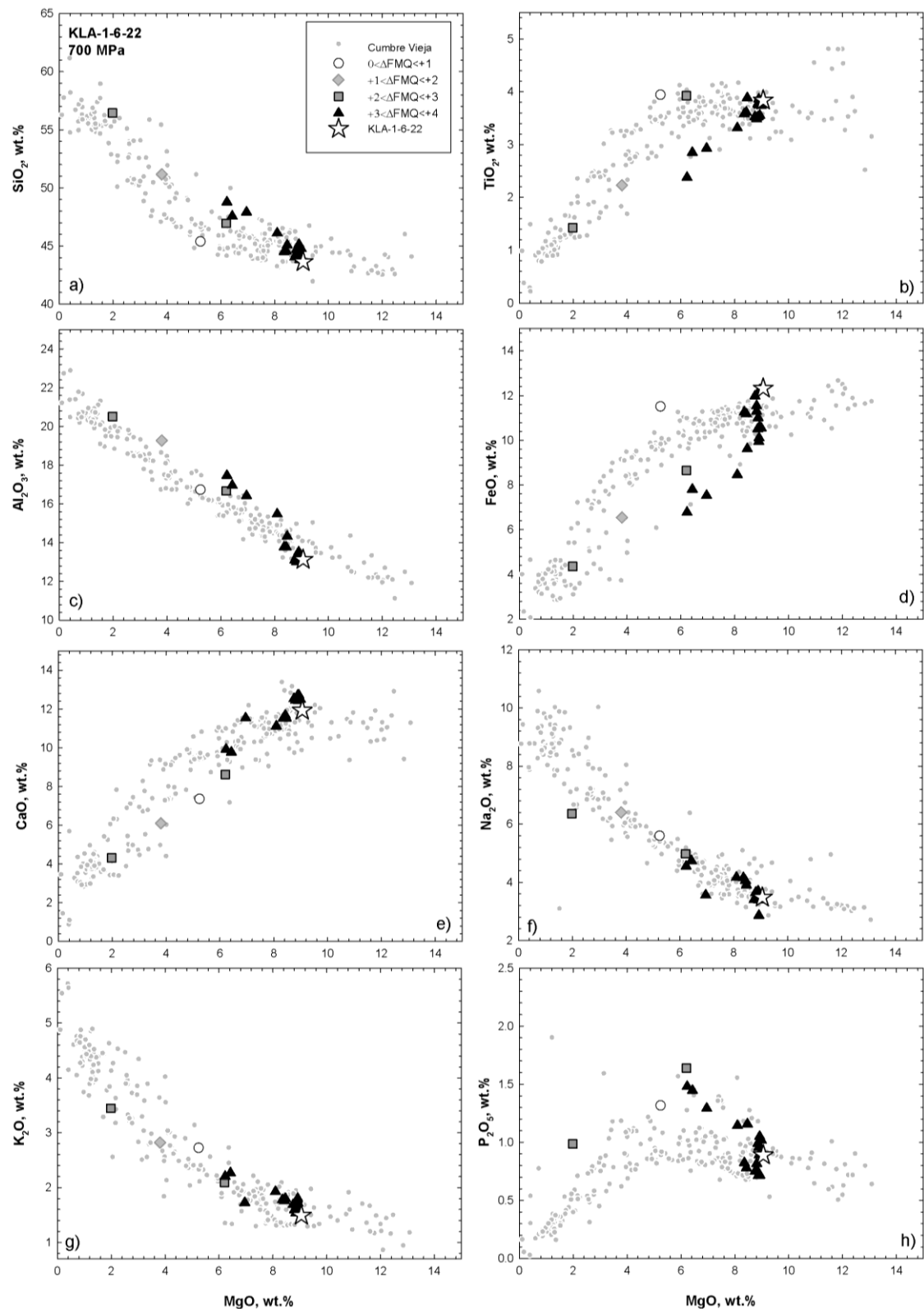
A 66: Effect of temperature ($^{\circ}\text{C}$) on the compositional evolution of experimental residual melts in equilibrium with Ol+Cpx+Mt as a function of MgO content (wt.%) using sample KLA-1-6-22 at 550 MPa in comparison to natural LLD of the Cumbre Vieja volcano (all compositions are normalized to 100%).



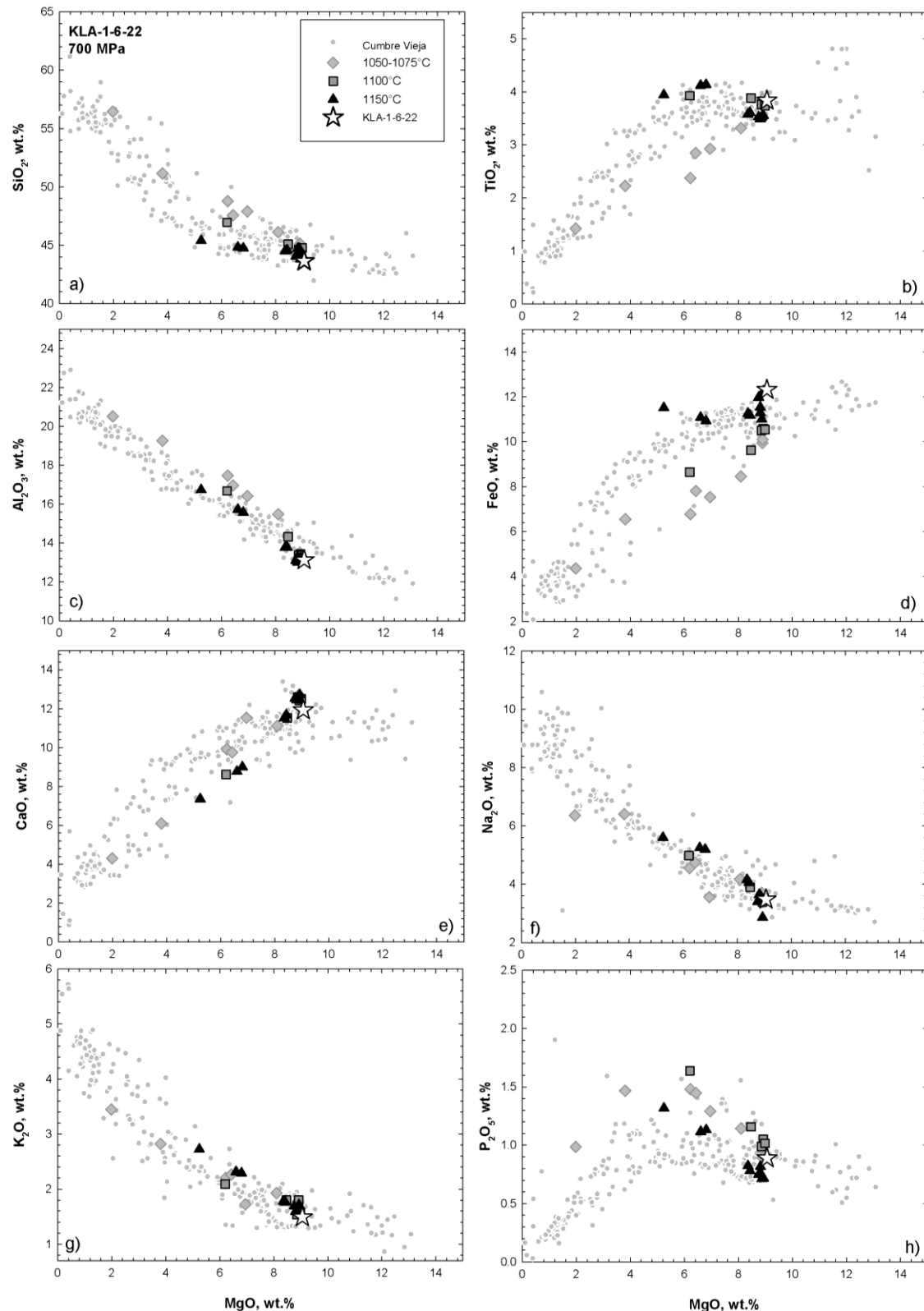
A 67: Effect of crystallizing phases on the compositional evolution of experimental residual melts as a function of MgO content (wt.%) using sample KLA-1-6-22 at 700 MPa in comparison to natural LLD of the Cumbre Vieja volcano (all compositions are normalized to 100%).



A 68: Effect of $a_{\text{H}_2\text{O}}$ on the compositional evolution of experimental residual as a function of MgO content (wt.%) using sample KLA-1-6-22 at 700 MPa in comparison to natural LLD of the Cumbre Vieja volcano (all compositions are normalized to 100%).



A 69: Effect of fO_2 on the compositional evolution of experimental residual melts as a function of MgO content (wt.%) using sample KLA-1-6-22 at 700 MPa in comparison to natural LLD of the Cumbre Vieja volcano (all compositions are normalized to 100%).



A 70: Effect of temperature (°C) on the compositional evolution of experimental residual as a function of MgO content (wt.%) using sample KLA-1-6-22 at 700 MPa in comparison to natural LLD of the Cumbre Vieja volcano (all compositions are normalized to 100%).

Lebenslauf

Persönliche Angaben

Parveen Fuchs
Geboren am 17.05.1983
Geburtsort: Bielefeld
Nationalität: deutsch

Akademischer Werdegang

Nov. 2010 - März 2014	Wissenschaftliche Mitarbeiterin am Institut für Mineralogie an der Leibniz Universität Hannover <i>Titel des PhD Projektes: "Petrogenese von Basanit-Phonolith-Serien eines ozeanischen Intraplattenvulkans: Kombination experimenteller Untersuchungen mit Geländebeobachtungen"</i>
Okt. 2008 - Okt. 2010	M.Sc. Studium in Geowissenschaften mit Schwerpunkt in Mineralogie/Petrologie an der Freien Universität Berlin Abgeschlossen mit dem Titel Master of Science in Geowissenschaften - mit "sehr gut" bestanden <i>Titel der M.Sc-Arbeit: "Metamorphoseentwicklung im westlichen Kaokogürtel, NW-Namibia: Phasenpetrologische und geochronologische Untersuchungen panafrikanischer Metasedimente"</i>
Sept. 2009 - Okt. 2010	Tutorin an der Freien Universität Berlin Petrologie und Polarisationsmikroskopie von Magmatiten & Metamorphiten Einführung in die Polarisationsmikroskopie Einführung in die Mineralogie und Kristallographie
März 2008 - Aug. 2009 4.1	Hilfswissenschaftlerin am GeoForschungsZentrum Potsdam , Sektion Experimentelle Geochemie und Mineralphysik (Dr. D. Harlov)
Apr. 2007 - Sept. 2008	B.Sc. Studium in Geowissenschaften mit Schwerpunkt in Mineralogie/Petrologie an der Freien Universität Berlin Abgeschlossen mit dem Titel Bachelor of Science in Geowissenschaften <i>Titel der B.Sc-Arbeit: "Untersuchungen zur Magmengenese und Kristallisationsgeschichte des Eisenbühlvulkans"</i>
Aug. - Okt. 2007	Praktikum am Museum für Naturkunde Berlin (PD Dr. L. Hecht)
Okt. 2004 - März 2007	Grundstudium der Geologie / Paläontologie an der Universität zu Köln - erfolgreich abgeschlossen mit dem Vordiplom
Juli 2004	Abitur am Oberstufen-Kolleg an der Universität Bielefeld
Juli - Aug. 2003	Praktikum am GeoForschungsZentrum Potsdam (PD Dr. A. Brauer)

Auszüge der Konferenzbeiträge

DMG 2013 Tübingen

Fuchs, P., Almeev, R., Wengorsch, T., Klügel, A.: Magma storage conditions and melt evolution of the basanites-phonolite series from Cumbre Vieja Volcano (La Palma, Canary Islands): An experimental approach at 400, 550 and 700 MPa. (*Mündl. Vortrag*)

EMC 2012 Frankfurt

Fuchs, P., Almeev, R., Klügel, A.: Experimental constraints on the evolution of magmatic liquids and phenocrysts of Cumbre Vieja volcano (La Palma, Canary Islands). (*Mündl. Vortrag*)

EMPG 2012 Kiel

Fuchs, P., Almeev, R., Klügel, A.: Liquid lines of descent of basanite-phonolite series of the Cumbre Vieja volcano (La Palma, Canary Islands): First experimental results at 400 MPa. (*Poster Präsentation*)

Wengorsch, T., **Fuchs, P.**, Almeev, R., Klügel, A.: Revealing true liquid compositions for natural phonolites from Cumbre Vieja volcano, La Palma Island. (*Poster Präsentation*)

Goldschmidt 2011 Prag

Fuchs, P., Almeev, R., Klügel, A.: Phase equilibria constraints on the magma evolution of basanite-phonolite series of the Cumbre Vieja volcano (La Palma, Canary Islands). (*Poster Präsentation*)

IMA 2010 Budapest

Fuchs, P., Tajcmanova, L., Konopasek, J., Zeh, A.: Different metamorphic records in the Western Kaoko Zone (NW Namibia) and their timing. (*Poster Präsentation*)